

# TECHNICAL REPORT

**CISPR  
16-3**

2003

AMENDMENT 1  
2005-07

INTERNATIONAL SPECIAL COMMITTEE ON RADIO INTERFERENCE

---

---

## Amendment 1

**Specification for radio disturbance and immunity  
measuring apparatus and methods –**

**Part 3:  
CISPR technical reports**

© IEC 2005 Droits de reproduction réservés — Copyright - all rights reserved

International Electrotechnical Commission, 3, rue de Varembé, PO Box 131, CH-1211 Geneva 20, Switzerland  
Telephone: +41 22 919 02 11 Telefax: +41 22 919 03 00 E-mail: [inmail@iec.ch](mailto:inmail@iec.ch) Web: [www.iec.ch](http://www.iec.ch)

---

---



Commission Electrotechnique Internationale  
International Electrotechnical Commission  
Международная Электротехническая Комиссия

PRICE CODE

**S**

*For price, see current catalogue*

## FOREWORD

This amendment has been prepared by CISPR subcommittee A: Radio interference measurements and statistical methods.

The text of this amendment is based on the following documents:

DTR	Report on voting
CISPR/A/572/DTR	CISPR/A/586/RVC

Full information on the voting for the approval of this amendment can be found in the report on voting indicated in the above table.

The committee has decided that the contents of this amendment and the base publication will remain unchanged until the maintenance result date indicated on the IEC web site under "http://webstore.iec.ch" in the data related to the specific publication. At this date, the publication will be

- reconfirmed,
- withdrawn,
- replaced by a revised edition, or
- amended.

---

Page 10

## 4 Technical reports

*Add, on page 186, after the existing subclause 4.6, the following new subclause:*

### 4.7 Correlation between amplitude probability distribution (APD) characteristics of disturbance and performance of digital communication systems

#### 4.7.1 Introduction

The relationship between the degradation in quality of digital communication systems and APD of disturbance is shown in the following experimental results. Actual microwave ovens (MWO), such as the transformer and the inverter types, and a noise simulator, were used as a noise source in the following experiment. Bit Error Rate without error correction was basically used as a parameter of communication system performance (e.g., W-CDMA and PHS). Throughput is used if error correction could not be removed (e.g., W-LAN, Bluetooth and PHS).

Quantitative correlation between noise parameters and system performance is shown in 4.7.6 and 4.7.7 by using measured and simulated results.

These results show that APD measurement of disturbance is suitable for evaluating its interference potential on digital communication systems. Therefore APD measurement may be applicable to the compliance test of some products or product families, such as microwave ovens.

#### 4.7.2 Influence on a wireless LAN system

The set-up for measuring communication quality degradation is shown in Figure 4.7.1, and measurement conditions are shown in Table 4.7.1. Throughput was chosen as a measure for communication quality evaluation. It was calculated from the time taken to transmit and time to receive data of a fixed size.

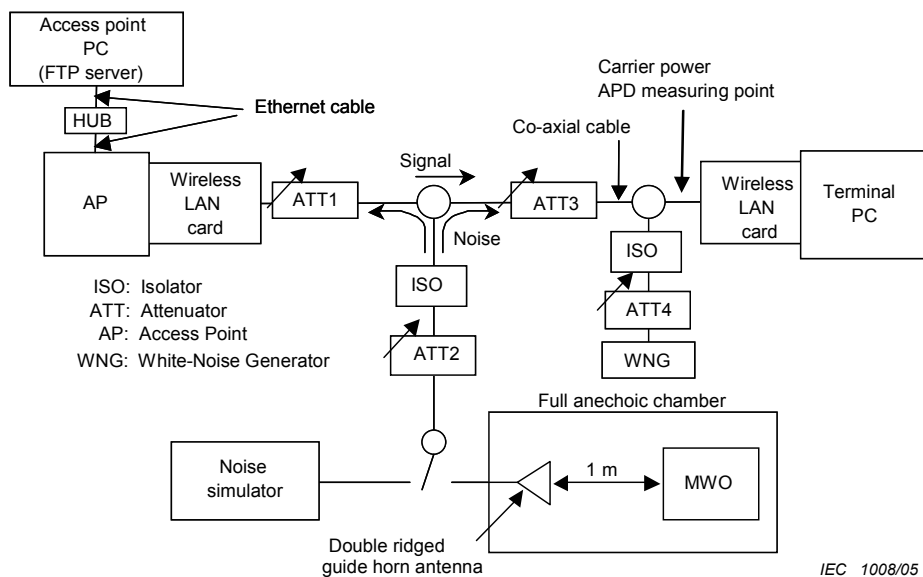


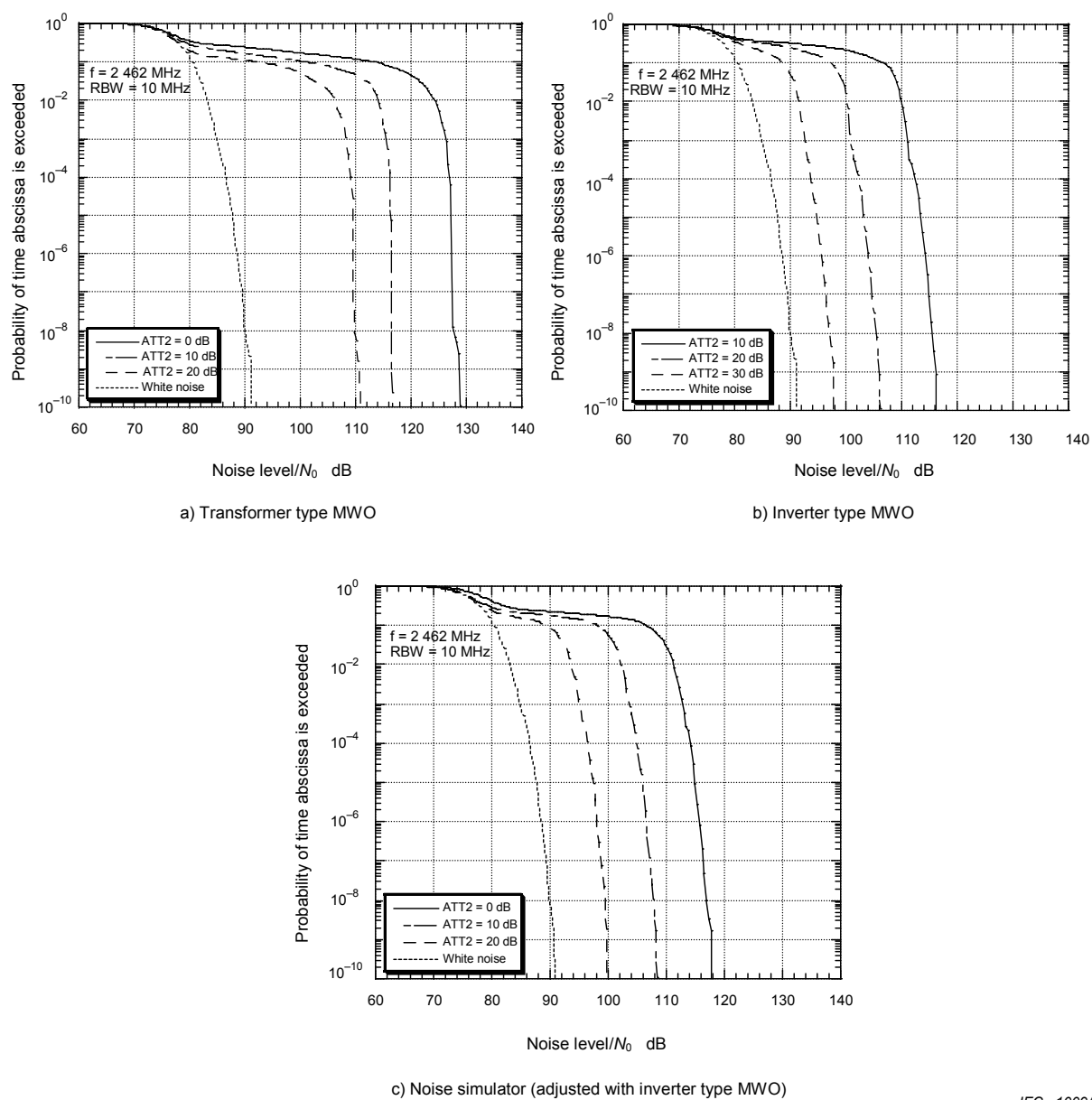
**Figure 4.7.1 – Set-up for measuring communication quality degradation of a wireless LAN**

**Table 4.7.1 – Conditions for measuring communication quality degradation**

<b>Wireless LAN</b>	Frequency (channel)	2 462 MHz (11ch)
	Transmission data	20 Mbyte
	Protocol	FTP (GET command from terminal PC)
	Transmission mode	Packet transmission
<b>Others</b>	Noise power density $N_0$ (dBm/Hz)	-154 dBm/Hz (set by ATT4)

The APDs of disturbance are shown in Figure 4.7.2. The horizontal axis shows the level of radiated noise normalized by  $N_0$ , which has been approximated as the noise level from the white noise generator. The main frequency for measuring APD was 2462 MHz. The average and root-mean-square (RMS) values of the noise level normalized by  $N_0$  derived from APD of the MWO noise and noise simulator noise are shown in Table 4.7.2.

APD of the noise simulator at  $ATT2 = 0$  dB was in good agreement with APD of the inverter type MWO at  $ATT2 = 10$  dB.



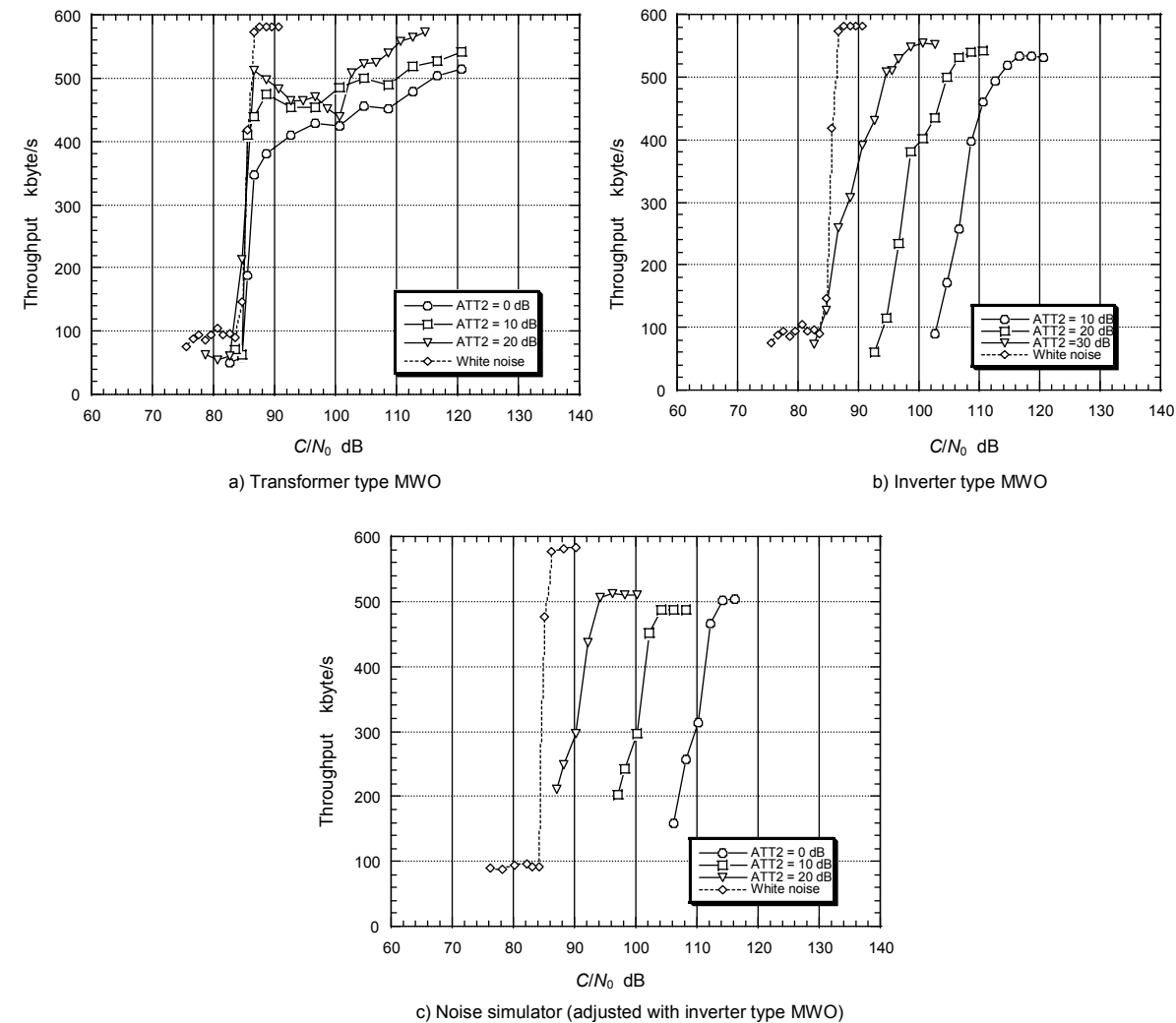
IEC 1009/05

**Figure 4.7.2 – APD characteristics of disturbance****Table 4.7.2 – Average and RMS values of noise level normalized by  $N_0$** 

		ATT2				White noise
		0 dB	10 dB	20 dB	30 dB	
Transformer type MWO	Average (dB)	111,2	101,0	92,6		77,6
	RMS (dB)	117,1	107,0	98,8		78,7
Inverter type MWO	Average (dB)		100,6	91,4	83,4	77,6
	RMS (dB)		104,4	94,8	86,2	78,7
Noise simulator	Average (dB)	100,6	91,9	83,8		77,5
	RMS (dB)	105,1	96,2	87,6		78,6

The measured communication quality degradation for various amounts of attenuation of injected noise is shown in Figure 4.7.3.

The horizontal axis shows  $C/N_0$ , where  $C$  is the sub-carrier power and  $N_0$  is the noise power density.



IEC 1010/05

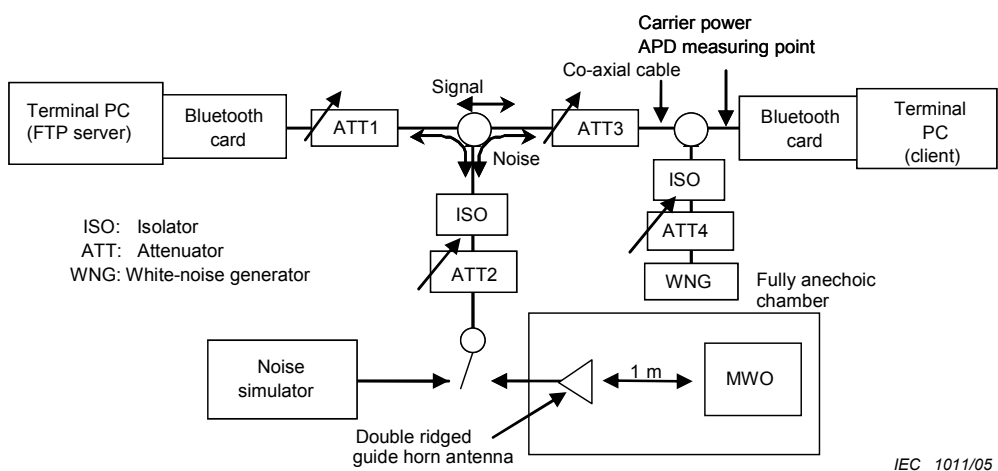
**Figure 4.7.3 – Wireless LAN throughput influenced by noise**

The throughput influenced by a transformer type MWO is 400 kbytes/s or more when  $C/N_0$  is 90 dB or more, and decreases rapidly when  $C/N_0$  is below 90 dB. This tendency is almost the same irrespective of the noise level. On the other hand, the throughput influenced by an inverter type MWO decreases almost in proportion to the noise level. The throughput influenced by a noise simulator has almost the same degradation characteristics as that for an inverter type MWO.

#### 4.7.3 Influence on a Bluetooth system

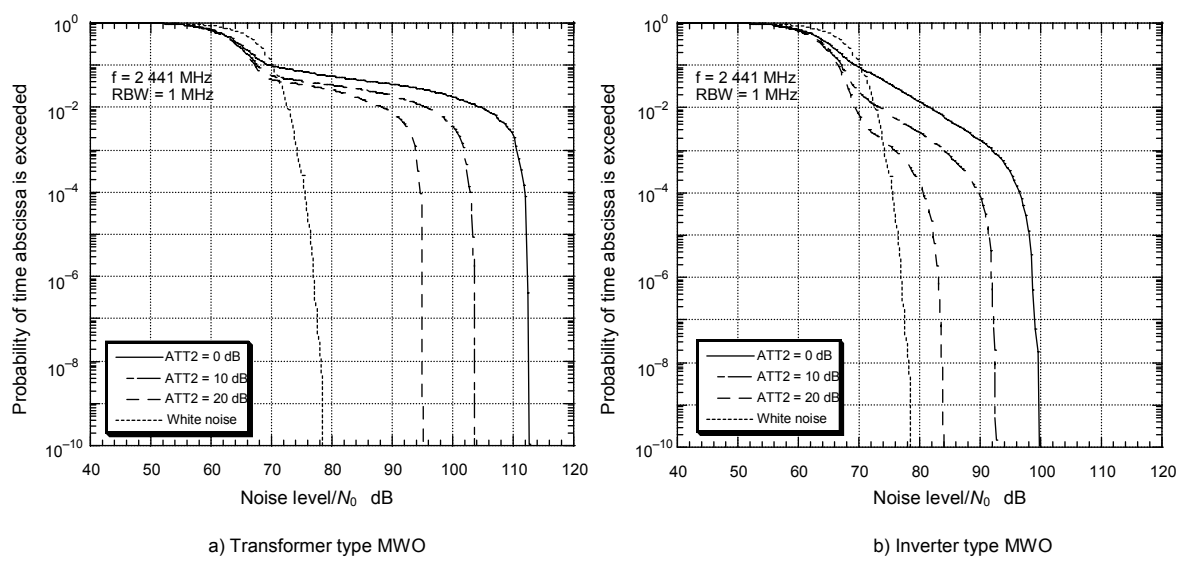
The setup for measuring communication quality degradation is shown in Figure 4.7.4, and measurement conditions are shown in Table 4.7.3.

Throughput was chosen as the measure for communication quality evaluation.

**Figure 4.7.4 – Set-up for measuring the communication quality degradation of Bluetooth****Table 4.7.3 – Conditions for measuring communication quality degradation of Bluetooth**

<b>Bluetooth</b>	Frequency	2 400 – 2 483,5 MHz
	Transmission data	2,5 Mbyte
	Protocol	FTP (GET command from terminal PC)
	Transmission mode	Packet exchange data transmission mode
<b>Others</b>	Noise power density $N_0$ (dBm/Hz)	-148 dBm/Hz (set by ATT4)

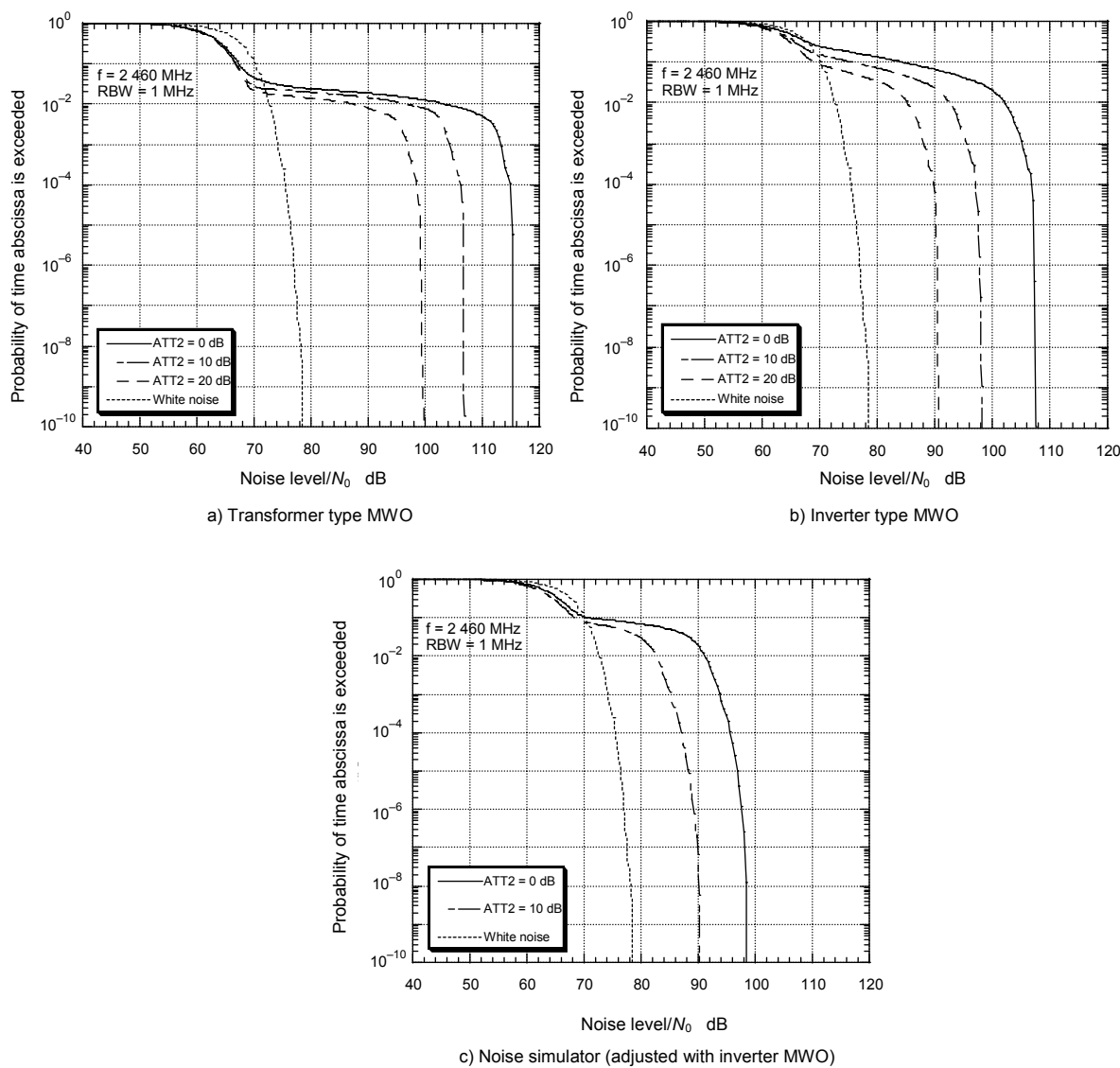
The APDs at a frequency of 2 441 MHz are shown in Fig. 4.7.5, and the average and RMS values of noise level normalized by  $N_0$  are shown in Table 4.7.4.

**Figure 4.7.5 – APD of disturbance of actual MWO (2 441MHz)**

**Table 4.7.4 – Average and RMS values of noise level normalized by  $N_0$** 

		ATT2				White noise
		0 dB	10 dB	20 dB	30 dB	
Transformer type MWO	Average (dB)	89,8	80,8	73,7		67,1
	RMS (dB)	99,2	90,2	82,5		68,3
Inverter type MWO	Average (dB)	70,7	65,4	63,5		67,1
	RMS (dB)	80,6	73,3	66,0		68,3

The APDs measured at 2 460 MHz, where the noise level of an MWO is at maximum, are shown in Figure 4.7.6, and the average and RMS values of noise normalized by  $N_0$  are shown in Table 4.7.5. The noise level is about 10 dB larger than that at the frequency of 2 441 MHz. The APD of the noise simulator at  $ATT2 = 0$  dB is in good agreement with that of the inverter type MWO at  $ATT2 = 10$  dB.



IEC 1013/05

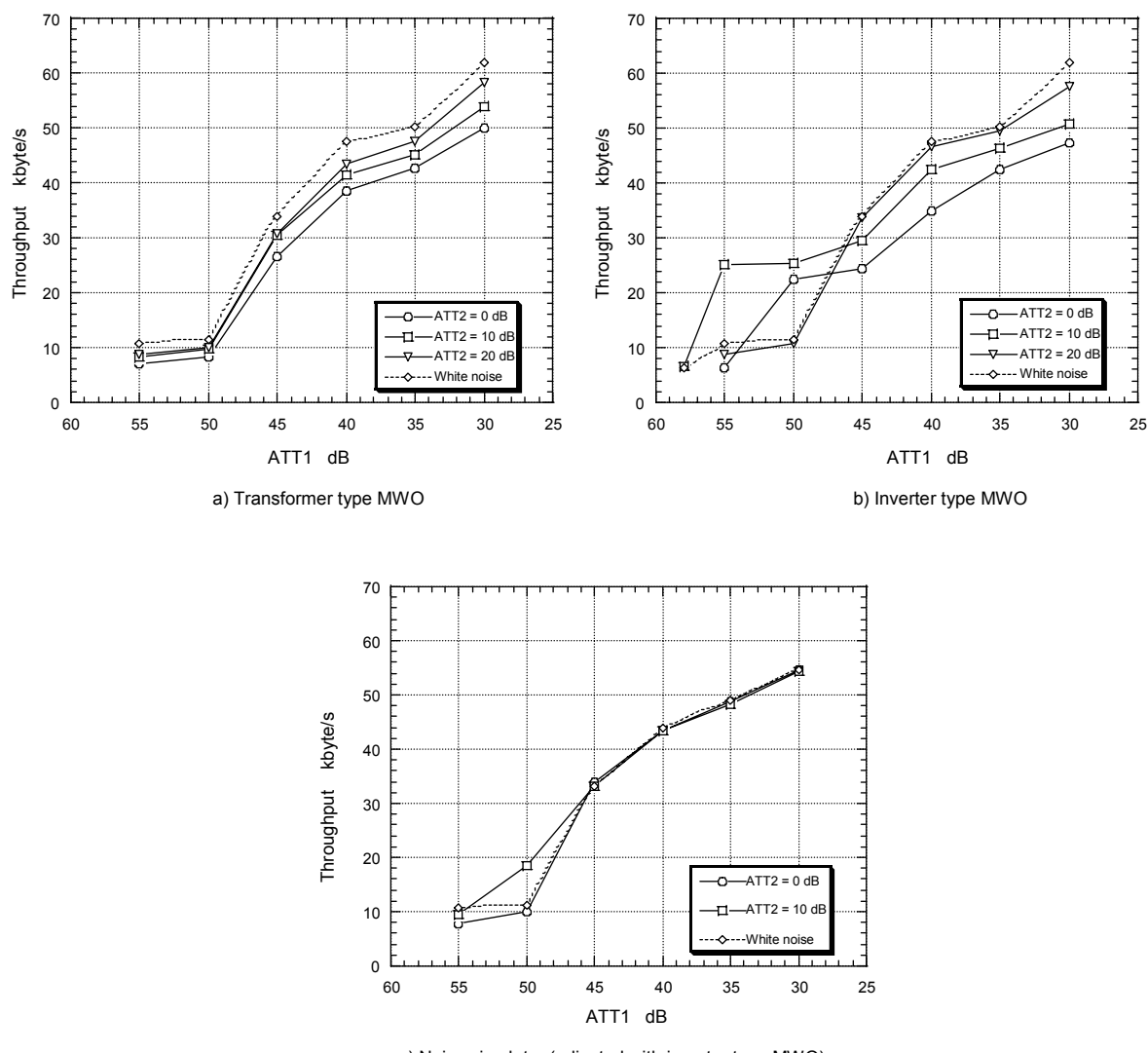
**Figure 4.7.6 – APD characteristics of disturbance (2 460 MHz)**

**Table 4.7.5 – Average and RMS values of noise level normalized by  $N_0$** 

		ATT2				White noise
		0 dB	10 dB	20 dB	30 dB	
Transformer type MWO	Average (dB)	87,8	78,4	71,4		67,1
	RMS (dB)	94,9	85,4	78,0		68,3
Inverter type MWO	Average (dB)	70,7	65,4	63,5		67,1
	RMS (dB)	80,6	73,3	66,0		68,3
Noise simulator	Average (dB)	77,6	69,8			67,1
	RMS (dB)	84,1	75,5			68,3

The measured communication quality degradation for various amounts of attenuation of injected noise is shown in Figure 4.7.7.

There is only a minor difference in degradation caused by the level of noise between a transformer and an inverter type MWO. This is because Bluetooth performs frequency hopping, and is hard to be influenced by noise continuously. Furthermore, there is almost no difference in communication quality degradation for a noise simulator.

**Figure 4.7.7 – Throughput of Bluetooth influenced by noise**

IEC 1014/05

According to the specifications, Bluetooth controls the transmission power automatically depending on the communication situation. The sub-carrier power at the reception point cannot be obtained uniquely since transmission power may change when ATT1 is changed. The horizontal axis in this figure shows the attenuation of signal power.

#### 4.7.4 Influence on a W-CDMA system

The set-up for measuring communication quality degradation is shown in Figure 4.7.8, and measurement conditions are shown in Table 4.7.6.

Bit error rate (BER) was chosen as the measure for communication quality evaluation.

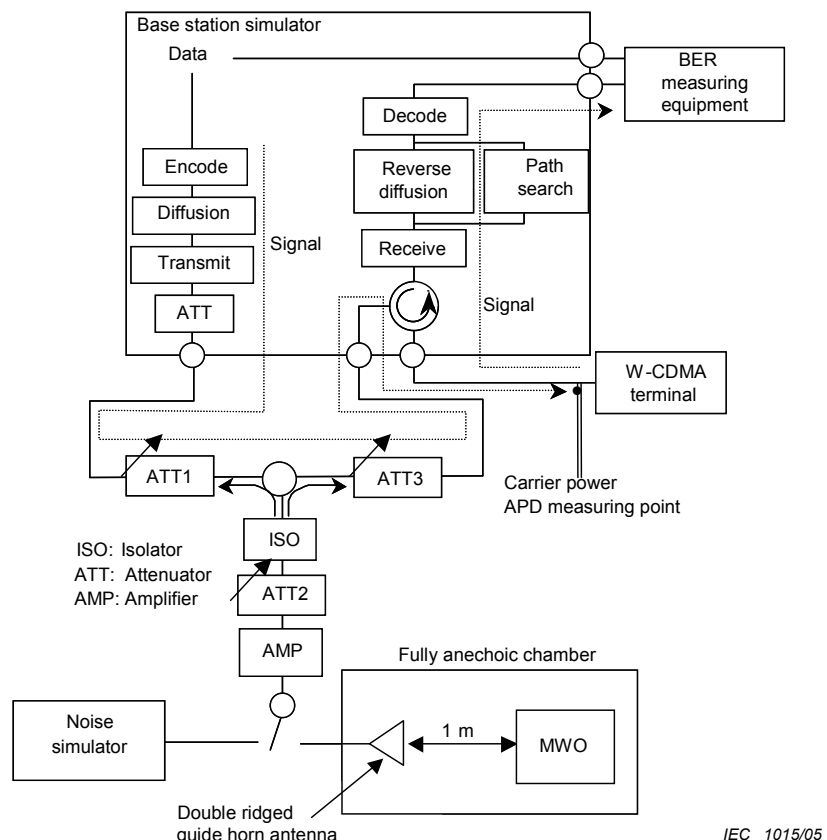
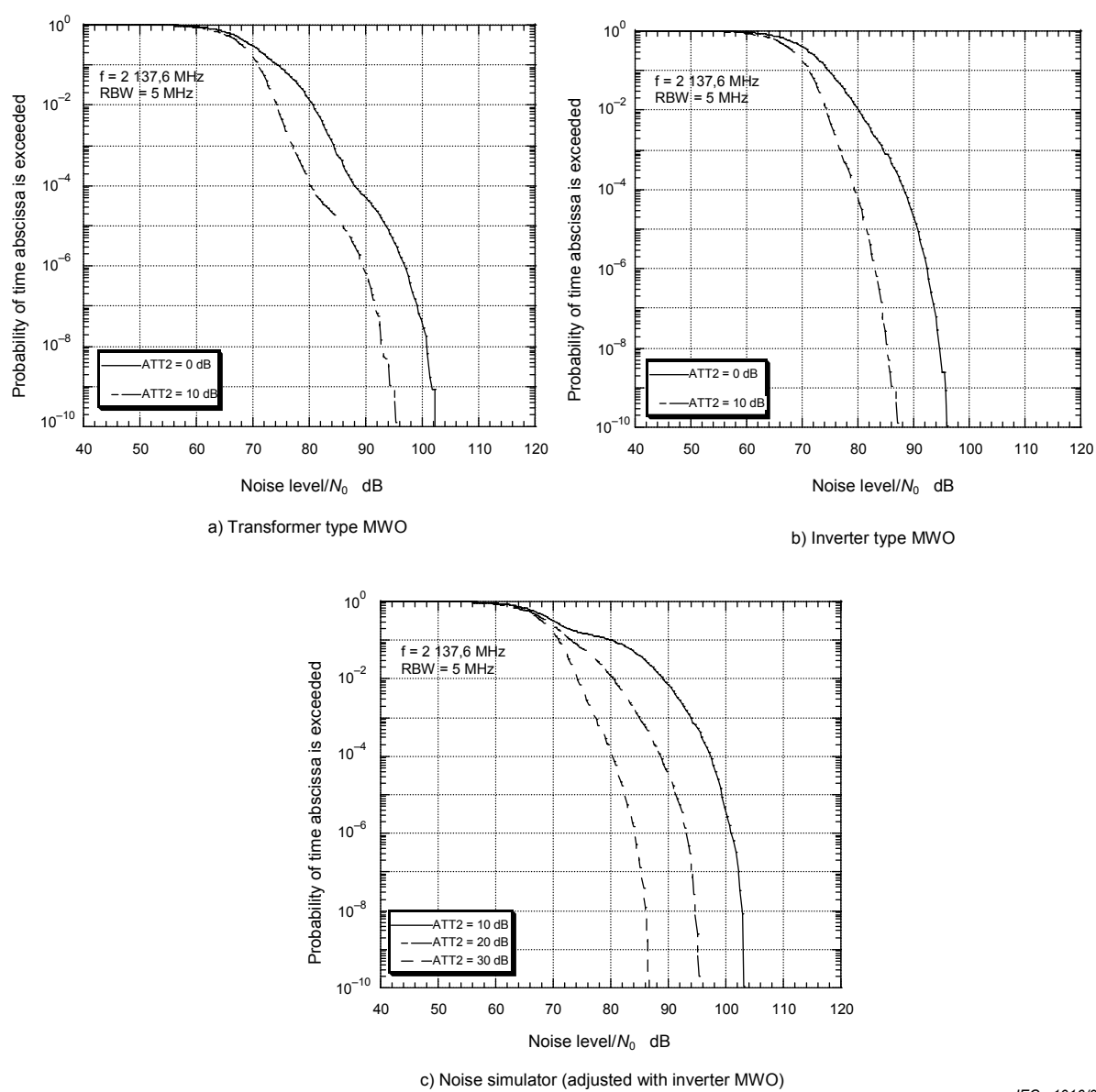


**Figure 4.7.8 – Setup for measuring the BER of W-CDMA**

**Table 4.7.6 – Conditions for measuring communication quality degradation of W-CDMA**

<b>Base band simulator</b>	Frequency	2 137,6 MHz (downlink)
	Chip rate	3,84 Mcps
	Spread rate	Uplink: DPDCH 64 / downlink: DPCH 128
	Data rate	12,2 kbps (acoustic)
	Transmission data	6 Mbit
	Transmission mode	RMC communication test (UE turn) 3GPP TS34.121

The measured APDs of the noise are shown in Figure 4.7.9, and the average and RMS values of the noise level normalized by  $N_0$  are shown in Table 4.7.7. The APD of the noise simulator at ATT2 = 0 dB is in good agreement with the APD of the inverter type MWO at ATT2 = 10 dB.



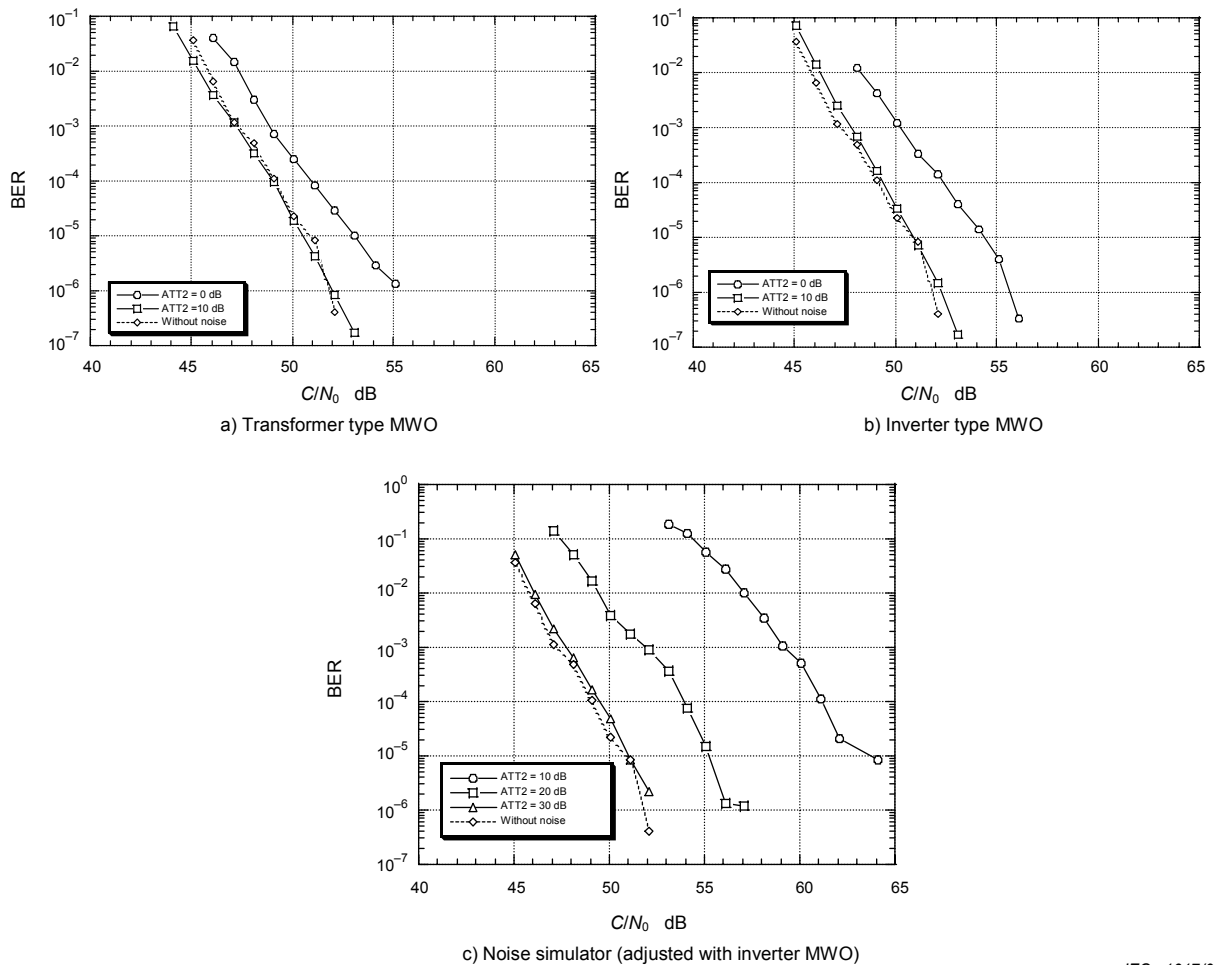
IEC 1016/05

**Figure 4.7.9 – APD characteristics of disturbance****Table 4.7.7 – Average and RMS values of noise level normalized by  $N_0$** 

		ATT2				Receiver noise
		0 dB	10 dB	20 dB	30 dB	
Transformer type MWO	Average (dB)	71,1	67,7			67,2
	RMS (dB)	75,1	69,4			68,6
Inverter type MWO	Average (dB)	71,6	68,0			67,2
	RMS (dB)	74,7	69,4			68,6
Noise simulator	Average (dB)		77,1	70,4	67,7	67,2
	RMS (dB)		83,3	74,7	69,3	68,6

The measured communication quality degradation for various amounts of attenuation of injected noise is shown in Figure 4.7.10.

For both types of MWO, the BER was degraded by several dB after a 10 dB change in noise level. Moreover, BER characteristics influenced by the noise simulator are in good agreement in these measurement results.



IEC 1017/05

**Figure 4.7.10 – BER of W-CDMA caused by radiation noise**

#### 4.7.5 Influence on Personal Handy Phone System (PHS)

The set-ups for measuring communication quality degradation are shown in Figures 4.7.11 and 4.7.12, and conditions for measuring throughput and BER are shown in Tables 4.7.8 and 4.7.9.

Throughput and BER were chosen as measures for evaluating the communication quality of PHS.

The measured APDs are shown in Figure 4.7.13, and the average and RMS values of noise normalized by  $N_0$  are shown in Table 4.7.10.

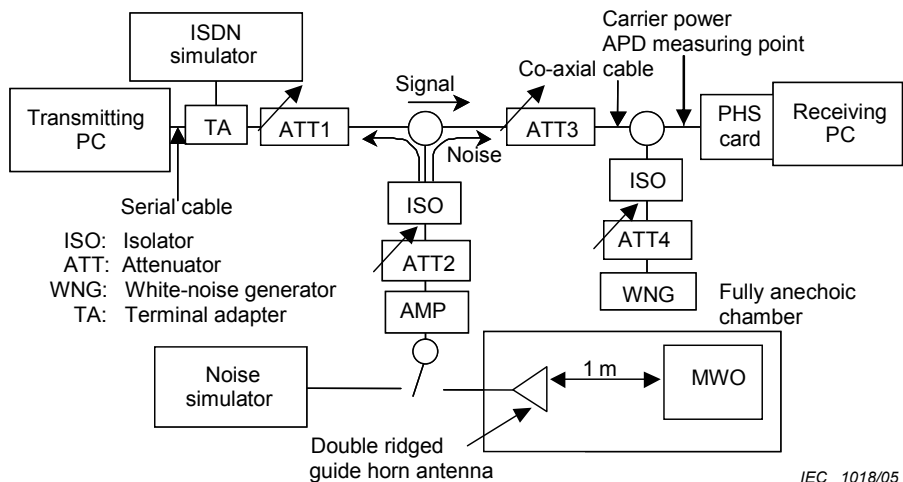


**Figure 4.7.11 – Set-up for measuring the PHS throughput**

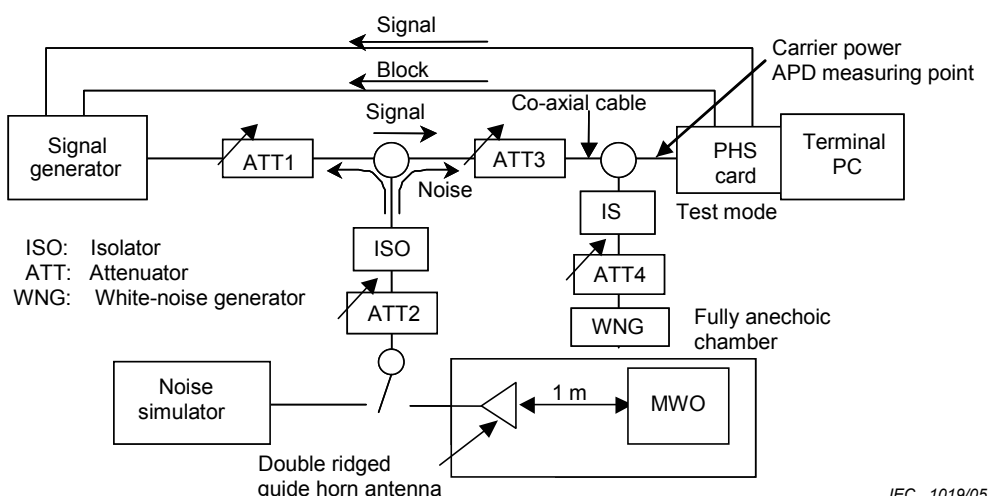


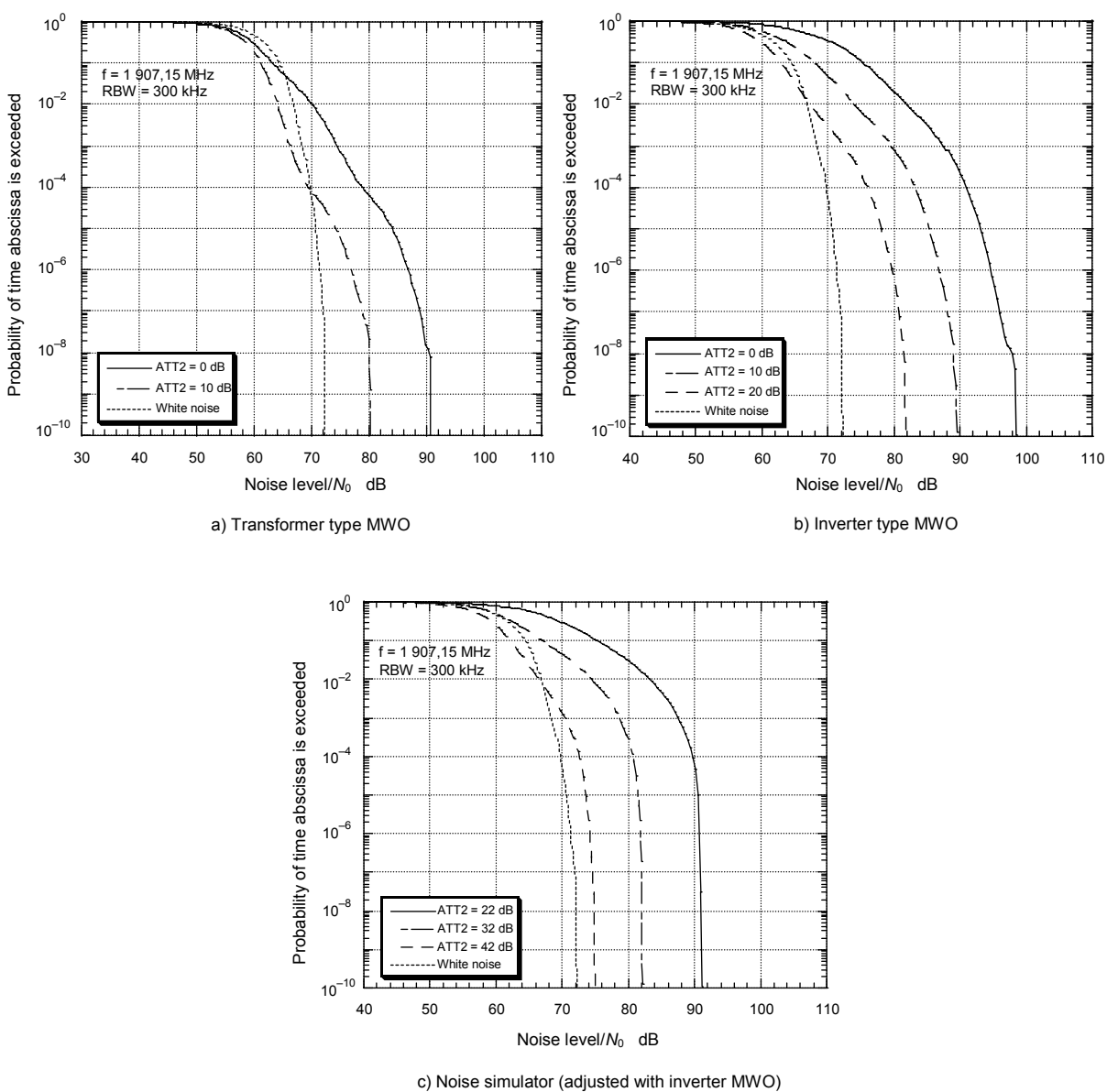
**Figure 4.7.12 – Set-up for measuring the BER of PHS**

**Table 4.7.8 – Conditions for measuring the PHS throughput**

<b>PHS</b>	Transmission data	About 376 kbytes data
	Transmission system	Non protocol
	Transmission mode	32 kbps real time data transmission
<b>Others</b>	Noise power density $N_0$ (dBm/Hz)	-160 dBm/Hz (set by ATT4)

**Table 4.7.9 – Conditions for measuring the BER of PHS**

<b>PHS</b>	Frequency (channel)	1 907,15 MHz (41ch)
	Transmission data	5 Mbit PN9
	Data rate	32 kbps
<b>Others</b>	Noise power density $N_0$ (dBm/Hz)	-160 dBm/Hz (set by ATT4)



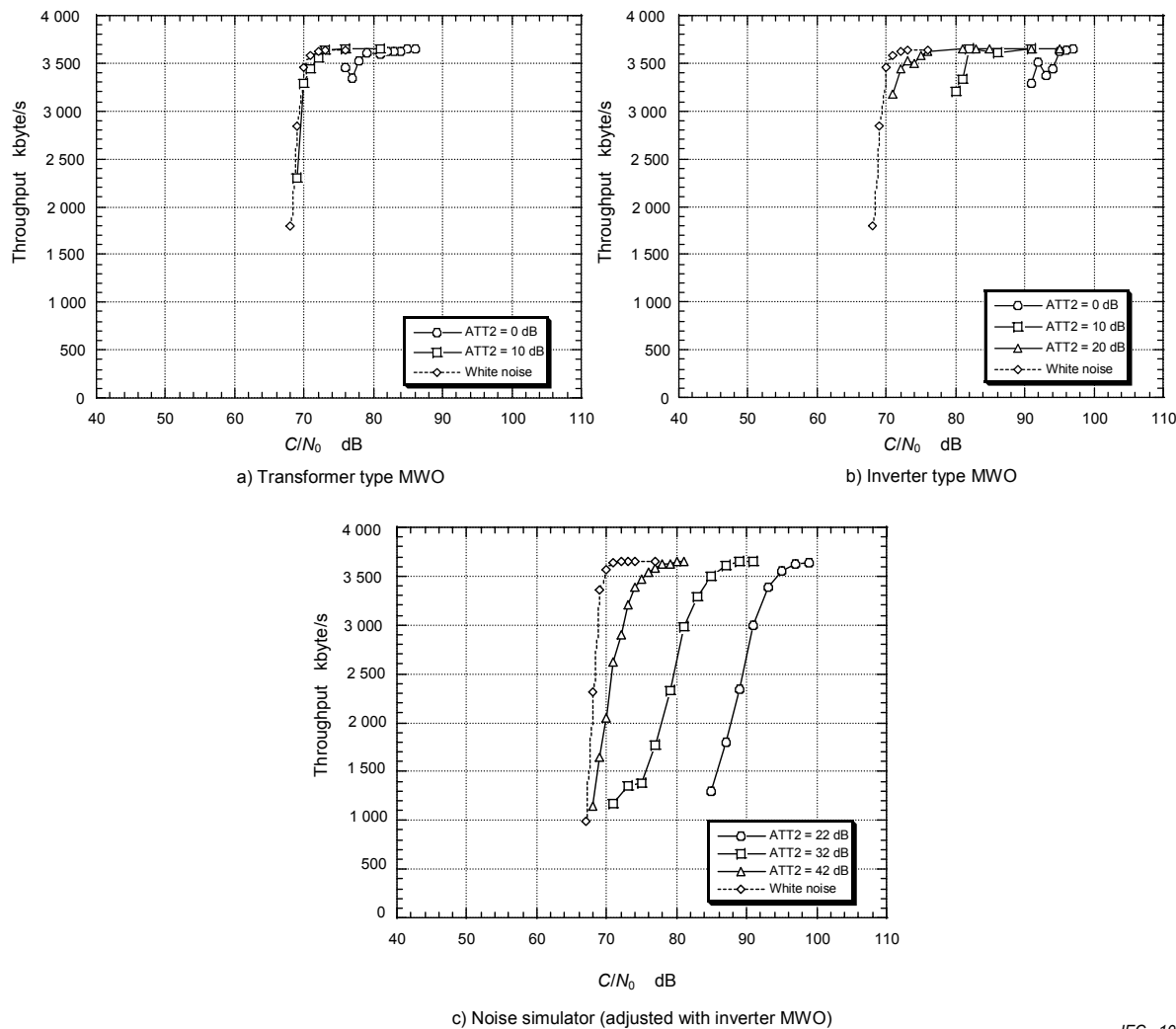
IEC 1020/05

**Figure 4.7.13 – APD characteristics of disturbance****Table 4.7.10 – Average and RMS values of noise level normalized by  $N_0$** 

		ATT2				White noise
		0 dB	10 dB	20 dB	30 dB	
Transformer type MWO	Average (dB)	60,6	58,1			61,2
	RMS (dB)	64,9	59,4			62,4
Inverter type MWO	Average (dB)	72,6	64,9	59,9	58,0	61,2
	RMS (dB)	76,7	68,9	62,5	59,3	62,4
Noise simulator	Average (dB)	72,3	64,2	59,1	57,8	61,2
	RMS (dB)	77,0	68,2	61,1	59,0	62,4

NOTE The values of ATT2 are 22, 32, 42 and 52 dB, respectively for the noise simulator.

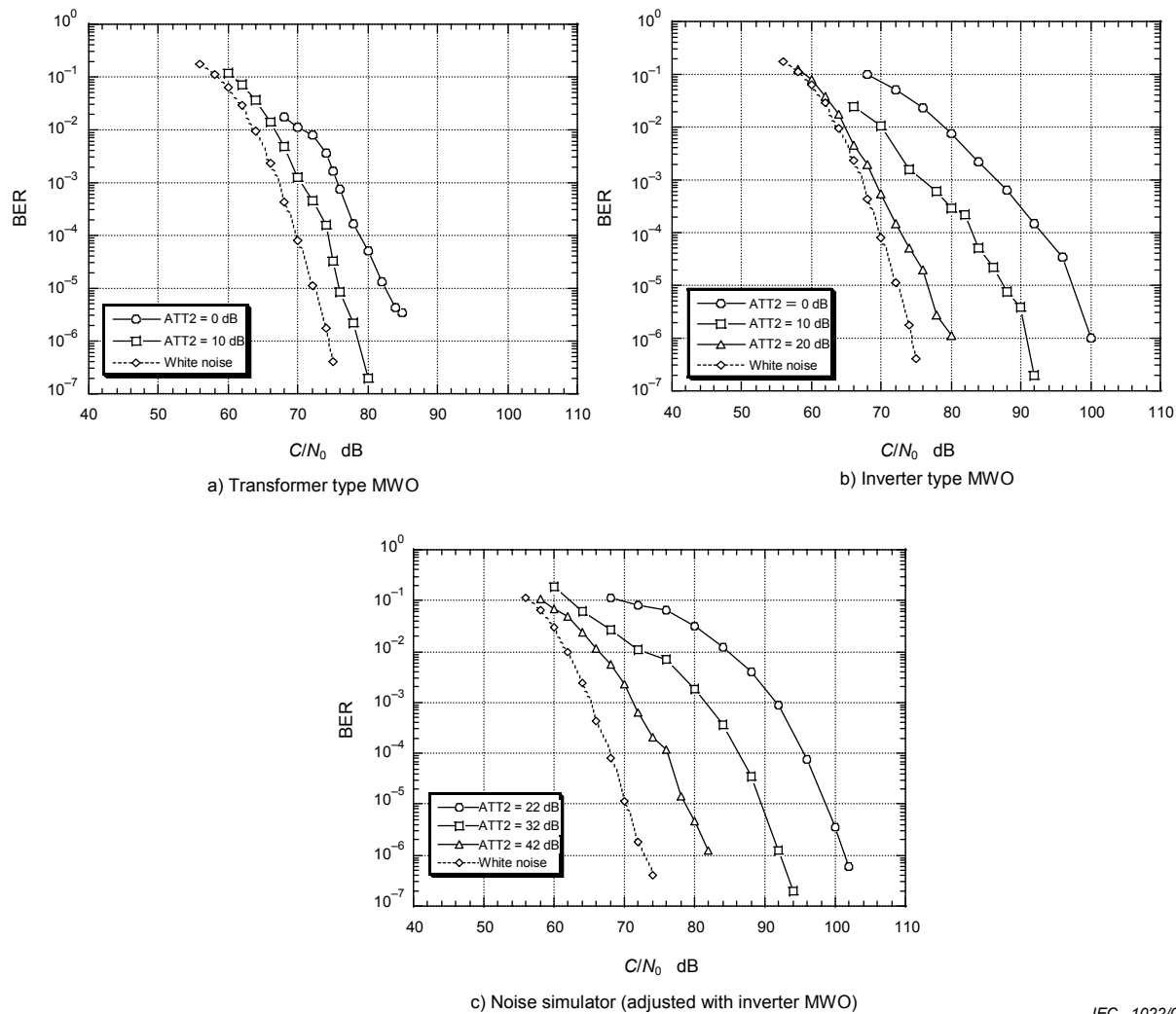
The measured throughput for various amounts of attenuation of injected noise is shown in Figure 4.7.14.



IEC 1021/05

**Figure 4.7.14 – PHS Throughput caused by radiation**

Similarly, the measured BER is shown in Figure 4.7.15. The BER characteristics caused by the noise simulator were in good agreement in the measurement results of the inverter type MWO.



IEC 1022/05

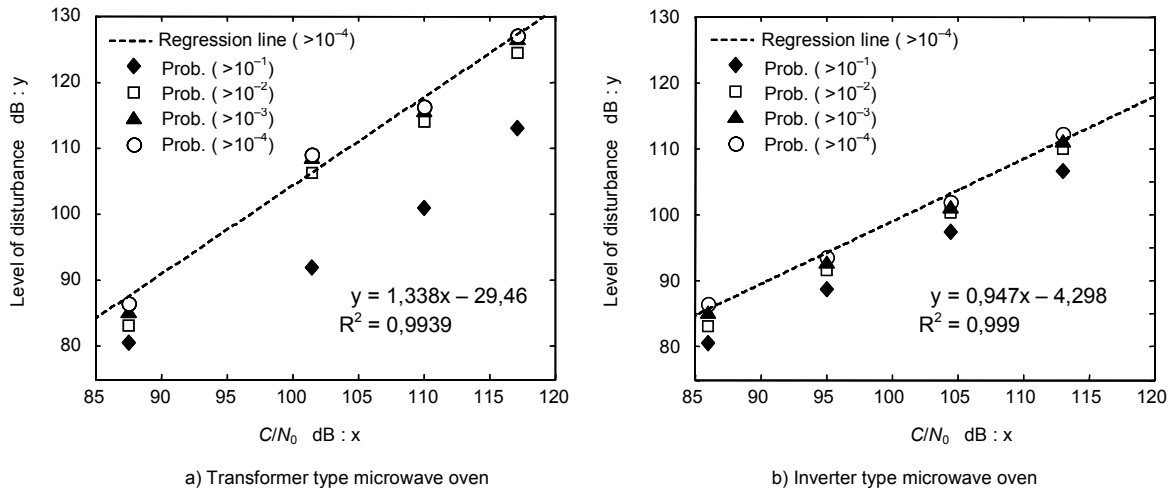
**Figure 4.7.15 – BER of PHS caused by radiation noise**

#### 4.7.6 Quantitative correlation between noise parameters and system performance

Correlations between the noise parameter of the disturbance (levels of disturbance correspond to certain probability that is derived from APD) and degradation of system performance (throughput and/or Bit Error Rate) are evaluated for the communication systems described in 4.7.2 to 4.7.5.

##### 4.7.6.1 Wireless LAN (throughput)

From Figures 4.7.2(a) and (b), the disturbance voltage for each probability, e.g.,  $10^{-1}$ ,  $10^{-2}$ ,  $10^{-3}$ ,  $10^{-4}$ , was read.  $C/N_0$  values that are necessary to assure the throughput of 500 kByte/s under microwave oven disturbance were obtained from Figures 4.7.3(a) and (b). The correlation between the disturbance voltages and the  $C/N_0$  values is plotted in Figures 4.7.16(a) and (b) for a transformer type oven and inverter type oven, respectively.



IEC 1023/05

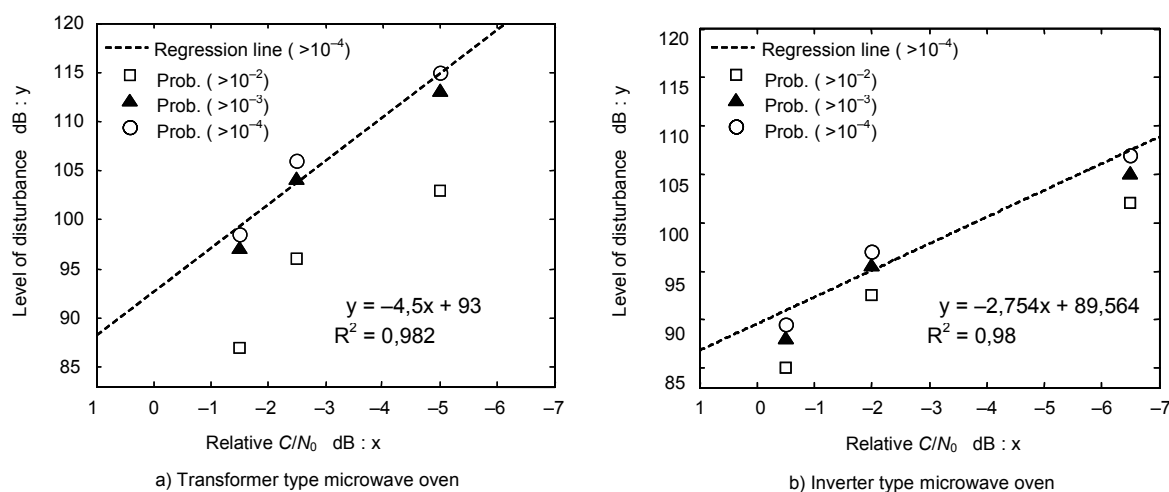
**Figure 4.7.16 – Correlation of the disturbance voltages with the system performance(C/N<sub>0</sub>)**

In Figure 4.7.16, the linear regression line by using the values for  $10^{-4}$  probability is also plotted with the equation and correlation coefficients  $R$ . It is found that  $10^{-4}$  probability values are well correlated to the  $C/N_0$  and thus these values are suitable for the noise parameters to estimate the degradation of the system performance.

#### 4.7.6.2 Bluetooth (throughput)

From Figures 4.7.6(a) and (b), the disturbance voltage for each probability was read. As shown in Figure 4.7.4, not only MWO disturbance but also white noise was injected to the communication link. Then, disturbance voltages are meaningful only when MWO disturbance exceeds the white noise. Therefore, probability of  $10^{-1}$  value was ignored and probability of  $10^{-2}$ ,  $10^{-3}$  and  $10^{-4}$  values were used in the evaluation below.

Relative  $C/N_0$  values that are necessary to assure the throughput of 40 kByte/s under microwave oven disturbance were obtained from Figures 4.7.7(a) and (b) (Relative  $C/N_0 = 0$  dB corresponds to ATT1= 43 dB). The correlation between the disturbance voltages and the relative  $C/N_0$  values are plotted in Figures 4.7.17(a) and (b) for a transformer type oven and inverter type oven, respectively.



IEC 1024/05

**Figure 4.7.17 – Correlation of the disturbance voltages with the system performance**

In Figure 4.7.17, the linear regression line by using the values for  $10^{-4}$  probability is also plotted with the equations and correlation coefficients. The same results were obtained as in subclause 4.7.6.1.

#### 4.7.6.3 W-CDMA (BER)

From Figures 4.7.9(a) and (b), disturbance voltages for each probability, e.g.,  $10^{-2}$ ,  $10^{-3}$ ,  $10^{-4}$ , were read.  $C/N_0$  values that are necessary to assure the BER of  $10^{-4}$  under microwave oven disturbance were obtained from Figures 10(a) and (b). Because only two curves available in the APD and BER, regression analyses were not performed.

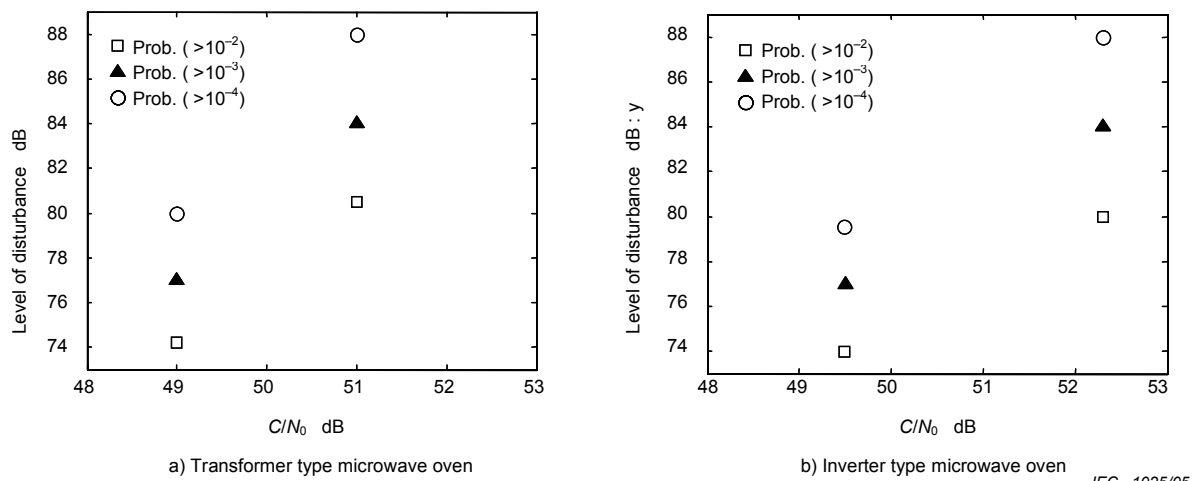


**Figure 4.7.18 – Correlation of the disturbance voltages with the system performance**

IEC 1025/05

#### 4.7.6.4 PHS (BER and throughput)

Same analyses were performed on PHS data.  $C/N_0$  values correspond to the signal input that is necessary to assure the BER of  $10^{-4}$  under microwave oven disturbance. The correlation between the disturbance level and the  $C/N_0$  values is plotted in Figures 4.7.19(a) and (b) for a transformer type oven and inverter type oven, respectively.

Because only one set of data was usable in the APD and BER for the transformer type oven, regression analysis was not performed. On the other hand, excellent correlation was confirmed in the case of inverter type oven.

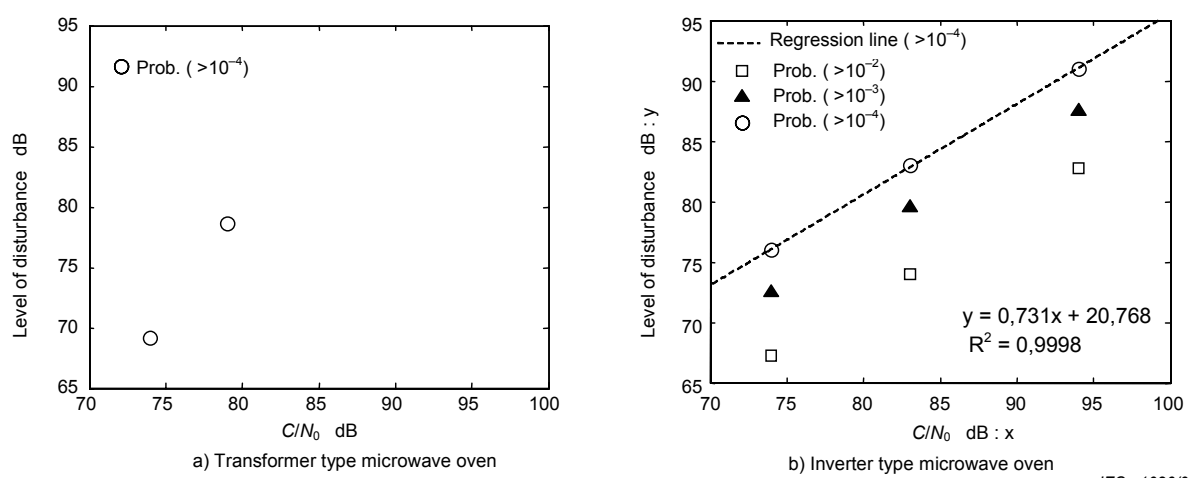


**Figure 4.7.19 – Correlation of the disturbance voltages with the system performance( $C/N_0$ )**

IEC 1026/05

Additional analyses were performed on PHS data. From Figures 4.7.13(a) and (b), disturbance voltages for each probability were read.  $C/N_0$  values correspond to the signal input that is necessary to assure the throughput of 3,5 kByte/s under microwave oven disturbance were read from Figures 4.7.14(a) and (b). The correlation between the disturbance level and the  $C/N_0$  values are plotted in Figures 4.7.20(a) and (b) for a transformer type oven and inverter type oven, respectively. Same results were obtained as for the correlation with BER.

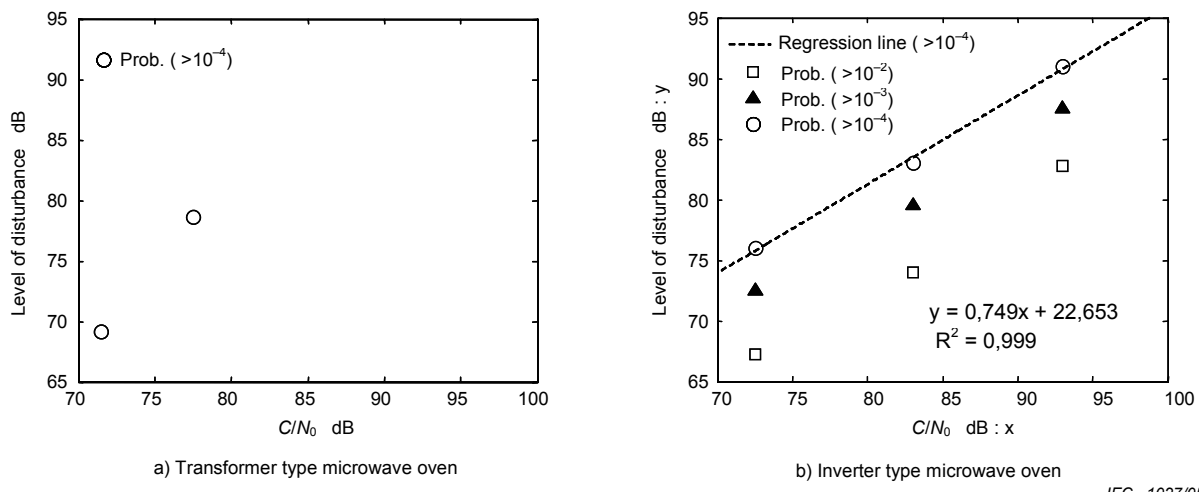
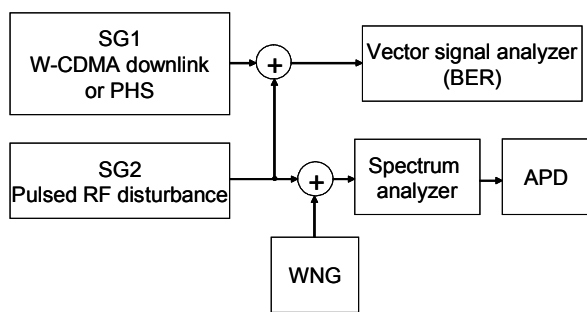


**Figure 4.7.20 – Correlation of the disturbance voltages with the system performance( $C/N_0$ )**

IEC 1027/05

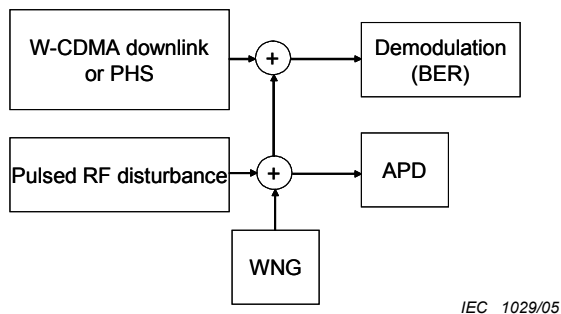
#### 4.7.7 Quantitative correlation between noise parameters of repetition pulse and system performance of PHS and W-CDMA (BER)

Correlations between APD of repetition pulse noise and communication quality degradation of PHS and W-CDMA are obtained by the following additional experiment and simulation. The experimental set-up for measuring communication quality degradation of the PHS or W-CDMA is shown in Figure 4.7.21. Repetition pulses combined with Gaussian noise are used as a disturbance. The Gaussian noise level is adjusted to the same noise floor level of vector signal analyzer for BER measurement and spectrum analyzer for APD measurement. Concerning repetition pulses, the pulse width is constant (100 µs) and the repetition frequency is variable. Figure 4.7.22 shows a block-diagram of numerical simulation for estimating communication quality degradation. In this simulation, the same noise parameters are used as for the experiment.



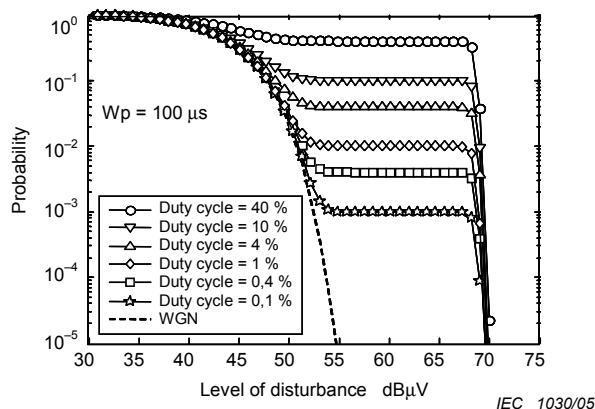
IEC 1028/05

**Figure 4.7.21 – Experimental set-up for measuring communication quality degradation of a PHS or W-CDMA**



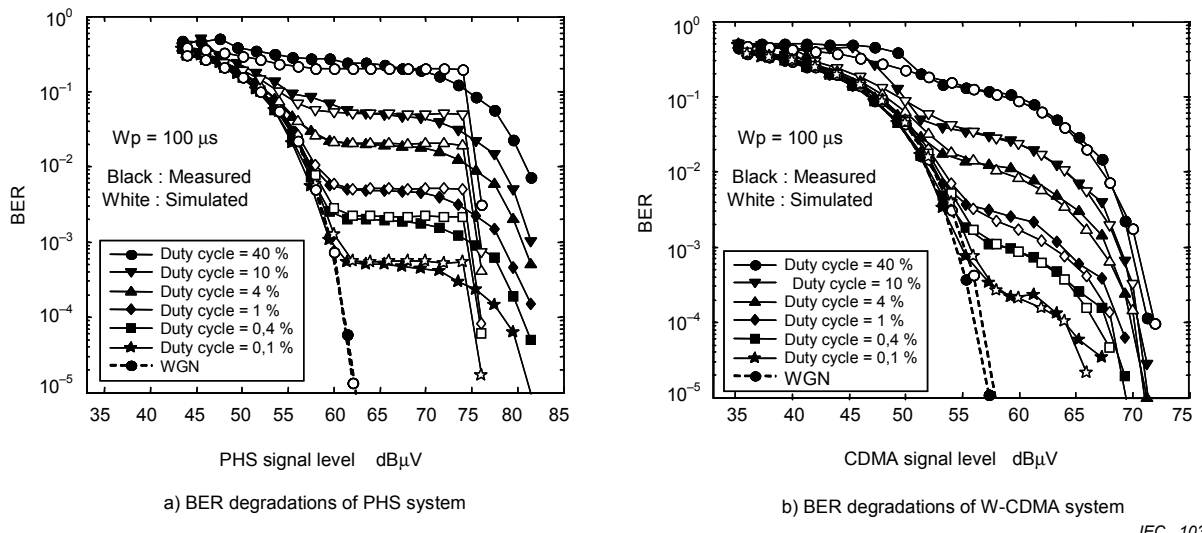
**Figure 4.7.22 – Simulation set-up for estimating communication quality degradation of a PHS or W-CDMA**

Measured APD are shown in Figure 4.7.23. Marker type represents the duty cycle of the pulse disturbance, i.e., circle, inverted triangle, triangle, diamond, square and star indicate 40 %, 10 %, 4 %, 1 %, 0,4 %, respectively. The dashed line shows the APD of Gaussian noise without repetition pulse.



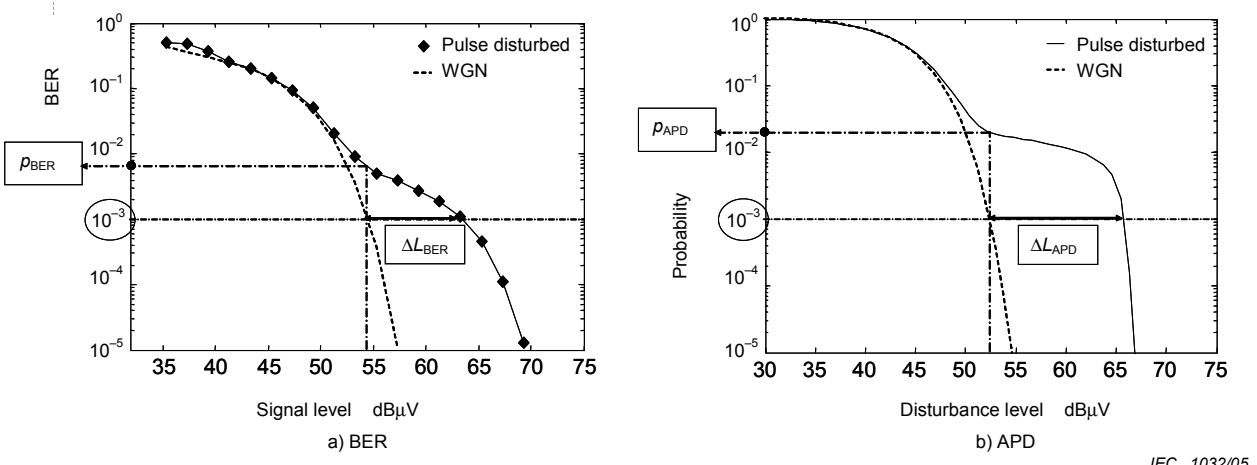
**Figure 4.7.23 – APD of pulse disturbance**

Measured BER and estimated BER by numerical simulations are shown in Figures 4.7.24 (a) and (b) for PHS system and W-CDMA system, respectively. Measured BER can be verified by the numerical simulation results. In the case of PHS results, simulation results do not show fully agreements at high signal level since the simulation model of receiver is simplified as  $\pi/4$  QPSK with a synchronized detector that is different from the experimental setup.



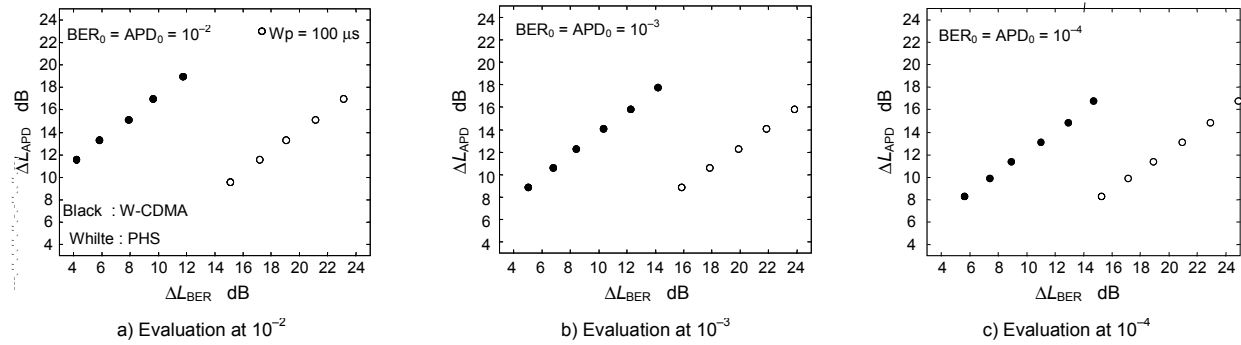
**Figure 4.7.24 – BER degradation of PHS and W-CDMA caused by repetition pulse (Carrier power; -35 dBm)**

Figure 4.7.25 explains the evaluation method for quantitative correlation between BER and APD. For the level comparison,  $\Delta L_{BER}$  and  $\Delta L_{APD}$  can be defined as disturbance effects on BER and APD. They are measured by the difference of level between Gaussian noise (without repetition pulse) and disturbance (with repetition pulse) at a certain rate of BER and at a certain probability of APD, respectively. Similarly,  $p_{BER}$  and  $p_{APD}$  are defined as the probabilities caused by disturbance on BER and APD, respectively.



**Figure 4.7.25 – Evaluation method of the correlation between BER and APD**

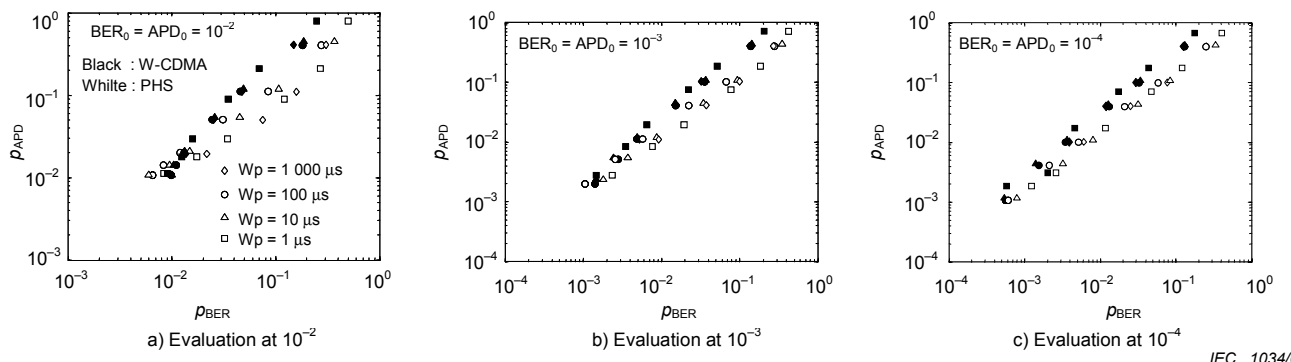
Correlation between measured  $\Delta L_{BER}$  and  $\Delta L_{APD}$  for several pulse amplitudes are shown in Figure 4.7.26, where the pulse has constant duty cycle (10 %, pulse width: 100  $\mu$ s). The disturbance is generated by modulating a carrier with the repetition pulse. The carrier power is set from -45 dBm to -35 dBm with 2 dB step. Black mark and white mark show the characteristics of W-CDMA and PHS, respectively. BER and probability values ( $BER_0$ ,  $APD_0$ ) selected for these evaluations are (a)  $10^{-2}$ , (b)  $10^{-3}$  and (c)  $10^{-4}$ .



IEC 1033/05

**Figure 4.7.26 – Correlation between measured  $\Delta L_{BER}$  and  $\Delta L_{APD}$** 

Correlation between measured  $p_{BER}$  and  $p_{APD}$  for several duty cycles of the pulse disturbance are also shown in Figure 4.7.27, where the disturbance has constant carrier power (-35 dBm). The duty cycle is changed as 40 %, 10 %, 4 %, 1 %, 0,4 % and 0,1 %. Black mark and white mark show the characteristics of W-CDMA and PHS respectively. Diamond, circle, triangle and square marks indicate the results for the pulse width 1 000 µs, 100 µs, 10 µs and 1 µs respectively. BER and probability values ( $BER_0$ ,  $APD_0$ ) selected for these evaluations are (a)  $10^{-2}$ , (b)  $10^{-3}$  and (c)  $10^{-4}$ .



IEC 1034/05

**Figure 4.7.27 – Correlation between measured  $p_{BER}$  and  $p_{APD}$** 

In all cases, APD indices ( $\Delta L_{APD}$ ,  $p_{APD}$ ) have close correlation with BER degradation indices ( $\Delta L_{BER}$ ,  $p_{BER}$ ), respectively. It is therefore concluded that APD measurement of the disturbance is one of the most effective methods for evaluating the interference potential on digital communication systems.

ISBN 2-8318-8100-5

A standard linear barcode representing the ISBN number 2-8318-8100-5.

9 782831 881003

---

**ICS 33.100.10; 33.100.20**

---

Typeset and printed by the IEC Central Office  
GENEVA, SWITZERLAND

# TECHNICAL REPORT

**CISPR  
16-3**

Second edition  
2003-11

---

---

---

INTERNATIONAL SPECIAL COMMITTEE ON RADIO INTERFERENCE

---

---

**Specification for radio disturbance and immunity  
measuring apparatus and methods –**

**Part 3:  
CISPR technical reports**



Reference number  
CISPR 16-3/TR:2003(E)

## **Publication numbering**

As from 1 January 1997 all IEC publications are issued with a designation in the 60000 series. For example, IEC 34-1 is now referred to as IEC 60034-1.

## **Consolidated editions**

The IEC is now publishing consolidated versions of its publications. For example, edition numbers 1.0, 1.1 and 1.2 refer, respectively, to the base publication, the base publication incorporating amendment 1 and the base publication incorporating amendments 1 and 2.

## **Further information on IEC publications**

The technical content of IEC publications is kept under constant review by the IEC, thus ensuring that the content reflects current technology. Information relating to this publication, including its validity, is available in the IEC Catalogue of publications (see below) in addition to new editions, amendments and corrigenda. Information on the subjects under consideration and work in progress undertaken by the technical committee which has prepared this publication, as well as the list of publications issued, is also available from the following:

- **[IEC Web Site \(www.iec.ch\)](http://www.iec.ch)**
- **Catalogue of IEC publications**

The on-line catalogue on the IEC web site ([www.iec.ch/searchpub](http://www.iec.ch/searchpub)) enables you to search by a variety of criteria including text searches, technical committees and date of publication. On-line information is also available on recently issued publications, withdrawn and replaced publications, as well as corrigenda.

- **IEC Just Published**

This summary of recently issued publications ([www.iec.ch/online\\_news/\\_justpub](http://www.iec.ch/online_news/_justpub)) is also available by email. Please contact the Customer Service Centre (see below) for further information.

- **Customer Service Centre**

If you have any questions regarding this publication or need further assistance, please contact the Customer Service Centre:

Email: [custserv@iec.ch](mailto:custserv@iec.ch)  
Tel: +41 22 919 02 11  
Fax: +41 22 919 03 00

# TECHNICAL REPORT

**CISPR  
16-3**

Second edition  
2003-11

---

---

---

INTERNATIONAL SPECIAL COMMITTEE ON RADIO INTERFERENCE

---

---

## **Specification for radio disturbance and immunity measuring apparatus and methods –**

### **Part 3: CISPR technical reports**

© IEC 2003 — Copyright - all rights reserved

No part of this publication may be reproduced or utilized in any form or by any means, electronic or mechanical, including photocopying and microfilm, without permission in writing from the publisher.

International Electrotechnical Commission, 3, rue de Varembé, PO Box 131, CH-1211 Geneva 20, Switzerland  
Telephone: +41 22 919 02 11 Telefax: +41 22 919 03 00 E-mail: [inmail@iec.ch](mailto:inmail@iec.ch) Web: [www.iec.ch](http://www.iec.ch)



Commission Electrotechnique Internationale  
International Electrotechnical Commission  
Международная Электротехническая Комиссия

PRICE CODE **XJ**

*For price, see current catalogue*

## CONTENTS

FOREWORD .....	3
INTRODUCTION .....	5
TABLE RECAPITULATING CROSS-REFERENCES .....	6
1 Scope .....	7
2 Normative references .....	7
3 Definitions .....	7
4 Technical reports .....	10
4.1 Correlation between measurements made with apparatus having characteristics differing from the CISPR characteristics and measurements made with CISPR apparatus .....	10
4.2 Interference simulators .....	16
4.3 Relationship between limits for open-area test site and the reverberating chamber .....	22
4.4 Characterization and classification of the asymmetrical disturbance source induced in telephone subscriber lines by AM broadcasting transmitters in the LW, MW and SW bands .....	27
4.5 The predictability of radiation in vertical directions at frequencies above 30 MHz ....	60
4.6 The predictability of radiation in vertical directions at frequencies up to 30 MHz ....	118
5 Background and history .....	187
5.1 The history of the CISPR .....	187
5.2 Historical background to the method of measurement of the interference power produced by electrical household and similar appliances in the VHF range.....	190

## INTERNATIONAL ELECTROTECHNICAL COMMISSION

**SPECIFICATION FOR RADIO DISTURBANCE  
AND IMMUNITY MEASURING APPARATUS AND METHODS –****Part 3: CISPR technical reports****FOREWORD**

- 1) The International Electrotechnical Commission (IEC) is a worldwide organization for standardization comprising all national electrotechnical committees (IEC National Committees). The object of IEC is to promote international co-operation on all questions concerning standardization in the electrical and electronic fields. To this end and in addition to other activities, IEC publishes International Standards, Technical Specifications, Technical Reports, Publicly Available Specifications (PAS) and Guides (hereafter referred to as "IEC Publication(s)"). Their preparation is entrusted to technical committees; any IEC National Committee interested in the subject dealt with may participate in this preparatory work. International, governmental and non-governmental organizations liaising with the IEC also participate in this preparation. IEC collaborates closely with the International Organization for Standardization (ISO) in accordance with conditions determined by agreement between the two organizations.
- 2) The formal decisions or agreements of IEC on technical matters express, as nearly as possible, an international consensus of opinion on the relevant subjects since each technical committee has representation from all interested IEC National Committees.
- 3) IEC Publications have the form of recommendations for international use and are accepted by IEC National Committees in that sense. While all reasonable efforts are made to ensure that the technical content of IEC Publications is accurate, IEC cannot be held responsible for the way in which they are used or for any misinterpretation by any end user.
- 4) In order to promote international uniformity, IEC National Committees undertake to apply IEC Publications transparently to the maximum extent possible in their national and regional publications. Any divergence between any IEC Publication and the corresponding national or regional publication shall be clearly indicated in the latter.
- 5) IEC provides no marking procedure to indicate its approval and cannot be rendered responsible for any equipment declared to be in conformity with an IEC Publication.
- 6) All users should ensure that they have the latest edition of this publication.
- 7) No liability shall attach to IEC or its directors, employees, servants or agents including individual experts and members of its technical committees and IEC National Committees for any personal injury, property damage or other damage of any nature whatsoever, whether direct or indirect, or for costs (including legal fees) and expenses arising out of the publication, use of, or reliance upon, this IEC Publication or any other IEC Publications.
- 8) Attention is drawn to the Normative references cited in this publication. Use of the referenced publications is indispensable for the correct application of this publication.
- 9) Attention is drawn to the possibility that some of the elements of this IEC Publication may be the subject of patent rights. IEC shall not be held responsible for identifying any or all such patent rights.

The main task of IEC technical committees is to prepare International Standards. However, a technical committee may propose the publication of a technical report when it has collected data of a different kind from that which is normally published as an International Standard, for example "state of the art".

CISPR 16-3, which is a technical report, has been prepared by CISPR subcommittee A: Radio interference measurements and statistical methods.

This second edition of CISPR 16-3, together with CISPR 16-4-1, CISPR 16-4-3 and CISPR 16-4-4 cancels and replaces the first edition of CISPR 16-3, published in 2000, and its amendment 1 (2002). It contains the relevant clauses of CISPR 16-3 without technical changes.

This publication has been drafted in accordance with the ISO/IEC Directives, Part 2.

A bilingual version of this publication may be issued at a later date.

The committee has decided that the contents of this publication will remain unchanged until 2006. At this date, the publication will be

- reconfirmed;
- withdrawn;
- replaced by a revised edition, or
- amended.

The text of this report is based on the following documents:

Report 33 – p/o CISPR 8, 1969; Report 38 – p/o CISPR 8, 1969; Report 49 – p/o CISPR 8C, 1980; Report: CIS/A(Sec)67 + CIS/A(Sweden)29; RM 2828/CISPR/A, 1985; CIS/A(CO)32, 1985; CIS/A(Sec)58, 1983; CIS/A(Sec)58A, 1983; CIS/A(Sec)67, 1985; CIS/A(CO)77A, 1993; CIS/A(CO)81, 1987; CIS/A(CO)82, 1994; CIS/A(CO)84, 1994; CIS/A(Sec)84, 1987; CIS/A(Sec)88, 1988; CIS/A(Sec)88A, 1988; CIS/A(Sec)94, 1989; CIS/A(Sec)115, 1991; CIS/A(Sec)115A, 1991; CIS/A(Sec)116, 1991; CIS/A(Sec)124, 1991; CIS/A(Sec)128, 1992; CIS/A(Sec)132, 1993; CIS/A/166/CD, 1995.

## INTRODUCTION

CISPR 16-1, CISPR 16-2, CISPR 16-3 and CISPR 16-4 have been reorganised into 14 parts, to accommodate growth and easier maintenance. The new parts have also been renumbered. See the list given below.

Old CISPR 16 publications		New CISPR 16 publications	
CISPR 16-1	Radio disturbance and immunity measuring apparatus	CISPR 16-1-1	Measuring apparatus
		CISPR 16-1-2	Ancillary equipment – Conducted disturbances
		CISPR 16-1-3	Ancillary equipment – Disturbance power
		CISPR 16-1-4	Ancillary equipment – Radiated disturbances
		CISPR 16-1-5	Antenna calibration test sites for 30 MHz to 1 000 MHz
CISPR 16-2	Methods of measurement of disturbances and immunity	CISPR 16-2-1	Conducted disturbance measurements
		CISPR 16-2-2	Measurement of disturbance power
		CISPR 16-2-3	Radiated disturbance measurements
		CISPR 16-2-4	Immunity measurements
CISPR 16-3	Reports and recommendations of CISPR	CISPR 16-3	CISPR technical reports
		CISPR 16-4-1	Uncertainties in standardised EMC tests
		CISPR 16-4-2	Measurement instrumentation uncertainty
		CISPR 16-4-3	Statistical considerations in the determination of EMC compliance of mass-produced products
CISPR 16-4	Uncertainty in EMC measurements	CISPR 16-4-4	Statistics of complaints and a model for the calculation of limits

More specific information on the relation between the ‘old’ CISPR 16-3 and the present ‘new’ CISPR 16-3 is given in the table after this introduction (TABLE RECAPITULATING CROSS REFERENCES).

Measurement instrumentation specifications are given in five new parts of CISPR 16-1, while the methods of measurement are covered now in four new parts of CISPR 16-2. Various reports with further information and background on CISPR and radio disturbances in general are given in CISPR 16-3. CISPR 16-4 contains information related to uncertainties, statistics and limit modelling.

## TABLE RECAPITULATING CROSS-REFERENCES

First edition of CISPR 16-3 Clauses, subclauses	Second edition of CISPR 16-3 Clauses, subclauses
1.1	1
1.2	2
1.3	3
4	4
4.1	4.1
4.2	4.2
4.3	4.3
4.4	4.4
4.5	4.5
4.6	4.6
5	5
5.1	5.1
5.2	5.2

## **SPECIFICATION FOR RADIO DISTURBANCE AND IMMUNITY MEASURING APPARATUS AND METHODS –**

### **Part 3: CISPR technical reports**

#### **1 Scope**

This part of CISPR 16 contains specific technical reports and information on the history of CISPR.

Over the years, the CISPR prepared a number of recommendations and reports that have significant technical merit but were not generally available. Reports and recommendations were for some time published in CISPR 7 and 8.

At its meeting in Campinas, Brazil, in 1988, subcommittee A agreed on the table of contents of part 3 and to publish the reports for posterity by giving the reports a permanent place in part 3.

With the reorganization of CISPR 16 in 2003, the significance of CISPR limits has been moved to CISPR 16-4-3, whereas recommendations on statistics of disturbance complaints and on the report on the determination of limits has been moved to CISPR 16-4-4. The contents of Amendment 1 (2002) has been moved to CISPR 16-4-1.

#### **2 Normative references**

The following referenced documents are indispensable for the application of this document. For dated references, only the edition cited applies. For undated references, the latest edition of the referenced document (including any amendments) applies.

CISPR 11, *Industrial, scientific and medical (ISM) radio-frequency equipment – Electromagnetic disturbance characteristics – Limits and methods of measurement*

CISPR 16-1 (all parts), *Specification for radio disturbance and immunity measuring apparatus and methods – Radio disturbance and immunity measuring apparatus*

CISPR 16-2 (all parts), *Specification for radio disturbance and immunity measuring apparatus and methods – Methods of measurement of disturbances and immunity*

CISPR 16-4 (all parts), *Specification for radio disturbance and immunity measuring apparatus and methods – Uncertainties, statistics and limit modelling*

ITU-R Recommendation BS. 468-4, *Measurement of audio-frequency noise voltage level in sound broadcasting*

#### **3 Definitions**

For the purpose of this part of CISPR 16, the definitions of CISPR 16-1 and IEV 60050(161) as well as the following definitions apply.

##### **3.1**

##### **bandwidth ( $B_n$ )**

width of the overall selectivity curve of the receiver between two points at a stated attenuation, below the midband response. The bandwidth is represented by the symbol  $B_n$ , where  $n$  is the stated attenuation in decibels

### 3.2 impulse bandwidth ( $B_{\text{imp}}$ )

$$B_{\text{imp}} = A(t)_{\text{max}} / (2G_o \times IS)$$

where

- $A(t)_{\text{max}}$  is the peak of the envelope at the IF output of the receiver with an impulse area  $IS$  applied at the receiver input;
- $G_o$  is the gain of the circuit at the centre frequency.

Specifically, for two critically coupled tuned transformers,

$$B_{\text{imp}} = 1.05 \times B_6 = 1.31 \times B_3$$

where  $B_6$  and  $B_3$  are respectively the bandwidths at the  $-6$  dB and  $-3$  dB points (see CISPR 16-1-1 for further information)

### 3.3 impulse area (sometimes called impulse strength) ( $IS$ ) the voltage-time area of a pulse defined by the integral:

$$IS = \int_{-\infty}^{+\infty} V(t)dt \text{ (expressed in } \mu\text{Vs or } \text{dB}(\mu\text{Vs}))$$

NOTE Spectral density ( $D$ ) is related to impulse area and expressed in  $\mu\text{V/MHz}$  or  $\text{dB}(\mu\text{V})/\text{MHz}$ . For rectangular impulses of pulse duration  $T$  at frequencies  $f \ll 1/T$ , the relationship  $D (\mu\text{V/MHz}) = 2 \times 10^6 / IS (\mu\text{Vs})$  applies since  $D$  is calibrated in r.m.s. values of a corresponding sine wave.

### 3.4 electrical charge time constant ( $T_C$ )

time needed after the instantaneous application of a constant sine-wave voltage to the stage immediately preceding the input of the detector for the output voltage of the detector to reach 63 % of its final value

NOTE This time constant is determined as follows. A sine-wave signal of constant amplitude and having a frequency equal to the mid-band frequency of the i.f. amplifier is applied to the input of the stage immediately preceding the detector. The indication,  $D$ , of an instrument having no inertia (for example, a cathode-ray oscilloscope) connected to a terminal in the d.c. amplifier circuit so as not to affect the behaviour of the detector, is noted. The level of the signal is chosen such that the response of the stages concerned remains within the linear operating range. A sine-wave signal of this level, applied for a limited time only and having a wave train of rectangular envelope is gated such that the deflection registered is 0,63D. The duration of this signal is equal to the charge time of the detector.

### 3.5 electrical discharge time constant ( $T_D$ )

time needed after the instantaneous removal of a constant sine-wave voltage applied to the stage immediately preceding the input of the detector for the output of the detector to fall to 37 % of its initial value

NOTE The method of measurement is analogous to that for the charge time constant, but instead of a signal being applied for a limited time, the signal is interrupted for a definite time. The time taken for the deflection to fall to 0,37D is the discharge time constant of the detector.

### 3.6 mechanical time constant ( $T_M$ ) of a critically damped indicating instrument

$$T_M = T_L / 2\pi$$

where  $T_L$  is the period of free oscillation of the instrument with all damping removed.

NOTE 1 For a critically damped instrument, the equation of motion of the system may be written as

$$T_M^2(d^2\alpha / dt^2) + 2T_M(d\alpha / dt) + \alpha = ki$$

where

- $\alpha$  is the deflection;
- $i$  is the current through the instrument;
- $k$  is a constant.

It can be deduced from this relation that this time constant is also equal to the duration of a rectangular pulse (of constant amplitude) that produces a deflection equal to 35 % of the steady deflection produced by a continuous current having the same amplitude as that of the rectangular pulse.

NOTE 2 The methods of measurement and adjustment are deduced from one of the following:

- a) The period of free oscillation having been adjusted to  $2\pi T_M$ , damping is added so that  $\alpha_{TM} = 0,35 \alpha_{max}$ .
- b) When the period of oscillation cannot be measured, the damping is adjusted to be just below critical such that the overswing is not greater than 5 % and the moment of inertia of the movement is such that  $\alpha_{TM} = 0,35 \alpha_{max}$ .

### **3.7 overload factor**

ratio of the level that corresponds to the range of practical linear function of a circuit (or a group of circuits) to the level that corresponds to full-scale deflection of the indicating instrument.

The maximum level at which the steady-state response of a circuit (or group of circuits) does not depart by more than 1 dB from ideal linearity defines the range of practical linear function of the circuit (or group of circuits)

### **3.8 symmetric voltage**

in a two-wire circuit, such as a single-phase mains supply, the symmetric voltage is the radio-frequency disturbance voltage appearing between the two wires. This is sometimes called the differential mode voltage. If  $V_a$  is the vector voltage between one of the mains terminals and earth and  $V_b$  is the vector voltage between the other mains terminal and earth, the symmetric voltage is the vector difference ( $V_a - V_b$ )

### **3.9 asymmetric voltage**

radio-frequency disturbance voltage appearing between the electrical mid-point of the mains terminals and earth. It is sometimes called the common-mode voltage and is half the vector sum of  $V_a$  and  $V_b$ , i.e.  $(V_a + V_b)/2$ .

### **3.10 unsymmetric voltage**

amplitude of the vector voltage,  $V_a$  or  $V_b$  defined in 3.8 and 3.9. This is the voltage measured by the use of an artificial mains V-network

### **3.11 CISPR indicating range**

range specified by the manufacturer which gives the maximum and the minimum meter indications within which the receiver meets the requirements of CISPR 16-1-1.

## 4 Technical reports

### 4.1 Correlation between measurements made with apparatus having characteristics differing from the CISPR characteristics and measurements made with CISPR apparatus

#### 4.1.1 Introduction

CISPR standards for instrumentation and methods of measurement have been established to provide a common basis for controlling radio interference from electrical and electronic equipment in international trade.

The basis for establishing limits is that of providing a reasonably good correlation between measured values of the interference and the degradation it produces in a given communications system. The acceptable value of signal-to-noise ratio in any given communication system is a function of its parameters including bandwidth, type of modulation and other design factors. As a consequence, various types of measurements are used in the laboratory in research and development work in order to carry out the required investigations.

The purpose of this subsection is to analyse the dependence of the measured values on the parameters of the measuring equipment and on the waveform of the measured interference.

#### 4.1.2 Critical interference measuring instrument parameters

The most critical factors in determining the response of an instrument for measuring interference are the following: the bandwidth, the detector, and the type of interference being measured. Considered to be of secondary importance, but, nevertheless, quite significant in correlating instruments under particular circumstances, are: overload factor, AGC design (if used), image and other spurious responses, and meter time constant and damping.

For purposes of discussion, reference is made to three fundamental types of radio noise: impulse, random and sine wave. The dependence of the response to each of these on the bandwidth and the type of detector is given in table 4.1-1. In this table,  $\delta$  is the magnitude of the impulse strength,  $\Delta f_{\text{imp}}$  is the impulse bandwidth,  $\Delta f_{\text{rn}}$  is the random noise bandwidth,  $P(\alpha)$  is the pulse response for the quasi-peak detector,  $f_{\text{PR}}$  is the pulse repetition frequency, and  $E'$  is the spectral amplitude of the random noise. The relative responses of various detectors to impulse interference for one instrument are shown in figure 4.1-1.

Table 4.1-1 shows that the dependence of the noise meter response on bandwidth is different for all three types of interference. If the waveform being measured can be defined as being any of the three types listed in table 4.1-1, and if a standard source provides that type of waveform, then by using the substitution method, a satisfactory calibration can be obtained for any instrument with adequate overload factor independent of its bandwidth. Thus, with a purely random interference or a purely impulsive interference of known repetition rate, calibration can be made using a corresponding source, or a correlation factor calculated on the basis of known circuit parameters.

If a particular interference waveform is of a type intermediate between these three types, then the correction or correlation factors will also be intermediate. In any given case, it will be necessary to classify the noise waveform in such a manner that a significant correlation factor can be established. Hence, in order to develop this subject to any significant extent, it will be necessary to examine typical interference sources and to determine the extent to which they are of impulsive, random, or sine-wave type.

If an interference measuring set with several types of detectors is available, for example, peak, quasi-peak and average, the type of interference can be assessed by measuring the ratios of the readings obtained with these detectors. These ratios will, of course, depend

upon the bandwidth and other characteristics of the instrument being used for the measurement.

#### **4.1.3 Impulse interference – Correlation factors**

The quasi-peak detector response of any interference measuring set to regularly repeated impulses of uniform amplitude can be determined by the use of the "pulse response curve" which is shown in figure 4.1-2. This figure shows the response of the detector in percentage of peak response for any given bandwidth and value of charge resistance and discharge resistance. Applying this curve, it should be noted that the peak itself is dependent upon the bandwidth, so that as the bandwidth increases, peak value increases, but the percentage of peak, which is read by the detector, decreases; over a narrow range of bandwidth, these effects tend to counteract each other. The bandwidth used in this curve is the 6 dB bandwidth, which, for the passband characteristics typical of most interference measuring equipment, is about 5 % less than the so-called impulse bandwidth. A theoretical comparison of instruments having various bandwidths and detector parameters with the CISPR instrument is shown in figure 4.1-3.

The response of the average detector to impulsive noise is an interesting case. The reading of an average detector for impulsive noise is independent of the bandwidth of the pre-detector stages. It is, of course, directly proportional to the repetition rate. In most cases, the reading obtained with an average detector for impulsive noise is so low as to be of no practical value unless the noise meter bandwidth is exceedingly narrow, such as of the order of a few hundred hertz. For a repetition rate of 100 Hz and a bandwidth of the order of 10 kHz, the average value would be approximately 1 % of the peak value. Such a value is too low to measure with any degree of precision. Furthermore, for many communication systems, the annoyance effect may be well above the reading obtained with the average meter. This, of course, is one of the justifications for the use of the quasi-peak instrument.

#### **4.1.4 Random noise**

The response of a noise meter to random noise is proportional to the square root of the bandwidth. This result is independent of the type of detector used. The ratio of the random noise bandwidth to the 3 dB bandwidth is a function of the type of filter circuit. On the other hand, it has been shown that for many circuits typical of those used in interference measuring equipment, a ratio of effective random noise bandwidth to the 3 dB bandwidth of about 1,04 is a reasonable figure.

#### **4.1.5 The r.m.s. detector**

One of the advantages of the r.m.s. detector in correlation work is that for broadband noise the output obtained from it will be proportional to the square root of the bandwidth, i.e. the noise power is directly proportional to the bandwidth. This feature makes the r.m.s. detector particularly desirable and is one of the main reasons for adopting the r.m.s. detector to measure atmospheric noise. Another advantage is that the r.m.s. detector makes a correct addition of the noise power produced by different sources, for example, impulsive noise and random noise, thus for instance allowing a high degree of background noise.

The r.m.s. values of noise often give a good assessment of the subjective effect of interference to a.m. sound and television reception. However, the very wide dynamic range needed when using very wide-band instruments for measuring impulsive noise, limits the use of r.m.s. detectors to narrow-band instruments.

#### **4.1.6 Discussion**

The preceding paragraphs have indicated the theoretical basis for comparing measurements obtained with different instruments. As mentioned previously, the possibility of establishing significant correlation factors depends upon the extent to which noise can be classified and identified so that the proper correlation factors may be used. In many frequency ranges, impulsive interference appears to be the most serious; however, for

power lines where corona interference is the primary concern, random interference would be expected to be more characteristic. Additional quantitative data are needed on typical interference characteristics. Another important parameter is the overload factor.

#### 4.1.7 Application to typical noise sources

##### *Commutator motors*

The noise generated by commutator motors is usually a combination of impulse and random noise. The random noise originates in the varying brush contact resistance, while the impulse noise is generated from the switching action at the commutator bars. For optimum adjustment of commutation the impulse noise can be minimized. However, where variable loading is possible, measurements have confirmed that for the peak and quasi-peak detectors, the dominant noise is of impulse type and the random component may be neglected. While the repetition rate may be of the order of 4 kHz, the effective rate is lower because the amplitude of the impulses is usually modulated at twice the line frequency. Hence, experimental results have shown that quasi-peak readings are consistent with bandwidth variations if the repetition rate of the impulse is assumed to be twice the line frequency.

Peak measurements show fluctuating levels on such noise because of the irregular nature of the commutator switching action.

The quasi-peak to average ratio is lower than would be obtained for pure impulse noise for two reasons.

- 1) The modulation of the commutator switching transients by line frequency produces many pulses below the measured quasi-peak level. These pulses do not contribute to the quasi-peak value but do contribute to the average.
- 2) The relatively low level, but continuous, random noise can likewise contribute substantially only to the average value. Experimental values of quasi-peak to average ratio ranged from 13 dB to 23 dB with the highest ratios for the widest bandwidths (120 kHz).

##### *Impulsive sources*

Tests on an ignition model, commutator motor appliances, and appliances using vibrating regulators showed reasonable agreement on instruments with the same nominal bandwidth, but with time constant ratios of the order of 3 to 1 on restricted portions of the output indicator scale. Deviations at higher scale values are without explanation. Relatively poor correlation was obtained on sources producing very low repetition rate pulses.

##### *Ignition interference*

CISPR Recommendation 35 recognizes that correlation between quasi-peak and peak detectors can be established as a practical matter. The conversion factor of 20 dB is explained partly on the basis of theory for uniform repeated impulses, and partly on the basis of the actual irregularity of the amplitude and wave shape of such impulses.

##### *Noise from high-voltage lines*

Comparative tests were made with an instrument meeting CISPR specification and one meeting those of the U.S.A. Standards Institute. The latter read 0 dB to 1 dB higher in one test and 1 dB to 3 dB higher in another (see IEEE Special Publication 31C44).

### *Dependence on bandwidth*

Comparisons of measurements made in the U.K. with two instruments having bandwidths of 90 kHz and 9 kHz respectively have been reported to show that for most interference sources, the values obtained are in the ratio 14 dB to 18 dB. This figure is consistent with the concept that the interference is dominated by impulse type noise but that some random components are present.

#### **4.1.8 Conclusions**

Analysis of data comparing the responses of various instruments shows that it is possible to explain in almost every case the differences in measured values on the basis of theoretical and practical considerations. In many instances, it is indicated that waveform characteristics are known to predict correlation factors adequately with an accuracy of 2 dB to 4 dB.

Further studies are needed

- a) to characterize in some detail the waveforms of various sources of interference, and
- b) to correlate these waveform characteristics with measured values and the instrument parameters.

**Table 4.1-1 – Comparative response of slideback peak, quasi-peak and average detectors to sine wave, periodic pulse and Gaussian waveform**

Input waveform	Detector type			
	Slideback peak (sb)	Quasi-peak:1/600 (qp)	Field intensity (average)	RMS
CW sine wave	e†	e	e	e
Periodic pulse (no overlap)	$1,41 \delta \Delta f_{\text{imp}}$	$1,41 \delta \Delta f_{\text{imp}} P(\alpha)^*$	$1,41 \delta f_{\text{PR}}^+$	$1,41 \delta \sqrt{f_{\text{PR}} \Delta f_{\text{imp}}}$
Random ++	–	$1,85 \sqrt{\Delta f_m E'}^{**}$	$0,88 \sqrt{\Delta f_m E'}$	$\sqrt{\Delta f_m E'}$

† e is the r.m.s. value of the applied sine wave.  
 \*  $P(\alpha)$  is given in figure 4.1-2.  
 \*\*  $E'$  is spectral strength in r.m.s. volts/hertz bandwidth.  
 +  $\delta$  is impulse strength. It is assumed the instrument is calibrated in terms of the r.m.s. value of a sine wave.  
 ++ It is assumed that characteristics of the envelope are measured by the detector on random noise.

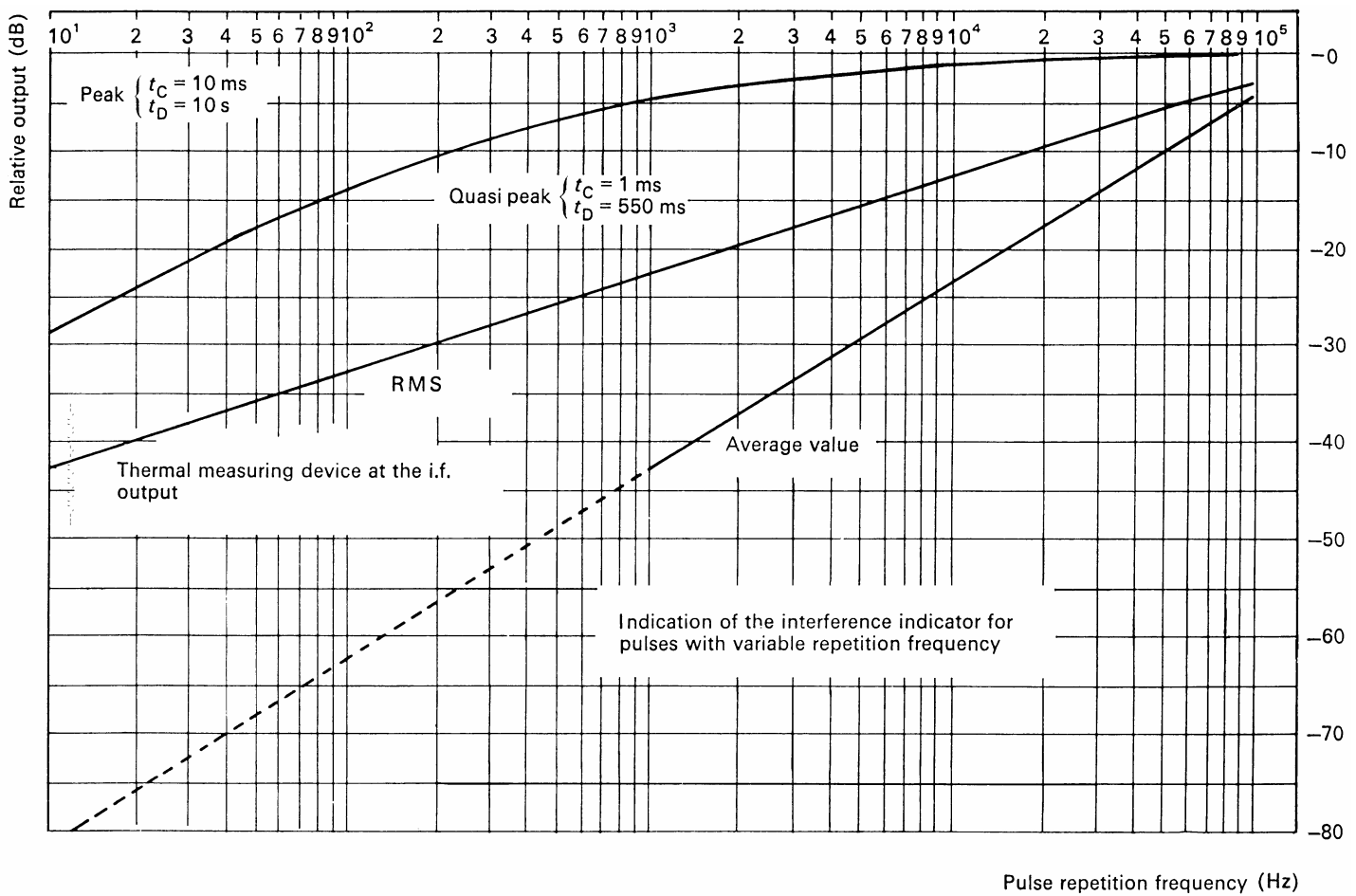
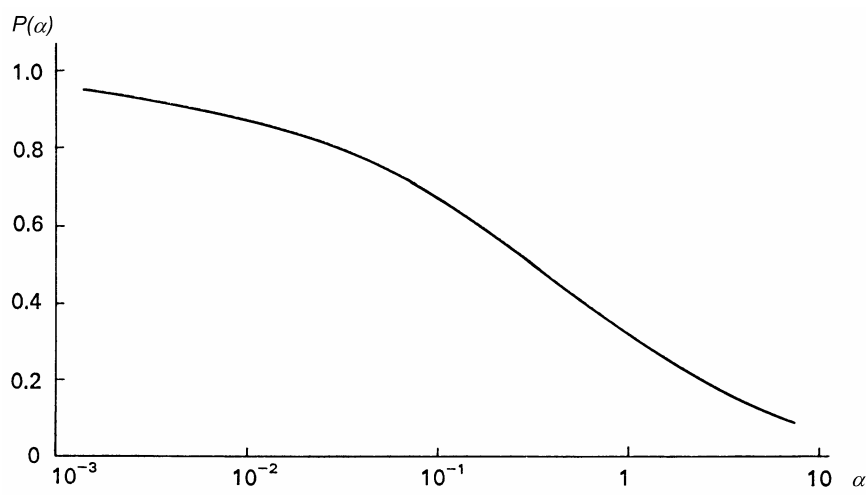


Figure 4.1-1 – Relative response of various detectors to impulse interference

IEC 784/2000

Pulse repetition frequency (Hz)

IEC 785/2000



$$\alpha = \frac{(\pi R_c \Delta F)}{(R_d f_{PR})}$$

 $R_c$  = charging resistance, in ohms $R_d$  = discharging resistance, in ohms $\Delta F$  = 6 dB bandwidth, in hertz $f_{PR}$  = pulse repetition frequency, in hertzFigure 4.1-2 – Pulse rectification coefficient  $P(\alpha)$

Copyright International Electrotechnical Commission

Provided by IHS under license with IEC  
No reproduction or networking permitted without license from IHS

Not for Resale

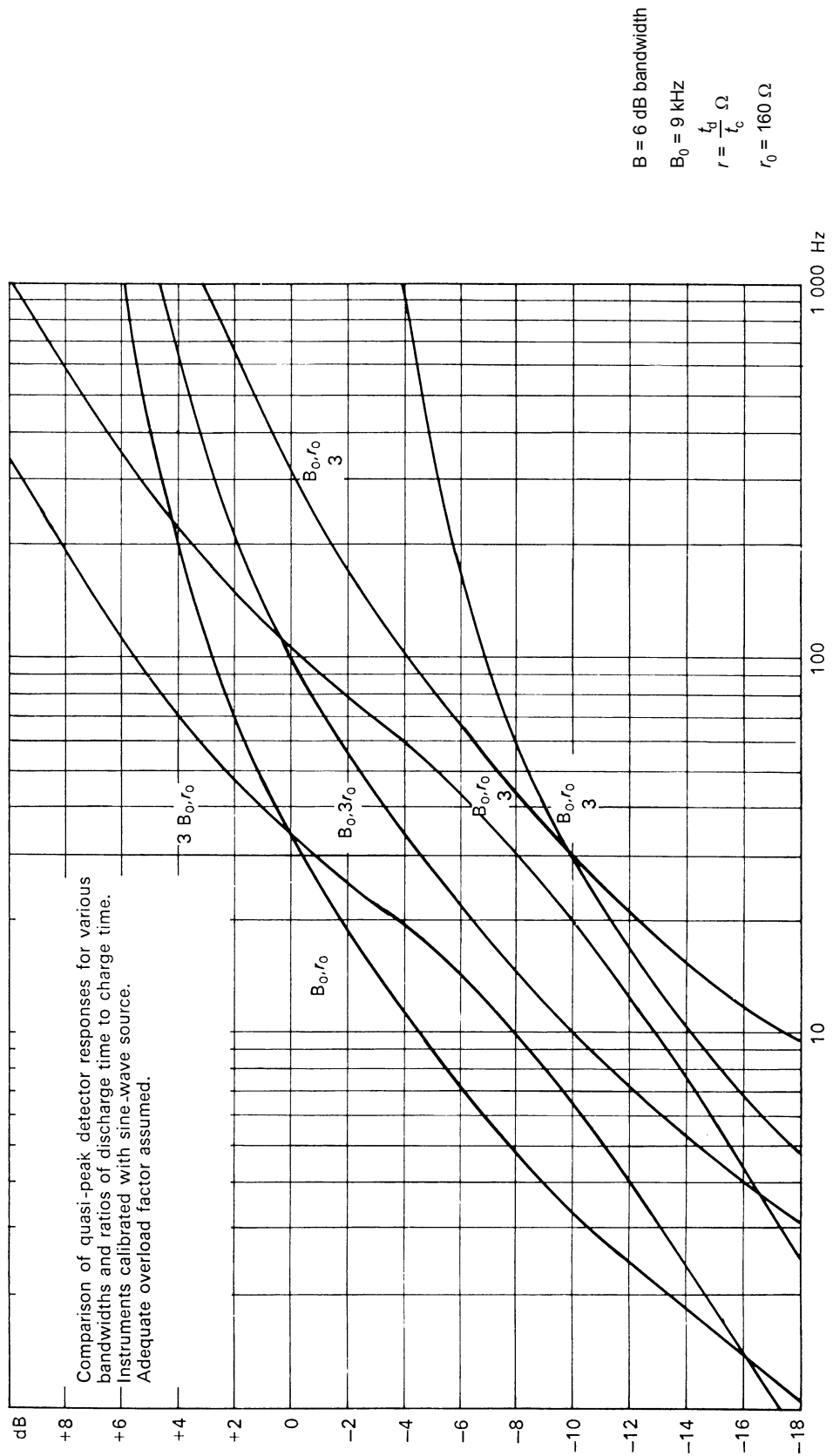


Figure 4.1-3 – Pulse repetition frequency

## 4.2 Interference simulators

### 4.2.1 Introduction

Interference simulators can be used for various applications, in particular to study signal processing in systems and equipment in the presence of interference (for example, overloading of receivers, synchronization of TV receivers, error rate of data signals, etc.) and for assessment of the annoyance caused by disturbances in broadcast and communication services.

A simulator should produce a stable and reproducible output signal, which requirement is normally not fulfilled by an actual interference source, and the simulator output waveform should show a good resemblance to the actual interference signal.

### 4.2.2 Types of interference signals

The following interference sources can be simulated.

- a) Narrowband interference sources generating sine-wave signals, for example receiver oscillators and ISM equipment. These sources can be simulated by an appropriate RF standard signal generator. ISM interference is often modulated by the mains voltage which can be simulated by modulating the RF signal with a full-wave rectified mains signal.
- b) Broadband interference sources producing continuous broadband noise, for example, gaseous discharges and corona. For simulating purposes a standard broadband noise source (saturated vacuum tube diode, zener diode or gas tube followed by a suitable broadband amplifier) can be used. In mains-fed sources of this type, mains modulation is present, but because of the non-linear behaviour of gaseous discharges the envelope of the actual noise signal can deviate appreciably from the normal full-wave rectified mains waveform. In this case, gating the noise of the simulator at a repetition frequency of twice the mains frequency can yield a good correspondence with the actual interference signal.
- c) Thyristor controlled regulators with phase control generate in a RF-channel narrow pulses of constant amplitude at a repetition frequency equal to twice the mains frequency. They can be simply simulated by standard pulse generators with narrow output pulses ( $10^{-7}$  s to  $10^{-9}$  s width) of the same repetition frequency.
- d) Ignition systems, mechanical contacts and commutator motors generate short periods (bursts) of quasi-impulsive noise. This type of noise is caused by very short pulses of regular or irregular height at random time intervals; if the average interval between adjacent pulses is less than the reciprocal of the channel bandwidth under test ( $\tau_{av} < 1/B$ ) the pulses overlap and because of the random phase conditions a random fluctuating output signal (noise) results. Therefore, bursts of quasi-impulsive interference of this type can be simulated by a gated broadband noise signal.

The duration and the repetition frequency of the bursts depend on the type of interference source (see table 4.2-1).

Ignition interference is characterized by burst durations between 20  $\mu$ s and 200  $\mu$ s and repetition frequencies between 30 bursts/s and 300 bursts/s depending on the number of cylinders and revolutions/minute of the engine.

Mechanical contacts produce bursts (clicks) which can vary between some milliseconds (snap-off switches) and more than 200 ms. In the case of a contact device in a mains-fed circuit, the noise during the burst is modulated with the full-wave rectified mains voltage.

Commutator motors produce much shorter bursts with durations between 20  $\mu$ s and 200  $\mu$ s at repetition frequencies between  $10^3$  bursts/s and  $10^4$  bursts/s, depending on the number of commutator bars and revolutions/minute of the rotor. Also in this case, mains supply causes a similar envelope modulation of the noise bursts.

#### 4.2.3 Circuits for simulating broadband interference

Simulators of this type should generate gated noise bursts with or without mains modulation according to the characteristics laid down in table 4.2-1. Figure 4.2-1 shows a straightforward design with a noise source followed by an appropriate amplifier of 70 dB to 80 dB gain, a gating circuit to simulate the bursts, a mains envelope modulator and an output attenuator to adjust the required output level.

**Table 4.2-1 – Characteristics of gate generator and modulator to simulate various types of broadband interference**

Simulator signal	Burst duration	Burst repetition frequency	Mains modulation <sup>a</sup>
Gaseous discharge		Continuous	Yes/no <sup>b</sup>
Ignition	20-200 µs	30-300 bursts/s	No
Switches	5-500 ms	0,2-30 bursts/min or single	Yes/no
Commutator motors	30-300 µs	10 <sup>3</sup> -10 <sup>4</sup> bursts/s	Yes/no

<sup>a</sup> Depending on a.c. or d.c. supply.  
<sup>b</sup> In the case of mains modulation, gating at a repetition frequency  $2f_{\text{mains}}$  and gate width of 1 ms to 2 ms may be more appropriate.

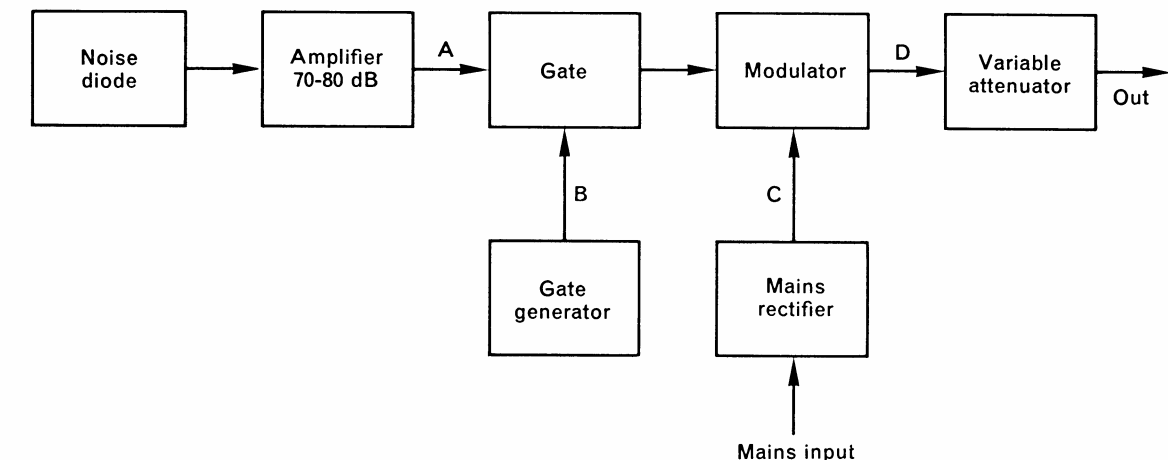
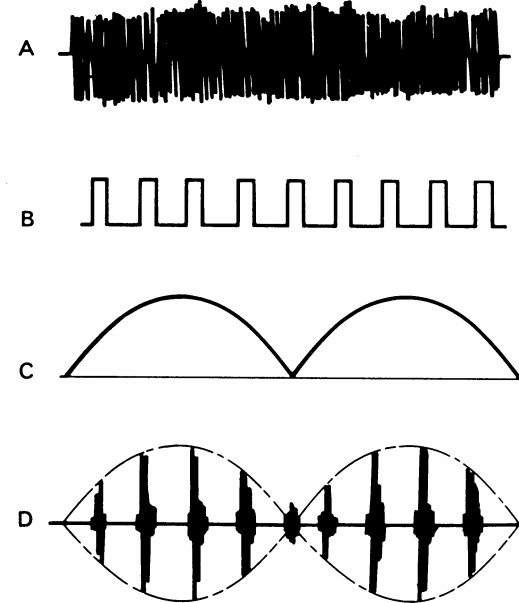
The disadvantage of this layout is that a wide usable frequency range requires a broad bandwidth for the entire circuit between noise source and output terminal. The most critical part in this respect is the high-gain amplifier. For applications in a wide frequency range (for example, 0 MHz to 1 000 MHz) such a range can be split up in several smaller ranges or a tunable amplifier may be used. Such a design complicates the construction of the simulator appreciably.

Another way to produce a gated wideband noise signal is given in the diagram of figure 4.2-2. In this design, nanosecond pulses are generated in the output stage, for example, a step recovery diode or similar device. These pulses of constant height are triggered at random time intervals and at a sufficiently high repetition rate to cause overlap in the RF channel under test in order to result in quasi-impulsive noise in the output of the channel. Average repetition rates of a few megahertz are required for measurements in a TV channel of at least 100 kHz for measurements in an FM channel and of at least 10 kHz in an AM channel. The random occurrence of the trigger pulses is obtained from the zero crossings of a broadband signal. For this purpose the output of a noise source is fed to an appropriate amplifier which is followed by a gating circuit for burst simulation. The gated noise signal is fed to a bistable multivibrator which converts the zero crossings into pulses of random varying width from which narrow trigger pulses at random distances are generated by the monostable multivibrator.

The advantage of this system over the circuit of figure 4.2-1 is that the usable frequency range is determined by the output pulses of the step recovery diode only. An example of such a circuit is given in figure 4.2-3, in which circuit output pulses are generated by the step recovery diode HP0102, the pulse width is determined by the length of a short-circuited coaxial cable  $L$ . Ringing effects are suppressed by the fast switch diode HP2301 and mains modulation can be effected simply by modulating the supply voltage of the step recovery diode with a full-wave rectified mains voltage. Pulses of 1 ns duration and 5 V amplitude are applicable and offer an output spectrum flat to about 500 MHz. Such a single pulse causes a 50 mV pulse in a TV channel and a 1 mV pulse in an FM channel; overlapping pulses add up, and the peak and quasi-peak value of the resulting signal is considerably higher.

The bandwidth of the preceding stages which generate the trigger signal (noise source, amplifier and gating circuit) should be sufficient for the required pulse repetition rate, so for measurements in a TV channel a bandwidth of 5 MHz to 10 MHz is quite satisfactory. Moreover, the linearity of these stages is not critical because only the position of the zero crossings is important. The multivibrators have to generate steep pulses of short duration (about 0,1 µs) to drive the step recovery diode.

In summary, the circuit according to figure 4.2-1 is very useful for broadband interference simulators to be operated in a limited frequency range, whereas the circuit of figure 4.2-2 is more suitable for simulators intended for wideband use.



Waveforms at position A - D of the diagram

Figure 4.2-1 – Block diagram and waveforms of a simulator generating noise bursts

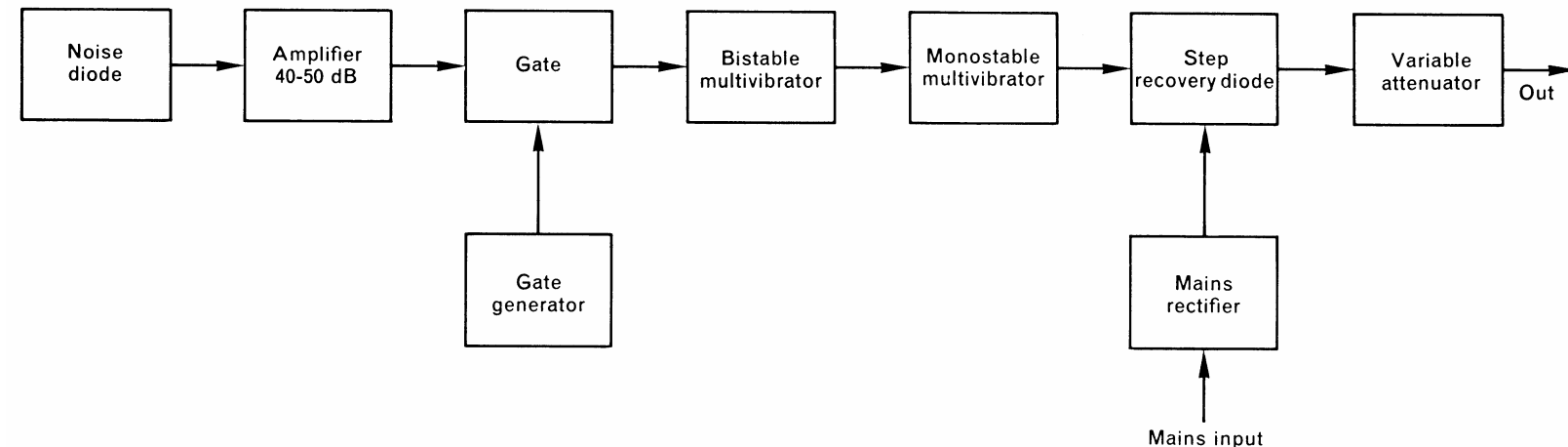


**Figure 4.2-2 – Block diagram of a simulator generating noise bursts according to the pulse principle**

012/80

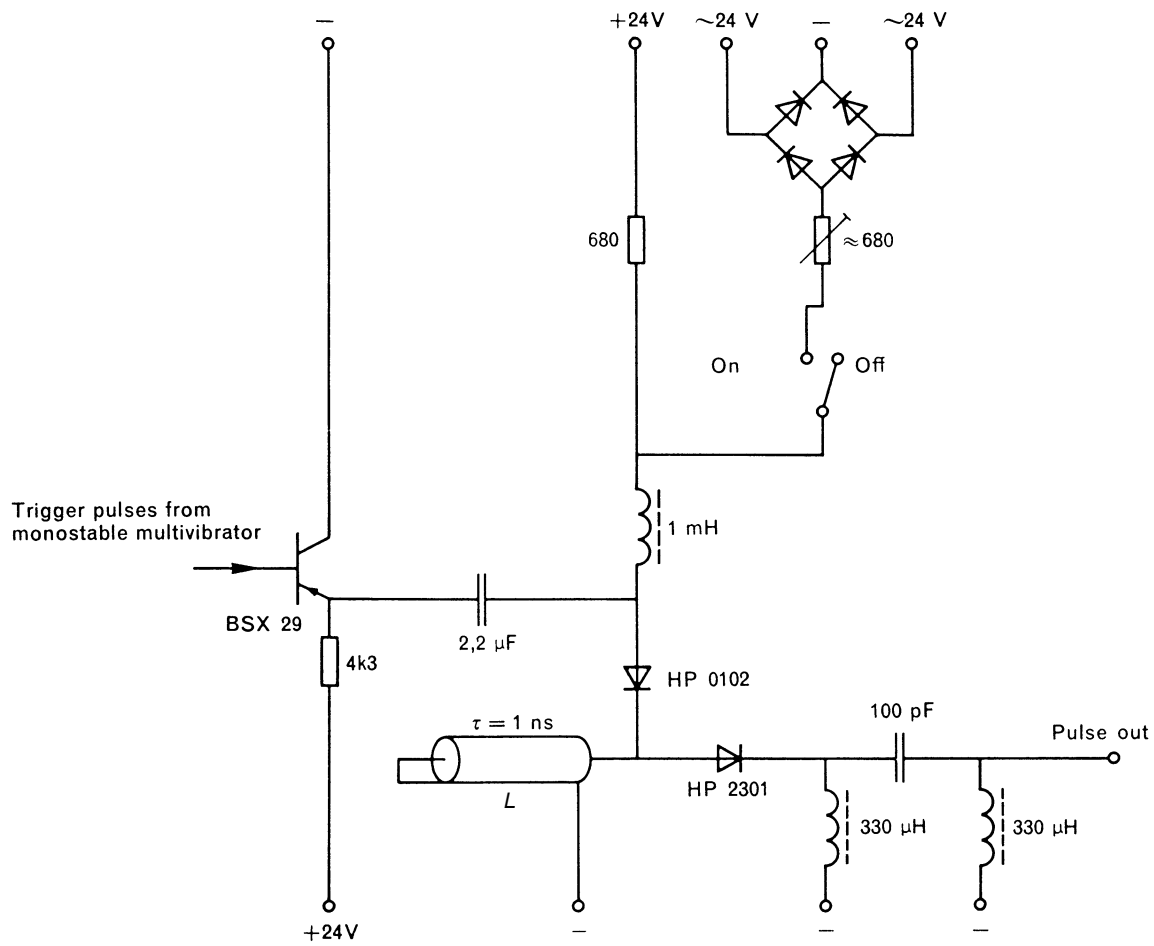


Figure 4.2-3 – Details of a typical output stage

### 4.3 Relationship between limits for open-area test site and the reverberating chamber

#### 4.3.1 Introduction

At present there are limits for use with the open-area test site method of measurement specified in several CISPR publications. For equipment which can be measured using the reverberating chamber method, a procedure is required to relate the limit to be used with the open-area test site limit. The procedure is described in this report.

#### 4.3.2 Correlation between measurements of the reverberating chamber and the open-area test site

The open-area test site measurement sets out to find the maximum level of radiation of the EUT (equipment under test). Whether the measurement is of the field strength or of power density at the measurement antenna, or of the power into an antenna in substitution of the EUT, the measured results can be expressed in the equivalent, radiated power from a half-wave dipole. Let this equivalent radiated power be  $P_q$  dB(pW).

The reverberating chamber measures the total radiated power of the EUT. Let the measured power be  $P_t$  dB(pW).

The two measurements are related to each other by the gain of the EUT as a radiator with respect to an isotropic radiator. Let this EUT gain be  $G$  dB. The relationship is given by equation (4.3-1). The equation is derived in the appendix.

$$P_t + G = P_q + 2 \quad (4.3-1)$$

#### 4.3.3 Limits for use with the reverberating chamber method

Consider the case of an EUT which is exactly on the limit,  $L_o$ , when measured in the open area test site, i.e.  $P_q = L_o$ .

This EUT should also be exactly on the corresponding limit,  $L_r$ , when it is measured in the reverberating chamber, i.e.  $P_t = L_r$ .

From equation (4.3-1), we can relate the two limits as in equation (4.3-2).

$$L_r = L_o + 2 - G \quad (4.3-2)$$

The value of  $L_r$  is dependent not only on  $L_o$ , but also on  $G$ . Since  $G$  will not be the same for EUTs, it is not possible to set  $L_r$  to treat EUTs in a manner identical to the effect of  $L_o$ . If say  $L_r = L_o$ , then it is correct only for EUTs with  $G = 2$ . EUTs with a  $G$  greater than 2 will find it easier to pass the reverberating limit, and vice versa.

It is necessary to determine the value of  $G$ . This can be done from measurements of  $P_q$  and  $P_t$ . Figure 1 shows the lines of  $P_w$  versus  $P_t$  for various values of  $G$ . The shaded region is for negative values of  $G$ . (Experimental points appearing in this region are caused by failure to locate the maximum open-site radiation, probably due to the maximum radiation lying outside of the horizontal plane.)

An example is given in figure 4.3-2. A number of microwave ovens were measured for  $P_q$  and  $P_t$ . It can be seen that

- for points lying in the positive  $G$  region, the majority have values around 2;
- more points lying in the positive  $G$  region as the frequency goes up, indicating that the radiation pattern is becoming more directional in the vertical direction.

On this evidence, the reverberating chamber can be related to the open site. It appears, in fact, to be a more effective method in the ability to measure a quantity representative of the maximum radiation.

#### **4.3.4 Procedure for the determination of the reverberating chamber limit**

The procedure is as follows.

- i) Measure a sample of equipment for the maximum radiation on the open-area site. Convert the measured quantities to the equivalent power from a half-wave dipole. Call this quantity  $P_q$ , in dB(pW).
- ii) Measure the same sample in the reverberating chamber for total radiated power. Call this quantity  $P_t$ , in dB(pW).
- iii) This relationship between the reverberating chamber limit and the open area test site limit can be found by the graphical method of figure 1, or by calculating the gain of each equipment, obtaining a representative value of  $G$  for the equivalent type using statistical methods, and applying equation (4.3-2).

## Annex 4.3-A

### Derivation of the formula

Consider the general case of a lossless antenna with gain  $g$  and input power  $p$ . At distance  $d$  in the direction of maximum radiation, the field strength  $e$  is given by the well-known formula:

$$e = (30 \times p \times g)^{1/2} / d$$

Thus, for two antennas, with gains  $g_1$  and  $g_2$  and input powers  $p_1$  and  $p_2$  producing the same field strength at a point at the same distance in the direction of maximum radiation

$$p_1 \times g_1 = p_2 \times g_2, \text{ or, in log form, } P_1 + G_1 = P_2 + G_2$$

and, in the case given in 4.3.2,  $P_1 = P_t$  and  $G_1 = G$ ;  $P_2 = P_q$  and  $G_2 = 2$  therefore the relationship is

$$P_t + G = P_q + 2$$

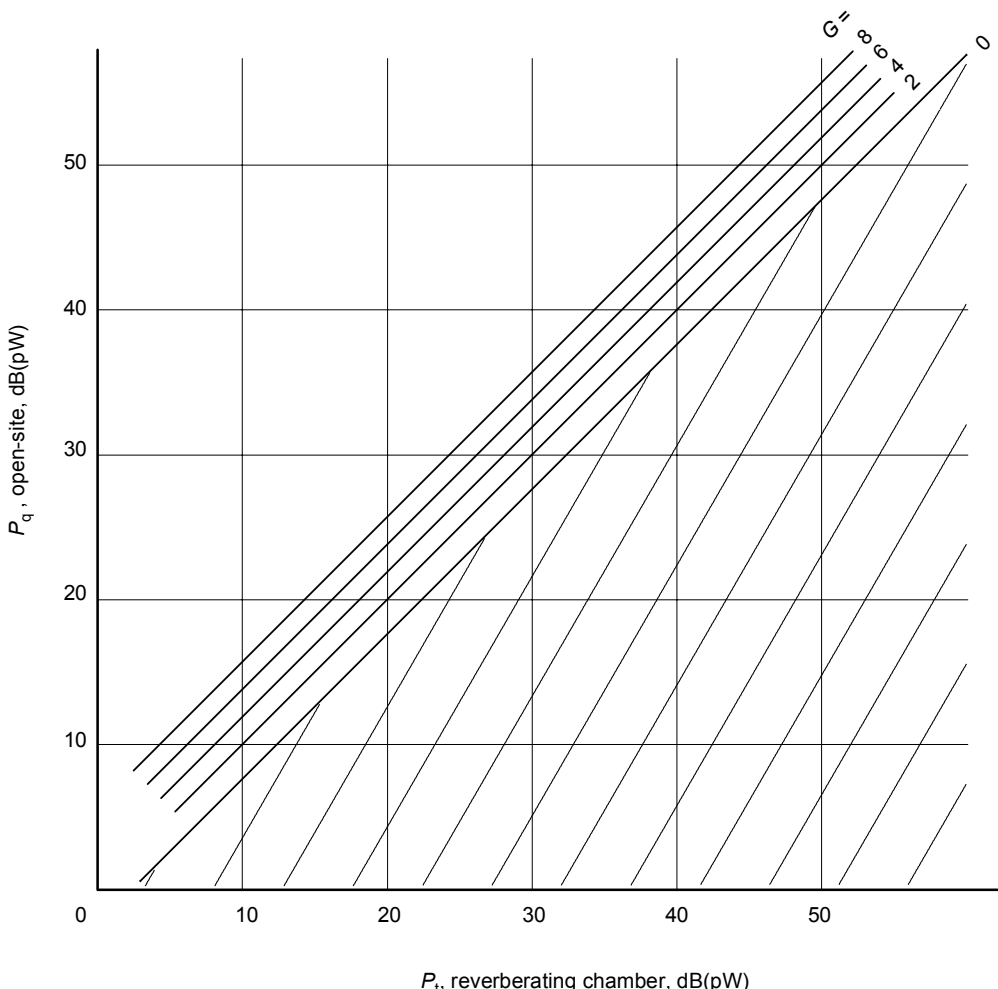
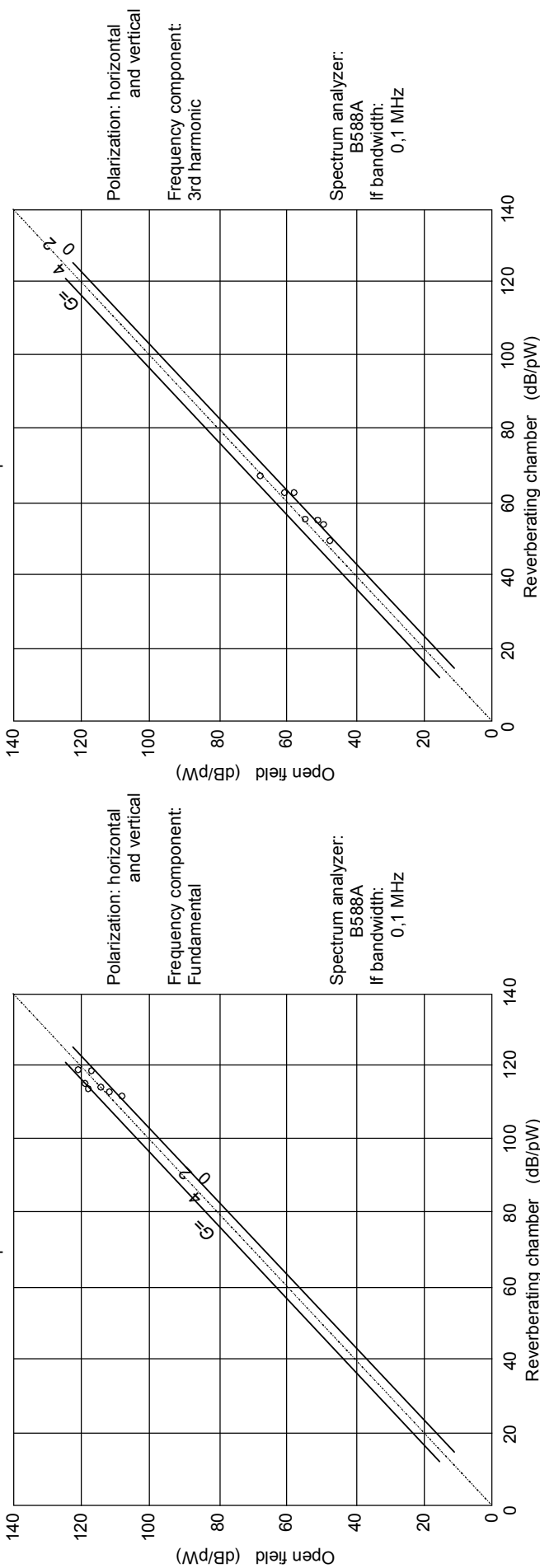


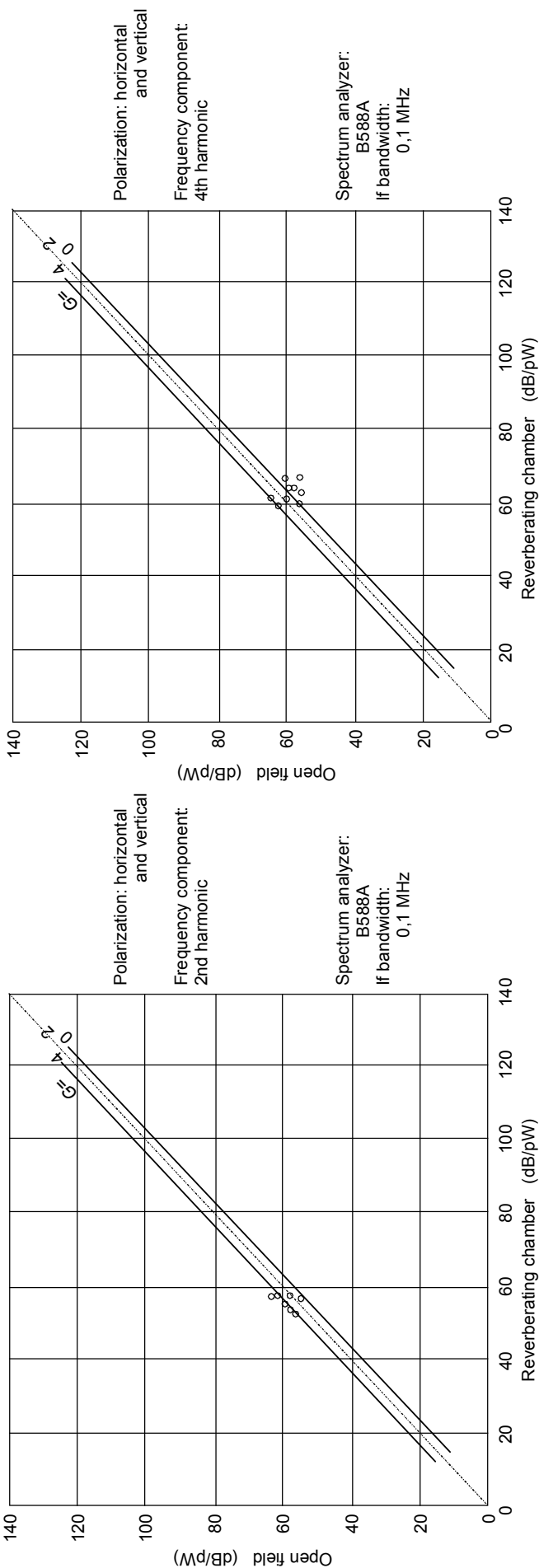
**Figure 4.3-1**

IEC 788/2000

Relation between substituted powers in chamber and calculated ERP in open field



Relation between substituted powers in chamber and calculated ERP in open field



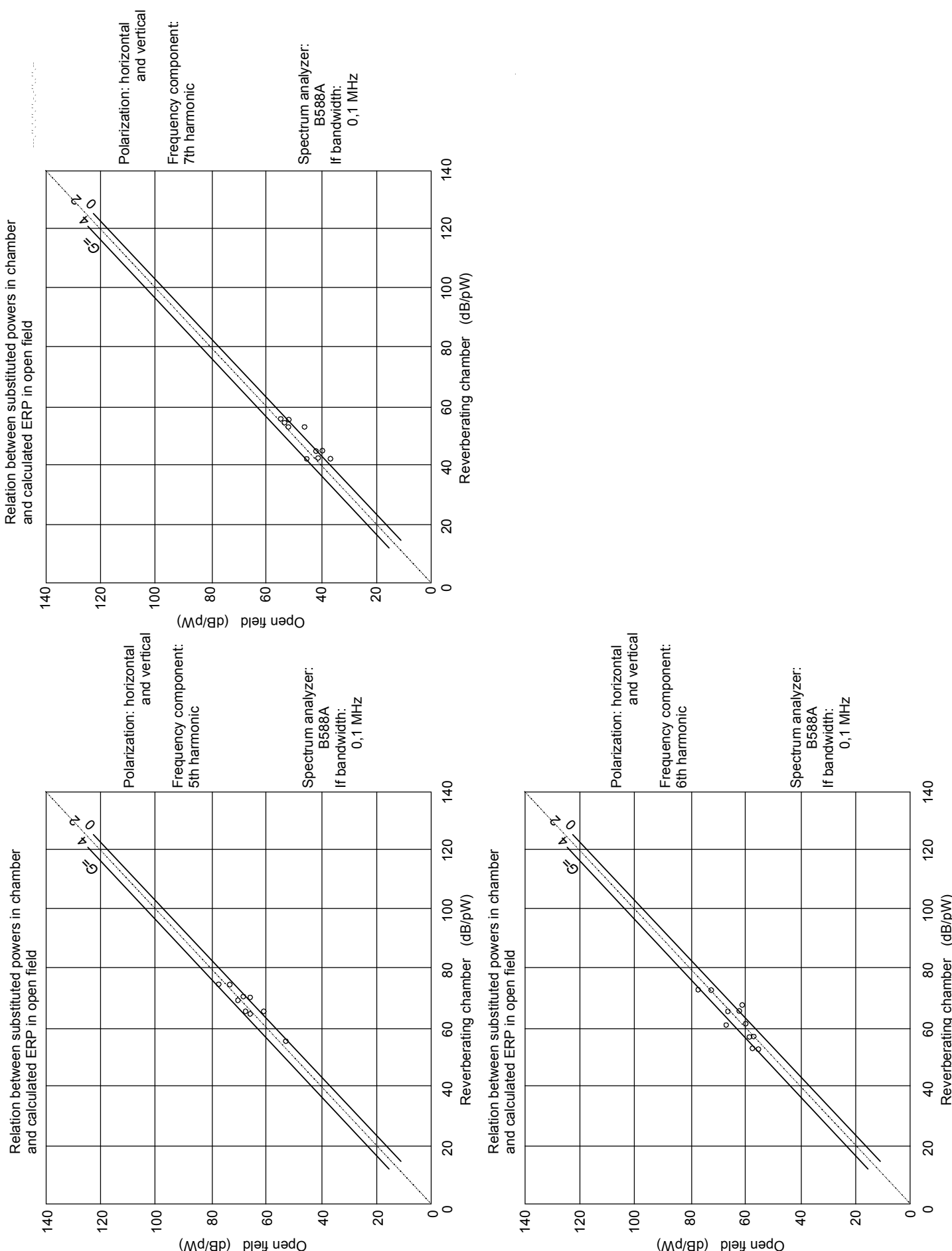


**Figure 4.3-2 – Examples of a number of microwave measured for  $P_q$  and  $P_t$**

#### **4.4 Characterization and classification of the asymmetrical disturbance source induced in telephone subscriber lines by AM broadcasting transmitters in the LW, MW and SW bands**

##### **4.4.1 Introduction**

The use of semiconductor devices in telephone terminal equipment (TTE) has created the need to verify the immunity to RF fields of this equipment, as non-linear semiconductor devices demodulate the induced RF signals [1-5]. The latter effect gives rise to a d.c. shift which may alter the operating point of such a device, thus, for example, reducing the noise margin of digital devices. In the case of amplitude-modulated RF fields, the non-linearity gives rise to a base-band signal which may become audible in the telephony system. An important class of RF-field sources is formed by AM broadcasting transmitters in the LW, MW and SW bands.

Because of the relatively small dimensions of TTE (compared to the wavelength of the disturbance signal) the asymmetrical (common-mode) source induced in telecommunication lines is expected to be the dominant disturbance source. Therefore, a conducted-immunity test (current-injection test) is relevant for this equipment. In this test, the disturbance signal is applied via the telecommunication lines. As a consequence, this report deals with the characterization of the unwanted antenna properties of telecommunication lines and with prediction models supplying information about the probability that certain parameter values will be met in practice. Moreover, it discusses the parameters which are of relevance when specifying the disturbance source used in the immunity test. The various considerations will be limited to parameters relevant at the subscriber end of the telephone lines.

In 4.4.2 the antenna properties will be expressed in terms of an antenna factor of the subscriber lines i.e. the induced asymmetrical open-circuit voltage normalized to the RF field strength, and an equivalent resistance of the induced asymmetrical source. The prediction models are needed in the classification of the RF fields and the induced asymmetrical disturbances, 4.4.3, and when setting immunity limits, 4.4.4. This report takes the view that the disturbance source in the immunity test is to be specified by an open-circuit voltage and a source impedance

All mathematical relations associated with the derivation of the models and those needed by the user of this report when applying the models to the respective geographical area are given in annex 4.4-A through 4.4-D.

This report is based on results of experimental investigations carried out on buried telephone-subscriber lines in Germany [6] [7] and in the Netherlands [8]. In these investigations induced-voltage and current data and magnetic-field-strength data were recorded at a large number of locations, permitting a statistical evaluation of the parameter values. A statistical approach was needed, as the telephone lines have random routing in the buildings and, consequently, random orientation with respect to the RF field have random coupling with nearby metal objects, while the buildings cause a random scattering of the RF fields.

It is to be expected that the contents of this report will also be applicable to other types of lines running through buildings in a similar manner to telephone-subscriber lines, for example, bus-system lines and signal and control lines.

##### **4.4.2 Experimental characterization**

A full description of the experimental characterization has been presented in [7] [8]. Therefore, this section contains only a summary of this method with regard to the parameters needed in this report.

The induced asymmetrical voltage was measured at the outlet of a telephone-subscriber line using a modified T-network [9] [10]. As a result of this modification, a voltage  $U_h$  could be measured across a  $10\text{ k}\Omega$  resistor and a voltage  $U_l$  across a  $150\text{ }\Omega$  resistor. The investigations showed that  $U_h$  can be considered as the induced open-circuit voltage. In practice, the reference for this voltage is generally unknown. During the measurements that reference was a special metal measuring cart connected via a copper strap to the central heating system (CH). The equivalent resistance  $R_a$  of the induced source is estimated from data pairs  $\{U_h, U_l\}$ .

At each location two magnetic-field-strength data of the broadcasting transmitter were measured using a loop antenna positioned in a vertical plane and rotated about its vertical axis to find the maximum reading. One datum,  $H_i$ , was measured near the outlet under investigation inside the building, and one datum,  $H_o$ , was measured outside the building at a distance of about 10 m from that building. In order to obtain a sufficiently high induced-signal-to-ambient-noise ratio, the measurements were carried out in areas with a relatively high value of the RF field strength. This is not expected to influence the applicability of the results, as the presence of a broadcasting transmitter is not taken into account in the layout of telephone-subscriber lines. Moreover, as mentioned in 4.4.1, the induced voltage will be normalized to the field strength and the resulting "antenna factor" will represent a property of the subscriber lines measured.

#### 4.4.2.1 Field strength and building effect

Although the RF field is not a characteristic of the subscriber lines, it forms the origin of the induced disturbances. Two aspects of the RF field will be considered in this section:

- The measured field strength  $H_o$  outside the buildings compared to the field strength  $H_c$  calculated from the simple far-field relation for a half-wave dipole (in its main direction)

$$H_c = \frac{7\sqrt{P}}{Z_0 r} \quad (4.4.2-1)$$

where  $P$  is the transmitter power,  $Z_0$  is free-space wave impedance ( $377\text{ }\Omega$ ) and  $r$  the distance between the transmitter and the point of observation. In the calculations, the values of  $P$  as given in [13] will be used.

NOTE Although broadcast transmitter antennas usually are monopoles (in the frequencies of interest), the half-wave dipole formula (4.4.2.1) has been used for convenience.

- The effect of the building on the field strength, which can be expressed in a building-effect parameter  $A_b$  defined by

$$A_b = H_o (\text{dB}\mu\text{A/m}) - H_i (\text{dB}\mu\text{A/m}) \quad (4.4.2-2)$$

This factor is often called the building attenuation. However, this factor not only depends on the attenuation properties of the building material itself, but also on the reradiation properties of metallic structures in and near the building, and, on the height above ground,  $H_o$  and  $H_i$  were measured. Therefore the term building effect is used in this report.

A consideration of these two aspects is needed in view of the antenna factors to be discussed in 4.4.2.2 and in view of the prediction models to be discussed in 4.4.2.3.

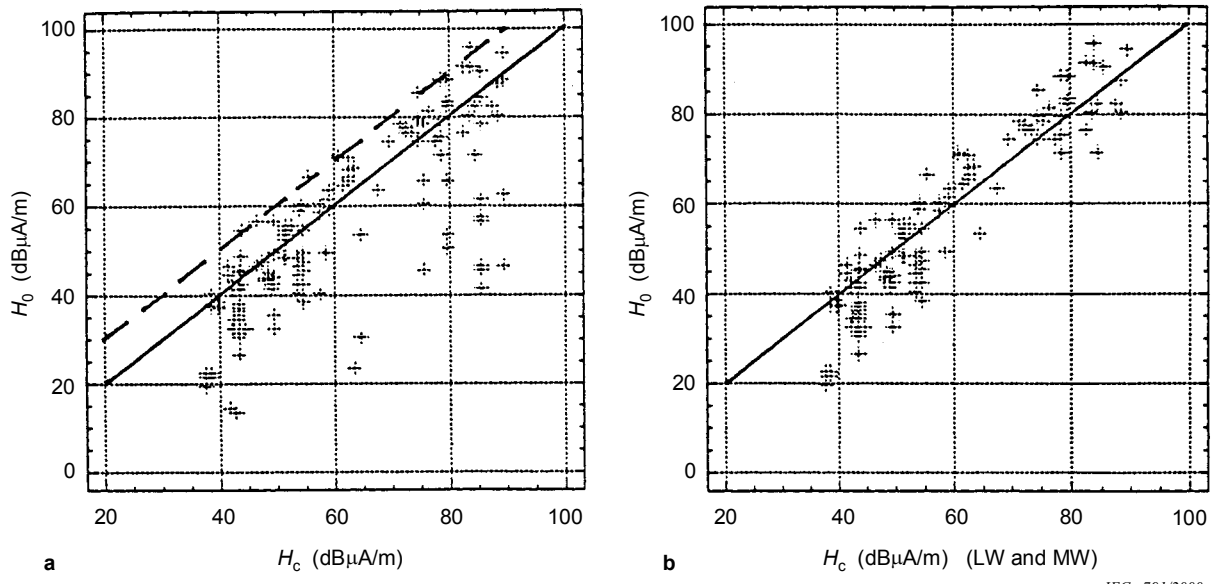


**Figure 4.4.2-1 – Scatter plot of the measured outdoor magnetic field strength  $H_o$  (dB $\mu$ A/m) versus the calculated outdoor magnetic field strength  $H_c$  (dB $\mu$ A/m)**  
a) all data; b) data of SW transmitters rejected

IEC 791/2000

The results of  $H_o(H_c)$  given in figure 4.4.2-1a show that large deviations from  $H_o = H_c$  are possible (drawn line), but that  $H_o \leq (H_c + 10)$  dB $\mu$ A/m (broken line), hence the measured value is at most a factor of 3 higher than the value calculated from equation 4.4.2-1. The largest deviations concern data of SW transmitters. This is understandable, as SW transmitters normally have a beamed antenna pattern, whereas the antenna patterns of the LW and MW transmitters are generally close to circular. Figure 4.4.2-1b gives the scatter plot  $H_o(H_c)$  after rejection of the SW transmitter data.

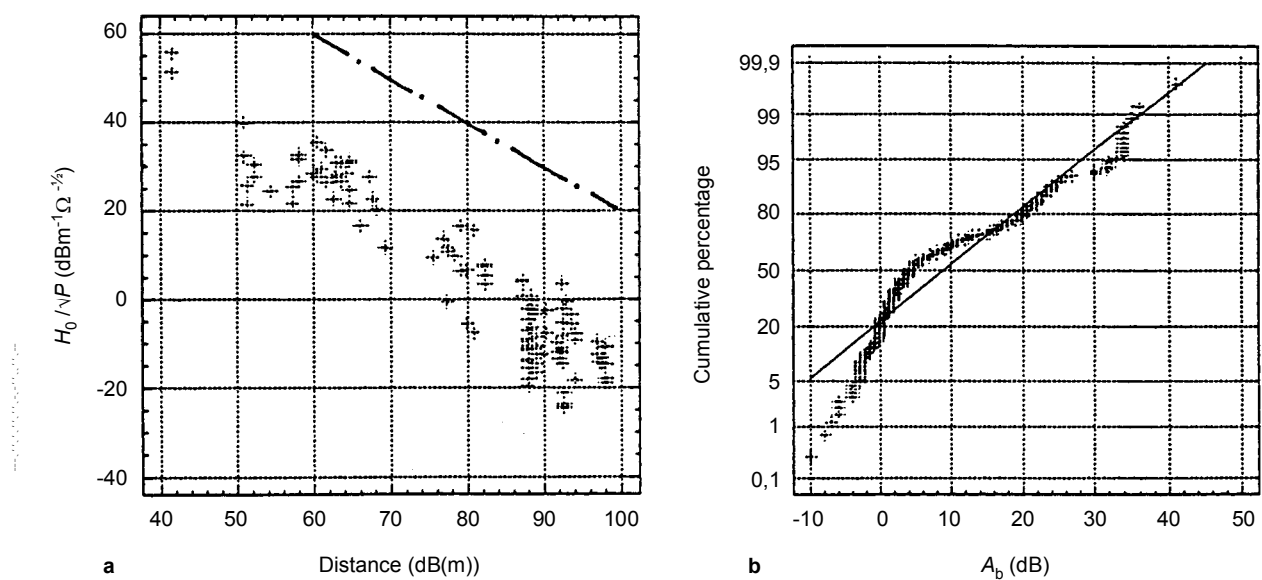
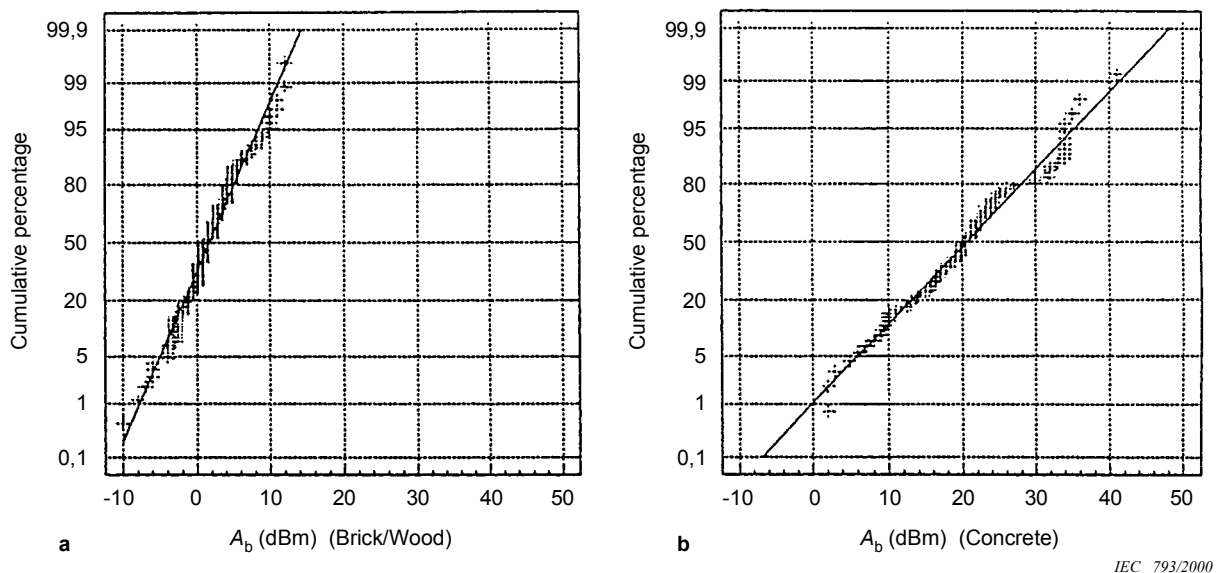


**Figure 4.4.2-2 –**  
a) Scatter plot of the measured outdoor magnetic field strength  $H_o$  normalized to the square root of the reported power [11] versus the distance  $d$  (m) to the transmitter,  
b) Normal probability plot of the building-effect parameter  $A_b$  (dB), all data

IEC 792/2000

Figure 4.4.2-2a shows the ratio  $H_o / \sqrt{P}$  versus the distance between the point of observation and the transmitter, and the dash-dot line indicates a slope  $-1$ . It can be concluded that, on average, the data follow this slope fairly well. The associated intercept is higher than that expected from equation 4.4.2-1, which is in agreement with the  $(H_c + 10) \text{ dB}\mu\text{A/m}$  limit observed in figure 4.4.2-1.

Figure 4.4.2-2b shows the normal probability plot of all building-effect data. If these data were normally distributed, a straight line would have resulted. This is not the case, and the data suggest that, in first-order approximation, two distributions are superimposed. The two distributions are found when distinguishing between data associated with buildings constructed from brick and/or wood (B/W) and data associated with buildings constructed from reinforced concrete (C). The normal probability plots of these distributions are given in figure 4.4.2-3a and b. The negative values of  $A_b$  predominantly stem from measurements where  $H_i$  was measured on an upper floor of the building, whereas  $H_o$  was already measured at about 1,5 m above ground level outside the building. Effects of reradiation also influence the actual field-strength data.



IEC 793/2000

**Figure 4.4.2-3 – Normal probability plot of the building-effect parameter  $A_b$  (dB)**  
**a) Buildings constructed from brick and/or wood;**  
**b) Buildings constructed from reinforced concrete**

The numerical results have been summarized in table 4.4.2-1. No clear frequency dependence of the  $A_b$  data could be observed (see 4.4.2.4).

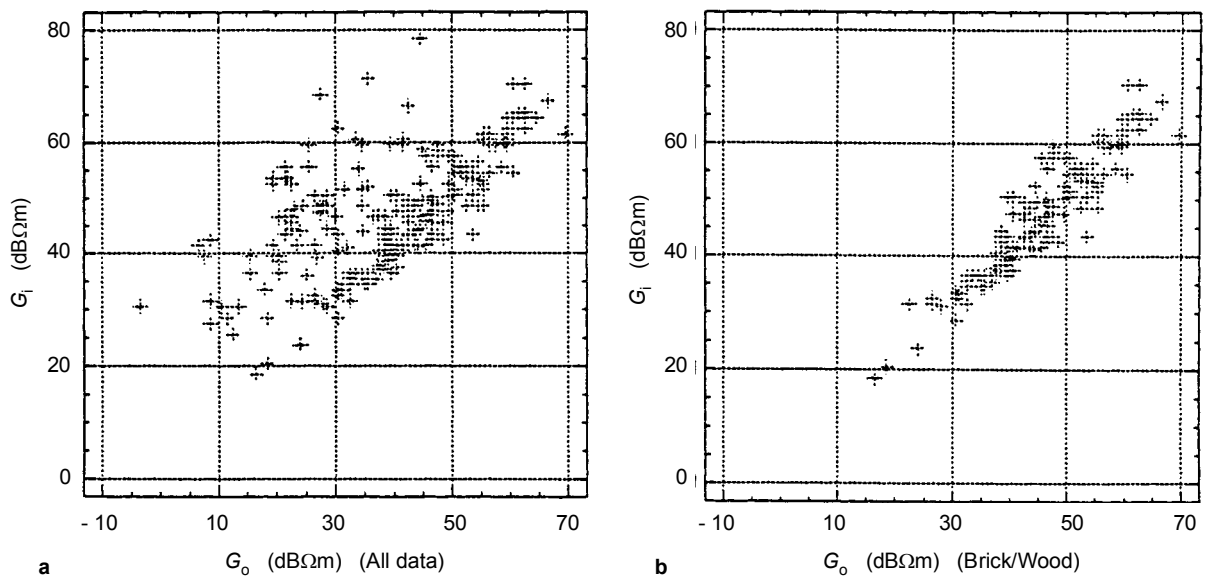
**Table 4.4.2-1 – Summary results of building-effect,  $A_b$ , analysis**

Building material	Average dB	Standard deviation dB	Median dB	Number of data
Brick and/or wood	1,6	4,0	1,0	138
Reinforced concrete	20,6	8,7	20,1	84

#### 4.4.2.2 The asymmetrical open-circuit voltage normalized to the field strength

The interface for the voltage measurements was the outlet to which the telephone set was connected during the measurements. The investigations showed that the influence of the telephone set and its standard lead (4 m long) on the measured voltages could be neglected.

The measured voltage will be normalized to the measured magnetic field strength in 4.4.2.2.1 and, assuming far-field conditions, to the electric field strength in 4.4.2.2.2. After that, 4.4.2.2.3 deals with truncation of the distributions found in 4.4.2.2.1 and 4.4.2.2.2.



IEC 794/2000

**Figure 4.4.2-4 – Scatter plot of the outdoor antenna factor  $G_o$  (dBΩm) versus the indoor antenna factor  $G_i$ :**

a) all data; b) data associated with buildings constructed from brick and/or wood

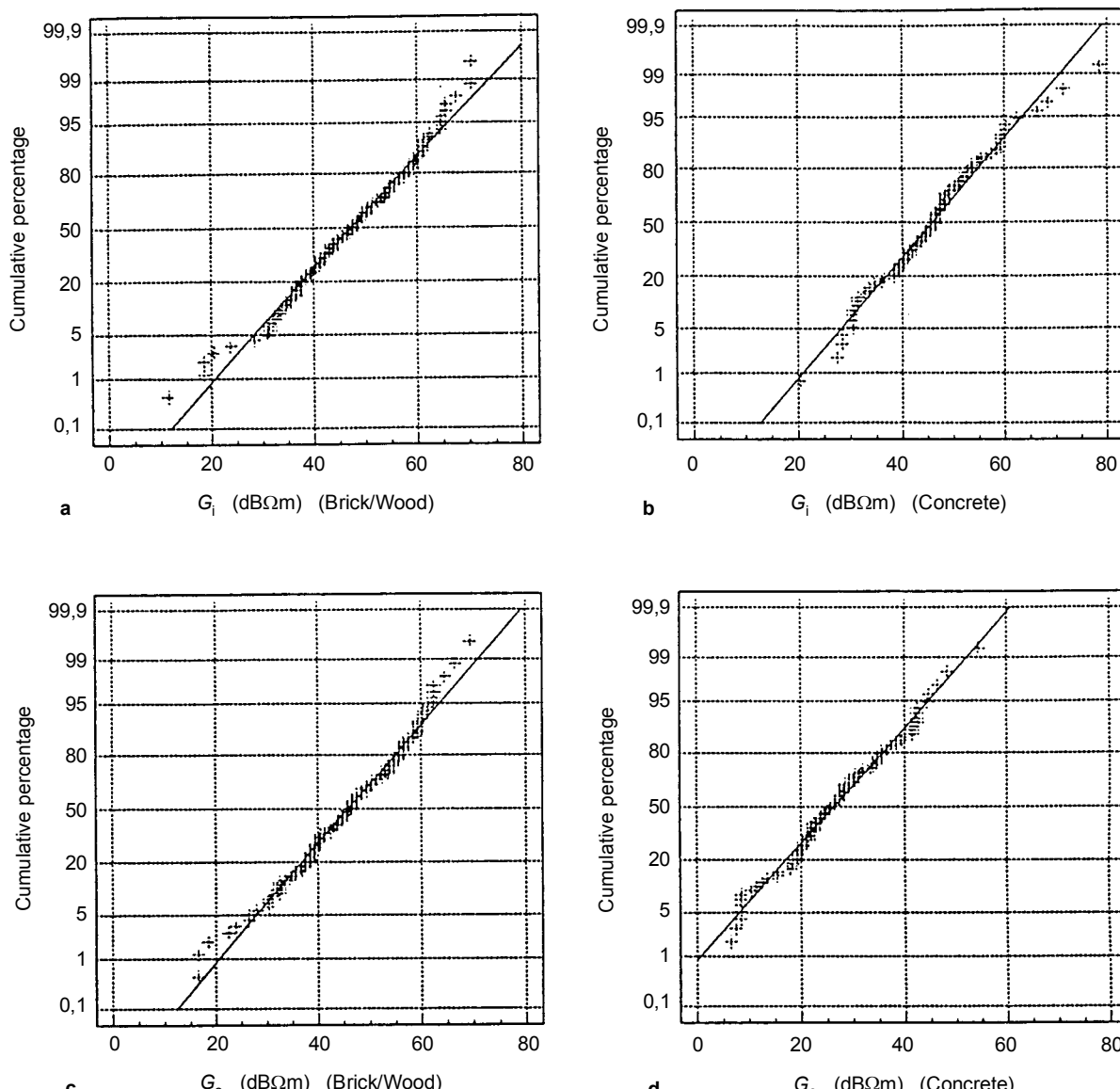
#### 4.4.2.2.1 G factors

To obtain an antenna property of the subscriber lines, the open-circuit voltage  $U_h$  is normalized to the field strength ( $H_i$  or  $H_o$ ), yielding the antenna factors  $G_j$  and  $G_o$  defined by

$$G_{i,o}(\Omega\text{m}) = \frac{U_h (\mu\text{V})}{H_{ino} (\mu\text{A}/\text{m})} \quad (4.4.2-3)$$

Figure 4.4.2-4a shows the scatter plot  $G_i(G_o)$  using all data. The plot suggests that there is one dominant "cloud" of data with a limited scattering and a second "cloud" with much more scattering. Further investigation revealed that the first cloud stems from data measured in buildings constructed from brick and/or wood, see figure 4.4.2-4b, while the other cloud is associated with buildings constructed (predominantly) from reinforced concrete. Consequently, the building effect discussed in 4.4.2.1 is of importance.

The normal probability plots of  $G_j$  (dBΩm) and  $G_o$  (dBΩm) associated with the two types of building material considered, are given in figure 4.4.2-5. It can be concluded that the data follow a normal distribution, which means lognormal distributions of the  $G$  factors in Ωm. The numerical results have been summarized in table 4.4.2-2, where  $G_U$  and  $G_L$  are the upper and lower limit of the range of experimental  $G$  data (see 4.4.2.2.3). The differences between  $G_i$  and  $G_o$  of the two classes of building material considered are in line with the building-effect data for these buildings (see table 4.4.2-1). No clear frequency dependence could be observed (see 4.4.2.4).



IEC 795/2000

**Figure 4.4.2-5 – Normal probability plots of the antenna factors:**  
**a)  $G_j$  (dBΩm) and c)  $G_o$  (dBΩm) associated with buildings constructed from brick and/or wood;**  
**b)  $G_j$  (dBΩm) and d)  $G_o$  (dBΩm) associated with buildings constructed from reinforced concrete**

**Table 4.4.2-2 – Summary of results of G-factor analysis**

<b>G factor</b>	<b>Building material</b>	<b>Average</b> dBΩm	<b>Standard deviation</b> dB	<b>Median</b> dBΩm	<b>Number of data</b>
$G_j$	B/W	47,3	11,2	47,5	135
$G_j$	C	45,9	10,5	46,5	88
$G_o$	B/W	45,8	10,6	46,4	134
$G_o$	C	26,5	10,9	26,0	90

#### 4.4.2.2.2 *L* factors

In 4.4.2.2.1,  $U_h$  was normalized to the measured magnetic field strength, thus yielding the  $G$  factors. Assuming far-field conditions, the electric field strength follows from  $E = H \cdot Z_0$  with  $Z_0 = 377 \Omega$ . If the outdoor field strength is considered, this assumption seems to be reasonable and the  $G_o$  factor can be converted into an  $L_o$  factor defined by

$$L_o = \frac{G_o}{Z_0} = \frac{U_h}{H_o Z_0} = \frac{U_h (\mu V)}{E_o (\mu V/m)} \quad (4.4.2-4)$$

The  $L$  factor can be considered as the effective length or effective height of the subscriber line acting as an antenna. The results for  $L_o$  have been summarized in table 4.4.2-3, where  $L_U$  and  $L_L$  are the upper and lower limit of the range of experimental  $L$  factors (see 4.4.2.2.3).

**Table 4.4.2-3 – Summary of  $L_o$  factors (far-field)**

$L$ factor	Building material	Average*	Standard deviation	$L_U$	$L_L$
		dBm	dB	dBm	dBm
$L_o$	B/W	-5,7	10,6	18,0	-35,0
$L_o$	C	-25,0	10,9	3,0	-55,0

\* Note that dBm refers to dB with respect to 1 m.

In the literature an  $L$  factor of -3,0 dBm average (standard deviation 10 dB, number of data 10) has been reported [12] for a cable running 1 300 m underground and 1 000 m to 3 000 m overhead (aerial cable) towards the subscriber. Broadcasting frequencies were 594 kHz and 1 242 kHz. No details were given about the field-strength measurements, the reference for the asymmetrical voltage and the properties of the building material. The results reported in [12] are in line with the results for  $L_o$  (B/W), as given in table 4.4.2-3. However, more recent investigations by the same team [15] indicate an average  $L$ -factor of 0 dBm.

$L_i$  factors might be derived from the  $G_i$  factors in a similar way as the  $L_o$  factors. However, it is to be expected that inside the buildings the far-field conditions are not satisfied and it has to be decided which wave impedance has to be taken. Therefore, no  $L_i$  data have been presented in table 4.4.2-3. See also note 2 at the end of 4.1.

#### 4.4.2.2.3 Truncation

In 4.4.2.2.1 it was concluded that the distribution  $f(G)$  of the  $G$  factors (antenna factors) is lognormal or in mathematical form

$$f(g)dG = \frac{1}{G\sigma\sqrt{2\pi}} e^{\frac{-(\ln G - \mu)^2}{2\sigma^2}} dG \quad (4.4.2-5)$$

However, by adopting this lognormal distribution it is automatically assumed that a  $G$  factor may range from zero to infinitely large. In practice, infinitely large will never occur as wavelength effects and effects of coupling with nearby structures create an upper limit ( $G_U$  or  $L_U$ ) of the antenna factors [13]. Consequently, for correct use in the prediction models (4.4.3 and 4.4.4)  $f(G)$  has to be truncated. Similarly, truncation has to be applied to the distribution of the building-effect parameters.

Unfortunately, no theoretical study is known which predicts the upper limit of  $G$  (or  $L$ ) of an actual telephone-subscriber line taking into account the length and the routing of a line inside the building and, buried, outside the building. However, it has to be expected that such a limit exists and the best approach is to use the experimental upper limit ( $G_U$  or  $L_U$ ).

In addition to the upper limit, one may also consider a lower limit ( $G_L$  or  $L_L$ ) and truncate  $f(G)$  at the lower end. It is found that in the range of parameter values to be considered in 4.4.3 and 4.4.4, the influence of  $G_L$  (or  $L_L$ ) is negligible.

The truncated probability density function reads

$$f_t(G)dG = \frac{f(G)dG}{\int_{G_L}^{G_U} f(G)dG} = \frac{f(G)dG}{F(G_U) - F(G_L)} = \alpha_t f(G)dG \quad (4.4.2-6)$$

The mathematical form of the cumulative distributions  $F(G_U)$  and  $F(G_L)$  is given in annex 4.4-D. Table 4.4.2-4 summarizes the truncation data of the  $G$  factors and the building-effect parameter  $A_b$ . Note that  $\alpha_t$  differs very little from 1, that is from the value of  $\alpha_t$  if  $-\infty \leq G$  ( $\text{dB}\Omega\text{m}$ )  $\leq \infty$  or  $-\infty \leq A_b$  (dB)  $\leq \infty$  since  $F(\infty) = 0,5$  and  $F(-\infty) = -0,5$ . The upper and lower limit in dBm of the  $L$  factor range are found by subtracting 51,5 dBΩ from the corresponding  $G$  factors in dBΩm.

**Table 4.4.2-4 – Summary of truncation parameters of  $f(G)$**

<b><math>G</math> factor or <math>A_b</math></b>	<b>Building material</b>	<b><math>G_U</math> (dBΩm) <math>A_{bu}</math> (dB)</b>	<b><math>G_L</math> (dBΩm) <math>A_{bl}</math> (dB)</b>	<b><math>F(G_U)</math> <math>F(A_{bu})</math></b>	<b><math>F(G_L)</math> <math>F(A_{bl})</math></b>	<b><math>\alpha t_G</math> <math>\alpha t_A</math></b>
$G_i$	B/W	70,5	11,5	0,4805	-0,4993	1,021
$G_i$	C	78,5	20,5	0,4985	-0,4922	1,009
$G_o$	B/W	69,5	16,5	0,4873	-0,4971	1,016
$G_o$	C	54,5	-3,5	0,4950	-0,4971	1,008
$A_b$	B/W	12,0	-10,0	0,4953	-0,4981	1,007
$A_b$	C	41,0	2,0	0,4905	-0,4837	1,026

#### 4.4.2.3 The equivalent asymmetrical-source resistance

The equivalent resistance of the induced asymmetrical source can be determined from data pairs  $\{U_h, U_l\}$ , where  $U_h$  is the open-circuit voltage and  $U_l$  the voltage measured across  $150 \Omega$ , using the simple relation

$$R_a = \frac{U_h - U_l}{U_l} 150 \text{ } (\Omega) \quad (4.4.2-7)$$

The normal probability plot of  $R_a$  (dBΩ) is given in figure 4.4.2-6. It can be concluded that  $R_a$  (dBΩ) follows a normal distribution and, hence,  $R_a$  in Ω follows a lognormal distribution. The numerical results have been summarized in table 4.4.2-5. The average value found is close to the value  $150 \Omega$  used in existing immunity tests [9] [14]. In table 4.4.2-5,  $R_{au}$  and  $R_{al}$  are the upper and lower limit of the range of experimental  $R_a$ -data. The relatively large and small values of  $R_{au}$  and  $R_{al}$  compared to the average value of  $R_a$  stem from

resonances and anti-resonances in the common mode circuit of the subscriber line. No clear-frequency dependence of  $R_a$  could be observed (see 4.4.2.4) and no influence of the building material was observed.

**Table 4.4.2-5 – Summary results of equivalent-resistance analysis**

$R_a$ (average) dBΩ	Standard deviation dB	Median dBΩ	$R_a$ (average) Ω	Number of data	$R_{au}$ dBΩ	$R_{al}$ dBΩ	$R_{au}$ Ω	$R_{al}$ Ω
44,2	6,8	43,5	162	204	63,7	25,2	1 531	18

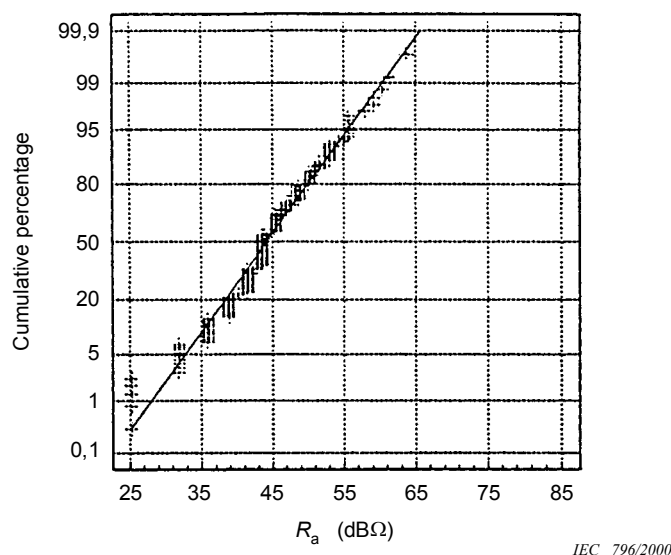
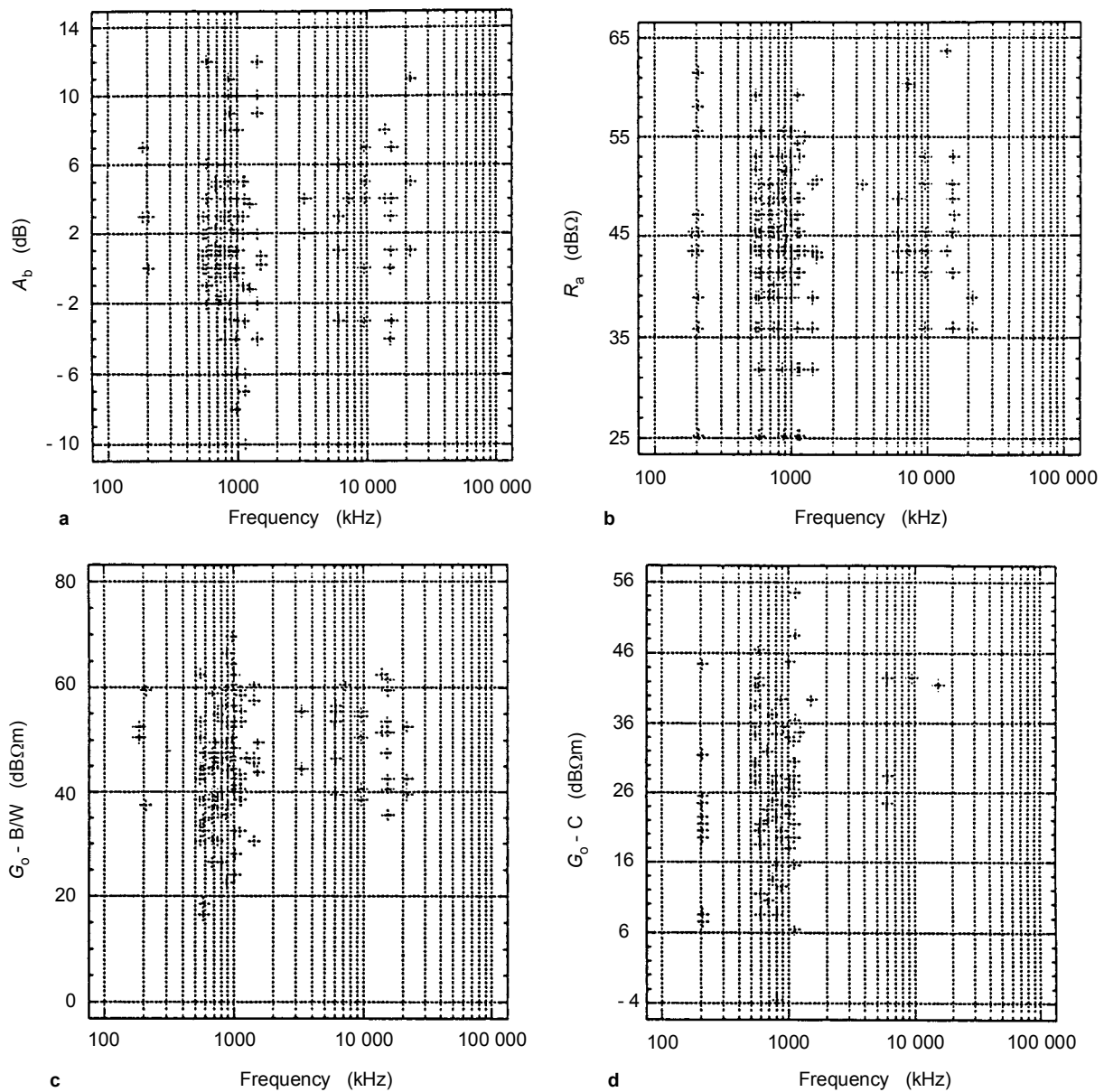


**Figure 4.4.2-6 – Normal probability plot of the equivalent asymmetrical resistance  $R_a$  (dBΩ)**

#### 4.4.2.4 Frequency dependence of the parameters

In the frequency range determined by the measurements in the LW, MW and SW bands, no clear frequency dependence of the building effect  $A_b$ , the  $G$  factors  $G_o$  and  $G_i$ , and the equivalent resistance  $R_a$  could be observed. This is illustrated in figures 4.4.2-7a and b the  $A_b$  data for brick/wood buildings, the  $R_a$  data, the  $G_o$  data for brick/wood buildings, and for reinforced concrete buildings.

Because no clear frequency dependence of the various quantities could be observed, it will be assumed in 4.4.3 and 4.4.4 that the building effect, the  $G$  and the  $L$  factors and the equivalent resistance are independent of the frequency in the frequency range of the LW, MW and SW bands. A possible frequency dependence is then incorporated in the standard deviation of the respective distributions.



IEC 797/2000

**Figure 4.4.2-7 – Examples of the frequency dependence of some parameters**

- a) the building effect  $A_b$  in the case of brick/wood buildings
- b) the equivalent resistance  $R_a$
- c) the  $G_o$  factor for brick/wood buildings, and
- d) the  $G_o$  factor for reinforced concrete buildings

#### 4.4.3 Prediction models and classification

This section presents some simple prediction models for fields and voltages needed in the process of classification of the electromagnetic environment and when setting immunity limits for the telephone sets to be connected to the subscriber lines.

Because the measuring locations were not chosen randomly in order to obtain a sufficiently high induced signal-to-ambient noise ratio, the basic data from which the parameters reported in 4.4.2 were derived cannot be used directly as they form a non-random sample from their actual distributions. The models to be discussed permit an estimate to be made of the complete distributions of the field strength and induced voltage. In addition, the

complete distributions allow for a classification of these quantities. This report gives only the procedure for this classification. The actual class limits are outside its scope.

#### 4.4.3.1 Field-strength classification

As mentioned in 4.4.2.1, the field strength is not a property of the subscriber line. Nevertheless, information about the field strength is needed in order to make a prediction of the induced voltages.

From the results given in 4.4.2.1, it follows that in first-order approximation the outdoor field strength, to be indicated by  $E_o$  and  $H_o$  for the electric and magnetic field component respectively, is inversely proportional to the distance  $r$  between the point of observation and the transmitter, and proportional to the square root of the transmitter power. From the results summarized in 4.4.2.1 it follows that, in the worst case, the constant of proportionality is a factor of 3 ( $= 10$  dB) larger than the constant of proportionality in the case of a half-wave dipole.

A classification of the outdoor electric or magnetic field strength may be based on the probability  $pr\{E_o \geq E_L\}$  or  $pr\{H_o \geq H_L\}$  that the outdoor field strength is equal to or larger than a given limit value, indicated by the subscript  $L$ . As explained in annex 4.4-A, this probability can be written as

$$pr\{H_o \geq H_L\} = \int_{R_L}^{H_{\max}} f_n(H) dH \text{ or } pr\{E_o \geq E_L\} = \int_{E_L}^{E_{\max}} f_n(E) dE \quad (4.4.3-1)$$

where  $f(H)$  and  $f(E)$  represent the normalized field-strength distribution and  $H_{\max}$  and  $E_{\max}$  the maximum field strength in the geographical region in which the probability has to be estimated. Under far-field conditions both relations in equation (4.4.3-1) are equivalent.

Considering a ring-shaped area (RSA) around a transmitter having a circular antenna pattern, it follows (see annex 4.4-A) that

$$pr\{E_o \geq E_L\} = \frac{(E_{\max}^2 - E_L^2)E_{\min}^2}{(E_{\max}^2 - E_{\min}^2)E_L^2} \approx \frac{E_{\min}^2}{E_L^2} \quad (4.4.3-2)$$

where  $E_{\max}$  is the field strength at the inner boundary of the RSA and  $E_{\min}$  the field strength at the outer boundary of the RSA. A similar expression is valid for the magnetic field strength, see annex 4.4-A.

The inner boundary of the RSA has to be specified, as the relation between  $E_o$  and  $r$  derived from the measuring data will not be valid arbitrarily close to the transmitter, i.e. in the near-field region of the transmitter. A non-zero outer boundary field strength is needed, as  $E_{\min} = 0$  would mean that  $pr\{E_o \geq E_L\} = 0$  for all values of  $E_L$ . Note that by definition  $pr\{E_o \geq E_L\} = 0$  and that  $pr\{E_o \geq E_{\min}\} = 1$  ( $= 100\%$ ). The approximation given in equation (4.4.3-2) is valid if  $E_{\max} \gg \{E_{\min}, E_L\}$ , which is normally the case. Hence, it can be concluded that in the present model the value of  $E_{\min}$  to be specified is very important. The choice of  $E_{\min}$  and  $E_{\max}$  will be discussed further in 4.4.4.

As an example, table 4.4.3-1 gives the values of  $E_L$  for a number of probability values, assuming  $E_{\max} = 60$  V/m, which is an example of a radiation-hazard limit in the MW band of frequencies, and  $E_{\min} = 0,01$  V/m ( $= 80$  dB $\mu$ V/m). The latter value is of the order of

magnitude of the minimum field strength in the service area of a broadcasting transmitter. Note that the probability values are almost completely determined by  $E_{\min}$ .

**Table 4.4.3-1 – Example of field-strength classification**

$pr\{E_o \geq E_L\}$ %	$E_L$ V/m	$E_{\min}$ $\sqrt{pr\{E_o \geq E_L\}}$	$P = 500$ kW	
			$k = 7$ $R_L$ m	$k = 22$ $R_L$ m
0	60	–	(80)	(260)
100	0,01	–	495000	1550000
$10^{-1}$	0,32	0,33	15652	49193
$10^{-2}$	1,00	1,00	4950	11556
$10^{-3}$	3,16	3,16	1565	4919
$10^{-4}$	9,86	10,00	495	1556

By expressing the RSA boundaries in terms of a field strength, and not, for example, in terms of the distance between the transmitter and the point of observation, equation (4.4.3-1) is applicable to any transmitter producing a field strength which is inversely proportional to the distance. However, after the classes have been established, a certain transmitter will have a certain value of the constant of proportionality  $k$ . Then class boundaries can be associated with distances  $R_L = k/P/E_L$  between transmitter and point of observation. In table 4.4.3-1 examples of  $R_L$  are given, assuming  $k = 7$  (as in the case of a half-wave dipole) and  $k = 22$  (the worst-case value found in 4.4.2.1), while the transmitter power  $P = 500$  kW. The  $R_L$  values for  $E_L = 60$  V/m have been put in between brackets, as, in the considered frequency range, the far-field condition is not valid at these distances.

The advantage of choosing the field-strength boundaries first is that the classes are the same for all kinds of transmitter, while the choice of a class is then determined by the probability that victim equipment will be at a certain distance from the chosen class of transmitters. In general, an estimate of the latter probability is easier than an estimate of the field-strength probability.

#### 4.4.3.2 Asymmetrical-voltage classification

A classification of the induced open-circuit common-mode voltage  $U_h$  may be based on the probability  $pr\{U_h \geq U_L\}$  that  $U_h$  is equal to or larger than a given limit value  $U_L$ . If  $f_t(G)$  describes the truncated distribution of  $G$  factors (see 4.4.2.2.3),  $f_n(H_0)$  the normalized field-strength distribution and use is made of the relation  $U_h = G_0 \cdot H_0$ , it is shown in annex 4.4-B that this probability can formally be written as

$$pr\{U_h \geq U_L\} = \int_{G_1}^{G_2} dG_0 \int_{U_1}^{U_2} dU_h \frac{1}{G_0} f\left(\frac{U_h}{G_0}\right) \cdot f_t(G_0) \quad (4.4.3-3)$$

where  $G_1$ ,  $G_2$ ,  $U_1$  and  $U_2$  are suitably chosen boundaries (see annex 4.4-B). In this equation the product of the two distributions, i.e. the joint distribution, is needed as  $pr\{U_h \geq U_L\}$  depends on simultaneously meeting a certain field-strength value  $H_0 (=U_h/G_0)$  and a certain value of  $G_0$ . In equation (4.4.3-3) the factor  $1/G_0$  stems from the transformation of  $f(H_0)$  into  $f(U_h/G_0)$ .

Note that equation (4.4.3-3) is not an explicit function of the distance between transmitter and point of observation as a consequence of the fact that the boundaries of the RSA have been defined by field-strength values. A similar remark has been made in connection with equation (4.4.3-1) and similar conclusions are possible here.

Considering again the ring-shaped area as introduced in 4.4.3.1, examples of the classification of  $U_h$ , i.e.  $U_L$  values corresponding with chosen values  $pr\{U_h \geq U_L\}$ , are given in table 4.4.3-2 classification. The relations used can be found in annex 4.4-B. As in 4.4.3.1, it was assumed that the outdoor field strength  $E_{max} = 60$  V/m ( $H_{max} = 0,16$  A/m) and  $E_{min} = 0,01$  V/m ( $H_{min} = 27$   $\mu$ A/m) have been specified. When using  $G_i$  and specifying the outdoor field strength, the building effect has to be taken into account, as is explained in annex 4.4-B.

**Table 4.4.3-2 – Example of voltage classification assuming for the outdoor field strength:  
 $E_{max} = 60$  V/m and  $E_{min} = 0,01$  V/m**

Building material	$G_i$		$G_o$	
	B/W	C	B/W	C
$A_b$ dB	1,6	20,6	–	–
$S_b$ dB	4,0	8,7	–	–
$A_{bu}$ dB	12,0	41,0	–	–
$A_{bl}$ dB	-10,0	2,0	–	–
$G_{i,o}$ dBΩm	47,3	45,9	45,8	26,5
$S$ dB	11,2	10,5	10,6	10,9
$G_U$ dBΩm	70,5	78,5	69,5	54,5
$G_L$ dBΩm	11,5	20,5	16,5	-3,5
$pr\{U_h \geq U_L\}$	$U_L$ dB $\mu$ V	$U_L$ dB $\mu$ V	$U_L$ dB $\mu$ V	$U_L$ dB $\mu$ V
$10^{-1}$	115	101	114	96
$10^{-2}$	125	111	124	106
$10^{-3}$	135	121	134	116
$10^{-4}$	145	131	143	125

#### 4.4.4 Characterization of the immunity-test disturbance source

The results presented in 4.4.2 and 4.4.3 of this report may be used to specify the open-circuit voltage and the internal impedance of the disturbance source in a conducted-immunity test needed to achieve a sufficiently high probability that TTE to be connected to the subscriber lines will be electromagnetically compatible.

The specification of the open-circuit voltage  $U_h$  should be based on the distribution of the voltages over all telephone outlets to be considered. Therefore, this distribution is calculated first, using models and parameter values derived in the preceding sections. Once the distribution is known it is possible to calculate  $N_o(U_h \geq U_L)$ , i.e. the number of outlets in the respective geographical region showing a voltage  $U_h \geq U_L$ , where  $U_L$  may be considered as the open-circuit voltage in the immunity test. The internal impedance may be chosen directly using the results given in table 4.4.2-3. After that, the relevant parameters for the specification of the disturbance source in the immunity test will be summarized in 4.4.4.2.

This section only gives the procedures to arrive at a specification of the parameters needed. The assignment of actual values is the prerogative of the Product Committees.

#### 4.4.4.1 Outlet-voltage distribution

The derivation of the outlet-voltage distribution is described in detail in annexes 4.4-B and 4.4-C. In this derivation, the following steps have been taken.

- 1) Determine the total probability density  $n(H_o)$  of the telephone outlets experiencing an outdoor magnetic field strength  $H_o$  in ring-shaped areas around the  $N$  transmitters to be considered, where the inner boundary of the areas is specified by a maximum field strength  $H_{\max}$  and the outer boundary by a minimum field strength  $H_{\min}$ .

(Again, the magnetic field strength is considered first, as this field strength was measured in the experimental characterization procedure. If far-field conditions are valid, so that the magnetic and electric field strength have a constant ratio, the results can be converted directly in terms of the electric field strength.)

- 2) Determine the joint probability density  $f(H_o, G_o) = f(H_o) \cdot f(G_o)$  describing the density of outlets where the field strength has a magnitude  $H_o$  and, simultaneously, the antenna factor of the subscriber lines has the magnitude  $G_o$ , and convert the result into the joint probability density  $f(U_h, G_o)$ , by using the relation  $U_h = H_o G_o$ .
- 3) Calculate the probability  $pr\{U_h \geq U_L\}$ . If  $N_T$  is the total number of outlets in the respective geographical region and the boundary conditions are taken into account such that  $N_o(U_h \geq U_L) = N_T$  (or = 0) if  $pr\{U_h \geq U_L\} = 1$  (or = 0), then the number of outlets  $N_o(U_h \geq U_L)$  equals  $N_T \cdot pr\{U_h \geq U_L\}$ .

It is the prerogative of a Product Committee to choose a value of  $N_o$  ( $U_h \geq U_L$ ) from which  $U_L$  follows and hence the open-circuit voltage of the disturbance source in the immunity test.

Assuming the field strength to be inversely proportional to the distance between the outlet and the transmitter and assuming constant densities of outlets around the transmitters, it is shown in annex 4.4-C that the field-strength distribution  $n(H_o)$  can be written as

$$n(H_o) = \frac{2\pi \sum_{j=1}^N \mu_j k_j^2 P_j}{E_o^3} = \frac{-C_{Eo}}{E_o^3} \quad (4.4.4-1)$$

where  $\mu_j$  is the outlet density,  $k_j$  the constant of proportionality of the  $j$ -th transmitter and  $N$  the total number of transmitters considered. If the density  $\mu$  is the same around all transmitters and all transmitters have the same constant of proportionality  $k$ ,  $C_{H_o}$  is simply a constant times the sum over all transistor powers.

When considering the electric field strength  $E_o = (k/P)/r$ , the distribution  $n(E_o)$  reads

$$n(E_o) = \frac{2\pi \sum_{j=1}^N \pi_j k_j^2 P_j}{E_o^3} = \frac{-C_{Eo}}{E_o^3} \quad (4.4.4-2)$$

so that  $C_{Eo} = C_{H_o} \cdot Z_o^2$ . In annexes 4.4-A and 4.4-B it is explained how the various relations change when the indoor field strength  $H_i$  or  $E_i$  is to be used.

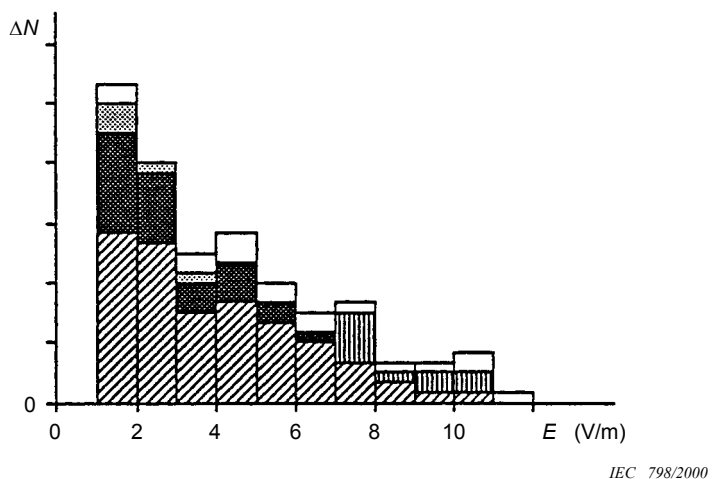


**Figure 4.4.4-1 – Example of the frequency histogram  $\Delta N(E_0, \Delta E_0)$ . The various shadings indicate schematically the contributions from various transmitters and non-homogeneous outlet densities. In this example the field-strength step  $\Delta E_0 = 1$  V/m.**

The outlet density will, in general, not be homogeneous around a transmitter. To derive  $n(H_0)$  in that case, a possible procedure is to determine a frequency histogram  $\Delta N(H_0, \Delta H_0)$  so that  $n(H_0)$  is approximated by  $n(H_0) = \Delta N(H_0, \Delta H_0) / \Delta H_0$ .

In practice, the magnitude of the electric field strength is mostly considered, so  $n(E_0)$  may be determined first, after which  $n(H_0)$  follows after assuming far-field conditions. An example of  $\Delta N(E_0, \Delta E_0)$  is given in figure 4.4.4-1, where the different shadings indicate the various contributions resulting from various transmitters and non-homogeneous outlet densities around these transmitters.

A drawback of the method leading to figure 4.4.4-1 and a drawback of the model leading to equations (4.4.4-1) and (4.4.4-2) is that, in particular in the lower field strength regions the fields of the various transmitters overlap. As a result, the same outlets in these regions are counted more than once if no discrimination is made with respect to the broadcast frequency. In 4.4.2.4 it has been explained that no real frequency dependence could be observed, so this discrimination is not possible, which leads to an over-estimate of  $\Delta N(E_0, \Delta E_0)$  at the lower field-strength values.

A procedure which might be followed is then to determine  $n_m(E_0)$ , the distribution of the maximum field strength in the respective geographical region resulting from the  $N$  relevant transmitters in (and in the direct vicinity of) that region. An example of such a distribution is given in figure 4.4.4-2. This distribution resulted for a part of Germany (having an area of  $2,5 \cdot 10^5$  km<sup>2</sup> and  $42 \cdot 10^6$  outlets) by calculating the maximum field strength in each node at a 1 km by 1 km grid over this region as caused by one of the 79 actual broadcasting transmitters in the respective frequency range, having a total ERP of 12,2 MW. The resolution of the field strength, i.e.  $\Delta E_0$  was taken to be 0,1 dB $\mu$ V/m. It was assumed that the density  $\mu$  was a constant ( $42 \cdot 10^6 / 2,5 \cdot 10^5 = 168$  km<sup>-2</sup>) throughout the region. When performing these calculations it was found that  $n_m(E_0)$  does not vary much after a certain number (50 in this case, with a total power of 7,5 MW) of transmitters had been taken into account.

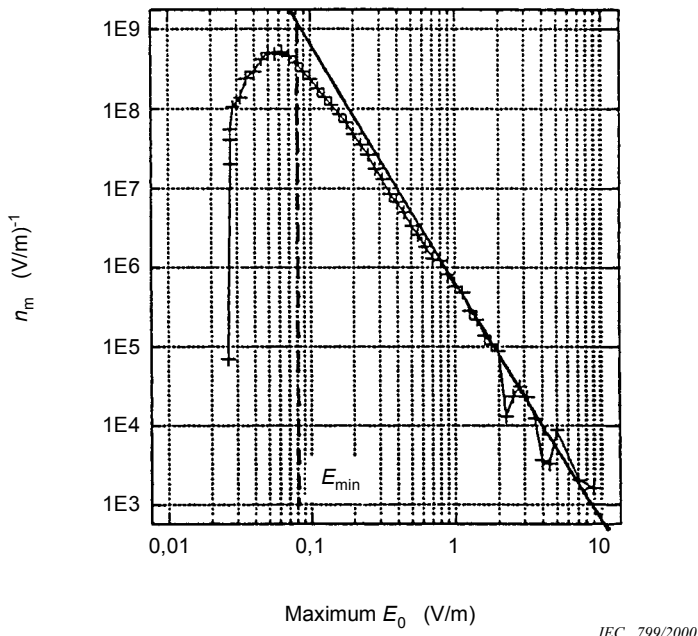


**Figure 4.4.4-2 – Example of  $n_m(E_o)$  the distribution of the outlets experiencing a maximum field strength  $E_o$  resulting from a given number of transmitters in (or near) the respective geographical region. The drawn line represents  $n(E_o) = -C_{Eo}/E_o^3$  with  $n(E_o = 1 \text{ V/m}) = n_m(E_o = 1 \text{ V/m}) \cdot E_{\min}$  has been chosen such that the integral over the field strength of  $n_m(E_o)$  and  $n(E_o)$  both yield the total number of outlets in that region**

The drawn line in figure 4.4.4-2 represents  $n(E_o) = -C_{Eo}/E_o^3$  with  $C_{Eo}$  taken such that  $n_m(E_o) = n(E_o)$  when  $E_o = 1 \text{ V/m}$ . This value is somewhat smaller than  $C_{Eo}$  calculated from equation 4.4.4-2 due to the aforementioned fact that  $n_m(E_o)$  seems to "saturate" when the number of transmitters is increased.

When integrating the distributions over the whole of the respective region, the total number of outlets  $N_T$  must follow, i.e.

$$N_T = \int_{E_{\min}}^{E_{\max}} n(E_o) dE_o = \frac{C_{Eo}}{2} \left\{ \frac{1}{E_{\min}^2} - \frac{1}{E_{\max}^2} \right\} \quad (4.4.4-3)$$

where the right-hand side of equation (4.4.4-3) follows when equation (4.4.4-2) is used. Equation (4.4.4-3) indicates that for a given or agreed maximum field strength  $E_{\max}$ , the value of  $E_{\min}$  follows when  $C_{Eo}$  is given or that  $C_{Eo}$  follows when  $E_{\min}$  is given. The former approach has been used to calculate  $E_{\min} = 0.08 \text{ V/m}$  as indicated in figure 4.4.4-2, assuming  $n_m(E_o = 1 \text{ V/m}) = C_{Eo}/E_o^3 = C_{Eo} \cdot 5.4 \cdot 10^5 (\text{V}^2/\text{m}^2)$ .

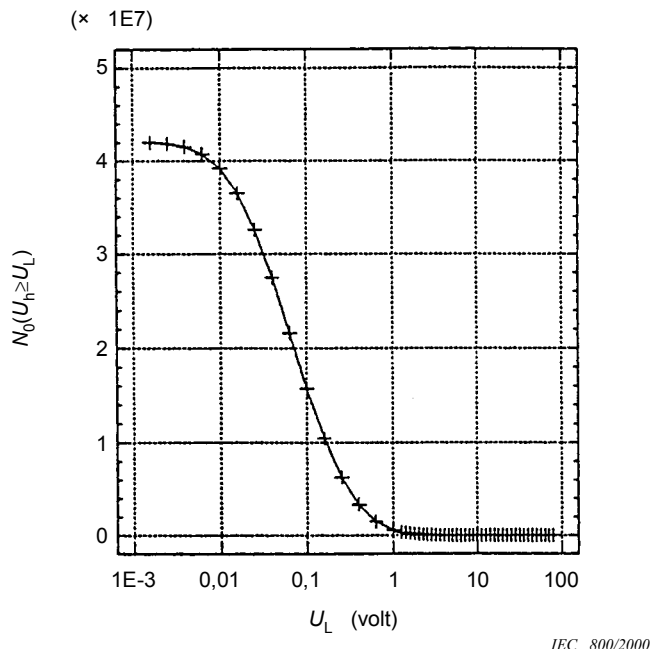
**Table 4.4.4-1 – Summary of the parameters used in the numerical examples presented in figures 4.4.4-3 and 4.4.4-4. Some curves have the same parameter values: Figure 4.4.4-4a) curve 2 and figure 4.4.4-3, and figure 4.4.4-4b curve 1 and figure 4.4.4-4a curve 3**

Figure	4.4.4-3	4.4.4-4a			4.4.4-4b		
Curve	–	1	3	4	2	3	4
$L$ -factor	$L_o$	$L_o$	$L_o$	$L_o$	$L_i^*$	$L_o$	$L_i^*$
Building material	B/W	B/W	B/W	B/W	B/W	C	C
$M_L$ dBm	–5,7	–5,7	–5,7	–5,7	–4,2	–25,0	–5,6
$S_L$ dB	10,6	10,6	10,6	10,6	11,2	10,9	10,5
$L_u$ dBm	18,0	+∞	18,0	18,0	19,0	3,0	27,0
$L_u$ m	7,9	+∞	7,9	7,9	8,9	1,4	22,4
$L_i$ dBm	–35,0	–∞	–35,0	–35,0	–40,0	–55,0	–31,0
$L_i$ m	0,02	–∞	0,02	0,02	0,01	0,002	0,03
$M_A$ dB	–	–	–	–	1,6	–	20,6
$S_A$ dB	–	–	–	–	4,0	–	8,7
$A_{bu}$ dB	–	–	–	–	12,0	–	41,0
$A_{bl}$ dB	–	–	–	–	–10,0	–	,0
$N_T$ millions	42	42	42	42	42	42	42
$C_{Eo}$ V <sup>2</sup> /m <sup>2</sup>	$5,4 \cdot 10^5$	$5,4 \cdot 10^5$	$5,4 \cdot 10^5$	$5,4 \cdot 10^5$	–	$5,4 \cdot 10^5$	–
$C_{Ei}$ V <sup>2</sup> /m <sup>2</sup>	–	–	–	–	$3,3 \cdot 10^4$	–	–
$E_{max}$ V/m	10,0	10,0	3,0	10,0	3,0	3,0	3,0
$E_{i,max}$ V/m	–	–	–	–	9,5	–	2,4
$E_{min}$ V/m	0,08	0,08	0,08	0,008	0,08	0,08	0,08
$E_{i,min}$ V/m	–	–	–	–	0,02	–	0,0007
$U_{max}$ V	79	+∞	24	79	85	42	53

\* See note 3 at the end of this subclause.

This subclause is concluded by giving several numerical examples of  $N_o(U_h \geq U_L)$ , i.e. of the number of outlets in the respective geographical region showing an induced open-circuit voltage  $U_h \geq U_L$ , where  $U_L$  may be considered as the open-circuit voltage in the immunity test. The region in these examples is the aforementioned part of Germany. The relations used in the calculation of  $N_o(U_h \geq U_L)$  can be found in annexes 4.4-B and 4.4-C. The values of the various parameters used in these calculations have been summarized in table 4.4.4-1.

Figure 4.4.4-2 shows an example of  $N_o(U_h \geq U_L)$  in the voltage range  $U_L \leq U_{max} = 79$  V, based on  $L_o$  data for buildings constructed from brick and/or wood (B/W) and assuming that all 42 million outlets are in these types of building.  $U_{max}$  (see also table 4.4.4-1) is given by  $U_{max} = E_{max}L_U$ , where  $E_{max}$  is the maximum outdoor field strength in the respective geographical region and  $L_U$  the upper limit of the range of  $L_o$ (B/W) data (see 4.4.2.2.2).  $U_{max}$  is quite large in this case. The maximum value measured in the experimental investigations was 22 V.

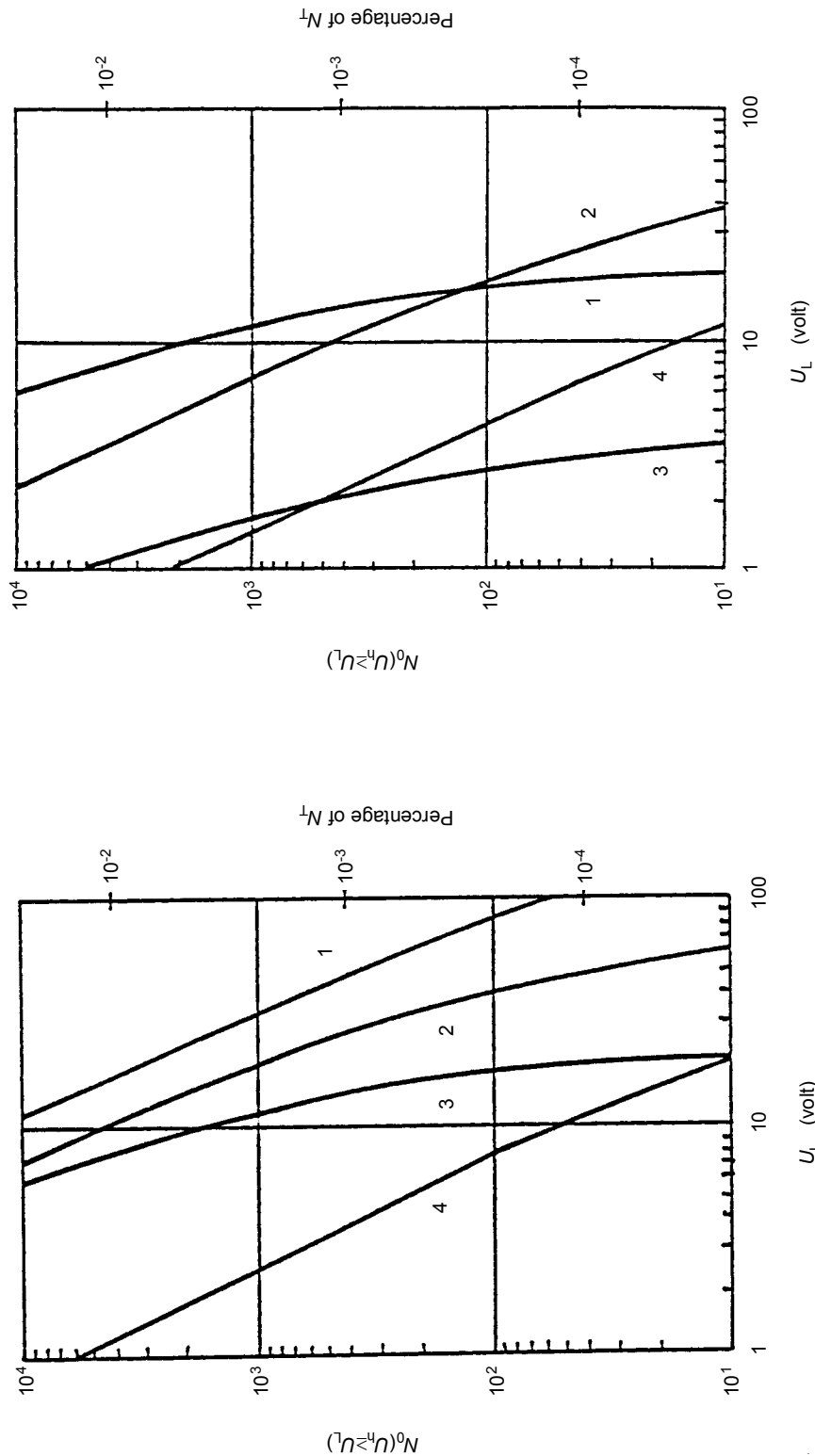


**Figure 4.4.4-3 – Example of the number of outlets with an induced asymmetrical open-circuit voltage  $U_L \leq U_h \leq U_{\max} = 79$  V, see table 4.4.4-1.**

**Total number of outlets  $N_T = 42 \cdot 10^6$**

To set the specifications for an immunity test the higher range of  $U_L$  values is of interest. Therefore, the results given in figure 4.4.4-3 have been replotted as Curve 2 in figure 4.4.4-4a. Curve 1 in figure 4.4.4-4a gives  $N_o(U_h \geq U_L)$  for the same situation as in figure 4.4.4-3 but neglecting the truncation of the  $L$  factor distribution. In that case  $U_{\max}$  is infinitely large, which is not very realistic. Curve 3 in figure 4.4.4-4a demonstrates how the results represented by Curve 2 are modified when  $E_{\max}$  is reduced from 10 V/m to 3 V/m. Then  $U_{\max} = 24$  V. Finally, Curve 4 in figure 4.4.4-4a demonstrates how the results represented by Curve 2 are modified when  $E_{\min}$  is reduced from 0,08 V/m to 0,008 V/m. The latter curve clearly demonstrates the importance of the minimum field strength in the geographical region.

In figure 4.4.4-4b the influence of the building material (B/W or reinforced concrete, C) and the choice of  $L$  factor ( $L_o$  or  $L_i$ ) on the results can be observed. Curve 1 in that figure is identical to Curve 3 in figure 4.4.4-4a, so it concerns  $L_o$  data for B/W-buildings. When using  $L_i$  data the building effect has to be taken into account as there is no direct model to predict the indoor field-strength distribution. By doing so, the results represented by Curve 2 are found. As for Curve 1 the maximum outdoor field-strength  $E_{\max} = 3$  V/m, but due to the building effect the maximum indoor field strength  $E_{i,\max} = E_{\max} A_{bi}$ , where  $A_{bi}$  is the lowest building effect as determined from the experimental data. In this case  $A_{bi} = -10$  dB, so that  $E_{i,\max} = 9,5$  V/m, hence an amplification of the outdoor field strength.



IEC 801/2000

**Figure 4.4.4-4 – Examples of number (left-hand scale) and relative number (right-hand scale) of outlets with  $U_L \leq U_h \leq U_{\max}$ . See table 4.4.4-1 for the various parameter values used. Total number of outlets  $42 \cdot 10^6$ , homogeneous density of the outlets:  $\mu = 168 \text{ km}^{-2}$**

a) B/W buildings

- Curve 1: nontruncated  $L_o$  factor,  $E_{\max} = 10 \text{ V/m}$ ,  $E_{\min} = 0,08 \text{ V/m}$
- Curve 2, truncated  $L_o$  factor,  $E_{\max} = 10 \text{ V/m}$ ;  $E_{\min} = 0,08 \text{ V/m}$
- Curve 3, truncated  $L_o$  factor,  $E_{\max} = 3 \text{ V/m}$ ;  $E_{\min} = 0,008 \text{ V/m}$
- Curve 4, truncated  $L_o$  factor,  $E_{\max} = 10 \text{ V/m}$ ;  $E_{\min} = 0,08 \text{ V/m}$

b) Truncated  $L$  factors, maximum outdoor field strength 3 V/m

- Curve 1: B/W buildings,  $L_o$  factor
- Curve 2: B/W buildings,  $L_i$  factor
- Curve 1: C buildings,  $L_o$  factor
- Curve 2: C buildings,  $L_i$  factor

One might argue that a negative value of  $A_{bi}$  is not realistic. As mentioned in 4.4.2.1, the negative values predominantly originated from measurements where the indoor field strength was measured at an upper floor of the building and the outdoor field strength at 1,5 m above ground level. Furthermore, reradiation effects also influenced the actual field-strength data. One may decide to truncate the building-effect distribution at the lower end at 0 dB. In that case  $E_{i,\max}$  and  $U_{\max}$  reduces from 85 V to  $L_u E_{\max} = 8,9 \times 3 = 27 \text{ V}$ .

Assuming that all 42 million outlets are located in reinforced concrete buildings the results represented by Curve 1 in figure 4.4.4-4b are modified into those represented by Curve 3, while Curve 4 follows if the  $L_i$  data are used. In practice, the outlets will be distributed over the B/W and C buildings. Then  $N_T$  in the calculations is the total number of outlets in a given type of building, and the results for both types of building have to be added.

**NOTE 1** Although the number of outlets  $N_o(U_h \geq U_L)$  as given in figure 4.4.4-4 may have noticeable values, the relative number is very low. This stresses the importance of the "tails" of the various distributions used and of the applied truncation. In addition, if the analytical expressions given in the annexes are not used, but a full-numerical calculation is made (for example, one starting with  $n_m(E_o)$ ), care has to be taken that the accuracy of the numerical calculations is sufficiently high. The very low values of the relative number  $N_o(U_h \geq U_L)/N_T$  form an indication of the accuracy needed. The relative number is identical to  $\text{pr}\{U_h \geq U_L\}$  in per cent.

**NOTE 2** In all calculations the density of the outlets  $\mu$  was considered to be a constant over the whole respective region. The results can be improved when, for example, the calculations leading to  $n_m(E_o)$ , see figure 4.4.4-2, take a location-dependent  $\mu$  into account.

**NOTE 3** Curves 2 and 4 in figure 4.4.4-4b are based on  $L_i$  and  $A_b$  data, and a warning has to be given here. As mentioned in 4.4.2, it is not very likely that inside the buildings the far-field condition will be satisfied and, formally speaking  $L_i$  cannot be derived from  $G_i$ . In addition  $A_b$  has been determined from magnetic field-strength data and  $A_b$  for the electric field need not be the same. In the calculations leading to curves 2 and 4, it has tacitly been assumed that  $L_i = G_i/Z_0$  ( $Z_0 = 377 \Omega$ ). However, the same curves for  $N_o(U_h \geq U_L)$  would have been found when correctly using the  $G_i$  and  $A_b$ , but quoting on Row 15 and 16 of table 4.4.4-1 the magnetic field quantities  $H_{\max} = E_{\max}/Z_0$  etc. and replacing  $C_{Ei}$  by  $C_{Hi} = C_{Ei}/Z_0^2$  (see clause 4.4.A-3 in annex 4.4-A).

#### 4.4.4.2 Summary of disturbance source parameters

Assuming that the disturbance source in the conducted-immunity test is sufficiently described by an open-circuit voltage and an internal impedance, the following parameters are of importance.

##### *The internal impedance*

The internal impedance may be specified as a purely resistive quantity, of which the magnitude is chosen on the basis of the results for the equivalent asymmetrical resistance  $R_a$ , as given in 4.4.2.3. The choice depends on the reference for the asymmetrical disturbance source considered to be relevant in the situations where interference problems

have to be prevented. An often used value is  $R_a = 150 \Omega$  [9] [10] [14] which is not in conflict with  $R_a$  results presented in 4.4.2.3.

### *The open-circuit voltage*

Because the induced asymmetrical voltage has been measured at non-random locations in order to have a sufficiently large induced-signal-to-ambient-noise ratio, the bare  $U_h$  data cannot be used and the procedure described in 4.4.4.1 has to be followed. From that procedure, described in more detail in annexes 4.4-B and 4.4-C, it can be concluded that the following parameters have to be considered (see also table 4.4.4-1).

- |                             |  |
|-----------------------------|--|
| a) $N_T$                    | The total number of outlets in the geographical region (country) to be considered. $N_T$ is either the grand total of outlets or the total number of outlets in a certain type of building (brick/wood or reinforced concrete).  |
| b) $M_G$ or $M_L$           | The average value of the $G$ or $L$ factor, in $\text{dB}\Omega\text{m}$ or $\text{dBm}$ , see tables 4.4.2-2 and 4.4.2-3. If the $G_i$ or $L_i$ factors are used, the following building effect parameters must be known (see tables 4.4.2-1 and 4.4.2-4):<br>$M_A$ : the average building effect $A_b$ in dB<br>$S_A$ : the standard deviation of $A_b$ in dB<br>$A_{bu}$ : the maximum building effect<br>$A_{bl}$ : the minimum building effect  |
| c) $S_g$ or $S_L$           | The standard deviation (in dB) associated with $M_G$ or $M_L$  |
| d) $G_U, G_L$<br>$L_U, L_L$ | The upper and lower limit of the $G$ -factor range or the $L$ -factor range  |
| e) $H_{\max}$ or $E_{\max}$ | The upper boundary of the outdoor field strength in $\text{A/m}$ or $\text{V/m}$ which determines the inner boundary of the areas around the transmitters to be considered.<br><br>This value may be chosen after considering radiation hazards. However, in particular in the case of mass-produced appliances the following consideration seems to be relevant. Choose (or agree on) a maximum field strength of $X$ ( $\text{A/m}$ or $\text{V/m}$ ) such that there is a high probability that all equipment will be electromagnetically compatible when the field strength is equal to or smaller than $X$ ( $\text{A/m}$ or $\text{V/m}$ ), and agree that special EMC hardening measures are to be taken in that part of the region where the field strength is larger than $X$ ( $\text{A/m}$ or $\text{V/m}$ ) and (simultaneously) a complaint occurs. |
| f) $H_{\min}$ or $E_{\min}$ | The minimum field strength determining the outer boundary of the areas around the transmitters (see 4.4.4.1).<br><br>This value has only to be chosen when the field-strength distribution $n(H)$ or $n(E)$ is unknown. If this distribution is known, $H_{\min}$ or $E_{\min}$ is calculated from an equation like equation (4.4.4-3).  |
| g) $n(H)$ or $n(E)$         | The field-strength distribution as discussed in 4.4.4.1 and annex 4.4-A.   |

#### 4.4.5 Bibliography

- [1] *Determining EMI in microelectronics – A review of the past decade*, J.J. Whalen, Proc. Intern. Symp. on EMC, pp 337-344, Zurich, Switzerland, March 1995
- [2] *A modified Ebers-Moll transistor model for RF interference analysis*, C.E. Larson and J.M. Roe, IEEE Trans. on MEC, vol. EMC-21, pp 283-290, Nov 1979
- [3] *The combined effects of internal noise and electromagnetic interference in CMOS VLSI circuits*, K. Liu and J.J. Whalen, Proc. 6th Intern. Symp. on EMC, p 303, York, United Kingdom, Sep 1988
- [4] *Interference effects in CMOS and TTL integrated circuits*, B. Demoulin, C. Lardé and P. Degauge, Proc. Intern. Symp. on EMC, pp 543-546, Zurich, Switzerland, March 1989
- [5] *EMI problems associated with non-linear device characteristics*, Proc. 1st Intern. Symp. on EMC, Madrid, Spain, Nov 1990
- [6] *EMC Working Group of the ZVEI (Union of Electrotechnical Industries)*, P.O. Box 700969, 6000 Frankfurt/Main 70, Germany
- [7] *RF disturbances on telephone-subscriber lines induced by AM broadcasting transmitters*, J.J. Doedbloed and G. Jeschar, Proc. Intern. Symp. on EMC, pp 537-542, Zurich, Switzerland, March 1989
- [8] *Characterization of transient and CW disturbances induced in telephone-subscriber lines*, J.J. Goedbloed and W.A. Pasman, Proc. Intern. Symp. on EMC, pp 211-218, York, United Kingdom, Aug 1990
- [9] *Funk-Entstörung von Anlagen und Geräten der Fernmelde Technik*, DIN/VDE 0878, Part 1/12.86, Dec 1986
- [10] Amendment of Publication 16, Part 1, Clause 20: T-type networks, CISPR/A(Secretariat)98, March 1989
- [11] *World Radio and TV Handbook*, 1986
- [12] *Radio broadcast induction voltage and pair unbalance in subscriber cable*, M. Hatori, F. Ohtsuki, T. Motomitsu and H. Koga, IEEE Intern. Symp. on EMC, pp 884-889, 1984
- [13] *Calculation of voltage induced into telecommunication lines from radio stations broadcasts and method of reducing interference*, CCITT Recommendation K.18
- [14] *Measurement of the immunity of sound and television broadcast receivers and associated equipment in the frequency range 1,5 MHz to 30 MHz by the current-injection method*, CISPR Publication 20, 1985
- [15] *Electromagnetic interference and countermeasures on metallic lines for ISDN*, M. Hattori and T. Ideguchi, IECEE trans. on Communications, Vol. E75-B, No. 1, Jan 1992

## Annex 4.4-A

### The field-strength distribution

This annex considers the probability  $pr\{H_o \geq H_L\}$  that in a ring-shaped area around a transmitter the outdoor magnetic field strength  $H_o$  is equal to or larger than a given field strength  $H_L$ . The magnetic field strength has been chosen because the experimental data presented in 4.4.2 are based on magnetic-field-strength measurements. At the end of this annex expressions will be given based on the outdoor electric field strength  $E_o$ , assuming that the far-field condition is fulfilled.

#### 4.4-A.1 $H_o$ -field expressions

Recalling the results given in 4.4.2, it is assumed that  $H_o$  can be written as

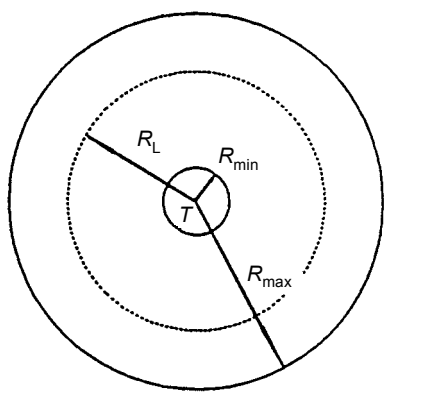
$$H_o = \frac{k\sqrt{P}}{rZ_0} \quad (r \geq R_{\min}) \quad (4.4\text{-A1})$$

where  $k$  is a constant,  $r$  the distance between the transmitter and the point of observation,  $P$  the transmitter power and  $Z_0$  the free-space wave impedance. The condition  $r \geq R_{\min}$  is needed to indicate that equation (4.4-A1) is not valid close to the transmitter, i.e. in the near-field region.

Using equation (4.4-A1), it follows that:

$$pr\{H_o \geq H_L\} = pr\left\{\frac{1}{r} \geq \frac{1}{R_L}\right\} = pr\{r \leq R_L\}, (R_L \leq R_{\max}) \quad (4.4\text{-A2})$$

where  $R_L = (k/P) / (H_L Z_0)$ . The latter probability is equal to the area of the ring determined by  $R_L$  and  $R_{\min}$ , see figure 4.4-A1, normalized to the area of the total ring, i.e. the ring determined by  $R_{\min}$  and  $R_{\max}$ . A finite outer boundary  $R_{\max}$  has to be specified, as an infinitely extended region around the transmitter would create an infinitely large region with field strength zero, thus meaning that  $pr\{H_o \geq H_L\}$  would be approaching zero for all values of  $H_L$  with  $R_L > R_{\min}$ .



IEC 802/2000

**Figure 4.4-A1 – Definition of the ring-shaped area round the transmitter T**

The probability can now be written as

$$pr\{H_o \geq H_L\} = \frac{\pi(R_L^2 - R_{min}^2)}{\pi(R_{max}^2 - R_{min}^2)} = \frac{H_L^{-2} - H_{max}^{-2}}{H_{min}^{-2} - H_{max}^{-2}} \quad (4.4-A3)$$

or as

$$pr\{H_o \geq H_L\} = \frac{(H_{max}^2 - H_L^2)H_{min}^2}{(H_{max}^2 - H_{min}^2)H_L^2} \quad (4.4-A4)$$

where  $H_{min} = (k/P) / (R_{max}Z_0)$  and  $H_{max} = (k/P)/(R_{min}Z_0)$ , i.e.  $H_{max}$  and  $H_{min}$  are the field strength at the inner boundary and the outer boundary of the ring-shaped area. In the case where  $H_{max} \gg \{H_L, H_{min}\}$  equation (4.4-A4) reduces to

$$pr\{H_o \geq H_L\} \approx \frac{H_{min}^2}{H_L^2} \quad (4.4-A5)$$

which means that  $pr\{H_o \geq H_L\}$  is no longer a function of  $H_{max}$ . By definition  $pr\{H_o \geq H_{max}\} = 0$  and  $pr\{H_o \geq H_{min}\} = 1$  so that  $H_L$  is not an explicit function of the distance  $r$ . Consequently, the choice of  $H_{min}$  is very important.

In annex 4.4-B and annex 4.4-C the distribution function  $f(H_o)$  has to be known. Since the cumulative distribution  $F(H_o) = pr\{H_o \leq H\} = 1 - pr\{H_o \geq H\}$  and, by definition,  $f(H_o)$  is the derivative of  $F(H_o)$  with respect to the field strength, the normalized distribution function  $f_n(H_o)$  can be calculated using equation (4.4-A4), yielding

$$f_n(H_o) = \frac{\partial}{\partial H} pr\{H_o \leq H\} = \frac{-2}{H_o^3 (1/H_{max}^2 - 1/H_{min}^2)} = \frac{-C_{Ho}}{H_o^3} = -C_{Ho} f(H_o) \quad (4.4-A6)$$

Hence the distribution function  $f(H_o) = 1/H^3$ . The constant of proportionality  $C_{Ho}$  in  $f_n(H_o) = C_{Ho} f(H_o)$  arose from normalizing  $f(H_o)$ . The constant  $C_{Ho}$  can formally be written as

$$C_{Ho}^{-1} = \int_{H_{min}}^{H_{max}} \frac{dH_o}{H_o^3} \quad (4.4-A7)$$

The relation  $f_n(H_o) = -C_{Ho}/H^3$  is applicable in all cases where the field strength varies in inverse proportion to that distance and no specification of the transmitter power  $P$  is needed. Of course,  $H_o$  is an implicit function of  $r$  and  $P$ .

Finally,  $pr\{H_o \geq H_L\}$  can be written formally as

$$pr\{H_o \geq H_L\} = \frac{\int_{H_L}^{H_{\max}} f(H_o) dH_o}{\int_{H_{\min}}^{H_{\max}} f(H_o) dH_o} \quad (4.4-A8)$$

#### 4.4-A.2 $H_i$ -field expressions

For the indoor field  $H_i$  no direct model is available as it is for the outdoor field  $H_o$ . Therefore the distribution  $f(H_i)$  has to be derived from  $f(H_o)$  and the distribution  $f(A_b)$  of the building effect.

Assuming  $f(H_o)$  and  $f(A_b)$  to be independent, the joint distribution  $f(H_o, A_b) = f(H_o)f(A_b)$ . The latter distribution represents the distribution of locations where the outdoor field strength equals  $H_o$  and, simultaneously, the building effect amounts  $A_b$ . By carrying out the transformation  $H_i = H_o/A_b$  the joint distribution  $f(H_i, A_b)$  is known. Since

$$f(H_i, A_b) dH_i = f(A_b) f(H_o) dH_o \quad \text{or} \quad f(H_i, A_b) = \frac{f(H_o) f(A_b)}{dH_i / dH_o} = A_b f(H_o) f(A_b) \quad (4.4-A9)$$

and  $f(H_o) = 1/H_o^3$  it follows that

$$pf\{H_i \leq H_L\} = \int_{H_i} dH_i \int_{A_b} dA_b \frac{f(A_b)}{A_b^2 H_i^3} = E[A_b^{-2}] \int_{H_i} \frac{dH_i}{H_i^3} \quad (4.4-A10)$$

where  $E[A_b^{-2}]$  is the expectation of  $A_b^{-2}$ . Using the truncated distribution of  $A_b$  with truncation factor  $\alpha_{tA}$ , see 4.4.2.1 and 4.4.2.2.3,  $E[A_b^{-2}]$  is given by

$$E[A_b^{-2}] = \int_{A_{bl}}^{A_{bu}} \frac{f(A_b) dA_b}{A_b^2} = \frac{\alpha_{tA}}{2} \{erf(z_u) - erf(z_i)\} e^{-2\pi_A + 2\sigma_A^2} \quad (4.4-A11)$$

where  $A_{bu}$  and  $A_{bl}$  are the upper and lower boundary of the range of experimental  $A_b$  data, as explained in 4.4.2.2.3,  $\mu_A = M_a \ln(10)/20$  and  $\sigma_A = S_a \ln(10)/20$  with  $M_A$  and  $S_A$  being the average value and the standard deviation of the lognormal distribution of  $A_b$ . In equation (4.4-A11) "erf" denotes the error function, see annex 4.4-D, while  $z_u$  and  $z_i$  are given by

$$z_u = \frac{\ln(A_{bu}) - \mu_A}{\sigma_A \sqrt{2}}, \quad z_i = \frac{\ln(A_{bl}) - \mu_A}{\sigma_A \sqrt{2}} \quad (4.4-A12)$$

By definition  $f(H_i)$  is the derivative of  $F(H_i)$  with respect to the field strength. Hence, the normalized distribution  $f_n(H_i)$  reads

$$f_n(H_i) = \frac{C_{Hi}}{H_i^3} \text{ with } C_{Hi}^{-1} = E \left\{ A_b^{-2} \right\} \int_{H_{i,\min}}^{H_{i,\max}} \frac{dH_i}{H_i^3} \quad (4.4-A13)$$

where  $H_{i,\min} = H_{\min}/A_u$  and  $H_{i,\max} = H_{\max}/A_t$  and  $H_{\min}$  and  $H_{\max}$  are the minimum and maximum outdoor field strength, respectively.

#### 4.4-A.3 $E_o$ -field expressions

Assuming far-field conditions, the outdoor magnetic field component  $H_o$  and the outdoor electric field component  $E_o$  have a constant ratio, i.e.  $E_o = H_o Z_0$ . If  $E_{\min}$  and  $E_{\max}$  are the field strength at the inner and outer boundary of the ring-shaped area, the probability that  $E_o \geq E_L$  can be written as

$$\text{pr}\{E_o \geq E_L\} = \frac{(E_{\max}^2 - E_L^2)E_{\min}^2}{(E_{\max}^2 - E_{\min}^2)E_L^2} \quad (4.4-A14)$$

In the classification of the field strength carried out in 4.4.3.1, use has been made of equation (4.4-A9) to determine the boundaries between the field-strength classes. In that application equation (4.4-A9) was rewritten as

$$E_L = \frac{E_{\min}}{\sqrt{\text{pr}\{E_o \geq E_L\}(1 - (E_{\min}/E_{\max})^2) + (E_{\min}/E_{\max})^2}} \approx \frac{E_{\min}}{\sqrt{\text{pr}\{E_o \geq E_L\}}} \quad (4.4-A15)$$

which equation follows directly from equation (4.4-A6), while the approximation is valid in the case where  $E_{\max} \gg \{E_{\min}, E_L\}$ . In the latter case  $E_L$  is independent of  $E_{\max}$ .

Similar to 4.4-A1 in the case of  $f(H_o)$ , the distribution function  $f(E_o)$  is given by

$$f_n(E_o) = \frac{-C_E}{E_o^3} = -C_E f(E_o) \text{ with } C_E^{-1} = \int_{E_{\min}}^{E_{\max}} \frac{dE_o}{E_o^3} \quad (4.4-A16)$$

and  $\text{pr}\{E_o \geq E_L\}$  is given by

$$\text{pr}\{E_o \geq E_L\} = \frac{\int_{E_L}^{E_{\max}} f(E_o) dE_o}{\int_{E_{\min}}^{E_{\max}} f(E_o) dE_o} \quad (4.4-A17)$$

The constants  $C_{Eo}$  and  $C_{Ho}$  are related via  $C_{Eo} = C_{Ho} Z_0^2$ .

Of course, in a similar way also  $f(H_i)$  and  $f_n(H_i)$  can be converted into  $f(E_i)$  and  $f_n(E_i)$ .

## Annex 4.4-B

### The induced asymmetrical open-circuit voltage distribution

In this annex the distribution function  $f(U_h)$  of the induced asymmetrical open-circuit voltage  $U_h$  will be derived by combining the distribution function of the field strength (see annex 4.4-A) and that of the  $G$  factors or the  $L$  factors. After that, the probability  $pr\{U_h \geq U_L\}$  that  $U_h$  is equal to or larger than a given value  $U_L$  is calculated. Results of this calculation have been used in 4.4.3.2.

As in annex 4.4-A, it is assumed that the outdoor magnetic field strength  $H_o$  can be written as  $H_o = (k/P) / rZ_0$  or  $E_o = (k/P)/r$ , where  $k$  is a constant,  $P$  the transmitter power,  $Z_0$  the free-space wave impedance and  $r$  the distance between the transmitter and the point of observation. As in annex 4.4-A, it is also assumed that the transmitter causing the field  $H_o$  or  $E_o$  is in the centre of a ring-shaped area with an inner radius  $R_{min}$  and an outer radius  $R_{max}$ . The field strength at the inner boundary is  $H_{max}$  or  $E_{max}$ , and that at the outer boundary  $H_{min}$  or  $E_{min}$ . The need for these boundaries has been explained in annex 4.4-A, where it was also explained that the derivation of the relations will start from the magnetic field strength, i.e. use is made of the  $G$  factors defined by  $U_h = G_o \cdot H$ . Electric-field-strength relations using the  $L$  factors defined by  $U_h = L_E$  will be addressed in clause B.2.

#### 4.4-B.1 $H$ -field-based relations

Assuming the field distribution  $f_n(H_o)$  and the  $G$  factor distribution  $f(G_o)$  to be independent, the joint distribution  $f(H_o, G_o) = f_n(H_o) \cdot f(G_o)$ . This joint distribution gives the distribution of the locations where the outdoor field strength equals  $H_o$  and, simultaneously, the outdoor  $G$  factor equals  $G_o$ . Then, by carrying out the transformation  $U_h = G_o \cdot H_o$ , the distribution is found of the situations where simultaneously the asymmetrical voltage equals  $U_h$  and the  $G$  factor equals  $G_o$ . Since

$$f(U_h) dU_h = f_n(H_o) dH_o \text{ or } f(U_h) = \frac{f_n(H_o)}{dU_h / dH_o} = \frac{f_n(H_o)}{G_o} \quad (4.4-B1)$$

it follows that

$$f(U_h, G_o) = \frac{f_n\left(\frac{U_h}{G_o}\right) f(G_o)}{G_o} = \frac{C_{Ho} G_o^2 f(G_o)}{U_h^3} \quad (4.4-B2)$$

where the right-hand part of this equation is valid if the distribution derived in annex 4.4-A is used, i.e. when it is assumed that  $f_n(H_o) = C_{Ho} / H_o^3$ , see equation (4.4-A6). If  $f(G_i)$  is used, the building effect  $A_b$  has to be taken into account and, hence,  $f_n(H_i)$  should be used as discussed in 4.4.A.2 of annex 4.4-A.

By integrating the joint distribution over the permissible ranges of  $U_h$  and  $G_o$ , the probability  $pr\{U_h \geq U_L\}$  can be calculated from

$$pr\{U_h \geq U_L\} = \int_{U_h} d_U \int_{G_o} dG \frac{C_{Ho} G_o^2 f(G_o)}{U_h^3} = \frac{C_{Ho}}{2} \int_{G_o} \left\{ \frac{G_o^2}{U_{h1}^2} - \frac{G_o^2}{U_{h2}^2} \right\} f(G_o) dG \quad (4.4-B3)$$

where  $U_{h1}$  and  $U_{h2}$  are relevant boundaries. To find the relevant ranges and boundaries of  $U_h$  and  $G$ , consider figure 4.4-B1 showing the  $U_h$ - $G$  plane. As the field strength ranges between  $H_{min}$  and  $H_{max}$  the voltage satisfies the relation  $H_{min}G \leq U_h \leq H_{max}G$ . Using a truncated lognormal distribution of the  $G$  factors (see 4.4.2.2.3), we have  $G_L \leq G \leq G_U$ .

If  $U_L$  has the value indicated in figure 4.4-B1,  $pr\{U_h \geq U_L\}$  is found by integrating the joint distribution over the range of  $U_h$  and  $G$  values indicated by the shaded area in figure 4.4-B1. From that figure it will be clear that  $U_L$  can only have values between  $U_a = H_{min}G_L$  and  $U_d = H_{max}G_U$ . The voltages  $U_b$  and  $U_c$  are defined by  $U_b = H_{max}G_L$  and  $U_c = H_{min}G_U$ , respectively.

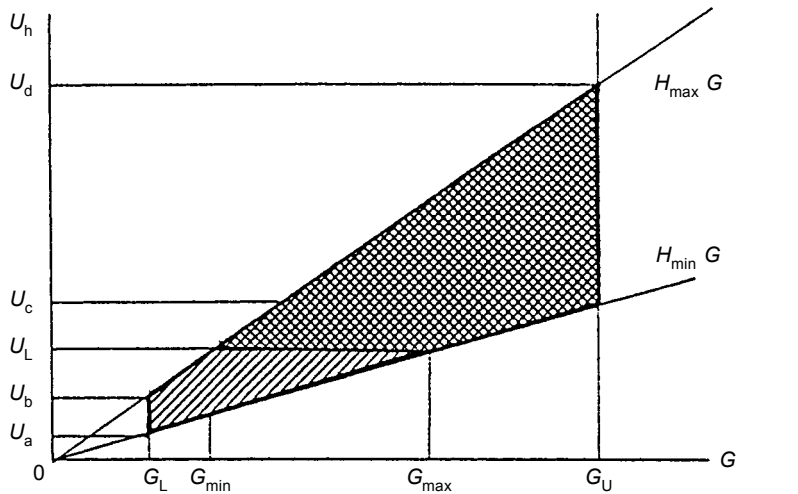


**Figure 4.4-B1 – The permissible ranges of  $U_h$  and  $G$  are within the polygon  $\{G_L, U_a\}, \{G_L, U_b\}, \{G_U, U_d\}, \{G_l, U_c\}$  and  $\{G_L, U_a\}$ . For the given value  $U_L$  the double-shaded area represents  $pr\{U_h \geq U_L\}$**

After straightforward calculations it follows from equation (4.4-B3) that  $pr\{U_h \geq U_L\}$  is given by

$$pr\{I_h \geq U_L\} = \frac{\alpha_{tG} C_{Ho}}{4} \left\{ \delta_U \frac{\operatorname{erf}(x_u) - \operatorname{erf}(x_i)}{H_{min}^2} - \frac{\operatorname{erf}(y_i) - \operatorname{erf}(y_u)}{H_{max}^2} + e^{2\mu_G + 2\sigma_G^2} \frac{\operatorname{erf}(z_u) - \operatorname{erf}(z_i)}{U_L^2} \right\} \quad (4.4-B4)$$

where  $\mu_G = M_G \cdot \ln(10)/20$  and  $\sigma_G = S_G \cdot \ln(10)/20$ ,  $M_G$  and  $S_G$  being the average value and the standard deviation of the relevant truncated lognormal  $G$  factor distribution with truncation factor  $\alpha_{tG}$ . The variables  $x_u$  and  $x_i$  are given in equation (4.4-B5), while  $y_u$ ,  $y_i$ ,  $z_u$ ,  $z_i$  and  $\delta$ , which depend on the value of  $U_L$ , are given by equations (4.4-6) and (4.4-8)

$$x_u = \frac{\ln(G_u) - \mu_G}{\sigma_G \sqrt{2}}, \quad x_i = \frac{\ln(U_L / H_{min}) - \mu_G}{\sigma_G \sqrt{2}} \quad (4.4-B5)$$

a)  $U_a \leq U_L < U_b$ :  $\delta_U = 1$ ,

$$y_u = \frac{\ln(G_u) - \mu_G}{\sigma_G \sqrt{2}}, \quad y_i = \frac{\ln(G_L) - \mu_G}{\sigma_G \sqrt{2}} \quad (4.4\text{-B6(a)})$$

$$z_u = \frac{\ln(U_L / H_{\min}) - \mu_G - 2\sigma_G^2}{\sigma_G \sqrt{2}}, \quad z_i = \frac{\ln(G_L) - \mu_G - 2\sigma_G^2}{\sigma_G \sqrt{2}} \quad (4.4\text{-B6(b)})$$

b)  $U_b \leq U_L < U_c$ :  $\delta_U = 1$

$$y_u = \frac{\ln(G_u) - \mu_G}{\sigma_G \sqrt{2}}, \quad y_i = \frac{\ln(U_L / H_{\max}) - \mu_G}{\sigma_G \sqrt{2}} \quad (4.4\text{-B7(a)})$$

$$z_u = \frac{\ln(U_L / H_{\min}) - \mu_G - 2\sigma_G^2}{\sigma_G \sqrt{2}}, \quad z_i = \frac{\ln(U_L / H_{\max}) - \mu_G - 2\sigma_G^2}{\sigma_G \sqrt{2}} \quad (4.4\text{-B7(b)})$$

b)  $U_c \leq U_L < U_d$ :  $\delta_U = 0$

$$y_u = \frac{\ln(G_u) - \mu_G}{\sigma_G \sqrt{2}}, \quad y_i = \frac{\ln(U_L / H_{\max}) - \mu_G}{\sigma_G \sqrt{2}} \quad (4.4\text{-B8(a)})$$

$$z_u = \frac{\ln(G_u) - \mu_G - 2\sigma_G^2}{\sigma_G \sqrt{2}}, \quad z_i = \frac{\ln(U_L / H_{\max}) - \mu_G - 2\sigma_G^2}{\sigma_G \sqrt{2}} \quad (4.4\text{-B8(b)})$$

In the case where the  $G_i$  factors are used, equation (4.4-4) is applicable provided that  $C_{Ho}$  is replaced by  $E[A_b^{-2}]C_{Hi}$ , and  $H_{\min}$  and  $H_{\max}$  by  $H_{i,\min}$  and  $H_{i,\max}$ , respectively (see clause 4.4.A.2 in annex 4.4-A).

Equations (4.4-B4) to (4.4-B8) have been used to calculate the data summarized in table 4.4.3-3 and to calculate the results displayed in figures 4.4.4-3 and 4.4.4-4.

#### 4.4-B.2 E-field-based relations

Assuming far-field conditions the outdoor electric field strength may be used to calculate  $pr\{U_h \geq U_L\}$  in connection with the  $L_o$  factors, see 4.4.2.2.2. In that case equations (4.4-B4) to (4.4-B8) can be used, provided that  $C_{Ho}$  is replaced by  $C_{Eo}$ ,  $H_{\max}$  by  $E_{\max}$ ,  $H_{\min}$  by  $E_{\min}$ ,  $G_o$  by  $L_o$ , and  $M_G$  and  $S_G$  by  $M_L$  and  $S_L$ . In other words, equations (4.4-B4) to (4.4-B9) can be used, provided that all magnetic-field-related quantities are replaced by the corresponding electric-field quantities.

Similar remarks are valid in the case where  $L_i$  factors are to be used, but see note 3 at the end of 4.1.

## Annex 4.4-C

### The outlet-voltage distribution

This annex considers the number of outlets  $N_o(U_h \geq U_L)$  showing an induced open-circuit voltage  $U_h$  equal to or larger than a given voltage  $U_L$ . This quantity is derived in a number of steps. First, the probability density  $n(H_o)$  giving the density of outlets experiencing a certain field strength  $H_o$  is considered. Use will be made of the simple models with the ring-shaped area (RSA) already discussed in annex 4.4-A and annex 4.4-B, and of the  $G_o$  factors, which give  $U_h$  normalized to the magnetic field strength. After that it is possible to calculate the joint distribution  $n(H_o, G_o)$  along the lines described in annex 4.4-B, and  $N_o(U_h \geq U_L)$  follows after integration of the joint distribution factor over the permissible values of the parameters concerned. When using the  $G_i$  factors in combination with the building effect  $A_b$  the same procedure can be followed as in annex 4.4-B.

#### 4.4-C.1 H-field-based relations

Assuming a homogeneous density of  $\mu$  outlets per square metre around the transmitter in question, the number  $dn(r)$  of outlets in an elementary ring-shaped area between  $r$  and  $r+dr$  is given by

$$dn(r) = \mu 2\pi r dr \quad (4.4-C1)$$

Using  $H_o = (k/P)/(rZ_0)$  (see annex 4.4-A), it follows from equation (4.4-C1) that the number of outlets  $dn(H_o)$  in the area determined by the field-strength range  $H_o(r)$  to  $H_o(r+dr)$ , is given by

$$dn(H_o) = 2\pi\mu \frac{k^2 P}{H_o^3 Z_0^2} dH_o \quad (4.4-C2)$$

In the case of  $N$  transmitters, where the  $j$ -th transmitter is characterized by  $\{k_j, P_j\}$  and the density of outlets around that transmitter is  $\mu_j$ ,  $dn(H_o)$  can be written as

$$dn(H_o) = \sum_{j=1}^N 2\pi\mu_j \frac{k_j^2 P_j}{Z_0^2} \frac{dH_o}{H_o^3} = \frac{dH_o}{Z_0^2 H_o^3} = \sum_{j=1}^N 2\pi\mu_j k_j^2 P_j = \frac{C_{Ho}}{H_o^3} dH_o \quad (4.4-C3)$$

Hence, in this model the normalized distribution  $n(H_o)$  is given by

$$n(H_o) = \frac{dn(H_o)}{dH_o} = \frac{C_{Ho}}{H_o^3} \quad \text{with } C_{Ho} = \frac{2\pi}{Z_0^2} \sum_{j=1}^N \mu_j k_j^2 P_j \quad (4.4-C4(a,b))$$

As had to be expected, the distribution  $n(H_o)$  is equal to  $f_n(H_o)$  discussed in annex 4.4-A.

If  $N_T$  is the total number of outlets in the RSA and if  $H_{\max}$  and  $H_{\min}$  determine the boundaries of that RSA, the following relation has to be satisfied

$$N_T = \int_{H_{\min}}^{H_{\max}} n(H) dH \quad (4.4-C5)$$

or, after substitution of equation (4.4-C4):

$$N_T = \frac{C_{Ho}}{2} \left\{ \frac{1}{H_{min}^2} - \frac{1}{H_{max}^2} \right\} \quad (4.4-C6)$$

If the connection between  $N_T$  and  $C_{Ho}$  is made via equation (4.4-C4), the expression for the number of outlets  $N_o(H_u \geq U_L)$  showing an induced open-circuit voltage  $U_h \geq U_L$  is identical to that for  $pr\{U_h \geq U_L\}$  as derived in annex 4.4-B, equation (4.4-B4). So  $N_o(U_h \geq U_L)$  reads

$$N_o \{U_h \geq U_L\} = \frac{\alpha_{tG} C_{Ho}}{4} \left\{ \delta_U \frac{\operatorname{erf}(x_u) - \operatorname{erf}(x_l)}{H_{min}^2} - \frac{\operatorname{erf}(y_u) - \operatorname{erf}(Y_l)}{H_{max}^2} + e^{2\mu_G + 2\sigma_G^2} \frac{\operatorname{erf}(z_u) - \operatorname{erf}(z_l)}{U_L^2} \right\} \quad (4.4-C7)$$

The parameters needed in equation (4.4-C7) have been explained in equations (4.4-B4) to (4.4-B8). In annex 4.4-B it has also been explained how to change equation (4.4-C7) to make a calculation using  $G_i$  factors possible.

When it is assumed that  $N_T$  is known and  $H_{max}$  has been chosen there remain two "unknowns" in equation (4.4-C6):  $C_{Ho}$  and  $H_{min}$ . If  $C_{Ho}$  is calculated for a certain geographical region from equation (4.4-C4b), then  $H_{min}$  is known, so that all parameters in equation (4.4-C7) are known. As discussed in 4.4.4, another possibility is to determine  $H_{min}$  in that region and  $C_{Ho}$  can be calculated by using equation (4.4-C6).

#### 4.4-C.2 E-field-based relations

Assuming far-field conditions, the outdoor electric field strength together with the  $L$  factors may be used to calculate  $N_o\{U_h \geq U_L\}$ . In that case equation (4.4-C7) can be used, provided that  $C_{Ho}$  is replaced by  $C_{Eo}$ ,  $H_{max}$  by  $E_{max}$ ,  $H_{min}$  by  $E_{min}$ ,  $G_o$  by  $L_o$  and  $M_G$  and  $S_G$  by  $M_L$  and  $S_L$ . In other words equation (4.4-C7) can be used, provided that all magnetic-field-related quantities are replaced by the corresponding electric-field quantities.

If  $E_0 = (k/P)/r$  the equivalent of equation (4.4-C4) reads

$$n(E) = \frac{dN(E)}{dE} = - \frac{C_{Eo}}{E^3} \text{ with } C_{Eo} = 2\pi \sum_{j=1}^N \mu_j k_j^2 P_j \quad (4.4-C8(a,b))$$

and the equivalent of equation (4.4-C6) reads

$$N_T = \frac{C_{Eo}}{2} \left\{ \frac{1}{E_{min}^2} - \frac{1}{E_{max}^2} \right\} \quad (4.4-C9)$$

See annex 4.4-B about how to change the various relations to make calculations using  $L_i$  factors possible, but see also note 3 at the end of 4.1.

## Annex 4.4-D

### Some mathematical relations

In this annex a number of mathematical relations involving the so-called Error Function, as used in annexes 4.4-B and 4.4-C, are summarized. In 4.4-D.1 a series expansion of the error function is also given which is sufficiently accurate to be used in computer calculations based on the analytical expressions presented in annexes 4.4-B and 4.4-C. Clause 4.4-D.2 summarizes some mathematical relations involving the lognormal distribution and the error function.

#### 4.4-D.1 The Error Function

By definition  $\text{erf}(x)$ , the error function of  $x$ , is given by equation (4.4-D1)

$$\text{erf}(x) = \frac{2}{\sqrt{\pi}} \int_0^x e^{-\alpha^2} d\alpha \quad (4.4-\text{D1})$$

The error function has the following properties

$$\text{erf}(0) = 0 \quad (4.4-\text{D2(a)})$$

$$\text{erf}(\infty) = 1 \quad (4.4-\text{D2(b)})$$

$$\text{erf}(-x) = \text{erf}(x) \quad (4.4-\text{D2(c)})$$

A useful series expansion of  $\text{erf}(x)$  is the following equation (4.4-D2)

$$\text{erf}(x) = 1 - (a_1 t + a_2 t^2 + a_3 t^3 + a_4 t^4 + a_5 t^5) e^{-x^2} + \varepsilon(x) \quad (4.4-\text{D3(a)})$$

$$t = \frac{1}{1+px}, |\varepsilon(x)| \leq 1,5 \times 10^{-7} \quad (4.4-\text{D3(b)})$$

where

$p = 0,28449\ 6736$ ;

$a_1 = 0,25482\ 9592$ ;

$a_2 = 0,28449\ 6736$ ;

$a_3 = 1,42141\ 3741$ ;

$a_4 = -1,45315\ 2027$ ;

$a_5 = 1,06140\ 5429$ .

#### 4.4-D.2 Application to the lognormal distribution

A quantity  $x$  has a lognormal distribution when the logarithm of  $x$  has a normal distribution. In mathematical form the lognormal distribution of  $x$  reads

$$f(x)dx = \frac{1}{x\sigma\sqrt{2\pi}} e^{-\frac{(\ln(x)-\mu)^2}{2\sigma^2}} dx \quad (4.4-D4)$$

where  $\mu$  is the average value of  $\ln(x)$  and  $\sigma$  the associated standard deviation. If the latter parameters are known in dB and  $M(\text{dB}...)$  is the average value and  $S(\text{dB})$  is the associated standard deviation,  $\mu = M \cdot \ln(10)/20$  and  $\sigma = S \cdot \ln(10)/20$ . The distribution function given in equation (4.4-D4) has the property that the integral of this function over all values of  $x$  equals 1 if  $-\infty \leq x \leq \infty$ . This means that  $f(x)$  given in equation 4.4-D4 is properly normalized. If  $f_t(x)$  is the truncated lognormal distribution of  $x$ , such that  $x_l \leq x \leq x_u$ , the distribution has to be normalized again. In that case  $f_t(x)$  can formally be written as  $f_t(x) = \alpha_t \cdot f(x)$  with

$$\alpha_t^{-1} = \int_{x_l}^{x_u} \frac{1}{x\sigma\sqrt{2\pi}} e^{-\frac{(\ln(x)-\mu)^2}{2\sigma^2}} dx = \frac{1}{\sqrt{\pi}} \int_{-\infty}^{y_u} e^{-y^2} dy - \frac{1}{\sqrt{\pi}} \int_{-\infty}^{y_l} e^{-y^2} dy \quad (4.4-D5(a))$$

so that

$$\alpha_t = \frac{\operatorname{erf}(y_u) - \operatorname{erf}(y_l)}{2} \quad (4.4-D5(b))$$

where  $y = \frac{\ln(x) - \mu}{\sigma\sqrt{2}}$ ,  $y_u = \frac{\ln(x_u) - \mu}{\sigma\sqrt{2}}$ ,  $y_l = \frac{\ln(x_l) - \mu}{\sigma\sqrt{2}}$  (4.4-D5(c))

When carrying out the integrations in annex 4.4-B, use has been made of the following integral solutions, which can easily be verified using the above relations.

In the case of equation (4.4-B4) leading to equation (4.4-B7), use was made of

$$\int_{x_l}^{x_u} x^2 f_t(x) dx = \alpha_t \frac{e^{2\mu+2\sigma^2}}{2} \{ \operatorname{erf}(z_u) - \operatorname{erf}(z_l) \} \quad (4.4-D6(a))$$

where  $z_u = y_u - \sigma\sqrt{2}$ ,  $z_l = y_l - \sigma\sqrt{2}$  (4.4-D6(b))

and in the derivation of equation (4.4-B5) use was made of

$$\int_{x_l}^{x_u} x^{-2} f_t(x) dx = \alpha_t \frac{e^{-2\mu+2\sigma^2}}{2} \{ \operatorname{erf}(z_u) - \operatorname{erf}(z_l) \} \quad (4.4-D7(a))$$

where  $z_u = y_u + \sigma\sqrt{2}$ ,  $z_l = y_l + \sigma\sqrt{2}$  (4.4-D7(b))

#### References

- D1 *Handbook of mathematical functions*, M. Abramowitz and I.A. Stegun, Dover Publications Inc., New York, 1972
- D2 *Approximations for digital computers*, C. Hastings Jr., Princeton Univ. Press, Princeton, N.J., 1959 (see also Ref. D1)

## 4.5 The predictability of radiation in vertical directions at frequencies above 30 MHz

### Summary

CISPR 11 sets limits for the electromagnetic disturbances emitted *in situ* near the ground from industrial, scientific and medical (ISM) radio-frequency equipment. In CISPR 11, referring to protection of safety of life services, it is stated "Many aeronautical communications require the limitation of vertically radiated electromagnetic disturbances. Work is continuing to determine what provisions may be necessary to provide protection for such systems".

This report considers the calculated vertical radiation patterns of the *E*-field which will be emitted at frequencies above 30 MHz from electrically small sources physically located close to the surface of real homogeneous plane ground. Its purpose is the study of the predictability of radiation in vertical directions based on *in situ* measurements of the strength of the *E*-field near the ground. The sources considered are electrically small balanced electric and magnetic dipoles excited in the frequency range from 30 MHz to 1 000 MHz.

The effects on the vertical radiation patterns caused by a wide range of the electrical properties of the ground, varying from wet ground to very dry ground – and the special case of a ground that behaves like a near-perfect conductor – have also been considered.

These studies show the limitations of the predictability of radiation at elevated angles when based on measurements near the ground. The report identifies some of the factors to be considered when developing and specifying limits of radiated electromagnetic disturbances and methods of measurement which are intended to protect aeronautical radionavigation and communication systems operating at frequencies above 30 MHz. For example, it shows that vertical patterns of the fields over good conductors do not represent the field patterns over real grounds. Moreover, the report shows that for good predictability of the field strengths at elevated angles the *in situ* measurements near the ground must not be made at fixed heights but instead they must use height scans and, in particular, must be made at a known distance from the equipment which is the source of the radiation.

#### 4.5.1 Scope

This report considers the predictability of radiation in vertical directions based on measurements of the strength of the electric (*E*) fields emitted by electrical equipment near the ground. It is intended to give guidance to the predictability of radiation emitted at elevated angles by electrical equipment *in situ*, in particular industrial, scientific, and medical (ISM) radio-frequency equipment. For that purpose, it studies the calculated vertical radiation patterns of the *E*-fields which will be emitted at frequencies above 30 MHz from electrically small sources located close to the surface of real homogeneous plane ground.

The vertical radiation patterns of the horizontally and vertically polarized *E*-fields, including the surface waves, have been calculated at distances of 10 m, 30 m and 300 m from various electrically small sources, so that the field variations with distance can be quantified. In this way, a general knowledge has been obtained of the shapes of the vertical radiation patterns, showing the magnitudes of the *E*-field strengths near ground compared with the magnitudes of the *E*-field components at elevated angles, and the ways in which the relative magnitudes can be expected to vary with distance over a plane ground.

The sources considered were electrically small balanced electric and magnetic dipoles excited in the frequency range from 30 MHz to 1 000 MHz. For the purposes of the study, an electrically small source is defined as one whose largest linear dimension is one-tenth or less of the free-space wavelength at the frequency of interest.

The report also considers the effects on the vertical radiation patterns caused by a range of electrical properties of the ground, varying from electrical conductivities and dielectric constants of wet ground to those of very dry ground [1] [2] and the special case of a ground that behaves like a near-perfect conductor.

The effects on wave propagation near the ground of walls, buildings, terrain irregularities, watercourses, vegetation cover, and so on, are not within the scope of this report. It is important to note, therefore, that the additional uncertainties in wave propagation caused by the presence of such discontinuities, and their effects on predictability based on measurements *in situ*, have not been considered.

#### 4.5.2 Introduction

In CISPR 11 [3], table VI in clause 5.3 provides radiation limits for the protection of specific safety services. The limits apply to ground level measurements of the electromagnetic disturbances emitted by ISM radio-frequency (RF) equipment *in situ*, not on a test site. Above 30 MHz the five frequency bands listed in table VI are all used for aeronautical services, including the instrument landing system or instrument low-approach system (ILS) marker beacon, localizer, and glide path frequencies, as well as a survival frequency and other radionavigation and communication frequencies bands. A note to table VI states: "Many aeronautical communications require the limitation of vertically radiated electromagnetic disturbances. Work is continuing to determine what provisions may be necessary to provide protection for such systems."

The *in situ* measuring distance specified in table VI, for all five frequency bands above 30 MHz, is 10 m "from (the) exterior wall outside the building in which the equipment is situated". It is important to note that the precise measuring distance from the ISM apparatus itself is not specified.

The heights at which measurements of horizontally and vertically polarized *E*-fields are to be made using a balanced dipole are specified in 7.2.4 of CISPR 11. "For Group 2 Class A equipment the centre of the antenna shall be  $3,0\text{ m} \pm 0,2\text{ m}$  above ground. For Group 1 and Group 2 Class B equipment the centre of the antenna shall be adjusted between 1 m and 4 m for maximum indication at each test frequency. The nearest point of the antenna to ground shall be not less than 0,2 m." The height above ground of the measuring antenna when measuring emissions from Group 1 Class A equipment (which might include, for example, large "switched mode power supplies (when not incorporated in an equipment)", see Annex 4.4-A, CISPR 11) is not specified. Generally, CISPR 11 allows Class A ISM equipment to be tested on a test site or *in situ* as preferred by the manufacturer, while requiring Class B ISM equipment to be measured on a test site. However, when providing for protection of specific safety services, CISPR 11 specifies that "...national authorities may require measurements to be made *in situ*...". This presumably includes *in situ* measurements for both Class A and Class B ISM equipment when the need arises, for example under the provisions of 5.3.

After considering the methods of specifying *in situ* measurement distance and measuring antenna height in CISPR 11, it is useful to address the following questions:

- 1) How well do measurements of the vertically and horizontally polarized *E*-fields, in a height scan of 1 m to 4 m at a horizontal distance of 10 m from the source over real ground, predict the field strengths emitted at elevated angles?
- 2) How predictable are the field strengths at elevated angles when the horizontal measuring distance is greater than 10 m but, beyond that fact, the actual distance is not known (not specified)?
- 3) How is the predictability affected when the height above ground to the centre of the measuring antenna is fixed, for example at a nominal 3 m?
- 4) What errors in judgement of the predictability of the vertical patterns may arise if calculations are made using the common approximation that the influence of the real ground can be simulated by replacing it with a perfect conductor?

To provide some answers in the frequency range 30 MHz to 1 000 MHz a number of vertical polar patterns and linear height scan patterns have been calculated for the *E*-field radiation emitted by four kinds of electrically small sources located close to the surface of real homogeneous plane ground. Predictability has been assessed by judging how well, or how badly, the calculated patterns show that ground-based measurements of the vertically and horizontally polarized *E*-fields emitted from the various sources will correlate with the maximum strengths of either vertically or horizontally polarized *E*-fields (whichever are greater) at elevated angles. The patterns have been calculated for the simplest of sources radiating into the half-space above ground. If these patterns identify problems of predictability, it is unlikely that predictability will be improved when real ISM devices, like plastics welders or RF diathermy machines, are the sources.

Vertical polar patterns and linear height scan patterns have also been calculated for the *E*-field radiation emitted from the small sources over a copper ground plane. A copper ground plane provides boundary conditions which distinguish, in effect, a perfect conductor from a real ground, and allows identification of the differences between the vertical radiation patterns that will exist close to the surface of a real ground when compared with those calculated close to the surface of a perfect conductor. The differences determine how large the errors will be if predictability is judged by considering vertical patterns calculated over a perfectly conducting ground plane.

The four kinds of source considered were electrically small vertical and horizontal balanced electric and magnetic dipoles. There is justification for the use of small dipole sources as models in the study of the predictability of radiation at elevated angles from real ISM equipment. Airborne measurements of the fourth harmonic field radiated from 27 MHz ISM apparatus over real ground reported in [4] have been studied further in [5]. In [5] it is shown that the vertical distribution of horizontally polarized fields at approximately 109 MHz, encountered by an aircraft during any single flight pass over the ISM apparatus, can be well matched with a field distribution produced at elevated angles by a simple small electric or magnetic dipole source. Some of the work in [5] is summarized in appendix 4.5-A.

#### **4.5.3 Method used to calculate field patterns in the vertical plane**

The *E*-field vertical polar patterns and linear height scan patterns have been calculated using a double precision version of the Method of Moments computer code known as the Numerical Electromagnetics Code (NEC) [6]. NEC2 with the companion code SOMNEC allows the Sommerfeld integral evaluation of the field interactions at the air-ground interface [7], and so includes the contribution of the Sommerfeld-Norton surface wave when calculating the total *E*-fields above real grounds (discussed in 4.5.4.3). The near fields were also included in the calculations for this report.

The small vertical and horizontal balanced electric dipoles, and vertical and horizontal balanced loops (magnetic dipoles) used as the models for the calculations each had a unit dipole moment (i.e. a dipole [current] moment of a A·m for the electric dipoles and a dipole moment of 1 A·m<sup>2</sup> for the loops). All were positioned with their centres at a height above ground of either 1 m or 2 m in order to show the effects of variations in the source height on the vertical radiation patterns. The effects include the appearance of additional major lobes of radiation – called grating lobes – as the spacing between the source and its image in the ground increases beyond  $\lambda/2$  with increasing frequency [8].

The geometries of the models, and the paths of the scans in vertical planes at constant radius about each source for the vertical polar pattern computations, are shown in the top right corner of each polar pattern plot.

The planes in which the linear height scan patterns were calculated are shown in the diagrams accompanying each linear height scan pattern plot.

#### 4.5.3.1 The frequencies of interest and the electrical constants of the ground

The five frequencies of interest at which the models were excited, in the five ITU designated bands [9] listed in table VI of CISPR 11, are shown here in table 4.5-1.

**Table 4.5-1**

Excitation frequency MHz	ITU designated bands
75	74,8-75,2 MHz, Aeronautical Radionavigation (Instrument Landing System (ILS) marker beacons, horizontal polarization)
110	108-137 MHz, Aeronautical Radionavigation and Aeronautical Mobile (R) (including ILS localizers (108-112 MHz), horizontal polarization)
243	243 MHz is for use by survival craft stations and equipment used for survival purposes
330	328,6-335,4 MHz, limited to ILS (glide path, horizontal polarization)
1 000	960-1 215 MHz, reserved on a worldwide basis for the use and development of airborne electronic aids to air navigation

Most attention has been devoted to the small sources placed above a "medium dry ground" [1] (CCIR – medium dry ground; rocks; sand; medium sized towns [2]). The electrical constants, the relative permittivity  $\epsilon_r$  and the conductivity  $\sigma$ , mS/m, for "medium dry ground" at 30 MHz and the other five frequencies of interest are listed in table 4.5-2.

**Table 4.5-2 – Electrical constants for "medium dry ground" [1]  
(CCIR – medium dry ground; rocks; sand; medium sized towns [2])**

Frequency MHz	$\epsilon_r$	$\sigma$ mS/m
30	15	1
75	15	1,5
110	15	2
243	15	4,5
330	15	7,5
1 000	15	35

Near the lower and upper ends of the frequency range, at frequencies of 75 MHz and 1 000 MHz, examples of two other types of grounds have been used with the electrically small vertical loop model (horizontal magnetic dipole) to illustrate the influence of differing values of the ground constants on the vertical radiation patterns (see 4.5.4.1). The electrical constants for "wet ground" and "very dry ground" at 30 MHz, 75 MHz and 1 000 MHz, are listed in table 4.5-3.

**Table 4.5-3 – Electrical constants for "wet ground" [1] (CCIR – marshes (fresh water); cultivated land [2]) and "very dry ground" [1] (CCIR – very dry ground; granite mountains in cold regions; industrial areas [2])**

Frequency MHz	"Wet ground"		"Very dry ground"	
	$\epsilon_r$	$\sigma$ mS/m	$\epsilon_r$	$\sigma$ mS/m
30	30	10	3	0,1
75	30	13	3	0,1
1 000	30	140	3	0,15

#### 4.5.4 Limitations of predictability of radiation at elevated angles

##### 4.5.4.1 Influence of the electrical constants of the ground

It is useful to observe the relatively small influence of widely differing values of the ground constants on the predictability of the field strengths at elevated angles. A small vertical loop (horizontal magnetic dipole) at a centre height of 2 m above ground has been chosen as the source model. The geometry of the model is shown in figure 4.5-1. For this source, the best predictability is obtained when the vertical  $E_z$  field component is measured near the ground to estimate the maximum strength of either the horizontally oriented  $E_x$  field or the vertically oriented  $E_z$  field at elevated angles.

###### 4.5.4.1.1 Influence of the ground constants at 75 MHz

In figure 4.5-1(a), the vertical polar patterns at 75 MHz show the horizontally polarized  $E_x$  field strengths in the Y-Z plane at scan radii  $R$  of 10 m, 30 m, and 300 m, over real grounds having the electrical constants in tables 4.5-2 and 4.5-3. It can be seen that at each of the three scan radii, the total *spread* in the maximum  $E_x$  fields in the vertical direction is less than 3 dB.

In figure 4.5-1(b), the height scan patterns calculated up to a height of 6 m at 75 MHz show the  $E_z$  field strengths in the Z-X plane at the three corresponding horizontal distances over the same three types of real ground. It can be seen that the *spread* in magnitudes of the  $E_z$  field strengths at ground level for the three ground types is much greater than 3 dB. However, if measurements of  $E_z$  are made at heights from 1 m to 4 m, then at a horizontal distance of 10 m the underestimates of the maximum  $E_x$  field strengths in the vertical direction range from about 3,9 dB to about 4,7 dB (a *spread* of only 0,8 dB), at a horizontal distance of 30 m, the underestimates range from about 5,1 dB to about 5,7 dB (a *spread* of only 0,6 dB), and at 300 m, the underestimates range from about 18,4 dB to about 22,1 dB (a *spread* of 3,7 dB). Thus, for the range of values of the ground constants and measuring distances considered here, the worst case *spread* or *variation* in the underestimates of maximum field strengths in the vertical direction is only 3,7 dB, and this occurs at the largest measuring distance of 300 m.

###### 4.5.4.1.2 Influence of the ground constants at 1 000 MHz

In figure 4.5-2(a), the vertical polar patterns at 1 000 MHz show the horizontally polarized  $E_x$  field strength in the Y-Z plane at the same three scan radii  $R$  around the small vertical loop over the same three types of real ground with the electrical constants at 1 000 MHz given in tables 4.5-2 and 4.5-3. It can be seen that for a source height of 2 m at this frequency, multiple grating lobes are established.

Figure 4.5-2(b) shows the vertical polar patterns of the vertically oriented  $E_z$  field strengths in the Z-X plane, and figure 4.5-2(c) shows the height scan patterns of the  $E_z$  field strengths calculated up to a height of 6 m in the Z-X plane, at the three scan distances and over the three types of real ground.

Figure 4.5-2(a) shows that the maximum strength of the  $E_x$  field occurs at an elevation angle between 77° and 78° at all three scan radii. A comparison of figure 4.5-2(b) with figure 4.5-2(a) also shows that, in the case of a "very dry ground", the maximum field strength is contributed by  $E_z$  at the scan radii of 30 m and 300 m at an elevation angle of 2° (that is, at heights of approximately 1,1 m and 10,5 m at the two radii respectively).

Inspection of figure 4.5-2 reveals the following information. If a vertically polarized antenna measures maximum  $E_z$  in height scans from 1 m to 4 m, then at 10 m horizontal distance the resulting underestimates of the maximum  $E_x$  field strengths range from about 1,8 dB to about 3,2 dB, a *spread* of only 1,4 dB. At 30 m horizontal distance, with "medium dry ground" or "wet ground", a 1 m to 4 m  $E_z$  height scan measurement underestimates the maximum  $E_x$  field strengths by about 1,4 dB ("medium dry ground") or about 2,9 dB ("wet ground"), a *spread* of only 1,5 dB. Over "very dry ground", the maximum field strength,  $E_z$ ,

is reached at a height of about 1,1 m, and will therefore be measured within the height scan from 1 m to 4 m.

At 300 m horizontal distance, over "medium dry ground" and "wet ground", a 1 m to 4 m height scan of  $E_z$  underestimates the maximum  $E_x$  field strengths (at about 77° elevation) by about 4,4 dB ("medium dry ground") or about 5,2 dB ("wet ground"), a *spread* of only 0,8 dB. Over "very dry ground" a measurement of  $E_z$  at a height of 4 m underestimates the maximum field strength (maximum  $E_z$  at an elevation angle of 2°, height approximately 10,5 m) by about 5,1 dB. The overall *spread* in the underestimates at 300 m distance therefore remains only 0,8 dB.

Thus, at 1 000 MHz, the calculations show that the differing values of the electrical constants of the ground we have considered here produce a worst-case *variation* or *spread* of only 1,5 dB in the underestimates of the maximum  $E$ -field strengths at elevated angles, when the estimates are based on 1 m to 4 m height scan measurements of  $E_z$  at horizontal distances ranging from 10 m to 300 m.

#### **4.5.4.1.3 Predictability estimated over a "medium dry ground"**

The foregoing shows that in the frequency range from 75 MHz to 1 000 MHz it is justifiable to make general judgements of the predictability of the strength of radiation in vertical directions above ground by considering the  $E$ -field patterns calculated over a real ground having the electrical constants of a "medium dry ground".

#### **4.5.4.2 Predictability based on height scan measurements near real ground at 10 m distance from the source**

Here we can provide an answer to the first question posed in 4.5.2.

In summary, the answer is that the predictability of the maximum  $E$ -field strengths at elevated angles by means of 1 m to 4 m height scan measurements at a horizontal distance of 10 m, for all four types of sources placed either 1 m or 2 m above a "medium dry ground", is very good. Underestimates at all five of the frequencies used for aeronautical services are less than 6 dB.

At the two lower frequencies of 75 MHz and 110 MHz, the larger underestimates occur when the source is either a small horizontal electric dipole 1 m above the ground or a small vertical loop (horizontal magnetic dipole) with a centre height 2 m above ground.

At the frequencies of 243 MHz and 330 MHz, the larger underestimates occur when the source is either a small vertical electric dipole or a small vertical loop with a centre height 1 m above ground.

At 1 000 MHz, the larger underestimate occurs when the source is a small vertical loop with a centre height 2 m above ground.

##### **4.5.4.2.1 Predictability at 75 MHz**

Figure 4.5-3(a) shows polar plots of  $E_x$  in the Y-Z plane and  $E_z$  in the Z-X plane, at 75 MHz, around the horizontal electric dipole placed 1 m above ground. At a scan radius of 10 m,  $E_x$  reaches a maximum field strength of almost 138 dB $\mu$ V/m at an elevation angle near 73°. The polar plots of  $E_z$  in the Z-X plane – the vertically polarized radiation emitted from the tips of a horizontal electric dipole over real ground [7] – show that vertically polarized measurements near the ground do not give the best predictions of field strength at high elevation angles. Therefore, figure 4.5-3(b) shows the height scan calculations of horizontally polarized  $E_x$  in the Y-Z plane, reaching an  $E_x$  magnitude of almost 133 dB $\mu$ V/m at a horizontal distance of 10 m and a height of 4 m. In consequence, 1 m to 4 m height scan measurements of  $E_x$  at a distance of 10 m will underestimate the maximum  $E_x$  at 73° elevation by almost 5 dB.

The vertical polar plots in figure 4.5-1(a) show that measurement of  $E_x$  at a distance of 10 m near the ground will not give a good prediction of the maximum field strength emitted at 75 MHz by a small vertical loop placed at a height of 2 m above a "medium dry ground".

$E_x$  field strength reaches a maximum of over 142 dB $\mu$ V/m in the vertical Y-Z plane. The calculated height scan patterns in figure 4.5-1(b) show that a vertically polarized measurement of  $E_z$  at a horizontal distance of 10 m in the Z-X plane will reach a maximum of almost 138 dB $\mu$ V/m at 1,2 m height. This underestimates by less than 5 dB the maximum strength of the radiation in the vertical direction.

Column (4) of table 4.5-4 summarizes the estimated errors to be expected in the predictability of radiation in vertical directions when based on measurements in height scans from 1 m to 4 m at a horizontal distance of 10 m from each of the four sources operating at 75 MHz. Column (1) lists the radiation sources and their heights. Column (2) lists the field components which contribute the maximum field strengths in the vertical polar patterns, and the elevation angles at which the maximum field strengths occur. Column (3) lists the field component which should be measured in a linear height scan at a horizontal distance of 10 m to provide the best estimates of the maximum field strengths.

**Table 4.5-4 – Estimates of the errors in prediction of radiation in vertical directions based on a measurement height scan from 1 m to 4 m at known distances,  $d$ .**  
**Frequency = 75 MHz (Adapted from [10])**

(1) Source of radiation @ height	(2) Max. $E$ , @ angle, in 10 m polar plot	(3) At hor. $d = 10$ m, measure this field	(4) Estimated prediction error, at $d = 10$ m	(5) Max. $E$ , @ angle, in 30 m polar plot	(6) At hor. $d = 30$ m, measure this field	(7) Estimated prediction error, at $d = 30$ m	(8) Max. $E$ , @ angle, in 300 m polar plot	(9) At hor. $d = 300$ m, measure this field	(10) Estimated prediction error, at $d = 300$ m
Vertical electric dipole @ 1 m	$Ez$ @ 15,25°	$Ez$	0 dB	$Ez$ @ 17,75°	$Ez$	-2 dB	$Ez$ @ 18°	$Ez$	-17,5 dB
Vertical electric dipole @ 2 m	$Ez$ @ 8°	$Ez$	0 dB	$Ez$ @ 12,75°	$Ez$	-1 dB	$Ez$ @ 13°	$Ez$	-16 dB
Horizontal electric dipole @ 1 m	$Ex$ @ 72,5° in Y-Z plane	$Ex$ in Y-Z plane	-5 dB	$Ex$ @ 67,5° in Y-Z plane	$Ex$ in Y-Z plane	-12 dB	$Ex$ @ 66° in Y-Z plane	$Ex$ in Y-Z plane	-31,5 dB
Horizontal electric dipole @ 2 m	$Ex$ @ 30° in Y-Z plane	$Ex$ in Y-Z plane	-1,5 dB	$Ex$ @ 28,75° in Y-Z plane	$Ex$ in Y-Z plane	-7 dB	$Ex$ @ 28,5° in Y-Z plane	$Ex$ in Y-Z plane	-26,5 dB
Vertical loop (horizontal magnetic dipole) @ 1 m	$Ez$ @ 17,5° in Z-X plane	$Ez$ in Z-X plane	-0,5 dB	$Ez$ @ 19,75° in Z-X plane	$Ez$ in Z-X plane	-2,5 dB	$Ez$ @ 20° in Z-X plane	$Ez$ in Z-X plane	-18 dB
Vertical loop (horizontal magnetic dipole) @ 2 m	$Ex$ @ 90°	$Ez$ in Z-X plane	-4,5 dB	$Ex$ @ 90°	$Ez$ in X-Z plane	-5,5 dB	$Ex$ @ 90°	$Ez$ in Z-X plane	-20,5 dB
Horizontal loop (vertical magnetic dipole @ 1 m	$Ey$ @ 37,5° in Z-X plane	$Ey$ in Z-X plane	-2,5 dB	$Ey$ @ 36,75° in Z-X plane	$Ey$ in Z-X plane	-9 dB	$Ey$ @ 36,5° in Z-X plane	$Ey$ in Z-X plane	-28,5 dB
Horizontal loop (vertical magnetic dipole) @ 2 m	$Ey$ @ 27° in Z-X plane	$Ey$ in Z-X plane	-1 dB	$Ey$ @ 25,5° in Z-X plane	$Ey$ in Z-X plane	-6,5 dB	$Ey$ @ 25° in Z-X plane	$Ey$ in Z-X plane	-25,5 dB

#### 4.5.4.2.2 Predictability at 110 MHz

Figure 4.5-4(a) shows vertical polar plots of  $E_x$  in the Y-Z plane and  $E_z$  in the Z-X plane, at 110 MHz, around a small horizontal electric dipole placed 1 m above the ground. At a scan radius of 10 m,  $E_x$  reaches a maximum field strength of over 141 dB $\mu$ V/m at an elevation angle of 41°. The polar plots of  $E_z$  in the Z-X plane show that vertically polarized measurements near the ground will not give good guidance to high-angle field strength. Figure 4.5-4(b) shows height scan calculations of  $E_x$  in the Y-Z plane. At a horizontal distance of 10 m the magnitude of  $E_x$  reaches almost 139 dB $\mu$ V/m at a height of 4 m, and a height scan measurement of horizontally polarized  $E_x$  therefore underestimates the maximum strength of  $E_x$  at 41° elevation by less than 3 dB.

Figure 4.5-5(a) shows vertical polar plots of  $E_x$  in the Y-Z plane and  $E_z$  in the Z-X plane, around a small vertical loop (horizontal magnetic dipole) placed at a centre height of 2 m above ground and excited at 110 MHz. The maximum field strength reached at a scan radius of 10 m is the vertical  $E_z$  component, 146 dB $\mu$ V/m at an elevation angle of 40°. The height scan plots of  $E_z$  in figure 4.5-5(b) show that at a horizontal distance of 10 m the magnitude of  $E_z$  is almost 144 dB $\mu$ V/m at a height of 1 m, which underestimates the strength of  $E_z$  at 40° elevation by less than 2,5 dB.

Column (4) of table 4.5-5 summarizes the errors expected in the predictability of radiation in vertical directions based on measurements in height scans from 1 m to 4 m at a horizontal distance of 10 m from each of the four sources operating at 110 MHz.

**Table 4.5-5 – Estimates of the errors in prediction of radiation in vertical directions based on a measurement height scan from 1 m to 4 m at known distances,  $d$ .**  
**Frequency = 110 MHz (Adapted from [10])**

(1) Source of radiation @ height	(2) Max. $E$ , @ angle, in 10 m polar plot	(3) At hor. $d = 10$ m, measure this field	(4) Estimated prediction error, at $d = 10$ m	(5) Max. $E$ , @ angle, in 30 m polar plot	(6) At hor. $d = 30$ m, measure this field	(7) Estimated prediction error, at $d = 30$ m	(8) Max. $E$ , @ angle, in 300 m polar plot	(9) At hor. $d = 300$ m, measure this field	(10) Estimated prediction error, at $d = 300$ m
Vertical electric dipole @ 1 m	$E_z$ @ 13,5°	$E_z$	0 dB	$E_z$ @ 15,25°	$E_z$	-1,5 dB	$E_z$ @ 15,25°	$E_z$	-17,5 dB
Vertical electric dipole @ 2 m	$E_z$ @ 36,5°	$E_z$	-1 dB	$E_z$ @ 10,75°	$E_z$	-0,5 dB	$E_z$ @ 11°	$E_z$	-15,5 dB
Horizontal electric dipole @ 1 m	$E_x$ @ 41° in Y-Z plane	$E_x$ in Y-Z plane	-2,5 dB	$E_x$ @ 40° in Y-Z plane	$E_x$ in Y-Z plane	-9,5 dB	$E_x$ @ 39,75° in Y-Z plane	$E_x$ in Y-Z plane	-29 dB
Horizontal electric dipole @ 2 m	$E_x$ @ 20° in Y-Z plane	$E_x$ in Y-Z plane	-0,5 dB	$E_x$ @ 19,25° in Y-Z plane	$E_x$ in Y-Z plane	-4,5 dB	$E_x$ @ 19,25° in Y-Z plane	$E_x$ in Y-Z plane	-23,5 dB
Vertical loop (horizontal magnetic dipole) @ 1 m	$E_x$ @ 90°	$E_z$ in Z-X plane	-2 dB	$E_y$ @ 90°	$E_z$ in Z-X plane	-3,5 dB	$E_y$ @ 90°	$E_z$ in Z-X plane	-19 dB
Vertical loop (horizontal magnetic dipole) @ 2 m	$E_y$ @ 40° in Z-X plane	$E_z$ in Z-X plane	-2,5 dB	$E_x$ @ 48° in Y-Z plane	$E_z$ in Z-X plane	-2,5 dB	$E_x$ @ 47,5° in Y-Z plane	$E_z$ in Z-X plane	-17,5 dB
Horizontal loop (vertical magnetic dipole) @ 1 m	$E_y$ @ 31,75° in Z-X plane	$E_y$ in Z-X plane	-1,5 dB	$E_y$ @ 31° in Z-X plane	$E_y$ in Z-X plane	-8 dB	$E_y$ @ 31° in Z-X plane	$E_y$ in Z-X plane	-27 dB
Horizontal loop (vertical magnetic dipole) @ 2 m	$E_y$ @ 19,25° in Z-X plane	$E_y$ in Z-X plane	-0,5 dB	$E_y$ @ 18,5° in Z-X plane	$E_y$ in Z-X plane	-4 dB	$E_y$ @ 18,25° in Z-X plane	$E_y$ in Z-X plane	-23 dB

#### 4.5.4.2.3 Predictability at 243 MHz

Figure 4.5-6(a) shows vertical polar plots of  $E_z$  and  $E_x$  in the Z-X plane, at 243 MHz, around the small vertical electric dipole placed at a centre height of 1 m above ground. At a scan radius of 10 m the maximum field strength of almost 144 dB $\mu$ V/m is contributed by  $E_z$  at an elevation angle of 33,75°. Calculations of the vertical field component  $E_z$  in a height scan from 1 m to 4 m at a horizontal distance of 10 m produce a peak magnitude of almost 143 dB $\mu$ V/m at a measuring height of 1,65 m, as shown in figure 4.5-6(b). This underestimates the maximum field strength by only 1 dB.

Figure 4.5-7(a) shows vertical polar plots of  $E_x$  in the Y-Z plane and  $E_z$  in the Z-X plane, around the small vertical loop placed at a centre height of 1 m above a "medium dry ground". It can be seen that, at a scan radius of 10 m, the maximum field strength of more than 159 dB $\mu$ V/m is reached by  $E_z$  at an elevation angle of 36,25° in the Z-X plane. The calculated  $E_z$  height scan patterns shown in figure 4.5-7(b) produce a peak field strength of 157 dB $\mu$ V/m, at 10 m horizontal distance and a height of 1,65 m. This underestimates the maximum  $E_z$  by approximately 2,5 dB.

The vertical polar plots of horizontally polarized  $E$ -field emitted at 243 MHz by a small horizontal loop placed at a height of 1 m above a "medium dry ground" are shown in figure 4.5-8(a). The peak of the major lobe, nearest the ground, occurs at an elevation angle of 17° and is therefore reached at a height of 2,9 m at a horizontal distance of 10 m. The height scan plot at a horizontal distance of 10 m in figure 4.5-8(b), which is of  $E_y$  in the Z-X plane in this example, underestimates the maximum field strength in a vertical polar scan by less than 0,5 dB.

Column (4) of table 4.5-6 summarizes the errors expected in the predictability of radiation in vertical directions based on measurements in height scans from 1 m to 4 m at a horizontal distance of 10 m from each of the four sources operating at 243 MHz.

**Table 4.5-6 – Estimates of the errors in prediction of radiation in vertical directions based on a measurement height scan from 1 m to 4 m at known distances,  $d$ .**  
**Frequency = 243 MHz (Adapted from [10])**

(1) Source of radiation @ height	(2) Max. $E$ , @ angle, in 10 m polar plot	(3) At hor. $d = 10$ m, measure this field	(4) Estimated prediction error, at $d = 10$ m	(5) Max. $E$ , @ angle, in 30 m polar plot	(6) At hor. $d = 30$ m, measure this field	(7) Estimated prediction error, at $d = 30$ m	(8) Max. $E$ , @ angle, in 300 m polar plot	(9) At hor. $d = 300$ m, measure this field	(10) Estimated prediction error, at $d = 300$ m
Vertical electric dipole @ 1 m	$E_z$ @ 33,75°	$E_z$	-1 dB	$E_z$ @ 10,5°	$E_z$	-0,5 dB	$E_z$ @ 10,5°	$E_z$	-16 dB
Vertical electric dipole @ 2 m	$E_z$ @ 18,25°	$E_z$	-0,5 dB	$E_z$ @ 18,25°	$E_z$	-0,5 dB	$E_z$ @ 7°	$E_z$	-13 dB
Horizontal electric dipole @ 1 m	$E_x$ @ 17,5° in Y-Z plane	$E_x$ in Y-Z plane	-0,5 dB	$E_x$ @ 17,5° in Y-Z plane	$E_x$ in Y-Z plane	-4 dB	$E_x$ @ 17,5° in Y-Z plane	$E_x$ in Y-Z plane	-22,5 dB
Horizontal electric dipole @ 2 m	$E_x$ @ 9° in Y-Z plane	$E_x$ in Y-Z plane	0 dB	$E_x$ @ 8,75° in Y-Z plane	$E_x$ in Y-Z plane	-0,5 dB	$E_x$ @ 8,75° in Y-Z plane	$E_x$ in Y-Z plane	-17 dB
Vertical loop (horizontal magnetic dipole) @ 1 m	$E_z$ @ 36,25° in Z-X plane	$E_z$ in Z-X plane	-2,5 dB	$E_z$ @ 36,5° in Z-X plane	$E_z$ in Z-X plane	-2 dB	$E_z$ @ 36,5° in Z-X plane	$E_z$ in Z-X plane	-17 dB

Vertical loop (horizontal magnetic dipole @ 2 m)	$E_x$ @ 70,5° in Y-Z plane	$E_z$ in Z-X plane	-2,5 dB	$E_x$ @ 69,25° in Y-Z plane	$E_z$ in Z-X plane	-3 dB	$E_x$ @ 69° in Y-Z plane	$E_z$ in Z-X plane	-15 dB
Horizontal loop (vertical magnetic dipole) @ 1 m	$E_y$ @ 17° in Z-X plane	$E_y$ in Z-X plane	-0,5 dB	$E_y$ @ 16,75° in Z-X plane	$E_y$ in Z-X plane	-3,5 dB	$E_y$ @ 16,75° in Z-X plane	$E_y$ in Z-X plane	-22,5 dB
Horizontal loop (vertical magnetic dipole) @ 2 m	$E_y$ @ 9° in Z-X plane	$E_y$ in Z-X plane	0 dB	$E_y$ @ 8,75° in Z-X plane	$E_y$ in Z-X plane	0 dB	$E_y$ @ 8,75° in Z-X plane	$E_y$ in Z-X plane	-17 dB

#### 4.5.4.2.4 Predictability at 330 MHz

Figure 4.5-9(a) shows vertical polar plots of  $E_z$  and  $E_x$  in the Z-X plane, at 330 MHz, around the small vertical electric dipole placed at a centre height of 1 m above ground. At a scan radius of 10 m the maximum field strength of almost 148 dB $\mu$ V/m is contributed by  $E_z$  at an elevation angle of 26°. Calculations of the vertically oriented  $E_z$  field in a height scan from 1 m to 4 m at 10 m horizontal distance produce a peak magnitude of almost 146 dB $\mu$ V/m at a measuring height of 1,45 m, as shown in figure 4.5-9(b). This underestimates the maximum field strength by less than 2 dB.

Figure 4.5-10(a) shows vertical polar plots of  $E_x$  in the Y-Z plane and  $E_z$  in the Z-X plane, around the small vertical loop placed at a centre height of 1 m above a "medium dry ground". It can be seen that, at a scan radius of 10 m, the maximum field strength of almost 167 dB $\mu$ V/m is reached by  $E_x$  at an elevation angle of 69° in the Y-Z plane. The calculated  $E_z$  height scan patterns in the Z-X plane shown in figure 4.5-10(b) produce a peak magnitude greater than 162 dB $\mu$ V/m at 10 m horizontal distance, measured at a height of 1,45 m. A height scan measurement of the vertical  $E_z$  field therefore underestimates the maximum strength of the radiation in vertical directions, the horizontal polarized  $E_x$  at an elevation angle of 69°, by approximately 4,5 dB.

It is interesting to observe the vertical polar plots of horizontally polarized  $E$ -field emitted at 330 MHz by a small horizontal loop placed at a height of 1 m above a "medium dry ground", shown in figure 4.5-11(a). The peak of the major lobe, nearest the ground, occurs at an elevation angle of only 12,75°. It is therefore measured at a height of only 2,2 m at a horizontal distance of 10 m, see figure 4.5-11(b). Thus, there is virtually no error in this example of the estimation of maximum field strength at elevated angles.

Column (4) of table 4.5-7 summarizes the estimated errors in the predictability of radiation in vertical directions based on measurements in height scans from 1 m to 4 m at a horizontal distance of 10 m from each of the four sources operating at 330 MHz.



**Table 4.5-7 – Estimates of the errors in prediction of radiation in vertical directions based on a measurement height scan from 1 m to 4 m at known distances,  $d$ .**  
**Frequency = 330 MHz (Adapted from [10])**

(1) Source of radiation @ height	(2) Max. $E$ , @ angle, in 10 m polar plot	(3) At hor. $d = 10$ m, measure this field	(4) Estimated prediction error, at $d = 10$ m	(5) Max. $E$ , @ angle, in 30 m polar plot	(6) At hor. $d = 30$ m, measure this field	(7) Estimated prediction error, at $d = 30$ m	(8) Max. $E$ , @ angle, in 300 m polar plot	(9) At hor. $d = 300$ m, measure this field	(10) Estimated prediction error, at $d = 300$ m
Vertical electric dipole @ 1 m	$Ez$ @ 26°	$Ez$	-2 dB	$Ez$ @ 26°	$Ez$	-0,5 dB	$Ez$ @ 9°	$Ez$	-15 dB
Vertical electric dipole @ 2 m	$Ez$ @ 27,25°	$Ez$	-0,5 dB	$Ez$ @ 5,75°	$Ez$	0 dB	$Ez$ @ 5,5°	$Ez$	-11,5 dB
Horizontal electric dipole @ 1 m	$Ex$ @ 13° in Y-Z plane	$Ex$ in Y-Z plane	0 dB	$Ex$ @ 12,75° in Y-Z plane	$Ex$ in Y-Z plane	-2 dB	$Ex$ @ 12,75° in Y-Z plane	$Ex$ in Y-Z plane	-20 dB
Horizontal electric dipole @ 2 m	$Ex$ @ 6,5° in Y-Z plane	$Ex$ in Y-Z plane	0 dB	$Ex$ @ 6,5° in Y-Z plane	$Ex$ in Y-Z plane	0 dB	$Ex$ @ 6,5° in Y-Z plane	$Ex$ in Y-Z plane	-14,5 dB
Vertical loop (horizontal magnetic dipole) @ 1 m	$Ex$ @ 69° in Y-Z plane	$Ez$ in Z-X plane	-4,5 dB	$Ex$ @ 68,25° in Y-Z plane	$Ez$ in Z-X plane	-3,5 dB	$Ex$ @ 68° in Y-Z plane	$Ez$ in Z-X plane	-17,5 dB
Vertical loop (horizontal magnetic dipole) @ 2 m	$Ex$ @ 66,75° in Y-Z plane	$Ez$ in Z-X plane	-2,5 dB	$Ex$ @ 66° in Y-Z plane	$Ez$ in Z-X plane	-2,5 dB	$Ex$ @ 66° in Y-Z plane	$Ez$ in Z-X plane	-12,5 dB
Horizontal loop (vertical magnetic dipole) @ 1 m	$Ey$ @ 12,75° in Z-X plane	$Ey$ in Z-X plane	0 dB	$Ey$ @ 12,5° in Z-X plane	$Ey$ in Z-X plane	-2 dB	$Ey$ @ 12,5° in Z-X plane	$Ey$ in Z-X plane	-20 dB
Horizontal loop (vertical magnetic dipole) @ 2 m	$Ey$ @ 6,5° in Z-X plane	$Ey$ in Z-X plane	0 dB	$Ey$ @ 6,5° in Z-X plane	$Ey$ in Z-X plane	0 dB	$Ey$ @ 6,5° in Z-X plane	$Ey$ in Z-X plane	-14,5 dB

#### 4.5.4.2.5 Predictability at 1 000 MHz

Figure 4.5-2 shows vertical polar plots of  $Ez$  and  $Ex$ , at 1 000 MHz, around a small vertical loop placed at a centre height of 2 m above ground. At a scan radius of 10 m over a "medium dry ground" the maximum field strength of 187 dB $\mu$ V/m is contributed by the horizontally polarized  $Ex$  at an elevation angle of 77,5° in the Y-Z plane. Calculations of the vertically oriented  $Ez$  field in a height scan from 1 m to 4 m at 10 m horizontal distance in the Z-X plane produce a peak field of almost 184 dB $\mu$ V/m at a height of 3,2 m, as shown in figure 4.5-2(c). A vertically polarized height scan measurement therefore underestimates the maximum field strength by approximately 3 dB.

It is interesting to observe the vertical polar plots of horizontally polarized  $E$ -field emitted at 1 000 MHz by a small horizontal loop placed at a height of 1 m above a "medium dry ground", shown in figure 4.5-12(a). The peak of the major lobe, nearest the ground, occurs at an elevation angle of only 4,25°. Shown again in figure 4.5-12(b), it occurs at a height of 0,74 m at a horizontal distance of 10 m, and therefore will not be measured in a 1 m to 4 m height scan measurement. The next grating lobe is encountered at a height of 2,3 m, and its measurement contributes an underestimate of less than 0,5 dB to the prediction of maximum field strength of the major (lower) lobe.

Column (4) of table 4.5-8 summarizes the errors estimated for the predictability of radiation in vertical directions based on measurements in height scans from 1 m to 4 m at a horizontal distance of 10 m from each of the four sources operating at 1 000 MHz.

**Table 4.5-8 – Estimates of the errors in prediction of radiation in vertical directions based on a measurement height scan from 1 m to 4 m at known distances,  $d$ .**  
**Frequency = 1 000 MHz (Adapted from [10])**

(1) Source of radiation @ height	(2) Max. $E$ , @ angle, in 10 m polar plot	(3) At hor. $d = 10$ m, measure this field	(4) Estimated prediction error, at $d = 10$ m	(5) Max. $E$ , @ angle, in 30 m polar plot	(6) At hor. $d = 30$ m, measure this field	(7) Estimated prediction error, at $d = 30$ m	(8) Max. $E$ , @ angle, in 300 m polar plot	(9) At hor. $d = 300$ m, measure this field	(10) Estimated prediction error, at $d = 300$ m
Vertical electric dipole @ 1 m	$E_z$ @ 17,5°	$E_z$	-0,5 dB	$E_z$ @ 4°	$E_z$	0 dB	$E_z$ @ 3,75°	$E_z$	-9,5 dB
Vertical electric dipole @ 2 m	$E_z$ @ 17,75°	$E_z$	-0,5 dB	$E_z$ @ 2°	$E_z$	0 dB	$E_z$ @ 2°	$E_z$	-5 dB
Horizontal electric dipole @ 1 m	$E_x$ @ 4,25° in Y-Z plane	$E_x$ in Y-Z plane	-0,5 dB	$E_x$ @ 4,25° in Y-Z plane	$E_x$ in Y-Z plane	0 dB	$E_x$ @ 4,25° in Y-Z plane	$E_x$ in Y-Z plane	-11 dB
Horizontal electric dipole @ 2 m	$E_x$ @ 2,25° in Y-Z plane	$E_x$ in Y-Z plane	0 dB	$E_x$ @ 2,25° in Y-Z plane	$E_x$ in Y-Z plane	0 dB	$E_x$ @ 2,25° in Y-Z plane	$E_x$ in Y-Z plane	-5,5 dB
Vertical loop (horizontal magnetic dipole) @ 1 m	$E_x$ @ 64,5° in Y-Z plane	$E_z$ in Z-X plane	-2,5 dB	$E_x$ @ 64,25° in Y-Z plane	$E_z$ in Z-X plane	-1 dB	$E_z$ @ 4° in Z-X plane	$E_z$ in Z-X plane	-9,5 dB
Vertical loop (horizontal magnetic dipole) @ 2 m	$E_x$ @ 77,5° in Y-Z plane	$E_z$ in Z-X plane	-3 dB	$E_x$ @ 77,25° in Y-Z plane	$E_z$ in Z-X plane	-1,5 dB	$E_z$ @ 2° in Z-X plane	$E_z$ in Z-X plane	-5 dB
Horizontal loop (vertical magnetic dipole) @ 1 m	$E_y$ @ 4,25° in Z-X plane	$E_y$ in Z-X plane	-0,5 dB	$E_y$ @ 4,25° in Z-X plane	$E_y$ in Z-X plane	0 dB	$E_y$ @ 4,25° in Z-X plane	$E_y$ in Z-X plane	-11 dB
Horizontal loop (vertical magnetic dipole) @ 2 m	$E_y$ @ 2,25° in Z-X plane	$E_y$ in Z-X plane	0 dB	$E_y$ @ 2,25° in Z-X plane	$E_y$ in Z-X plane	0 dB	$E_y$ @ 2,25° in Z-X plane	$E_y$ in Z-X plane	-5,5 dB

#### 4.5.4.3 Predictability based on height scan measurements near real ground at an unknown distance, greater than 10 m, from the radiation source

Here we can answer the second question posed in 4.5.2. This measurement situation is analogous to making measurements *in situ* at a distance of 10 m from the wall outside a building containing ISM equipment which is located at an unknown distance inside the building. As mentioned earlier, we do not consider here the attenuation which may be introduced by intervening building materials.

Calculations have been made of vertical polar patterns and linear height scan patterns at distances of 30 m and 300 m. The reader will have already seen that patterns for those distances have also been included in the figures.

The figures, together with the comprehensive summaries presented in columns (7) and (10) of tables 4.5-4 to 4.5-8, show that the predictability of fields at elevated angles based on height scan measurements near real ground becomes more prone to underestimation as the horizontal measuring distance increases beyond 10 m, especially at the lower frequencies. Underestimation can become very large at a distance of 300 m. At the lower frequencies underestimates can reach more than 30 dB at that distance when the source behaves as a small horizontal electric dipole. The underestimates for both horizontally and vertically polarized fields occur in spite of the significant contributions which can be made by surface waves at the lower frequencies near 30 MHz [11]. Predictability improves as the frequency increases, primarily because at higher frequencies the surface wave contributions decrease and the maximum field strength measured in the height scan is created by the sum of the direct and reflected space wave components (the sum is sometimes called, somewhat misleadingly, the "ground wave"). The contributions of the space wave signals increase at lower elevation angles as more grating lobes form with increasing frequency.

It is particularly important to recognize that, at horizontal distances of 30 m and more, the worst-case underestimations of the maximum levels of field strengths at elevated angles will generally occur when the fields are horizontally polarized. This is very unfortunate, because the signals for the ILS (marker beacons, localizer, and glide path, see table 4.5-1) are all horizontally polarized transmissions and therefore require the maximum protection from horizontally polarized disturbances.

The figures also provide guidance to the rates of change of the fields with distance. Calculations and measurements made at a constant height, avoiding nulls, show that the maximum rate of change of the fields with distance can approach a rate that is inversely proportional to distance squared. When surface wave contributions are negligible, then a grazing incidence in the far field a field strength inversely proportional to distance squared is to be expected at a constant measuring height [11] [12]. However, the space wave field strengths along radial paths at constant elevation angles vary in simple proportion with inverse distance, which is to be expected of such far fields propagating freely in space. Therefore it is to be expected that the fields measured near the ground (the so-called "ground waves") will, in general, attenuate more rapidly with increasing distance than do the fields from the same source which are propagating radially up into space.

If the horizontal distances at which height scan measurements are made *in situ* are not known, very large errors can arise – all of them underestimates – in the predictability of the strength of radiation in vertical directions from all four types of source and at all frequencies from 75 MHz to 1 000 MHz.

#### **4.5.4.4 Predictability based on measurement at a fixed height**

In its measurement procedures relating to the ways in which measuring antennas are to be used, CISPR 11 does not distinguish between measurements made *in situ* for the protection of specific safety services and those made for the protection of other services. Thus, if a measurement of emissions is made *in situ* from a Group 2 Class A ISM equipment in accordance with the specification, the measuring antenna is placed at a height of 3 m ± 0,2 m (7.2.4); no height scan is specified.

The obvious risk with fixed height measurements is that a measurement will be made at a null in the field strength pattern. The risk of this happening is increased if the electrical height above ground of the radiation centre of the source increases – for example with increasing frequency – which contributes to the formation of an increasing number of grating lobes, and hence nulls. A few examples of the effects these nulls can have on a measurement made at a height near 3 m (or any other *fixed* height) are shown in several of the figures.

For example, figure 4.5-2(c) shows that, depending on the type of ground over which the measurements are made, at a horizontal distance of 10 m from a small vertical loop source located at a height of 2 m the measured vertically polarized field strength at 1 000 MHz might vary by more than 6 dB for measurements made somewhere in the height tolerance

range of 2,8 m to 3,2 m, and that at 30 m horizontal distance a measurement made at 3 m height is also close to a null.

Figure 4.5-12(b) shows that a horizontal distance of 10 m from a small horizontal loop source located 1 m above ground with the measured horizontally polarized field strength at 1 000 MHz might vary by more than 12 dB in the CISPR measurement height tolerance range from 2,8 m to 3,2 m. It also shows how the field strength can vary with distance in an apparently anomalous manner when measurements are made at a fixed height. Note that at a height of 3 m the field strength at 30 m distance is the same as the field strength at 10 m distance. At other heights, the field strength at 30 m distance becomes greater than that at 10 m distance.

Comparison of the height scan curves in figure 4.5-13 with those in figure 4.5-12(b) shows that, at 1 000 MHz, as the small horizontal loop source height varies between 1 m and 2 m, deep nulls will pass through the measuring height of 3 m at horizontal measuring distance of 10 m and 30 m. These effects can be encountered at *greater horizontal measuring distances and lower frequencies* if the height of the radiating source is increased.

We are now in a position to answer the third question posed in 4.5.2. The answer is that predictability is degraded by fixed height measurements. Measurements at a fixed height should not be permitted, especially if they are being made to determine protection for specific safety services.

Height scans must be specified or, for measuring convenience, the measuring height *in situ* could be specified in the manner of [13], so that at a horizontal distance of 10 m, the measuring height would be specified as 4 m above the immediate terrain *or at such lower height at which the field strengths may exceed that at 4 m*.

#### **4.5.5 Differences between the fields over a real ground and the fields over a perfect conductor**

There are significant differences between the field distributions above a real earth plane and over a perfect conductor. There are several reasons for the differences, not the least being that the reflection factors for both polarizations over a perfect conductor always have a magnitude of unity at all angles of incidence, whereas over real ground they have a magnitude less than unity except at grazing incidence. In addition, for vertically polarized waves over a perfect conductor there is no Brewster's angle or, expressed in another way, at all reflection angles a vertically polarized image in a perfect conductor is always in phase with the vertically polarized source above the conductor. This contrasts with the situation of vertically polarized waves meeting a lossy dielectric like real ground, where reflections taking place below Brewster's angle experience a large phase change and the image can be visualized as being in approximate anti-phase with the source. It should also be observed that the reflection factor for a vertically polarized wave reflecting at Brewster's angle has a very small magnitude for most types of real ground encountered in practice.

The behaviour of the fields above a metal ground plane compared with the fields over an earthen ground plane is discussed at length in [11]. The brief discussion below, derived from [11], serves to provide an answer to the fourth question posed in 4.5.2.

##### **4.5.5.1 Vertically polarized fields over a perfect conductor**

The contribution of the vertically polarized surface wave over real ground can be significant. However, it cannot increase the total field strength created by a small vertical electric dipole over real ground to equal the strength of the fields created by the same vertical dipole moment over a perfect conductor. Figure 4.5-14 displays the vertical components of the fields emitted at 30 MHz from a small vertical electric dipole situated 1 m above a "medium dry ground", calculated using NEC and SOMNEC to include the surface wave, compared with the fields calculated over an almost perfect conductor (in this case annealed copper).

Comparisons of the fields over real ground with those over the good conductor show why vertically polarized measurements at 30 MHz on a measuring site with a metal ground plane are not comparable with measurements made on sites with earthen ground planes. Specifically, they show why measurements of vertically polarized disturbances made on a metal ground place for comparison with field strength disturbance limits developed for earth sites may penalize the equipment under test (EUT). The fields measured over a metal ground plane can exceed the limits, even when the fields from the same EUT over an earthen ground plane are comfortably below the limits. The comparisons also show why calculations of the vertically polarized fields created at 30 MHz over a perfect conductor or a metal ground plane, for a given dipole moment, are a bad guide to the predictability achievable for the fields created at elevated angles by that dipole moment over a real ground. If the fields over the good conductor are mistakenly believed to resemble those over a real ground, they will encourage a false sense of confidence that ground based measurements over real ground will give good guidance to the field strengths to be expected at elevated angles.

In figure 4.5-15, the height scan patterns of the vertical components of the *E*-fields emitted from the small vertical dipole show that at 1 000 MHz, just as was the case at 30 MHz, the vertically polarized fields developed near a metal ground plane at 1 000 MHz are much stronger than those developed near a "medium dry ground". The same conclusions which were reached at a frequency of 30 MHz regarding the possible penalties imposed on an EUT, when the disturbances measured on a metal ground plane site are compared with field strength disturbance limits developed for earth sites, also apply at a frequency of 1 000 MHz. Similarly, it can be seen in figure 4.5-15 that at 1 000 MHz the patterns of the vertically polarized fields over a metal ground plane are a bad guide to the predictability of the fields created at elevated angles by the same dipole moment over a real ground.

The height scan patterns in figure 4.5-15 also clearly illustrate the effect of the phase reversal of the vertical dipole image in a lossy dielectric when reflection take place below Brewster's angle. The dashed horizontal line across the height scan pattern for 10 m distance shows the height, approximately 1,6 m, to the field point which corresponds with a reflection taking place at Brewster's angle when the source is 1 m above the "medium dry ground".

It is quite clear in figure 4.5-15 that at 10 m distance the field nulls and maxima at heights greater than 1,6 m above both the copper ground plane and the "medium dry ground" are in phase, signifying that the images in the two kinds of ground planes have similar phases when reflection from the real ground takes place at elevation angles above Brewster's angle. However, it is also quite clear that vertically polarized waves reflected below Brewster's angle over the "medium dry ground" are reversed in phase with respect to the corresponding reflected waves over the copper ground plane. In other words, the vertical image in the lossy dielectric is reversed, producing destructive interference (a null) at the surface of the "medium dry ground" whereas constructive interference (a maximum) occurs at the surface of the copper ground plane (the direct and reflected path lengths being the same in both cases). With the vertical dipole source at a height of 1 m, a maximum occurs in the field at 10 m distance at a height of 0,75 m above the "medium dry ground", whereas a very deep null occurs at that height over the copper ground plane (the direct and reflected path lengths differ by  $\lambda/2$  in both cases).

The height scans at 30 m and 300 m, up to a height of 6 m, take place below Brewster's angle. Maxima in the height scanned fields over the metal ground plane therefore coincide with minima in the fields over real ground in both those height scans. This is largely the reason why it must not be believed that the height scanned vertically polarized fields calculated over a good conductor will resemble those over real ground, especially at the larger horizontal distances. Such a belief will create false confidence that measurements made near real ground, without regard for the horizontal distance from the source, can give good guidance to the field strengths to be expected at elevated angles.

#### 4.5.5.2 Horizontally polarized fields over a perfect conductor

Although the contribution of the horizontally polarized surface wave over real ground at 30 MHz is small, nevertheless the height scan patterns in figure 4.5-16 show that the horizontally polarized fields near the "medium dry ground" are stronger in this case than the corresponding fields near the copper ground plane.

In both cases a null is required in the vertical field pattern at the ground, to satisfy the boundary conditions, and the null is deeper in the copper ground plane example. This example shows that, in contrast with vertically polarized measurements, it is possible that measurements of horizontally polarized fields made on a metal ground plane for comparison with radiated disturbance limits developed for earth sites may slightly favour the EUT when measuring for compliance with the limits.

In figure 4.5-17, the height scan patterns of the horizontally polarized *E*-fields emitted at 1 000 MHz from the small horizontal electric dipole show that at height scan distance of 30 m and more, with no useful contribution from the surface wave, the maximum horizontally polarized fields over a "medium dry ground" are very similar to those over a copper ground plane. The similarity of magnitude in regions of constructive interference is caused by the similar reflection factors (magnitudes close to unity) over both surfaces at low angles of reflection. At higher reflection angles, and a shorter measurement distance of 10 m, the maximum horizontally polarized fields over a metal ground plane exceed those over an earthen ground plane because the magnitude of the reflection factor over the earth plane becomes significantly less than unity. The reflected wave then contributes less to the constructive interference occurring at the field maxima.

The behaviour of the horizontally polarized fields over an earthen ground plane is not complicated by a Brewster's angle phenomenon. In general, at frequencies of 30 MHz and above, the horizontally polarized field patterns over a real ground resemble the shapes of the corresponding patterns over a metal ground plane. Some small differences in field strengths are created over real ground compared with those over a metal ground plane at the lower frequencies by the presence of the surface wave over a real ground. Differences are also created at short horizontal distances, and higher frequencies at which the surface wave is insignificant, because the magnitude of the horizontal reflection factor decreases below unity as the waves reflect at higher angles from the earth plane.

#### 4.5.5.3 Fields over a perfect conductor as guides to the fields over real ground

We can now answer the fourth question posed in 4.5.2.

In summary, the horizontal polarized field patterns created over real ground at frequencies of 30 MHz and above resemble the corresponding patterns over a metal ground plane. There are some differences of a few decibels in field magnitudes. At the lower frequencies some small differences are also created by the existence of the surface wave over a real ground. At the higher frequencies the field strength differences at short measuring distances are caused by the decrease below unity of the magnitude of the horizontal reflection factor for real ground when reflection takes place at angles significantly above grazing incidence. Constructive interference of direct and reflected waves over real ground then produces field strength maxima of somewhat smaller magnitudes than those produced over a good conductor which has a reflection factor close to unity at all reflection angles.

However, very large differences are found when comparing the patterns of vertically polarized fields over a metal ground plane with those over a real ground. The differences are primarily created by the existence of Brewster's angle for the reflections of vertically polarized waves from a lossy dielectric like real ground. When reflections from real ground take place below Brewster's angle the minima in the fields occur at the same heights at which the maxima are produced with the same measuring geometry over the metal ground plane, most notably at the surface of the ground plane. This contrapositioning of minima and maxima is the main reason why the height scanned vertically polarized fields calculated over a good conductor must not be assumed to resemble those over real ground, especially

at the larger horizontal distances when reflection take place near grazing incidence. An assumption that there is a resemblance encourages false confidence that measurements near real ground, without regard for the horizontal distance from the source, can give good guidance to the field strengths to be expected at elevated angles.

Vertically polarized field patterns over a metal ground plane do not resemble the shapes and magnitudes of the vertically polarized field patterns to be expected from the same sources over a real ground.

#### 4.5.6 Uncertainty ranges

The information summarized in tables 4.5-4 to 4.5-8 can also be used to show pictorially the ranges of uncertainties in the predictability of the radiation emitted at elevated angles at frequencies above 30 MHz. The information has been used to construct bar charts illustrating the uncertainties for electrically small sources located 1 m or 2 m above ground when predictions of the field strengths at elevated angles are based on  $E$ -field measurements in 1 m to 4 m height scans at horizontal distances of 10 m, 30 m and 300 m.

Figure 4.5-18 illustrates the uncertainties in predictability based on measurements made at a horizontal distance of 10 m. The bar for the uncertainty range at 330 MHz shows that the best predictability at 330 MHz is obtained when the source behaves as either a small horizontal dipole (dh) or as a small horizontal loop (lh). There is nominally zero error predicting the maximum strength of the horizontally polarized  $Eh$  fields. The poorest predictability at 330 MHz results in an underestimate of approximately 4,5 dB for the maximum horizontally polarized field  $Eh$  emitted at elevated angles from a small vertical loop (lv).

When measurements are made in a height scan at a horizontal distance of 30 m, the bar for the uncertainty range at 110 MHz in figure 4.5-19 shows that the best predictability at 110 MHz occurs when the source behaves as a small vertical dipole (dv). There is a negligible underestimate, by 0,5 dB, predicting the  $Ez$  vertical component of the vertically polarized field. The poorest predictability at 110 MHz produces a greater underestimate, by 9,5 dB, of the horizontally polarized  $Eh$  field emitted at elevated angles from a small horizontal dipole source (dh).

Figure 4.5-20 graphically illustrates the very large uncertainties in predictability that occur if the horizontal measuring distance is as great as 300 m. At 243 MHz, the bar illustrating the uncertainty range shows that the poorest predictability at 243 MHz introduces a very large underestimate by 22,5 dB for the horizontally polarized  $Eh$  fields emitted at elevated angles from a small horizontal dipole (dh) and from a small horizontal loop (lh). The best predictability at 243 MHz also produces a large underestimate, by 13 dB, of the vertical  $Ez$  component of the vertically polarized field emitted at elevated angles from a small vertical dipole (dv). Figures 4.5-19 and 4.5-20, in particular, graphically illustrate the very large underestimates which can occur when attempts are made to predict the strength of radiation in vertical directions based on measurements near the ground at unknown horizontal distances greater than 10 m from the sources.

#### 4.5.7 Conclusions

The *in situ* measurement procedures at frequencies above 30 MHz which are specified in CISPR 11 can lead to significant underestimates of the field strengths emitted at elevated angles from ISM equipment. The underestimates can arise due to the ill-defined measurement distance; the measuring distance from the radiating ISM equipment is not defined.

The largest underestimates of the fields at elevated angles will generally occur for horizontally polarized fields. This is a cause for concern, because the aeronautical safety of life services requiring greatest protection from disturbances originating at the ground are

those provided by the horizontally polarized marker beacon, localizer, and glide path signals of the aeronautical ILS.

Under some conditions, measurements are specified in CISPR 11 at a fixed height of 3 m. Measurements at a fixed height should not be specified if they are being made to determine protection for specific safety services. There is a risk that fixed height measurements will be made in, or close to, a null. The risk increases at the higher frequencies and when the height to the radiation centre of the source is unknown. Fixed height measurements can seriously underestimate the true field strength near the ground and, in consequence, the maximum field strength at elevated angles.

Calculations or measurements of the field strength patterns of vertically polarized fields over a perfect conductor or metal ground plane do not provide good guidance to the fields to be expected over a real ground. At reflection angles below Brewster's angle over real ground the field minima and maxima are contraposed with those created by the same source over a metal ground plane.

To provide protection for aeronautical safety of life services, and other communication systems, height scan measurements and limits for radiated disturbances from *in situ* ISM equipment located near the ground must be *specified at a known horizontal distance from the equipment*. Height scan measurements at a horizontal distance of 10 m from an ISM equipment *in situ* allow accurate estimates to be made of the fields emitted at elevated angles. If for practical reasons the *in situ* measurements must be made at a distance greater than 10 m from the equipment which is the source of the radiation then the limits at the larger distance, particularly if it is more than 30 m, must be derived from the 10 m limits by adjusting them in inverse proportion with increasing distance squared. This must be so in order to prevent relaxation of the protection the limits are intended to provide for communication or radionavigation systems that are operated high above ground.

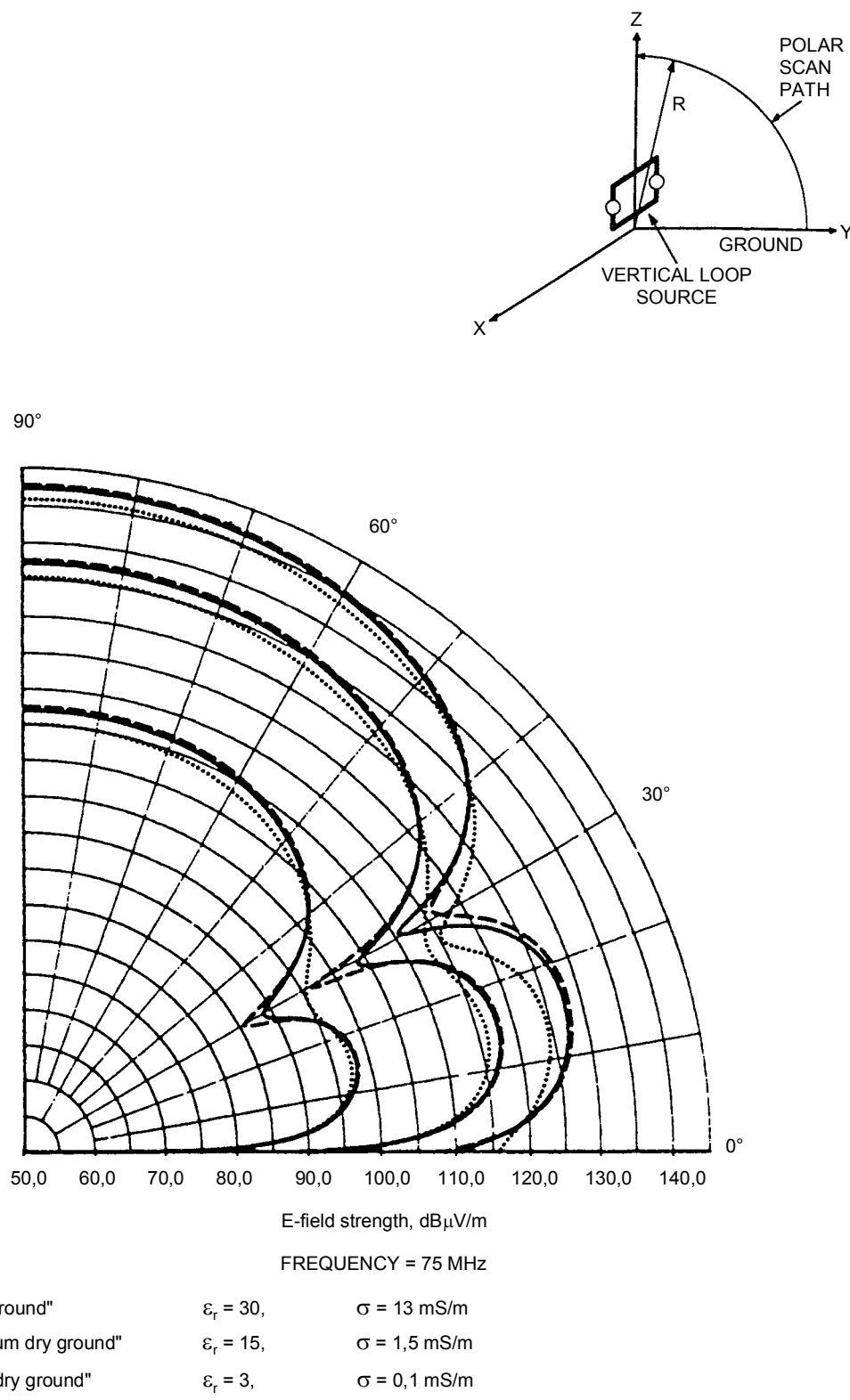
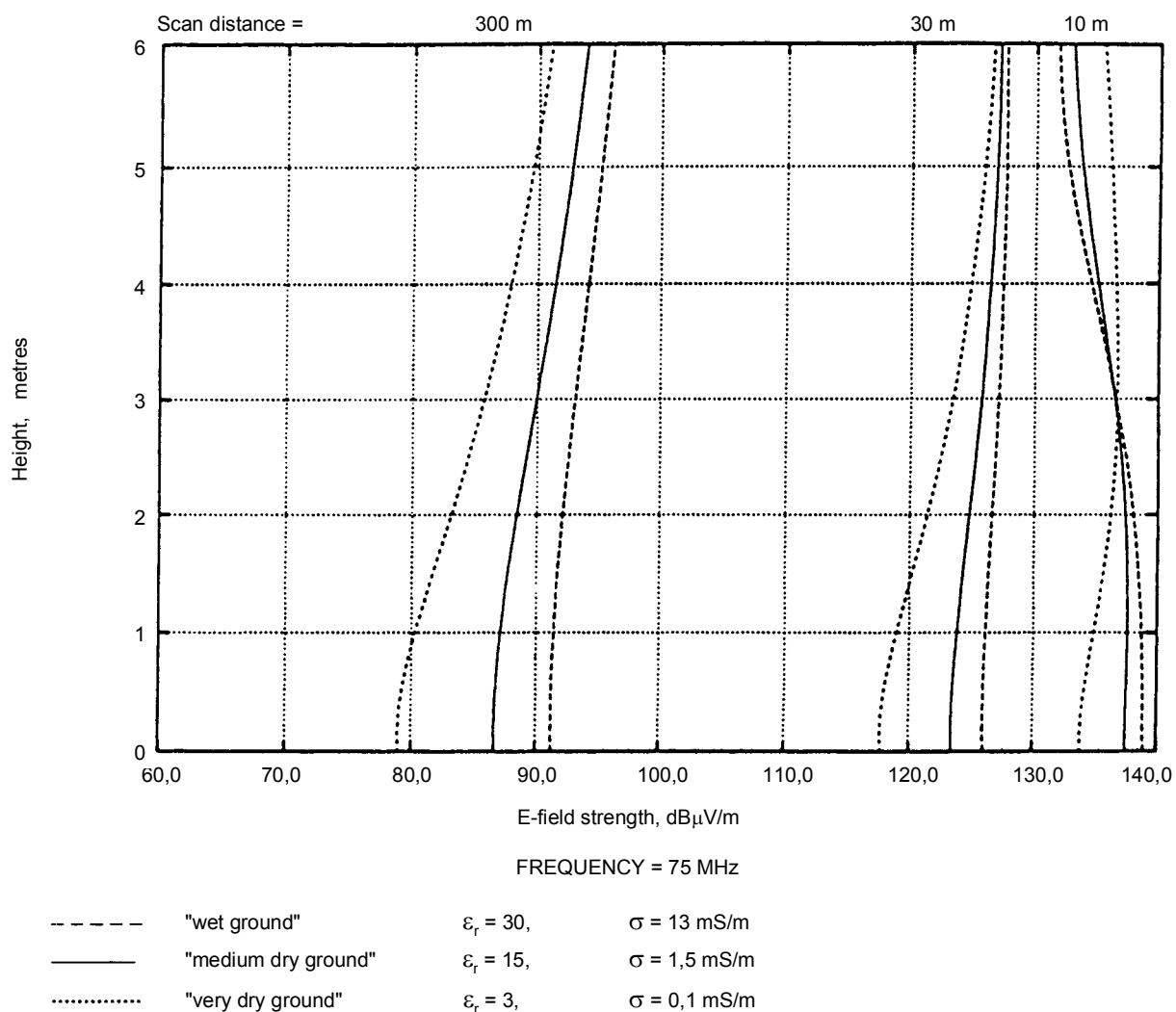
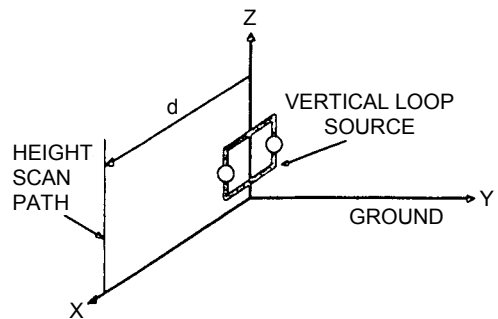


**Figure 4.5-1(a) – Vertical polar patterns of horizontally polarized  $Ex$  field strengths emitted at 75 MHz around the small vertical loop (horizontal magnetic dipole), at scan radii of 10 m, 30 m and 300 m in the Y-Z plane over three different types of real ground.**

Loop dimensions 0,1 m  $\times$  0,1 m. Loop centre height 2 m. Dipole moment 1 A $\cdot$ m<sup>2</sup>.  
(Reproduced from [10])

IEC 804/2000



IEC 805/2000

**Figure 4.5-1(b) Height scan patterns of vertically oriented  $E_z$  field strengths emitted at 75 MHz from the small vertical loop (horizontal magnetic dipole), at horizontal distances of 10 m, 30 m and 300 m in the Z-X plane over three different types of real ground.**

Loop dimensions  $0,1 \text{ m} \times 0,1 \text{ m}$ . Loop centre height 2 m. Dipole moment  $1 \text{ A}\cdot\text{m}^2$ .  
 (Reproduced from [10])

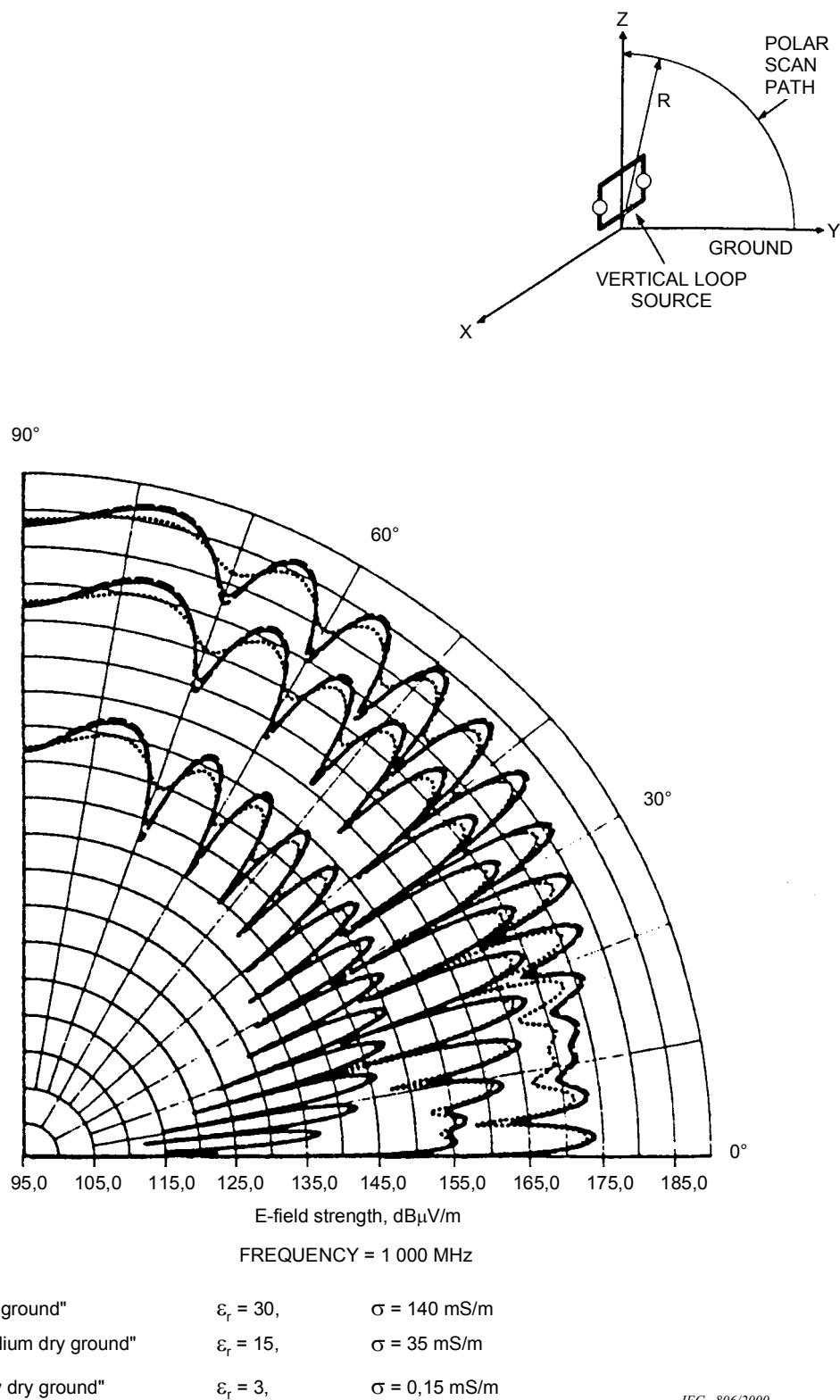


**Figure 4.5-2(a) – Vertical polar patterns of horizontally polarized  $Ex$  field strengths emitted at 1 000 MHz around the small vertical loop (horizontal magnetic dipole), at scan radii of 10 m, 30 m and 300 m in the Y-Z plane over three different types of real ground.**

**Loop dimensions 0,02 m × 0,02 m. Loop centre height 2 m. Dipole moment 1 A·m<sup>2</sup>. (Reproduced from [10])**

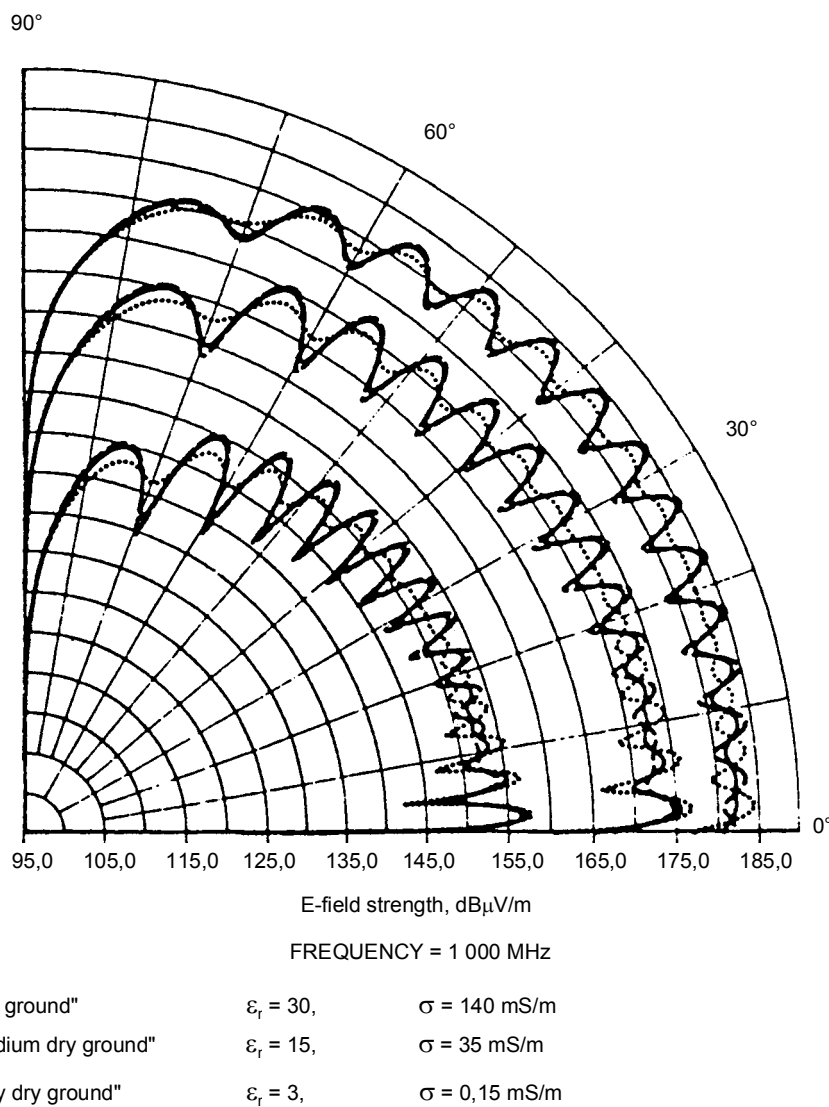
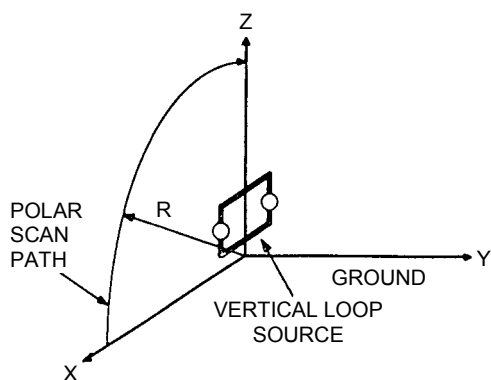


**Figure 4.5-2(b) – Vertical polar patterns of vertically oriented  $E_z$  field strengths emitted at 1 000 MHz around the small vertical loop (horizontal magnetic dipole), at scan radii of 10 m, 30 m and 300 m in the Z-X plane over three different types of real ground.**

Loop dimensions 0,02 m × 0,02 m. Loop centre height 2 m. Dipole moment 1 A·m<sup>2</sup>.  
(Reproduced from [10])

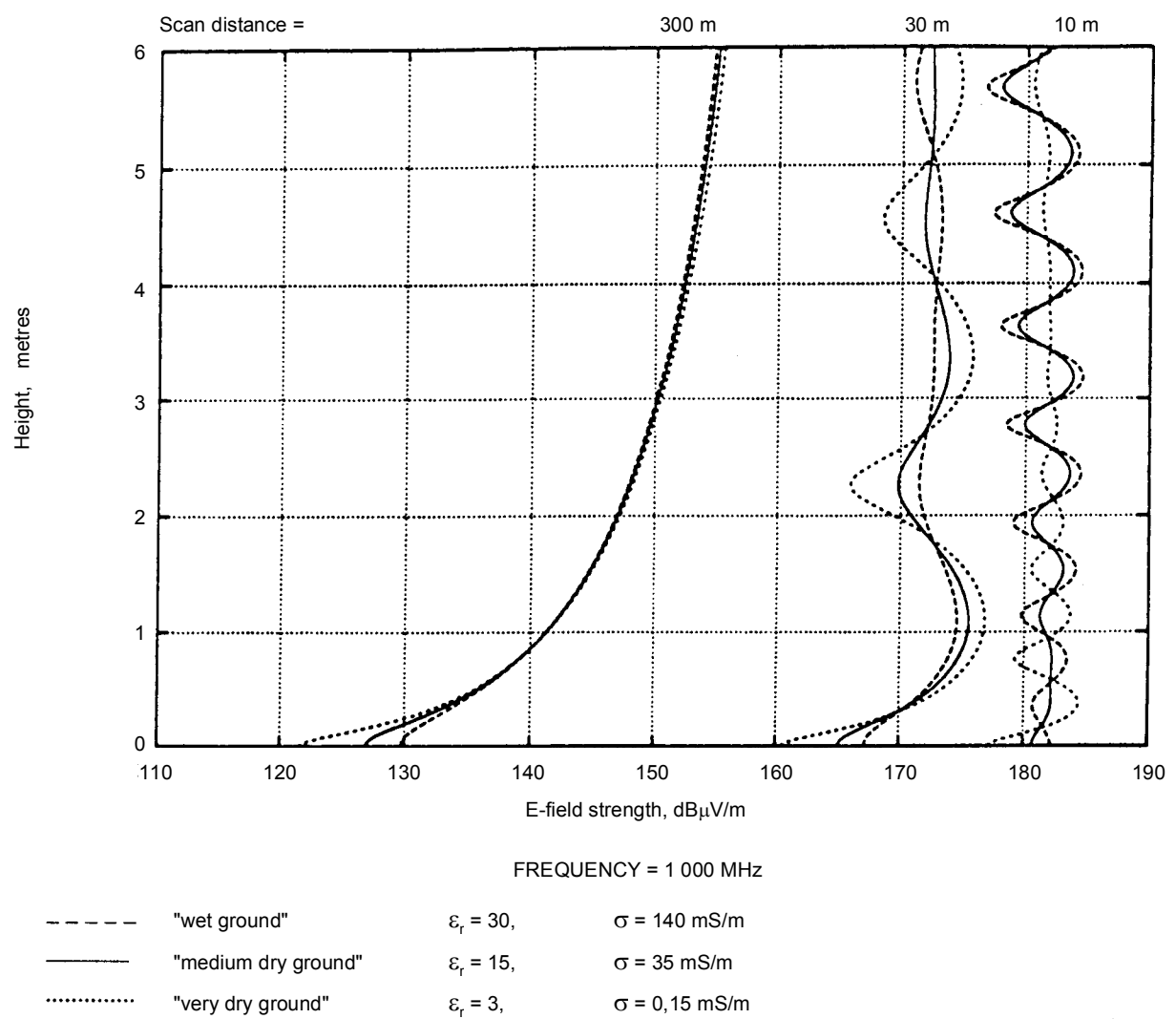
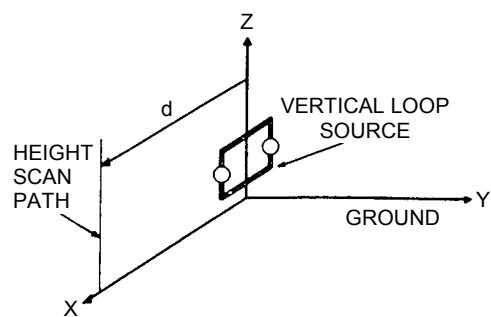


**Figure 4.5-2(c) – Height scan patterns of vertically oriented  $E_z$  field strengths emitted at 1 000 MHz from the small vertical loop (horizontal magnetic dipole), at horizontal distance of 10 m, 30 m and 300 m in the Z-X plane over three different types of real ground.**

Loop dimensions 0,02 m × 0,02 m. Loop centre height 2 m. Dipole moment 1 A·m<sup>2</sup>.  
(Reproduced from [10])

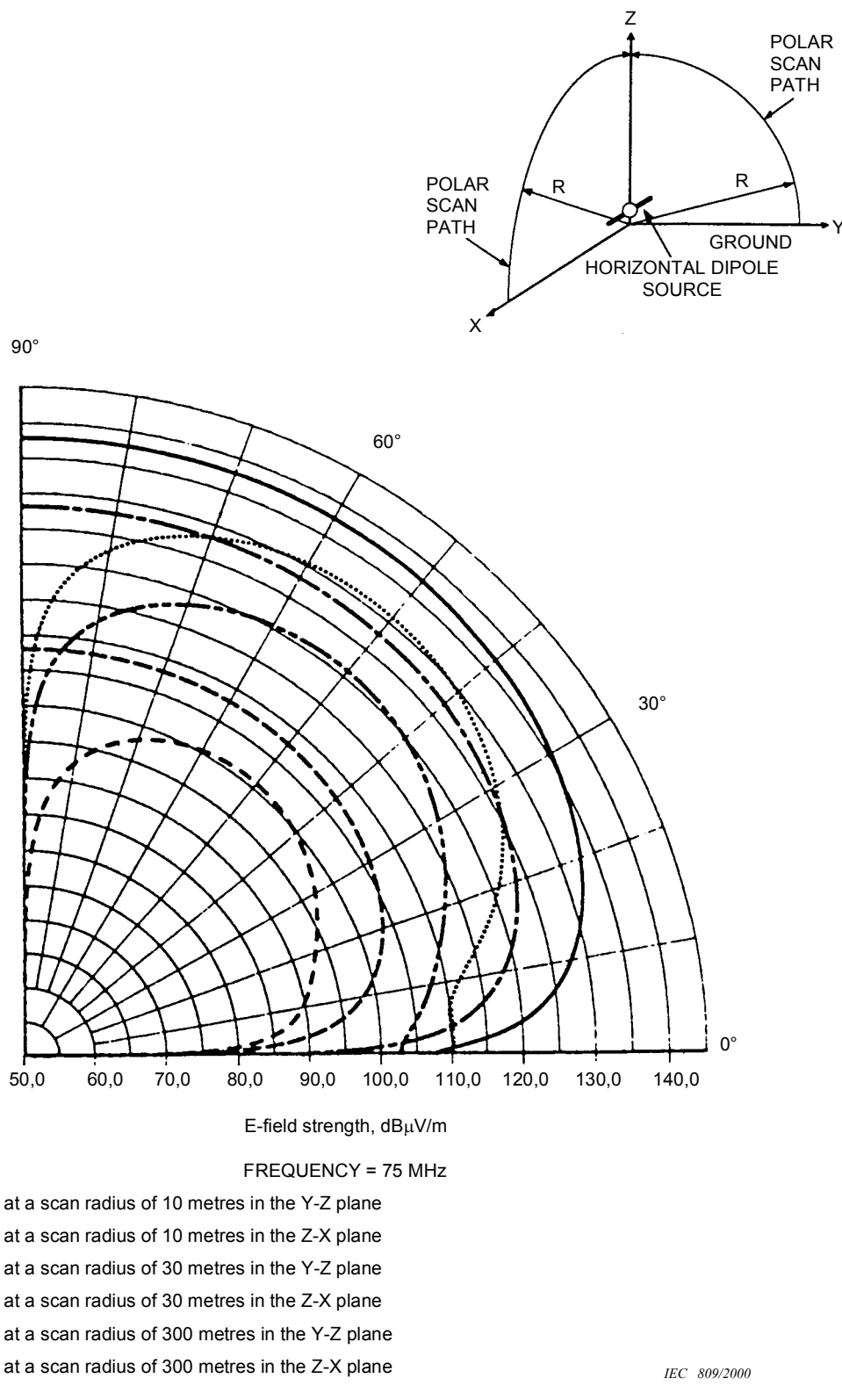


**Figure 4.5-3(a) – Vertical polar patterns of horizontally polarized  $E_x$  and vertically oriented  $E_z$  field strengths emitted at 75 MHz around the small horizontal electric dipole, at scan radii of 10 m, 30 m and 300 m in the Y-Z plane and the Z-X plane respectively.**  
**Dipole length 0,2 m. Dipole height 1 m. Dipole moment 1 A·m.**  
**Ground constants:  $\epsilon_r = 15$ ,  $\sigma = 1,5 \text{ mS/m}$ .**

(Reproduced from [10])

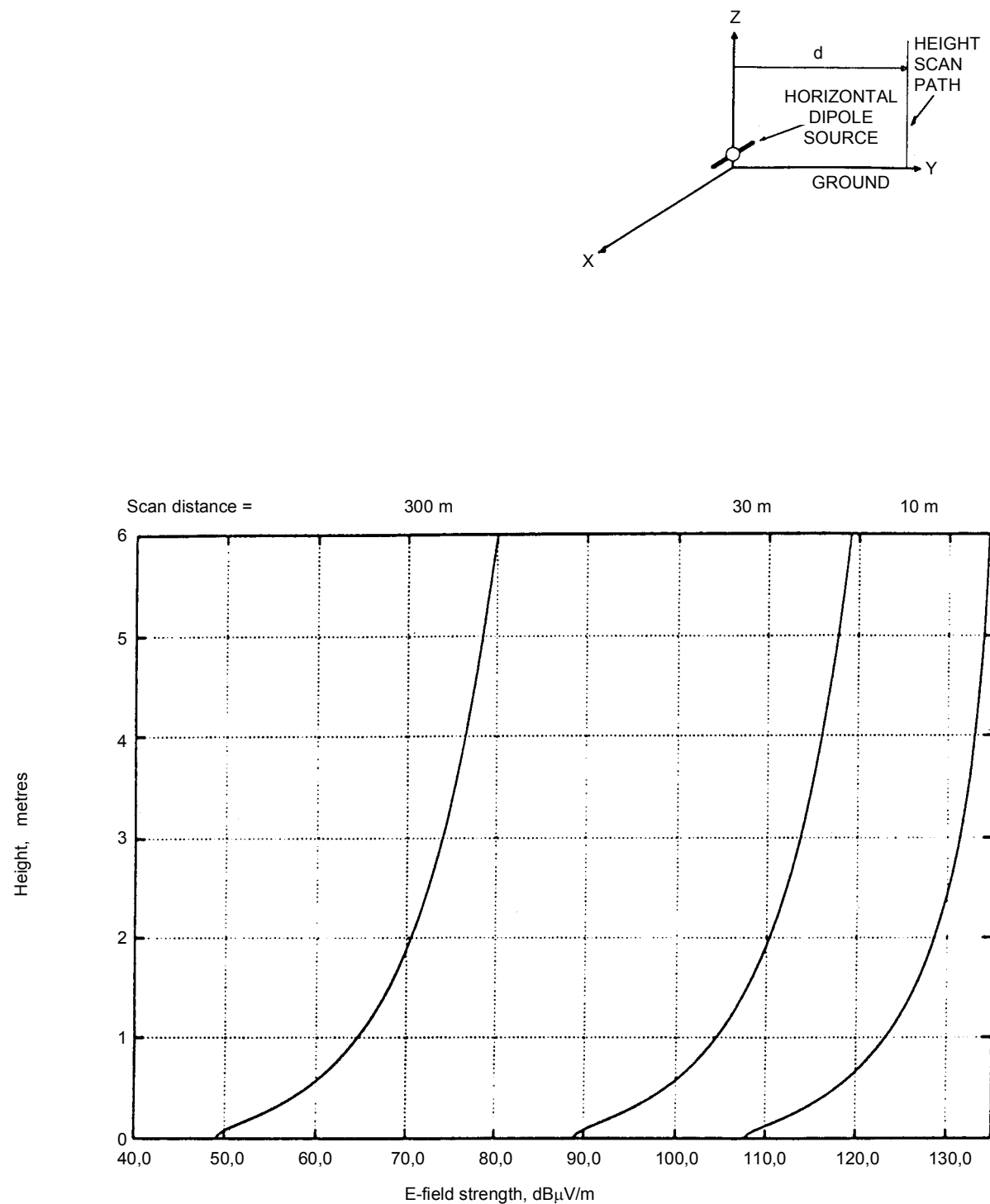


**Figure 4.5-3(b) – Height scan patterns of horizontally polarized  $Ex$  field strengths emitted at 75 MHz from the small horizontal electric dipole, at horizontal distances of 10 m, 30 m and 300 m in the Y-Z plane. Dipole length 0.2 m. Dipole height 1 m. Dipole moment 1 A·m. Ground constants:  $\epsilon_r = 15$ ,  $\sigma = 1.5 \text{ mS/m}$ .**  
 (Reproduced from [10])

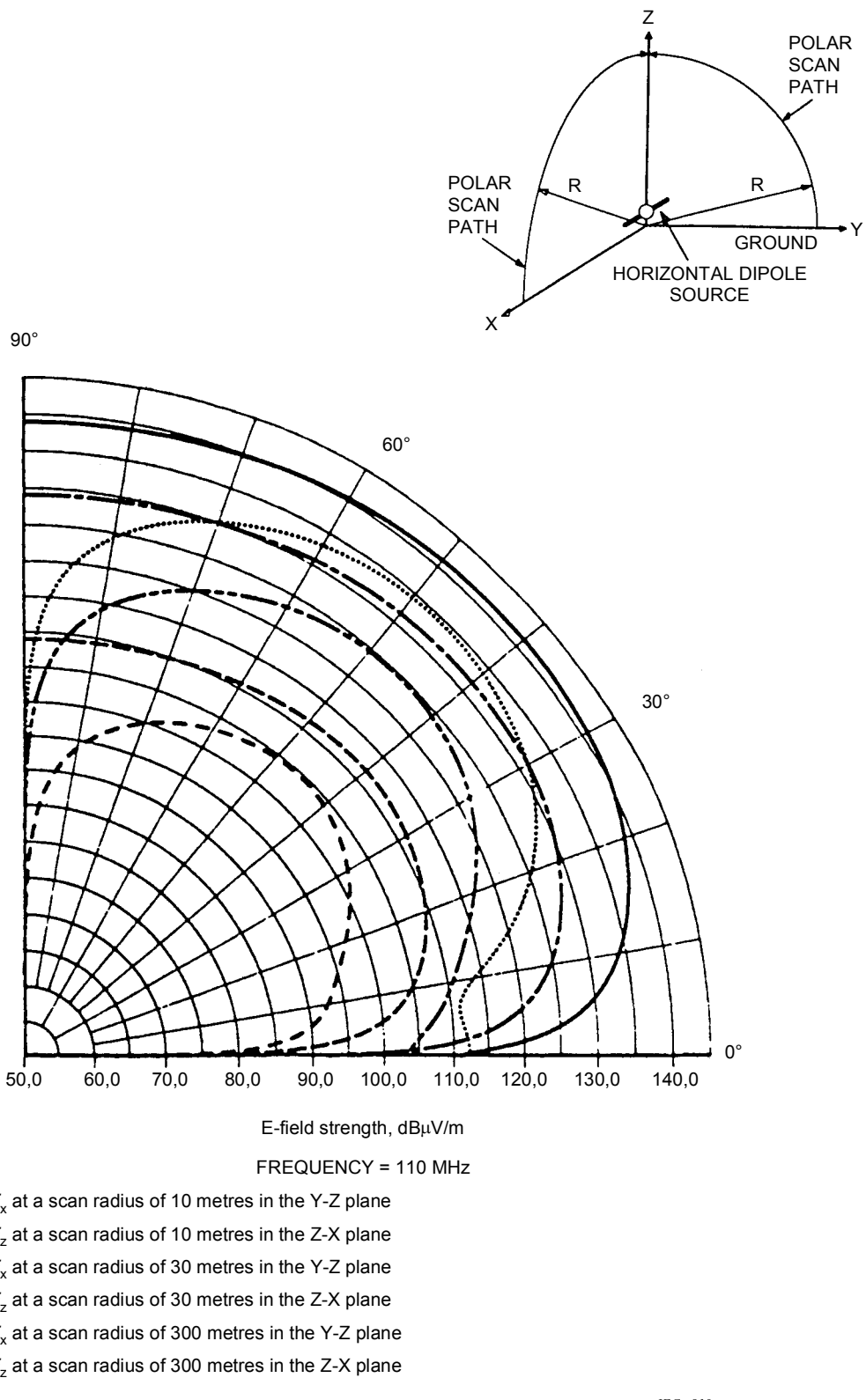
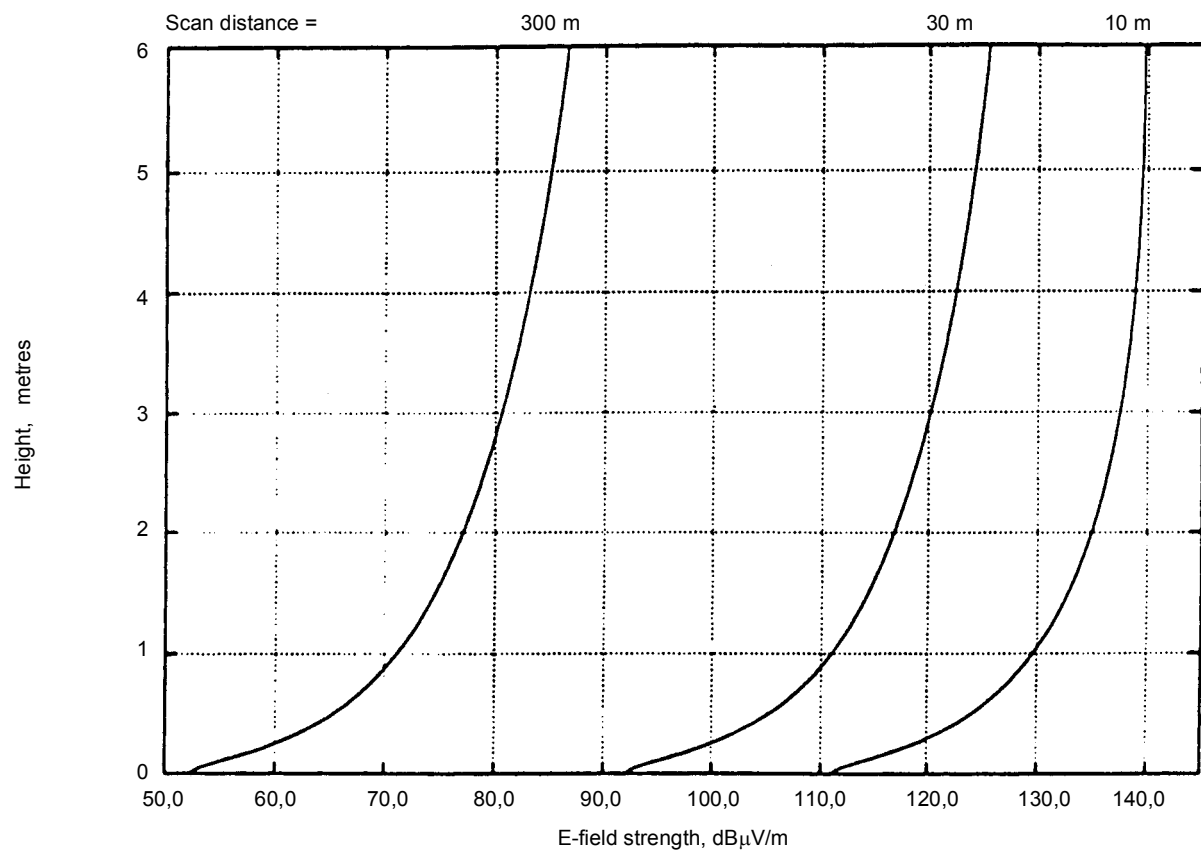
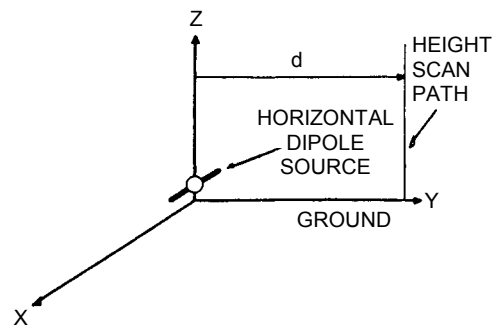


**Figure 4.5-4(a) – Vertical polar patterns of horizontally polarized  $E_x$  and vertically oriented  $E_z$  field strengths emitted at 110 MHz around the small horizontal electric dipole, at scan radii of 10 m, 30 m and 300 m, in the Y-Z plane and the Z-X plane respectively. Dipole length 0,2 m. Dipole height 1 m. Dipole moment 1 A·m. Ground constants:  $\epsilon_r = 15$ ,  $\sigma = 2 \text{ mS/m}$ .**

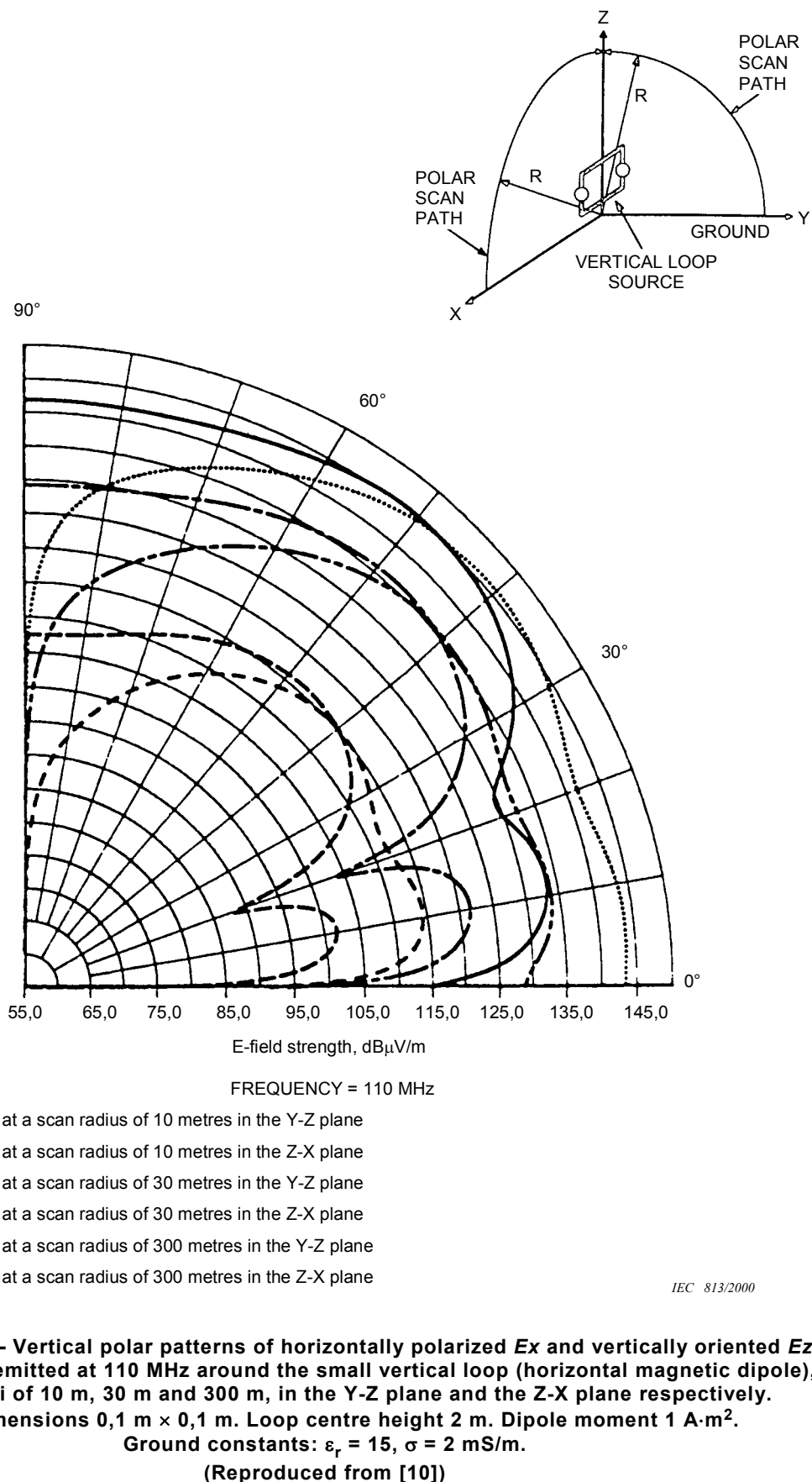
(Reproduced from [10])



FREQUENCY = 110 MHz

IEC 812/2000

**Figure 4.5-4(b) – Height scan patterns of horizontally polarized  $E_x$  field strengths emitted at 110 MHz from the small horizontal electric dipole, at horizontal distances of 10 m, 30 m and 300 m, in the Y-Z plane. Dipole length 0,2 m. Dipole height 1 m. Dipole moment 1 A·m. Ground constants:  $\epsilon_r = 15$ ,  $\sigma = 2 \text{ mS/m}$ .**  
**(Reproduced from [10])**



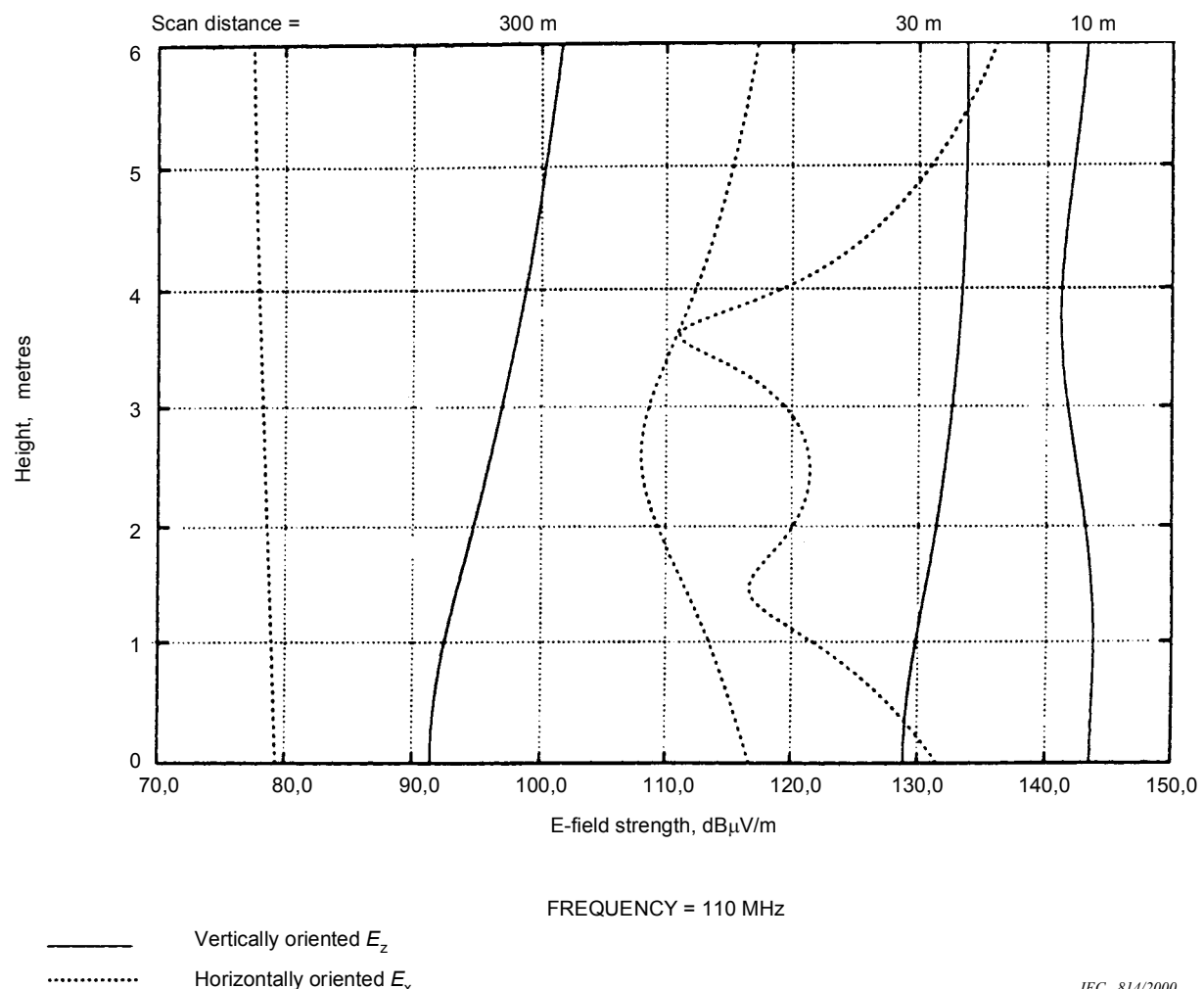
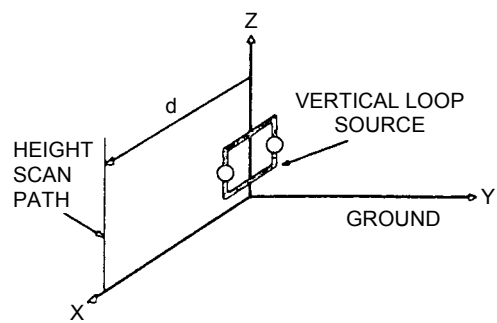
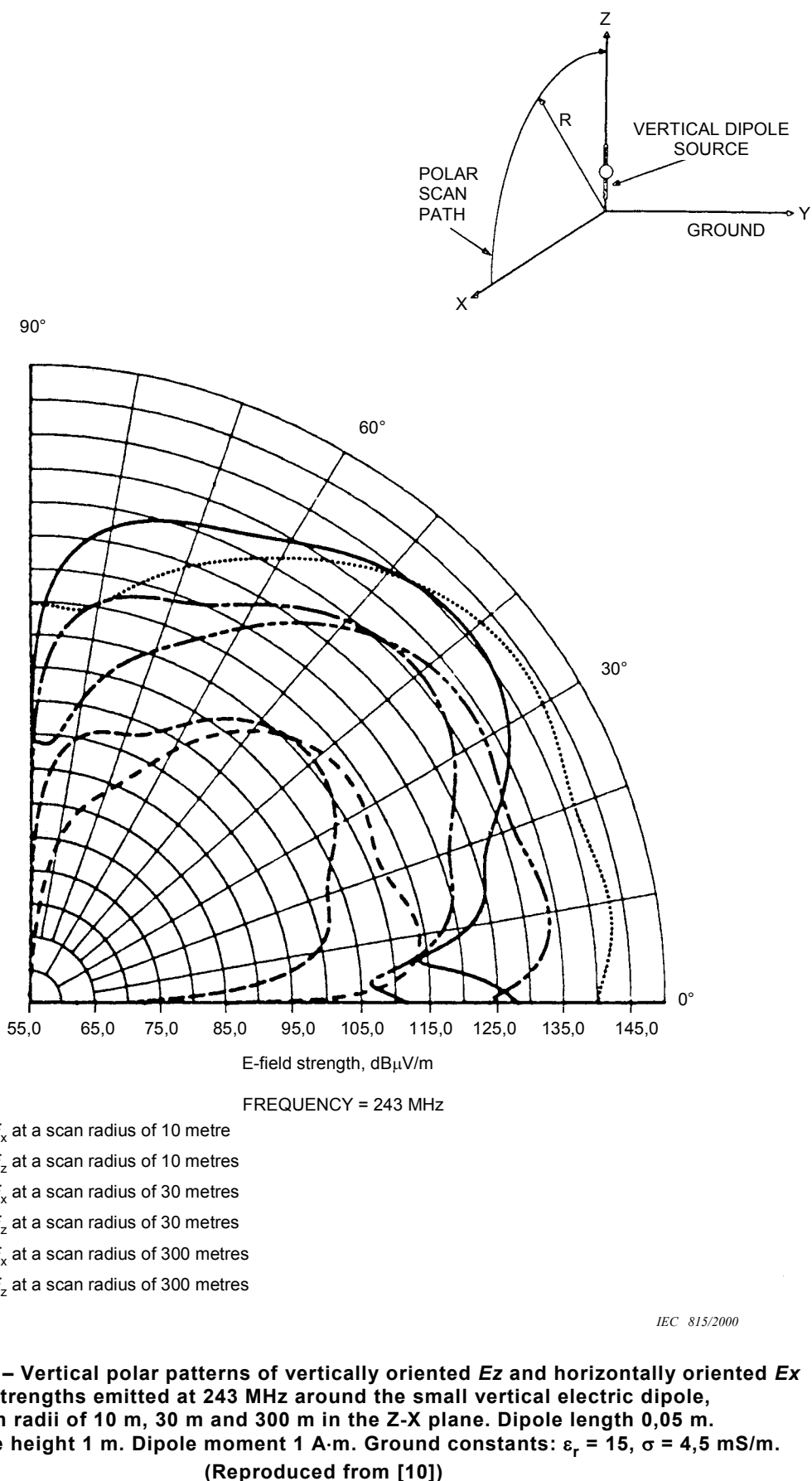


**Figure 4.5-5(b) – Height scan patterns of vertically oriented  $E_z$  and horizontally oriented  $E_x$  field strengths emitted at 110 MHz from the small vertical loop (horizontal magnetic dipole), at horizontal distances of 10 m, 30 m and 300 m, in the Z-X plane.**

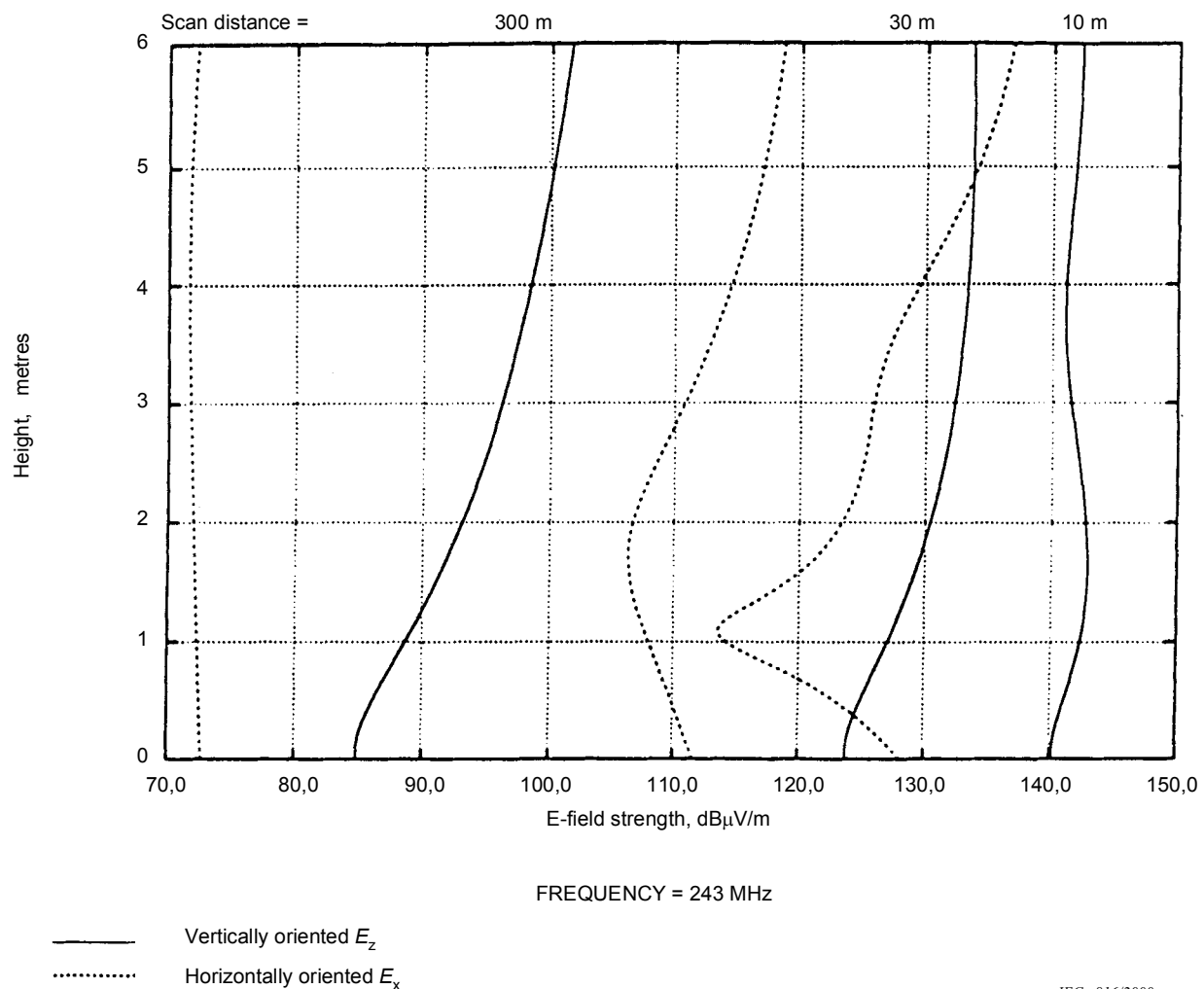
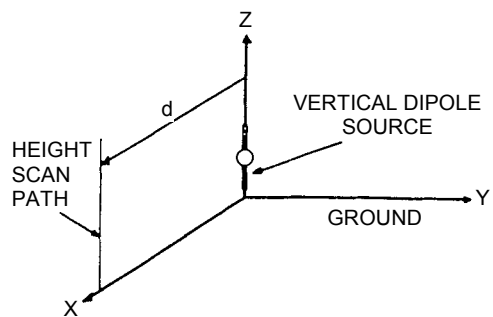
**Loop dimensions  $0,1 \text{ m} \times 0,1 \text{ m}$ . Loop centre height 2 m. Dipole moment  $1 \text{ A}\cdot\text{m}^2$ .**

**Ground constants:  $\epsilon_r = 15$ ,  $\sigma = 2 \text{ mS/m}$ .**

**(Reproduced from [10])**



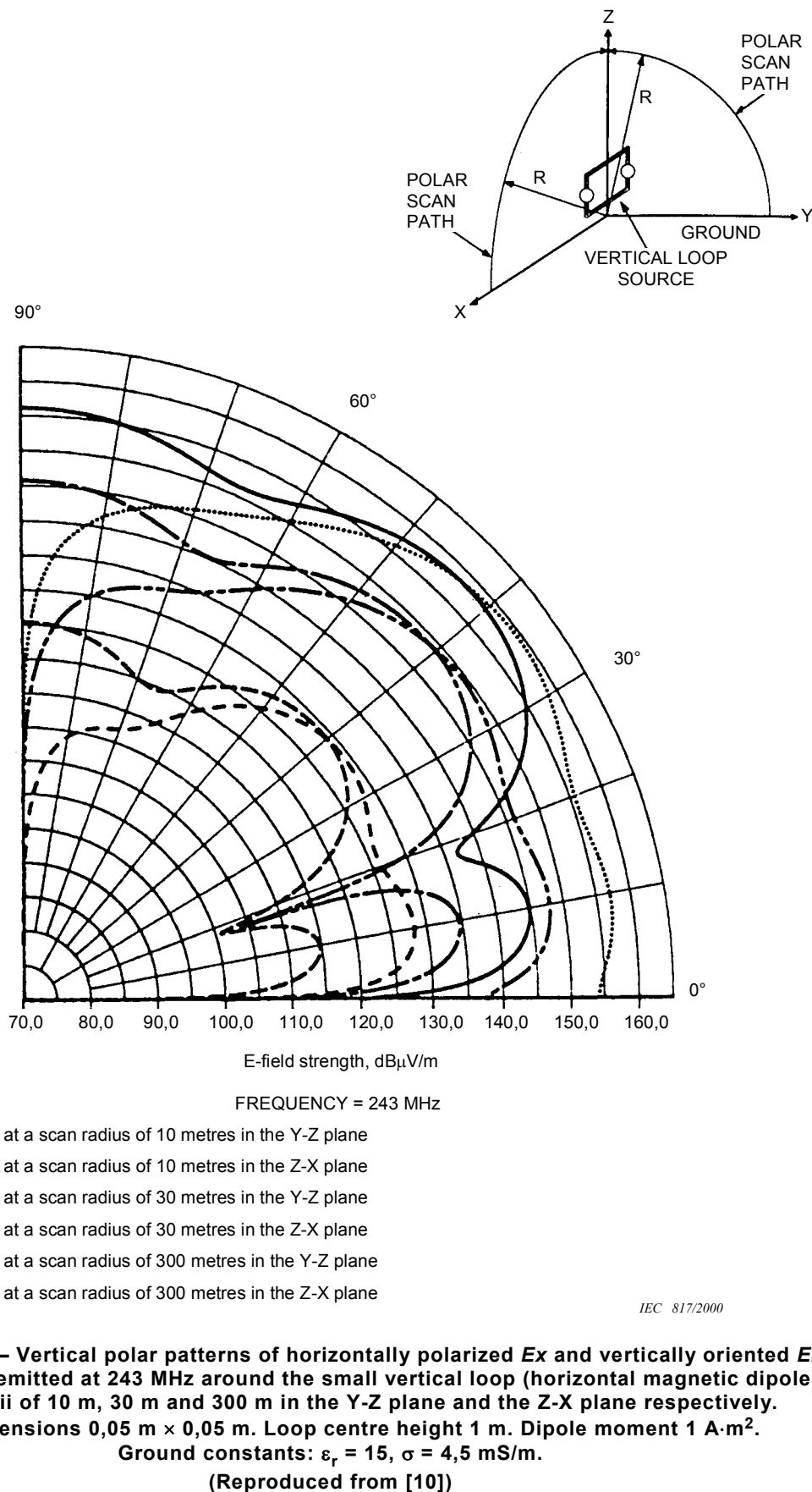
**Figure 4.5-6(a) – Vertical polar patterns of vertically oriented  $E_z$  and horizontally oriented  $E_x$  field strengths emitted at 243 MHz around the small vertical electric dipole, at scan radii of 10 m, 30 m and 300 m in the Z-X plane. Dipole length 0,05 m. Dipole centre height 1 m. Dipole moment 1 A·m. Ground constants:  $\epsilon_r = 15$ ,  $\sigma = 4,5 \text{ mS/m}$ .**  
**(Reproduced from [10])**

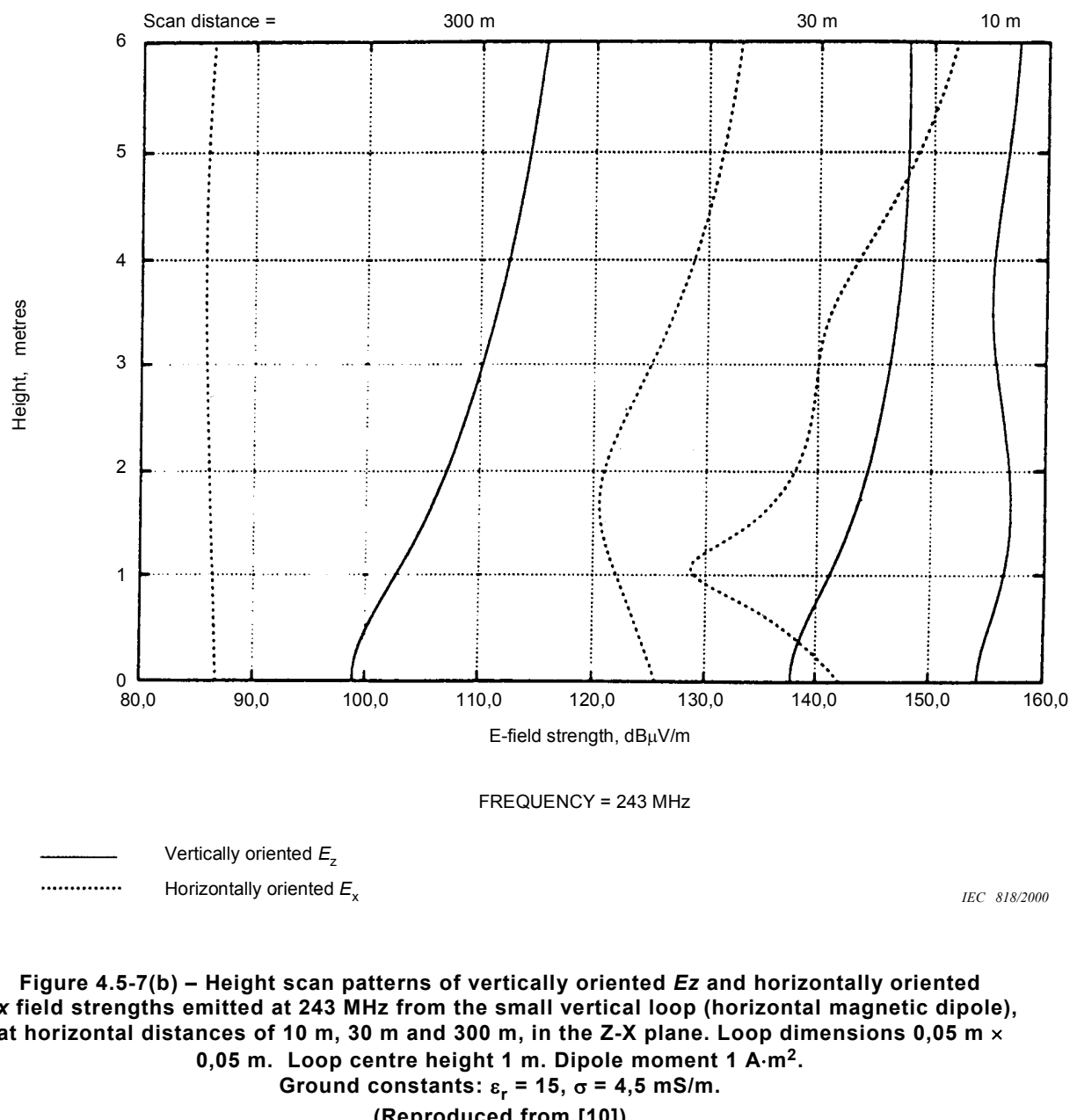
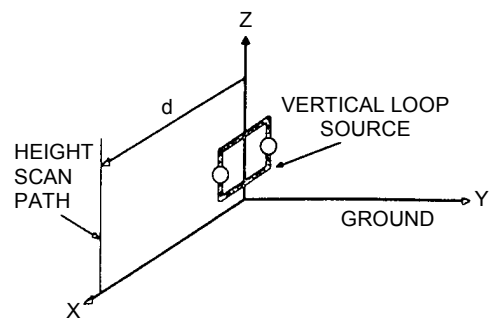


**Figure 4.5-6(b) – Height scan patterns of vertically oriented  $E_z$  and horizontally oriented  $E_x$  field strengths emitted at 243 MHz from the small vertical electric dipole, at horizontal distances of 10 m, 30 m and 300 m in the Z-X plane. Dipole length 0,05 m. Dipole centre height 1 m.**

Dipole moment 1 A·m. Ground constants:  $\epsilon_r = 15$ ,  $\sigma = 4,5 \text{ mS/m}$ .

(Reproduced from [10])





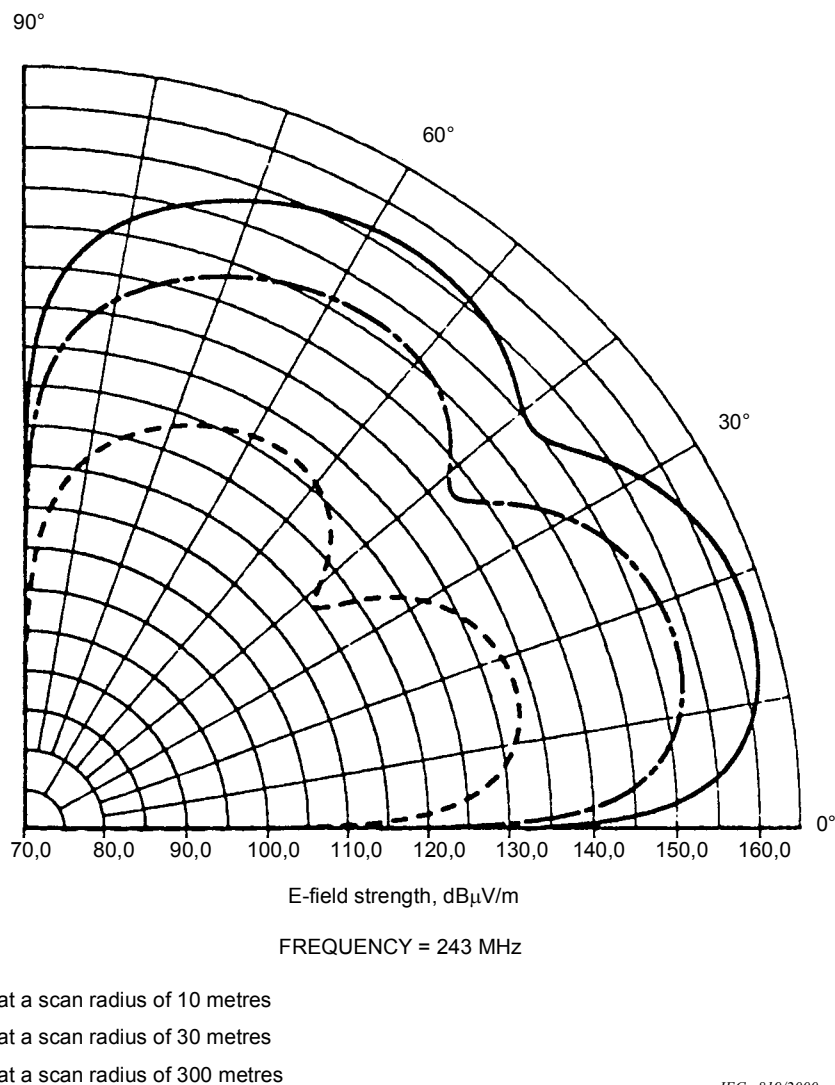
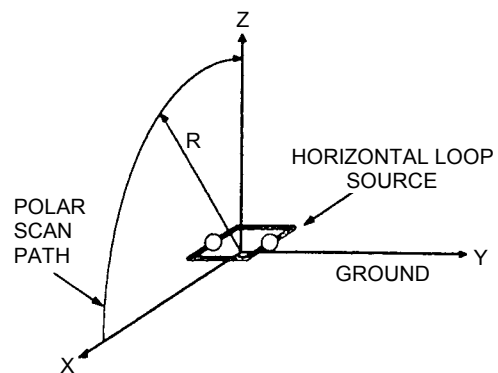
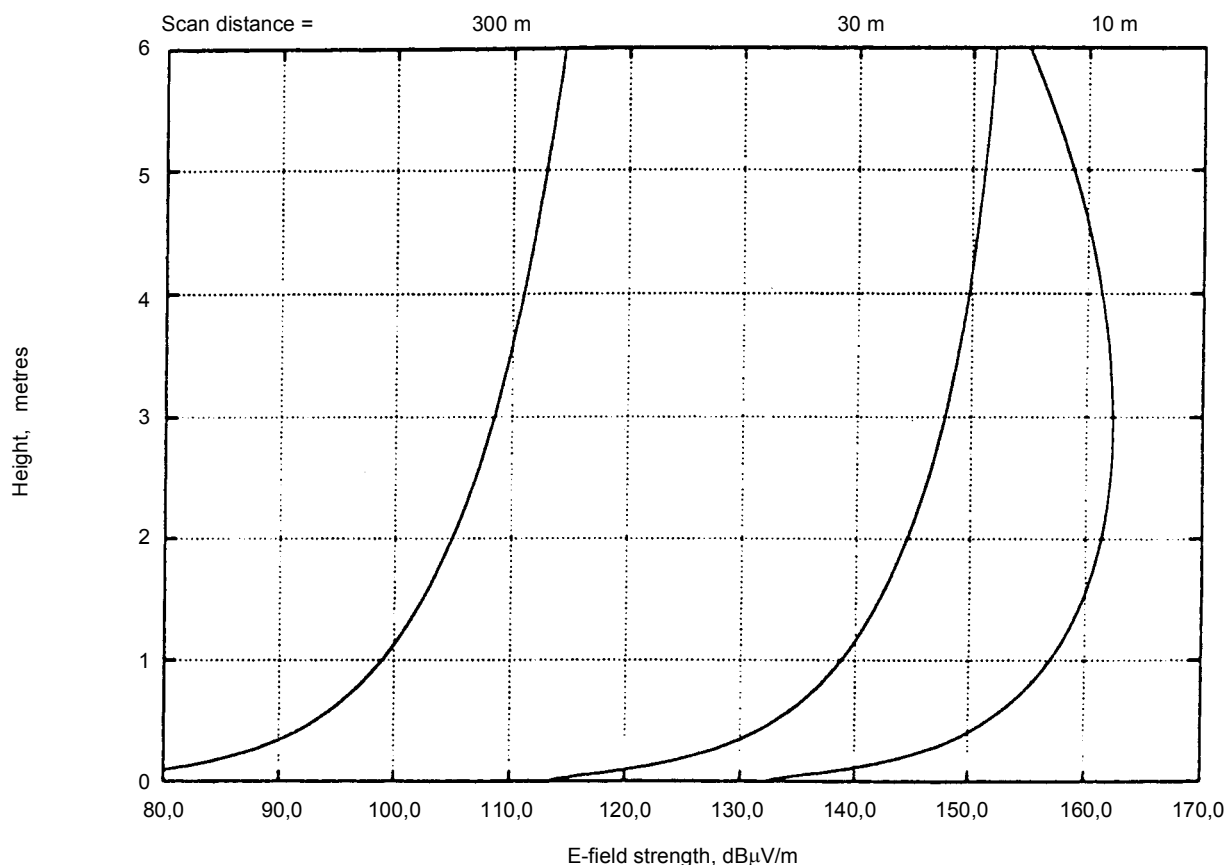
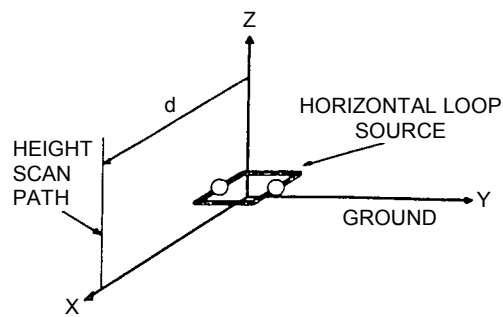


**Figure 4.5-8(a) – Vertical polar patterns of horizontally polarized  $E$ -field strength emitted at 243 MHz around the small horizontal loop (vertical magnetic dipole), at scan radii of 10 m, 30 and 300 m in the Z-X plane. Loop dimensions 0,05 m × 0,05 m. Loop height 1 m. Dipole moment 1 A·m<sup>2</sup>. Ground constants:  $\epsilon_r = 15$ ,  $\sigma = 4,5 \text{ mS/m}$ .**  
**(Reproduced from [10])**

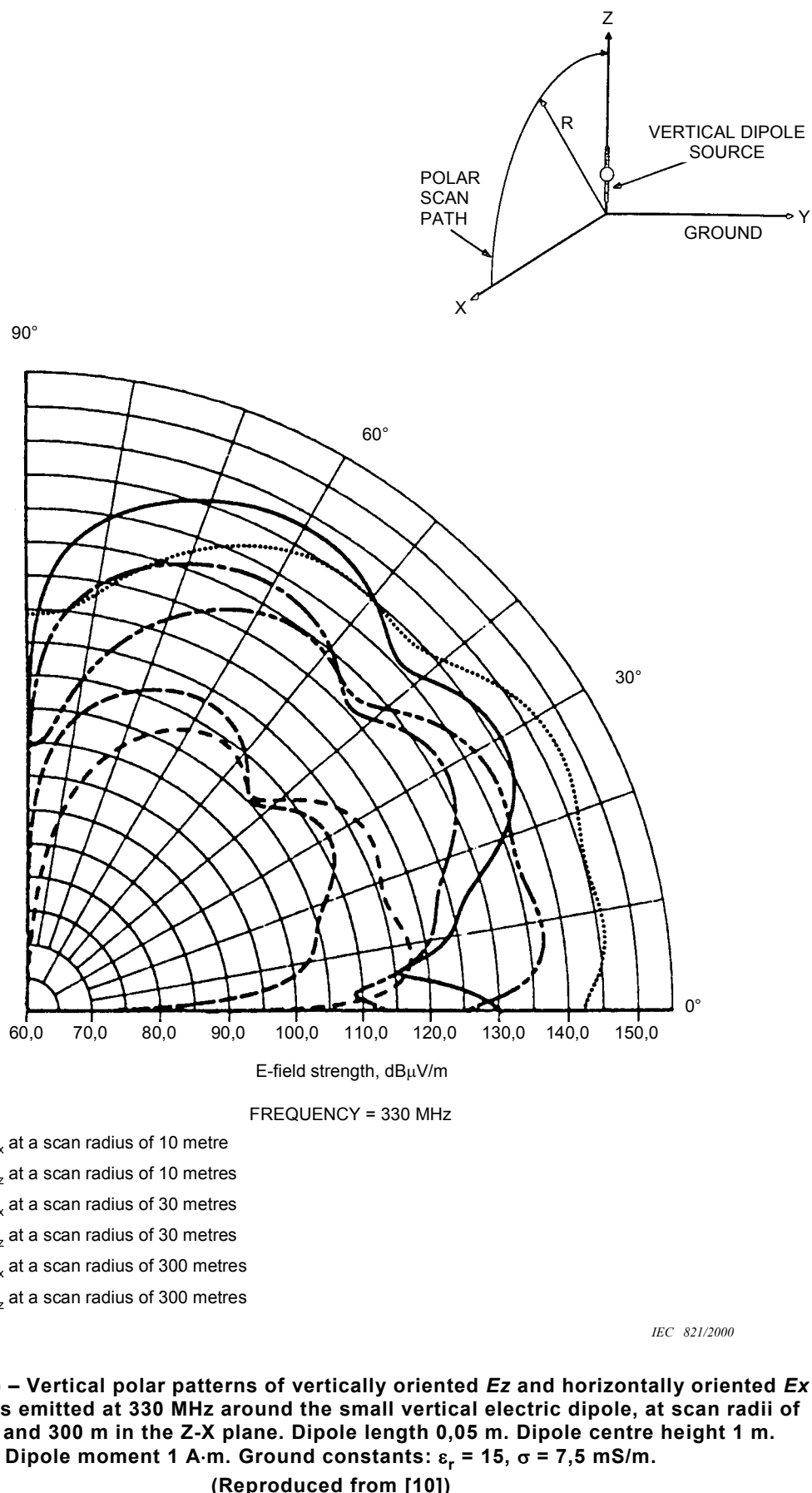


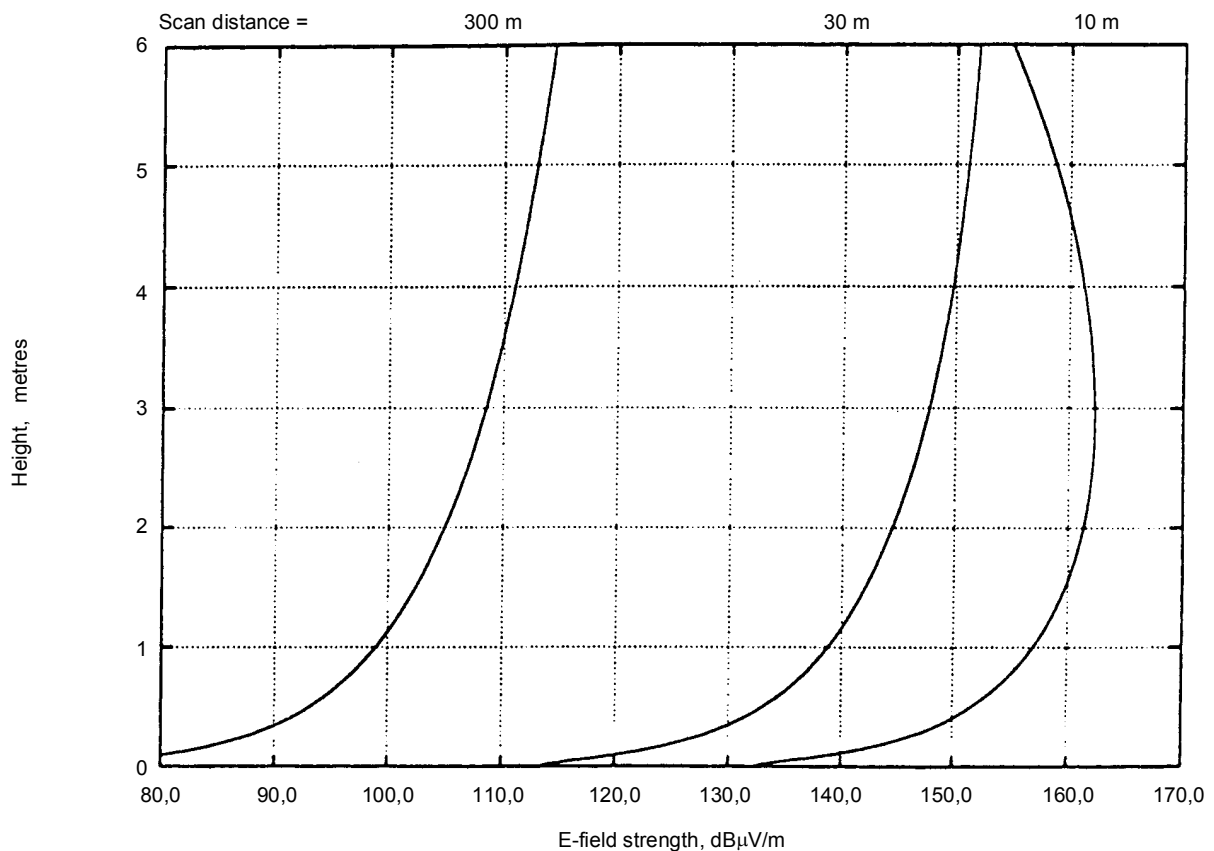
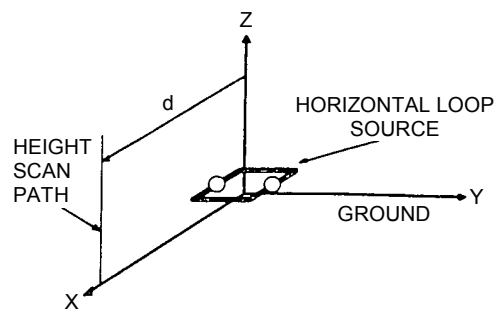
FREQUENCY = 243 MHz

IEC 820/2000

**Figure 4.5-8(b) – Height scan patterns of horizontally polarized  $E$ -field strength emitted at 243 MHz from the small horizontal loop (vertical magnetic dipole), at horizontal distances of 10 m, 30 m and 300 m in the Z-X plane. Loop dimensions  $0,05 \text{ m} \times 0,05 \text{ m}$ . Loop height 1 m. Dipole moment  $1 \text{ A} \cdot \text{m}^2$ . Ground constants:  $\epsilon_r = 15$ ,  $\sigma = 4,5 \text{ mS/m}$ .**

(Reproduced from [10])





FREQUENCY = 243 MHz

IEC 822/2000

**Figure 4.5-9(b) – Height scan patterns of vertically oriented  $E_z$  and horizontally oriented  $E_x$  field strengths emitted at 330 MHz from the small vertical electric dipole, at horizontal distances of 10 m, 30 m and 300 m in the Z-X plane. Dipole length 0,05 m. Dipole centre height 1 m.**

Dipole moment 1 A·m. Ground constants:  $\epsilon_r = 15$ ,  $\sigma = 7,5 \text{ mS/m}$ .  
(Reproduced from [10])

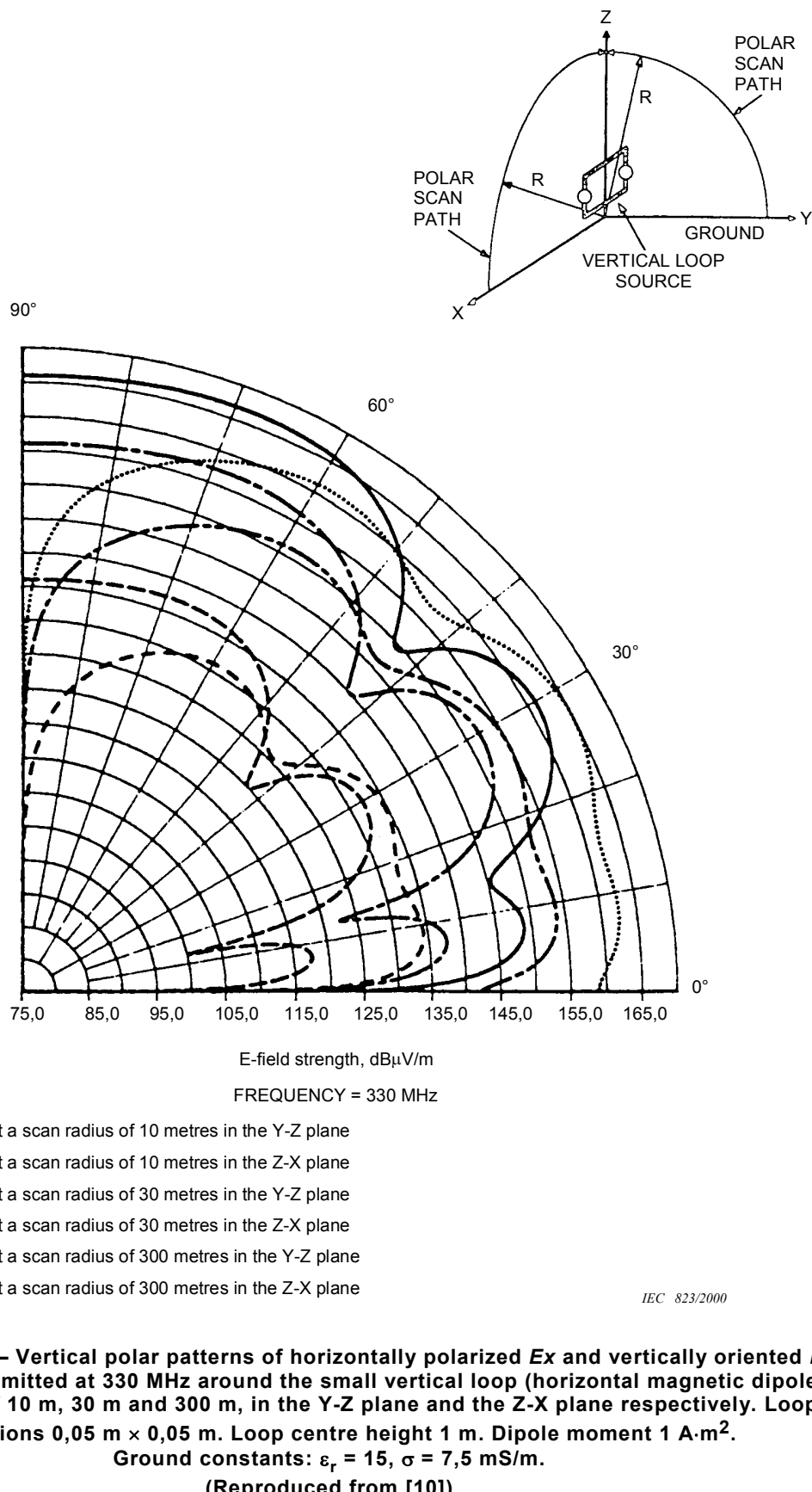


**Figure 4.5-10(a) – Vertical polar patterns of horizontally polarized  $E_x$  and vertically oriented  $E_z$  field strengths emitted at 330 MHz around the small vertical loop (horizontal magnetic dipole), at scan radii of 10 m, 30 m and 300 m, in the Y-Z plane and the Z-X plane respectively. Loop dimensions 0,05 m × 0,05 m. Loop centre height 1 m. Dipole moment 1 A·m<sup>2</sup>. Ground constants:  $\epsilon_r = 15$ ,  $\sigma = 7,5 \text{ mS/m}$ .**

(Reproduced from [10])

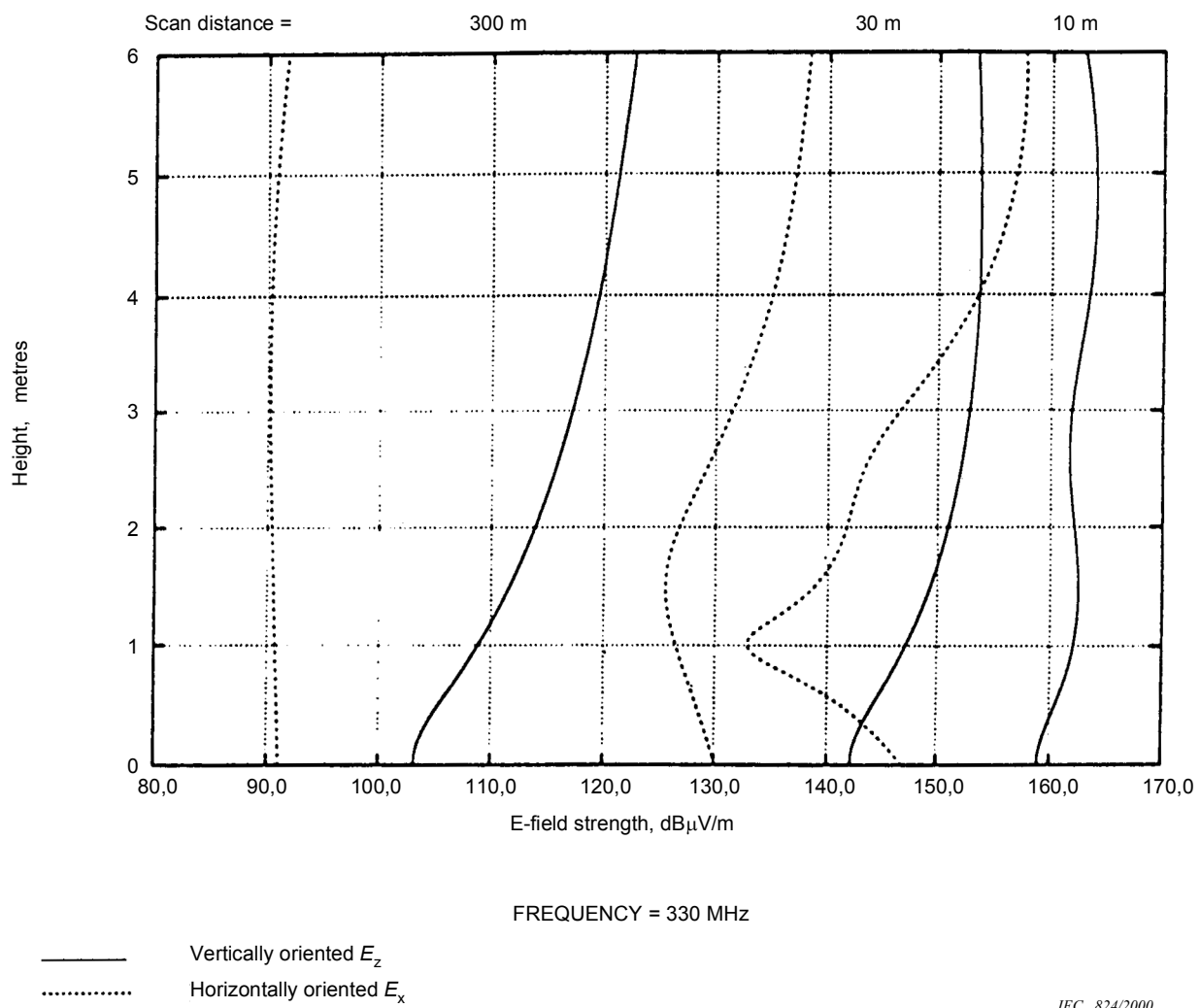
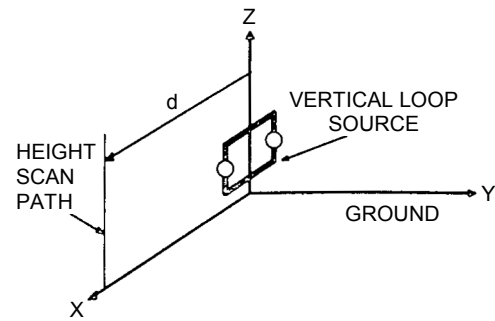


**Figure 4.5-10(b) – Height scan patterns of vertically oriented  $E_z$  and horizontally oriented  $E_x$  field strengths emitted at 330 MHz from the small vertical loop (horizontal magnetic dipole), at horizontal distances of 10 m, 30 m and 300 m in the Z-X plane.**

**Loop dimensions 0,05 m × 0,05 m. Loop centre height 1 m. Dipole moment 1 A·m<sup>2</sup>.**

**Ground constants:  $\epsilon_r = 15$ ,  $\sigma = 7,5 \text{ mS/m}$ .**

**(Reproduced from [10])**

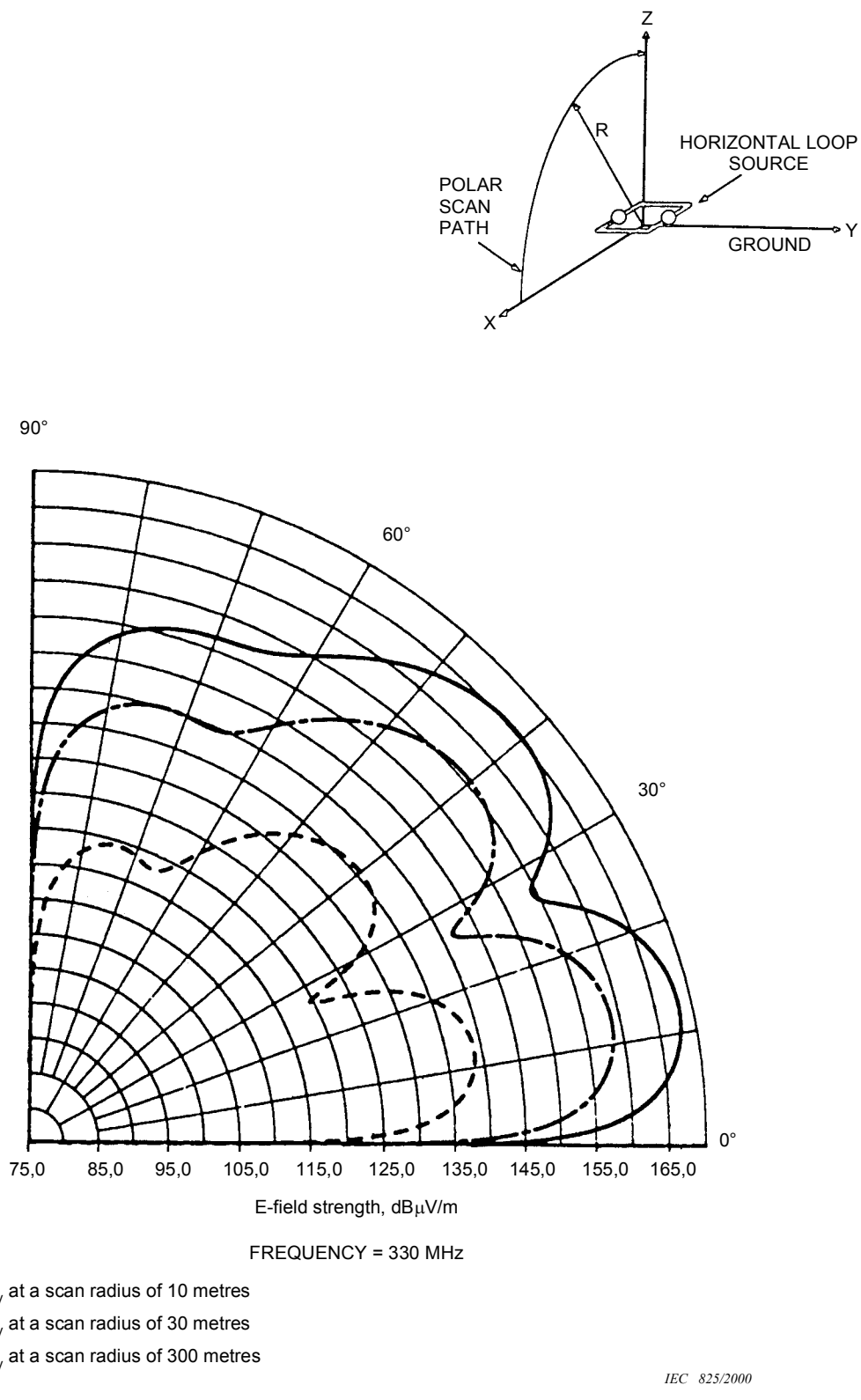
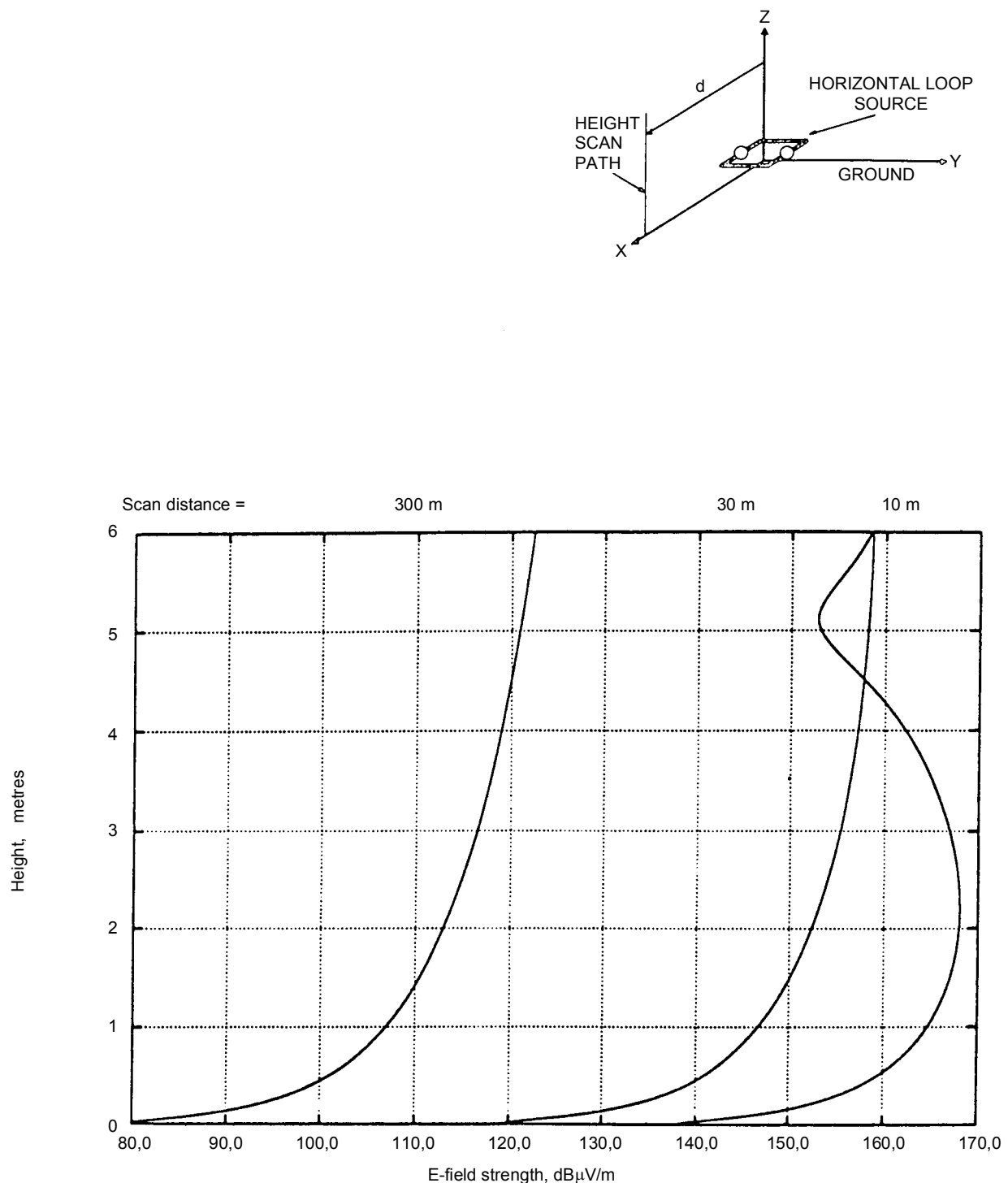


**Figure 4.5-11(a) – Vertical polar patterns of horizontally polarized E-field strength emitted at 330 MHz around the small horizontal loop (vertical magnetic dipole), at scan radii of 10 m, 30 m and 300 m in the Z-X plane. Loop dimensions 0,05 m × 0,05 m. Loop height 1 m. Dipole moment 1 A·m<sup>2</sup>. Ground constants:  $\epsilon_r = 15$ ,  $\sigma = 7,5 \text{ mS/m}$ .**  
**(Reproduced from [10])**



FREQUENCY = 330 MHz

IEC 827/2000

**Figure 4.5-11(b) – Height scan patterns of horizontally polarized  $E$ -field strength emitted at 330 MHz from the small horizontal loop (vertical magnetic dipole), at horizontal distances of 10 m, 30 m and 300 m in the Z-X plane. Loop dimensions 0,05 m  $\times$  0,05 m. Loop height 1 m. Dipole moment 1 A $\cdot$ m<sup>2</sup>. Ground constants:  $\epsilon_r = 15$ ,  $\sigma = 4,5$  mS/m.**  
**(Reproduced from [10])**

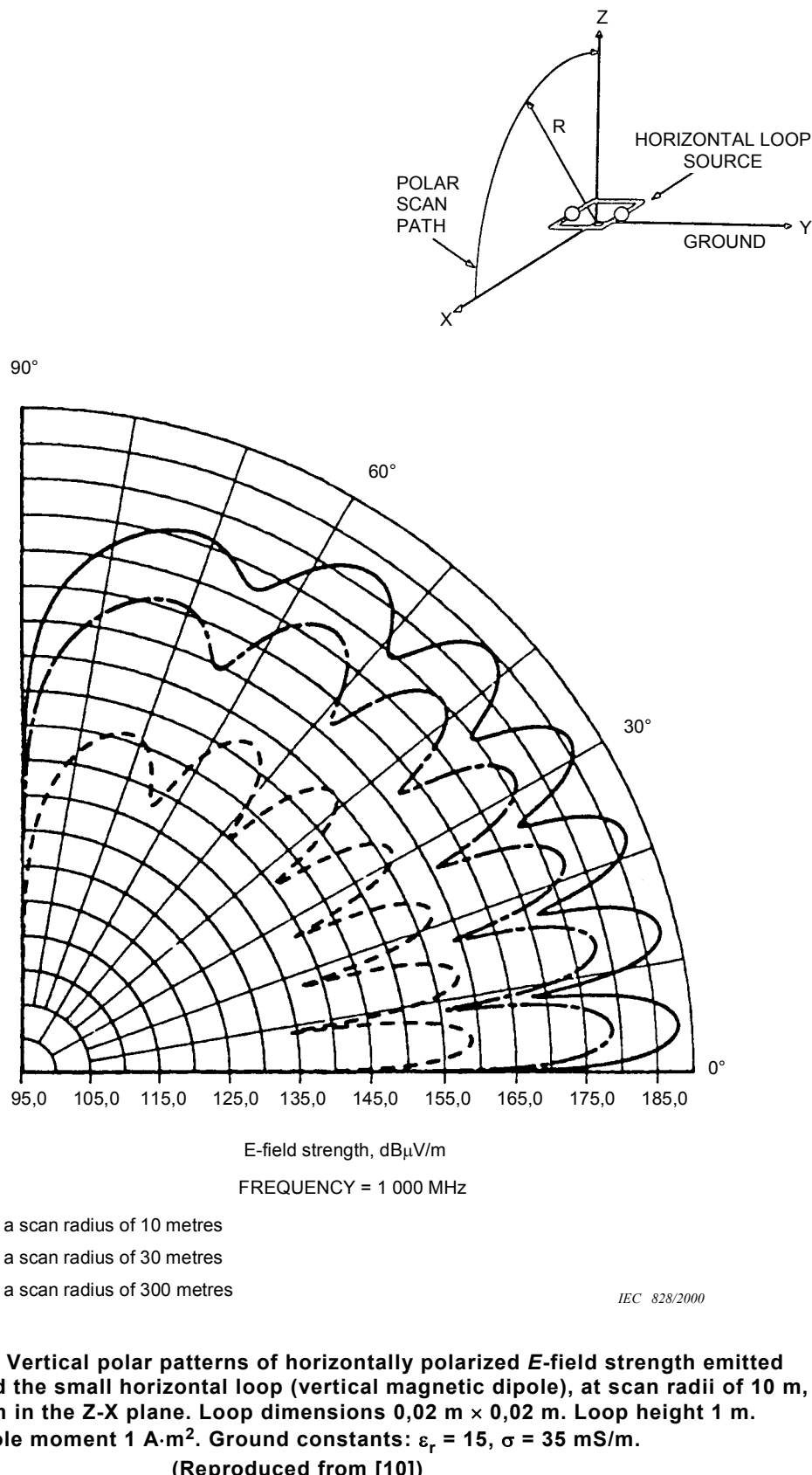


**Figure 4.5-12(a) – Vertical polar patterns of horizontally polarized  $E$ -field strength emitted at 1 000 MHz around the small horizontal loop (vertical magnetic dipole), at scan radii of 10 m, 30 m and 300 m in the Z-X plane. Loop dimensions 0,02 m × 0,02 m. Loop height 1 m. Dipole moment 1 A·m<sup>2</sup>. Ground constants:  $\epsilon_r = 15$ ,  $\sigma = 35$  mS/m.**  
**(Reproduced from [10])**

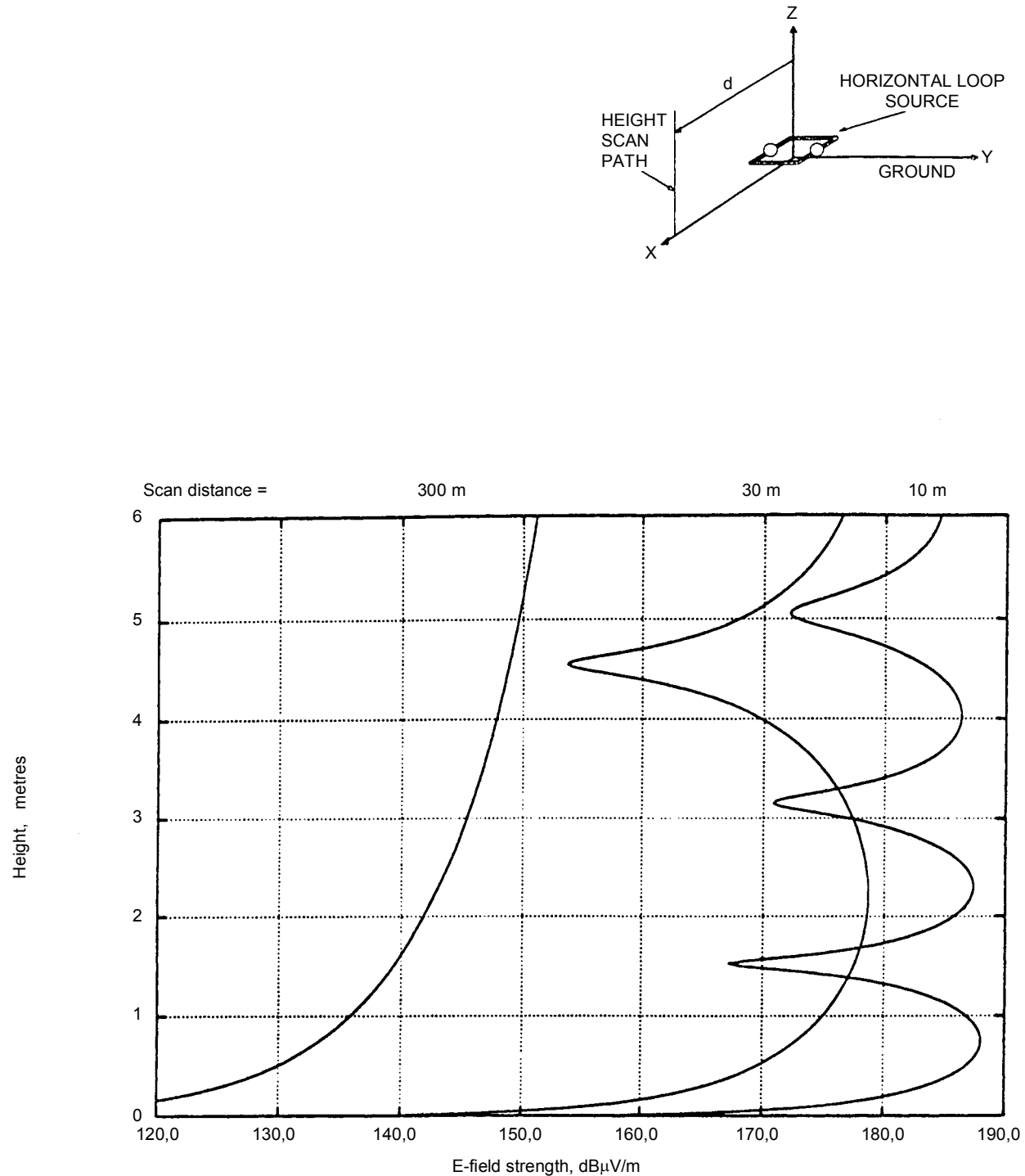


**Figure 4.5-12(b) – Height scan patterns of horizontally polarized  $E$ -field strength emitted at 1 000 MHz from the small horizontal loop (vertical magnetic dipole) at horizontal distances of 10 m, 30 m and 300 m in the Z-X plane. Loop dimensions  $0,02 \text{ m} \times 0,02 \text{ m}$ . Loop height 1 m.**

Dipole moment  $1 \text{ A}\cdot\text{m}^2$ . Ground constants:  $\epsilon_r = 15$ ,  $\sigma = 35 \text{ mS/m}$ .

(Reproduced from [10])

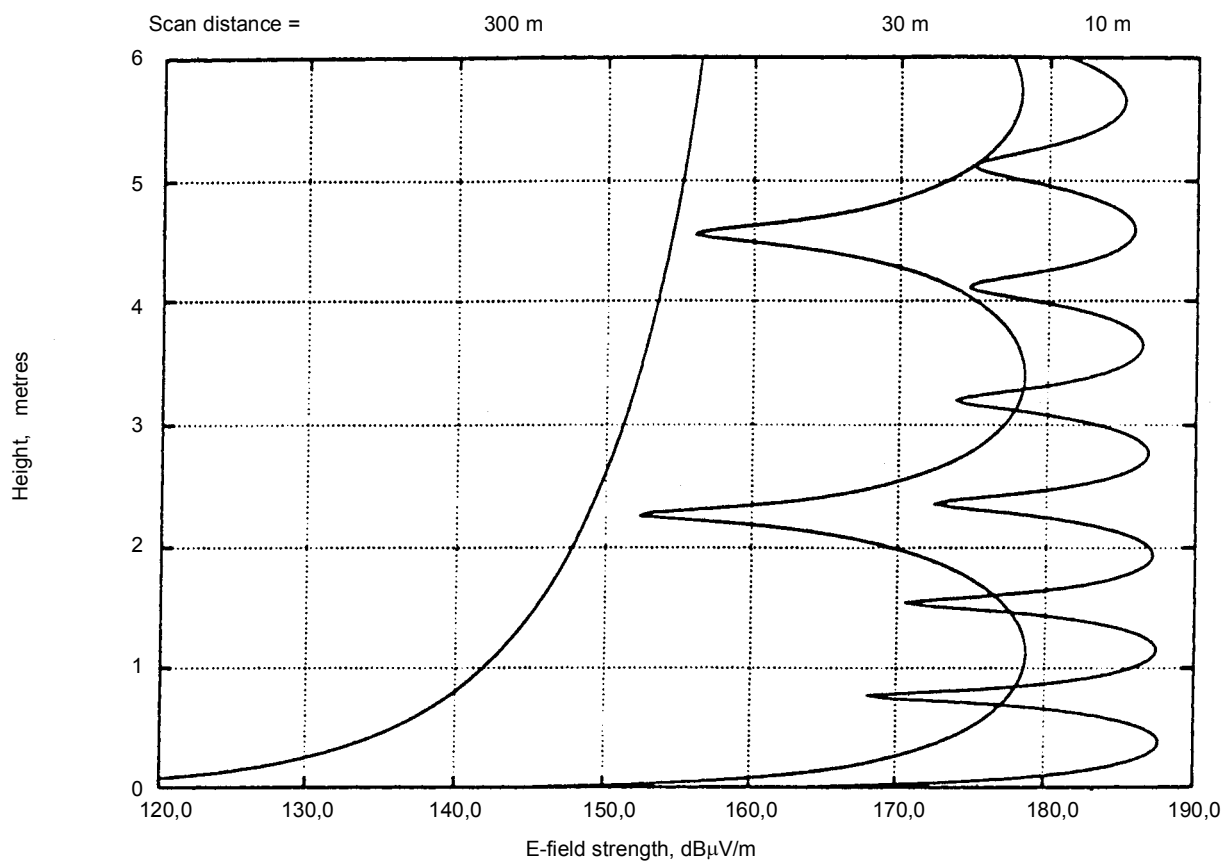
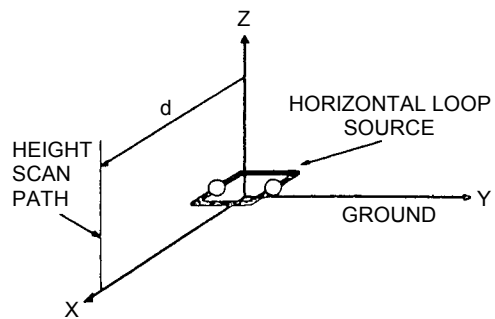


**Figure 4.5-13 – Height scan patterns of horizontally polarized  $E$ -field strength emitted at 1 000 MHz from the small horizontal loop (vertical magnetic dipole), at horizontal distances of 10 m, 30 m and 300 m in the Z-X plane. Loop dimensions  $0,02 \text{ m} \times 0,02 \text{ m}$ . Loop height 2 m. Dipole moment  $1 \text{ A}\cdot\text{m}^2$ . Ground constants:  $\epsilon_r = 15$ ,  $\sigma = 35 \text{ mS/m}$ .**  
**(Reproduced from [10])**

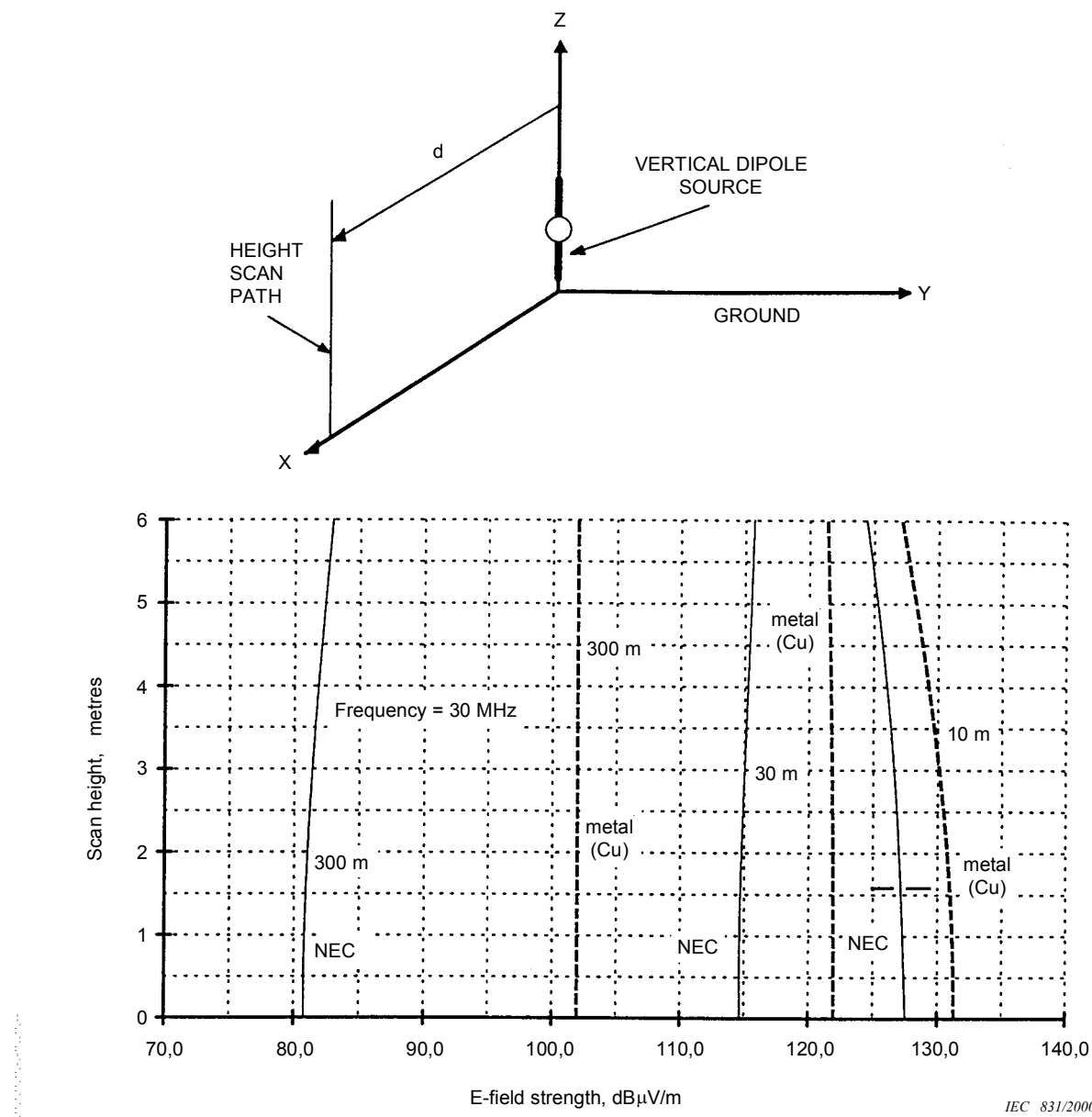


**Figure 4.5-14 – Height scan patterns of the vertical component of the  $E$ -fields emitted at 30 MHz from a small vertical electric dipole, at horizontal distances of 10 m, 30 m and 300 m.**  
**Fields calculated in NEC (solid lines) include the surface wave over real ground. Electrical constants used for the real ground plane were  $\epsilon_r = 15$ ,  $\sigma = 1 \text{ mS/m}$  ("medium dry ground"). The dashed curves were calculated geometrically to include the direct and reflected space waves from an infinitesimal vertical electric dipole over a metal ground plane. For the metal ground plane the electrical constants of copper were used, with  $\epsilon_r = 1$ ,  $\sigma = 5.81 \times 10^7 \text{ S/m}$ . Dipole moment = 1 A·m. Dipole centre height above ground = 1 m. In NEC the dipole length is 0.2 m.**  
**(Adapted from [11])**

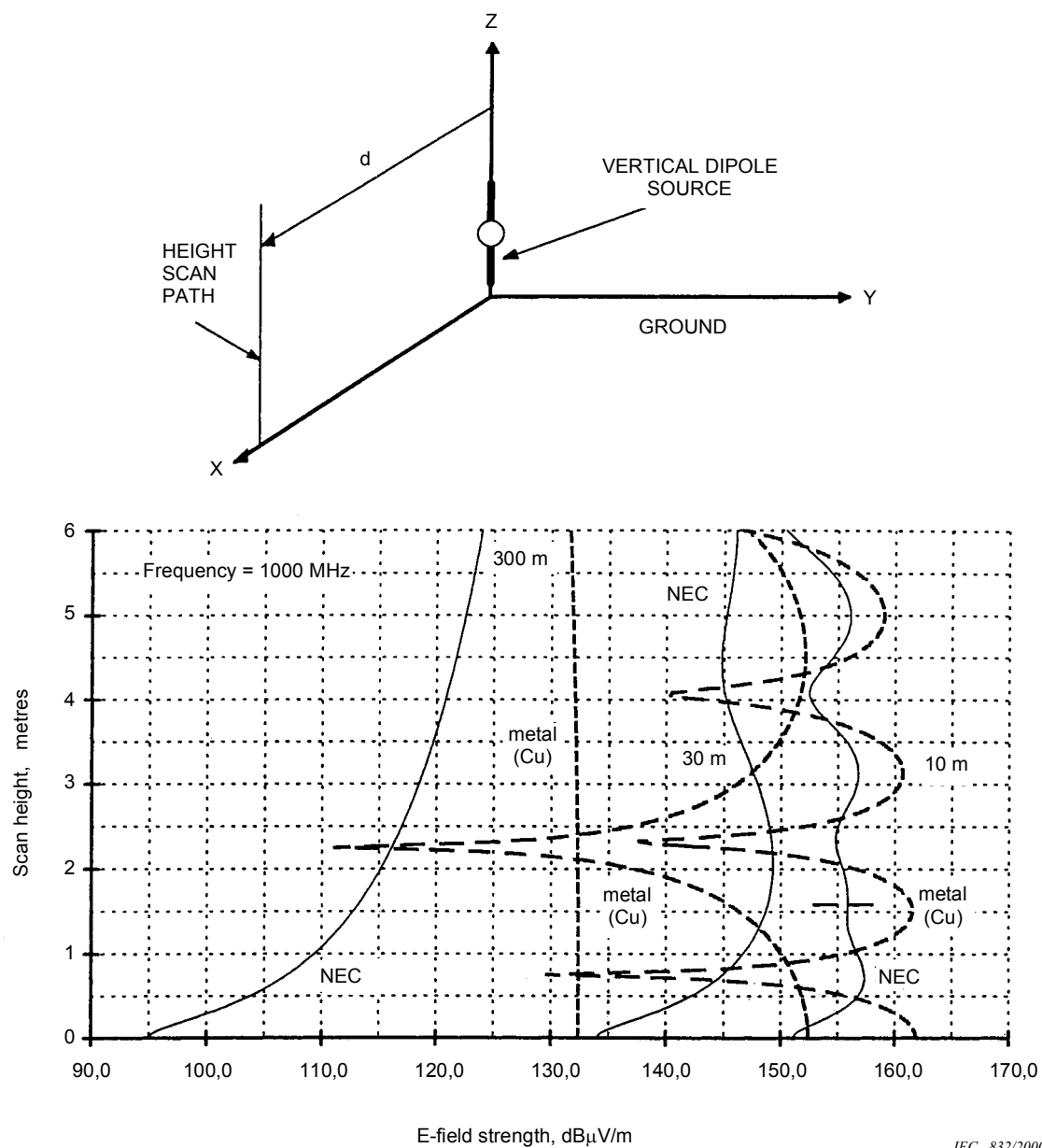


**Figure 4.5-15 – Height scan patterns of the vertical component of the  $E$ -fields emitted at 1 000 MHz from a small vertical electric dipole, at horizontal distances of 10 m, 30 m and 300 m. Fields calculated in NEC (solid lines) include the surface wave over real ground. Electrical constants used for the real ground plane were  $\epsilon_r = 15$ ,  $\sigma = 35 \text{ mS/m}$ . The dashed curves were calculated geometrically to include the direct and reflected space waves from an infinitesimal vertical electric dipole over a metal ground plane. For the metal ground plane the electrical constants of copper were used, with  $\epsilon_r = 1$ ,  $\sigma = 5,81 \times 10^7 \text{ S/m}$ .**

**Dipole moment = 1 A·m. Dipole centre height above ground = 1 m.**

**In NEC the dipole length is 0,02 m.**

**(Adapted from [11])**

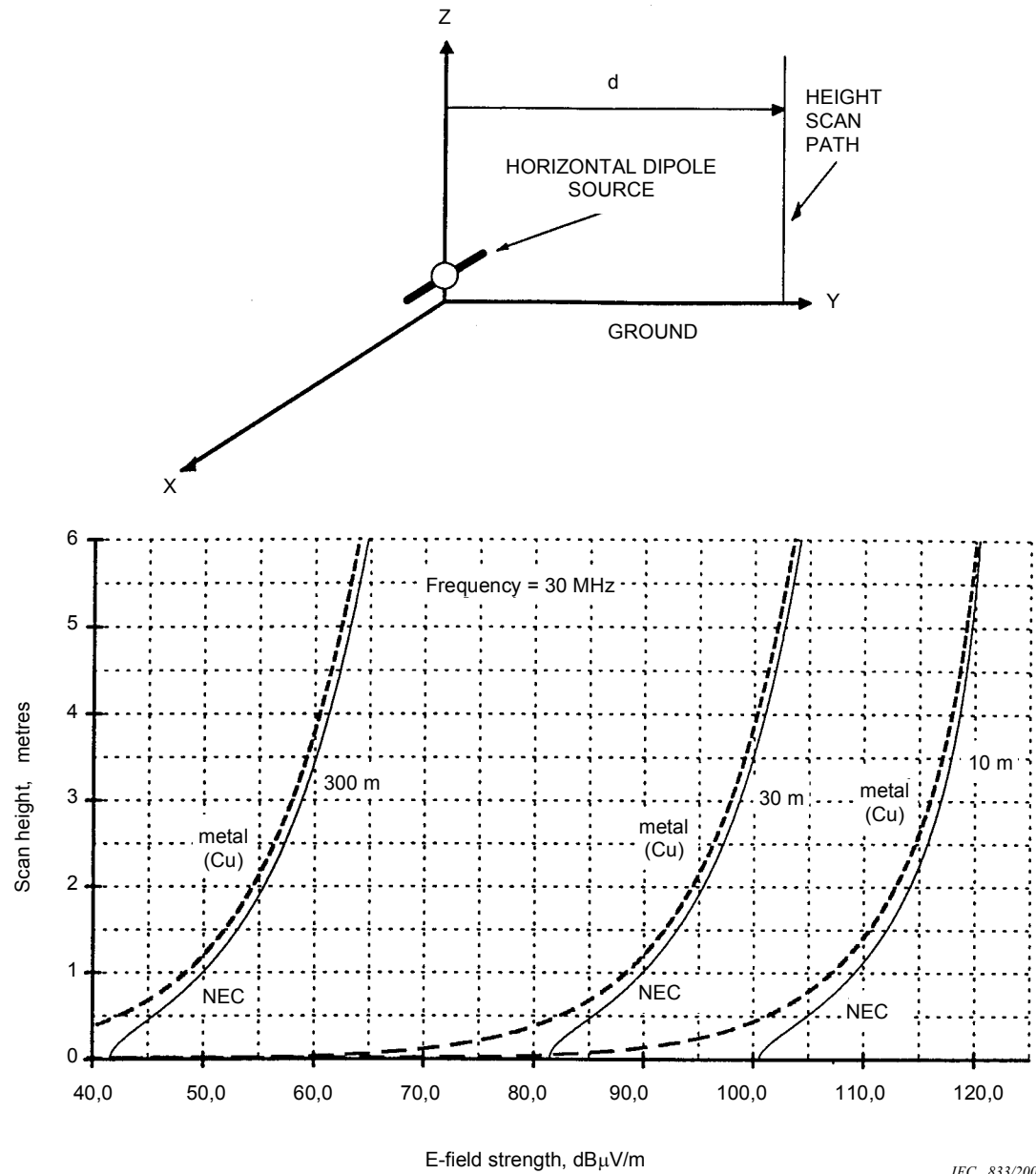


**Figure 4.5-16 – Height scan patterns of the horizontally polarized E-fields emitted at 30 MHz in the vertical plane normal to the axis of a small horizontal electric dipole, at horizontal distances of 10 m, 30 m and 300 m. Fields calculated in NEC (solid lines) include the surface wave over real ground. Electrical constants used for the real ground plane were  $\epsilon_r = 15$ ,  $\sigma = 1$  mS/m ("medium dry ground"). The dashed curves were calculated geometrically to sum the direct and reflected waves from an infinitesimal horizontal electric dipole over a metal ground plane. The electrical constants of copper were used for the metal ground plane,  $\epsilon_r = 1$ ,  $\sigma = 5,81 \times 10^7$  S/m. Dipole moment = 1 A·m. Dipole height above ground plane = 1 m.**

In NEC the dipole length is 0,2 m.  
(Adapted from [11])

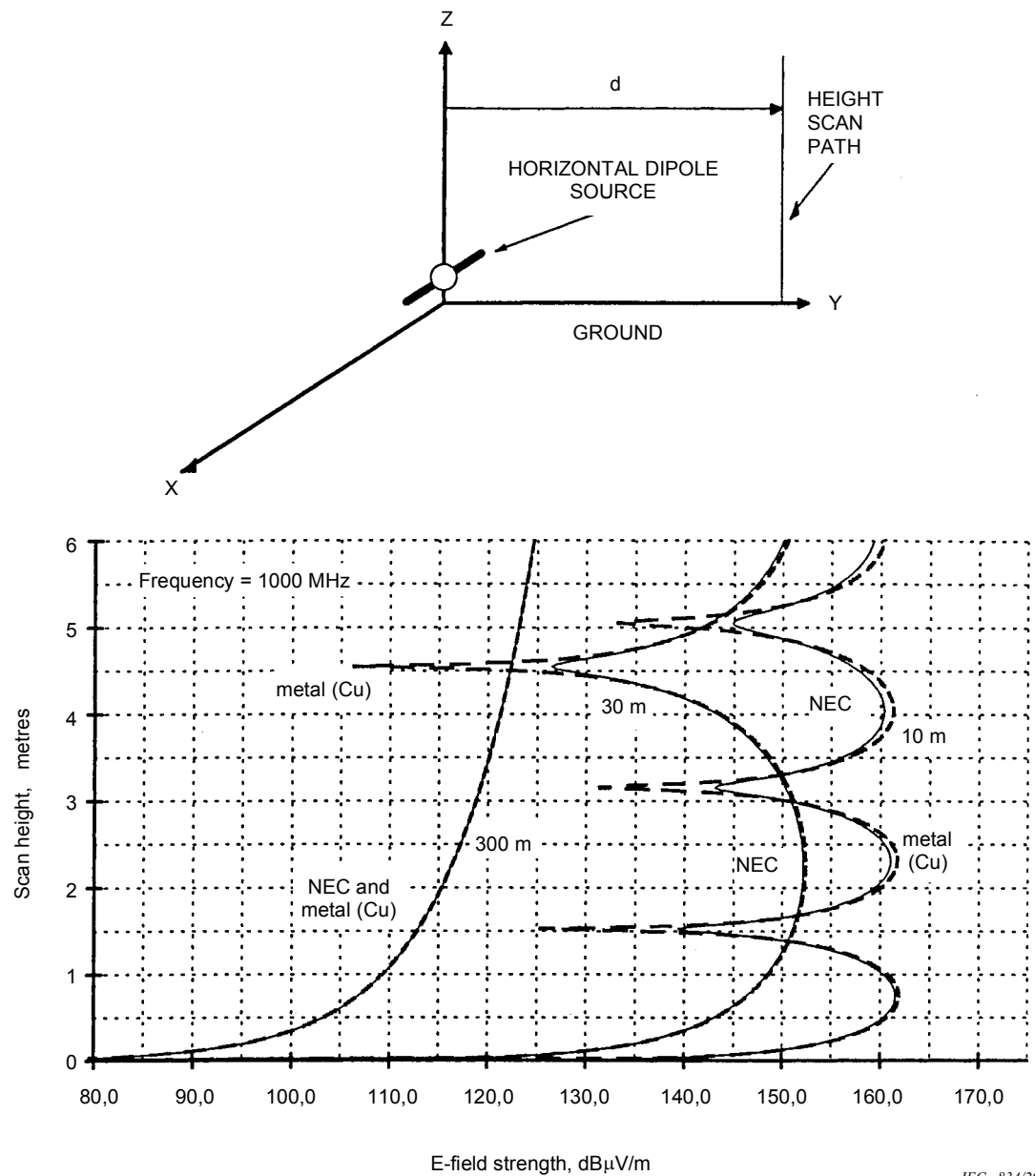
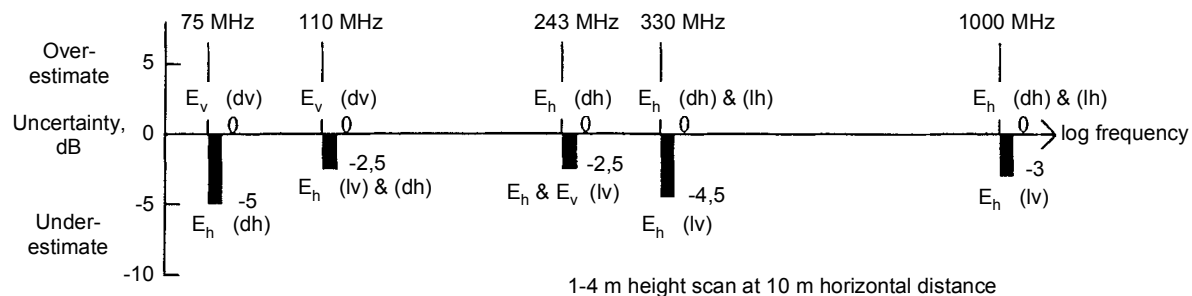


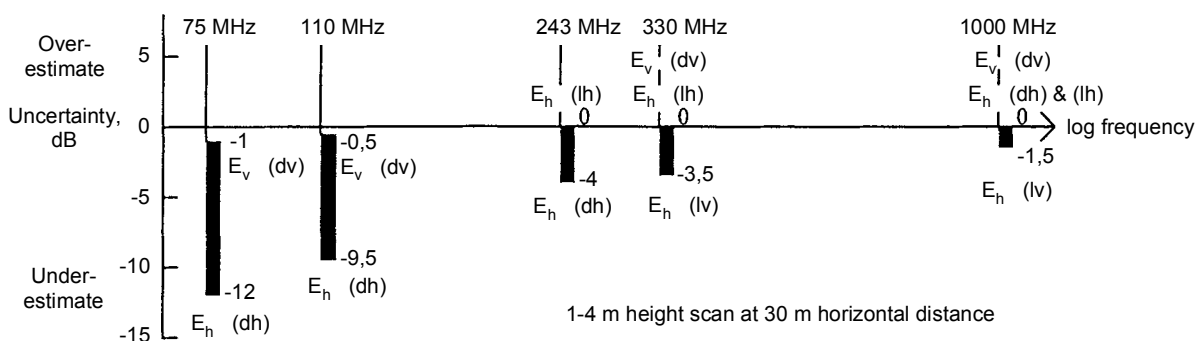
**Figure 4.5-17 – Height scan patterns of the horizontally polarized  $E$ -fields emitted at 1 000 MHz in the vertical plane normal to the axis of a small horizontal electric dipole, at horizontal distances of 10 m, 30 m and 300 m. Fields calculated in NEC (solid lines) include the surface wave over real ground. Electrical constants used for the real ground plane were  $\epsilon_r = 15$ ,  $\sigma = 35 \text{ mS/m}$  ("medium dry ground"). The dashed curves were calculated geometrically to sum the direct and reflected space waves from an infinitesimal horizontal electric dipole over a metal ground plane. The electrical constants of annealed copper were used for the metal ground plane,  $\epsilon_r = 1$ ,  $\sigma = 5,81 \times 10^7 \text{ S/m}$ . Dipole moment = 1 A·m. Dipole height above ground plane = 1 m. In NEC the dipole length is 0,02 m.**

(Adapted from [11])



IEC 6262000

**Figure 4.5-18 – Ranges of uncertainties in the predictability of radiation in vertical directions from electrically small sources located at a height of 1 m or 2 m above ground. The predictability is based on measurements of the horizontally and vertically polarized  $E$ -fields in a height scan from 1 m to 4 m at a horizontal distance of 10 m from the sources. The following example shows how the bar chart can be interpreted. At 243 MHz, the bar shows that the best predictability, with nominally zero error, is obtained when estimating the maximum strength of the horizontally polarized  $E_h$  field emitted at elevated angles from a source behaving as a small horizontal dipole (dh). The poorest predictability at 243 MHz, an underestimate by as much as 2.5 dB, can occur when predicting the maximum strengths of the horizontally polarized  $E_h$  fields and the  $E_z$  vertical component of the vertically polarized fields emitted at elevated angles from a source behaving as a small vertical loop (lv). (Reproduced from [10])**



IEC 6262000

**Figure 4.5-19 – Ranges of uncertainties in the predictability of radiation in vertical directions from electrically small sources located at a height of 1 m or 2 m above ground. The predictability is based on measurements of the horizontally and vertically polarized  $E$ -fields in a height scan from 1 m to 4 m at a horizontal distance of 30 m from the sources. The following example shows how the bar chart can be interpreted. At 330 MHz, the bar shows that the best predictability, with nominally zero error, is obtained when estimating the maximum strength of either the horizontally polarized  $E_h$  field emitted at elevated angles from a small horizontal loop (lh) or the  $E_z$  vertical component of the vertically polarized field emitted at elevated angles from a small vertical dipole (dv). But at 330 MHz the height scan measurements may provide an underestimate by as much as 3.5 dB when predicting the strength of the horizontally polarized  $E_h$  field, which is the maximum field emitted at elevated angles from a source behaving as a small vertical loop (lv) (Reproduced from [10])**

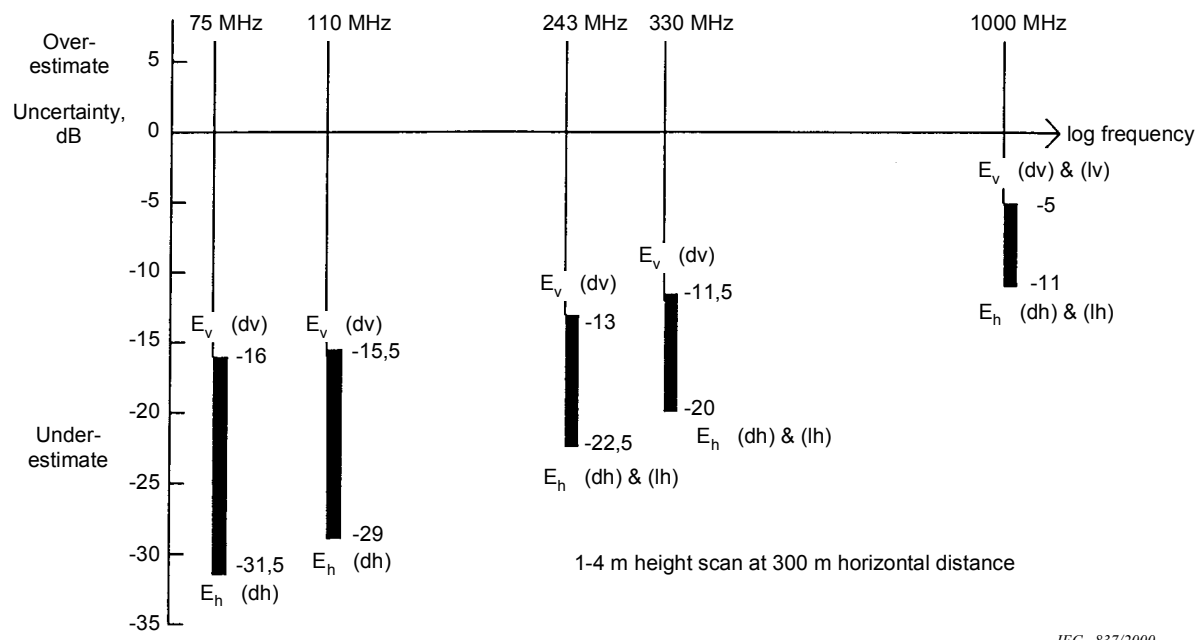


**Figure 4.5-20 – Ranges of uncertainties in the predictability of radiation in vertical directions from electrically small sources located at a height of 1 m or 2 m above ground. The predictability is based on measurements of the horizontally and vertically polarized  $E$ -fields in a height scan from 1 m to 4 m at a horizontal distance of 300 m from the sources. The following example shows how the bar chart can be interpreted. The bar at 1 000 MHz shows that the best predictability at that frequency, which is an underestimate by as much as 5 dB, will be obtained when predicting the maximum strength of the  $E_z$  vertical component of the vertically polarized field emitted at elevated angles from a source behaving as a small vertical loop (lv) or a small vertical dipole (dv). However, an underestimate by as much as 11 dB can occur at 1 000 MHz when predicting the maximum strength of the horizontally polarized  $E_h$  field emitted at elevated angles from a source behaving as a small horizontal loop (lh) or a small horizontal dipole (dh). (Reproduced from[10])**

## Annex 4.5-A

### Harmonic fields radiated at elevated angles from 27 MHz ISM equipment over real ground

A close match can be achieved between vertical radiation patterns calculated for simple electrically small electric dipoles and loops over real ground and the vertical radiation patterns created by real ISM equipment. This can be shown using airborne data, measured by Ohio University, of the harmonic field strengths from four different 27 MHz ISM machines positioned at ground level on an earthen open field site [4]. Each ISM machine was a RF plastics sealer, identified by a letter symbol A, B, C or D. Fundamental operating powers ranged from 2 kW to 27 kW. In [5], the horizontally polarized fourth harmonic field-strength data at approximately 109 MHz, collected by an aircraft flying at constant height and varying slant range, were converted to field strengths in vertical polar radiation patterns at a constant radial distance of 300 m, at elevation angles varying from approximately 4° up to 90°. The resultant far-field vertical radiation patterns were then compared with vertical radiation patterns calculated at the same distance from small electric dipoles and loops over real ground. The objective was to meet a tolerance of fit which was arbitrarily chosen as ±10 dB. The comparisons show that the vertical radiation patterns of harmonic radiation from ISM equipment, at 109 MHz in the aeronautical ILS localizer band, closely resemble the patterns calculated for simple dipoles and loops.

The in-flight field strength data gathered at varying slant distances from the ISM equipment were converted to vertical radiation patterns using the simple inverse distance law of attenuation in equation (4.5-A1)

$$E_{300} \text{ (dB}\mu\text{V/m)} = E_d \text{ (dB}\mu\text{V/m)} + 20 \log_{10} \left( \frac{d_s}{300} \right) \quad (4.5\text{-A1})$$

where

$E_d$  is the field strength measured at the aircraft at a particular elevation angle;

$d_s$  is the slant distance to the aircraft at that elevation angle;

$E_{300}$  is the calculated field strength at 300 m radial distance at the same elevation angle.

The values of  $E_{300}$  have been plotted against elevation angle to create two vertical radiation patterns for each flight. One vertical radiation pattern has been created for that part of the flight which took place to the south of the ISM device and another for that part of the flight which took place to the north of the ISM device. Each pattern therefore extends up to an elevation angle of 90°, which locates the common field point between the two patterns.

Sommerfeld-Norton surface wave contributions to the horizontally polarized fields at very low elevation angles have also been considered inasmuch as their presence might have complicated the adjustment with distance of the measured field strengths at those low angles. Surface waves at frequencies above 30 MHz have been studied in [11]. In [11] it is shown that at the distances and heights over ground at which the in-flight data were gathered, the contributions of surface waves are insignificant.

Figure 4.5-A1 illustrates vertical patterns of horizontally polarized fourth harmonic radiation from ISM Machine A (a 25 kW RF plastic sealer) with its RF shields removed, calculated from the data in [4] using equation (4.5-A1) and shown as solid line curves, compared with vertical patterns of horizontally polarized radiation calculated at 109 MHz for two electrically small horizontal electric dipoles (dashed curves). The in-flight field strength data were obtained at a flight altitude of 152 m (500 feet) and plotted in figure A-4, page 54 of reference [4].

The sharp step in the field strength from Machine A close to the elevation angle of 5° in figure 4.5-A1(b) corresponds with the switch-on of the ISM equipment. Note that, to match the patterns of the fields measured to the south of the ISM equipment, the dipole current moment  $I.dI$ , the dipole height above ground, and the radiated power required from the small electric dipole, are all different from those required to match the fields measured to the north.

Figure 4.5-A2 uses in-flight data for ISM Machine B operated with RF shields in place, collected at an altitude of 152 m. In figure 4.5-A2(b) the noise floor of the measurements is visible in the solid curve for elevation angles between 12° and 20°. Switch-on of the ISM equipment occurred near the elevation angle of 20°. Note that the horizontally polarized vertical field patterns created broadside to two electrically small vertical loops were used to provide the matching patterns in figure 4.5-A2. The dipole moments required were the same, but the source height and therefore the radiated power required to match the patterns to the north were different from those required to match the patterns to the south.

Figure 4.5-A3 compares the radiation at 109 MHz emitted from Machine C (a 3 kW RF plastics sealer), derived from in-flight data measured at an altitude of 152 m, with the calculated horizontally polarized field patterns for two small horizontal electric dipoles. Machine C was operated with its RF shields in place. The sharp step in the Machine C field strength close to the elevation angle of 20° in figure 4.5-A3(b) corresponds with the switch-on of the ISM equipment. The match in figure 4.5-A3(a) was obtained with a small horizontal electric dipole at a height of 2.7 m, slightly higher than the 2 m maximum source height considered elsewhere in this report.

Examples of pattern matching for ISM Machine D (a 2 kW RF plastic sealer), with its RF shields in place, are shown in figure 4.5-A4. In this example the horizontally polarized fields emitted broadside from two small vertical loops were used to provide the matching patterns. The match in figure 4.5-A4(a) was obtained using an electrically small vertical loop at a centre height of 0.85 m, slightly lower than the 1 m minimum source height considered elsewhere in this paper. Switch-off of the ISM equipment is shown by the field strength step near the elevation angle of 5° in figure 4.5-A4(a).

The figures all show how variable the field strengths of the disturbances radiated from ISM equipment can be during short periods of time. Each data gathering flight took place at an air speed of approximately 135 knots [5], from north to south over the ISM equipment. Only one ISM equipment operating cycle of approximately 1 min duration occurred during each flight.

However, after examination of the vertical radiation patterns, it can be concluded that – in spite of the field strength fluctuations – the horizontally polarized field distribution encountered by an aircraft at elevated angles, during any single flight pass over the ISM equipment, can be reasonably well matched (within  $\approx \pm 10$  dB) with field distributions created at elevated angles by simple electric or magnetic dipole sources. Given the relatively good match of the simple model patterns with the measured fields at angles above about 4°, and the boundary conditions which reduce the strength of the horizontally polarized fields near the ground, the patterns of the fields of the simple models calculated near the ground will be similar to the patterns of the real fields if they were measured at elevation angles below 4° (see [11]). These results support the belief that the predictability of far field radiation emitted at elevated angles by ISM equipment *in situ* can be judged by considering the vertical patterns of radiation emitted by simple electric and magnetic dipoles near the ground.

Moreover, there seems to be no obvious reason why vertically polarized fields emitted by typical ISM equipment should behave differently from the vertically polarized fields emitted over ground by small dipoles. Such small dipole models should also serve to indicate the predictability of vertically polarized fields.

More detailed studies of the measurements reported by the Avionics Engineering Center at Ohio University [4], and many more examples of matching the measured data with vertical patterns calculated for electrically small electric or magnetic dipole sources, have been described in [5]. Figures 4.5-A1 to 4.5-A4 are adapted from figures in [5].

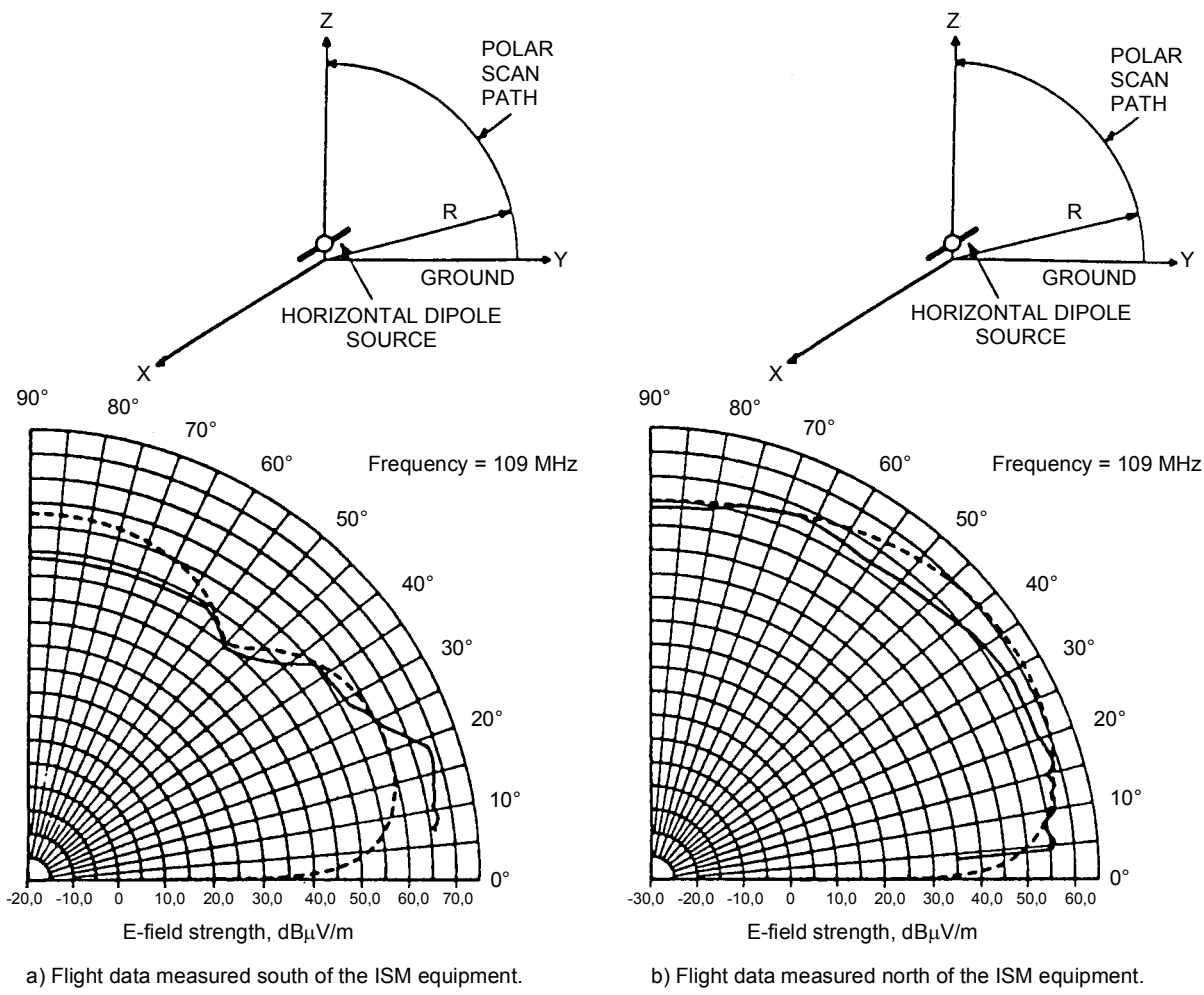
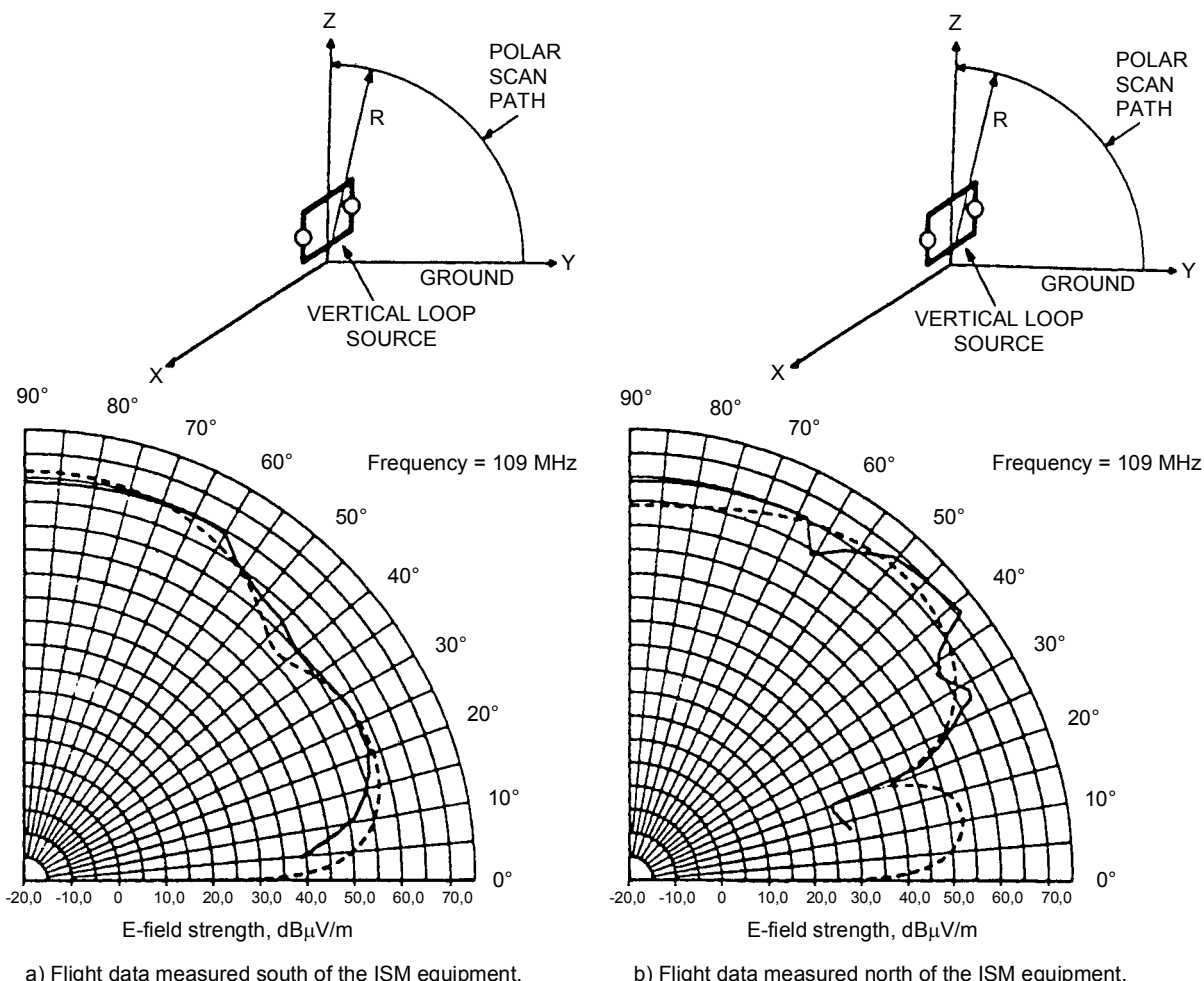


**Figure 4.5-A1 – Vertical radiation patterns of horizontally polarized fields, 109 MHz, 300 m scan radius (Adapted from [5])**

- Solid curves: Machine A (fundamental RF power 25 kW), 180° azimuth, flight altitude 152 m, RF shields removed, derived from in-flight field strength data in figure A-4 at page 54 in [4].
- a) Dashed curve: Source = horizontal electric dipole, centre height above ground 1,8 m, dipole (current) moment  $I.dI \approx 2,51$  mA·m, radiated power  $\approx 704$   $\mu$ W.
- b) Dashed curve: Source = horizontal electric dipole, centre height above ground 1,3 m, dipole (current) moment  $I.dI \approx 2,82$  mA·m, radiated power  $\approx 996$   $\mu$ W.

IEC 838/2000

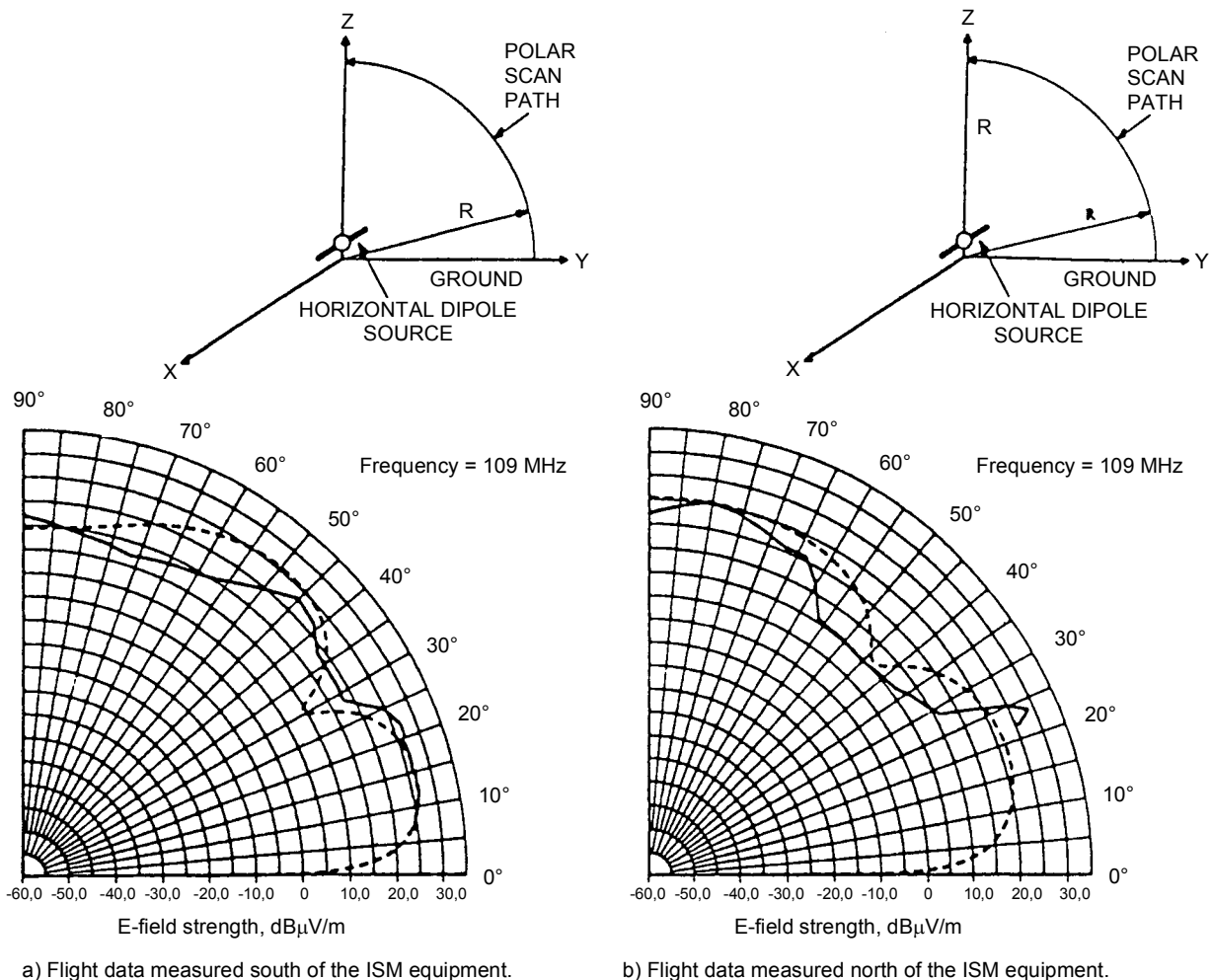


IEC 839/2000

**Figure 4.5-A2 – Vertical radiation patterns of horizontally polarized fields, 109 MHz, 300 m scan radius (Adapted from [5])**

Solid curves: Machine B (fundamental RF power 2 kW), 0° azimuth, flight altitude 152 m, RF shields in place, derived from in-flight field strength data in figure A-11 at page 62 in [4].

- a) Dashed curve: Source = small vertical loop, centre height above ground 1 m, dipole moment  $I.dA \approx 3,6 \text{ mA}\cdot\text{m}^2$ , radiated power  $\approx 6,56 \text{ mW}$ .
- b) Dashed curve: Source = small vertical loop, centre height above ground 2 m, dipole moment  $I.dA \approx 3,6 \text{ mA}\cdot\text{m}^2$ , radiated power  $\approx 8,33 \text{ mW}$ .



IEC 840/2000

**Figure 4.5-A3 – Vertical radiation patterns of horizontally polarized fields,  
109 MHz, 300 m scan radius (Adapted from [5])**

- Solid curves: Machine C (fundamental RF power 3 kW), 20° azimuth, flight altitude 152 m, RF shields in place, derived from in-flight field strength data in figure A-13 at page 65 in [4].
- a) Dashed curve: Source = horizontal electric dipole, centre height above ground 2,7 m, dipole (current) moment  $I \cdot dl \approx 50,1 \mu\text{A} \cdot \text{m}$ , radiated power  $\approx 0,31 \mu\text{W}$ .
- b) Dashed curve Source = horizontal electric dipole, centre height above ground 2 m, dipole (current) moment  $I \cdot dl \approx 28,2 \mu\text{A} \cdot \text{m}$ , radiated power  $\approx 0,096 \mu\text{W}$ .

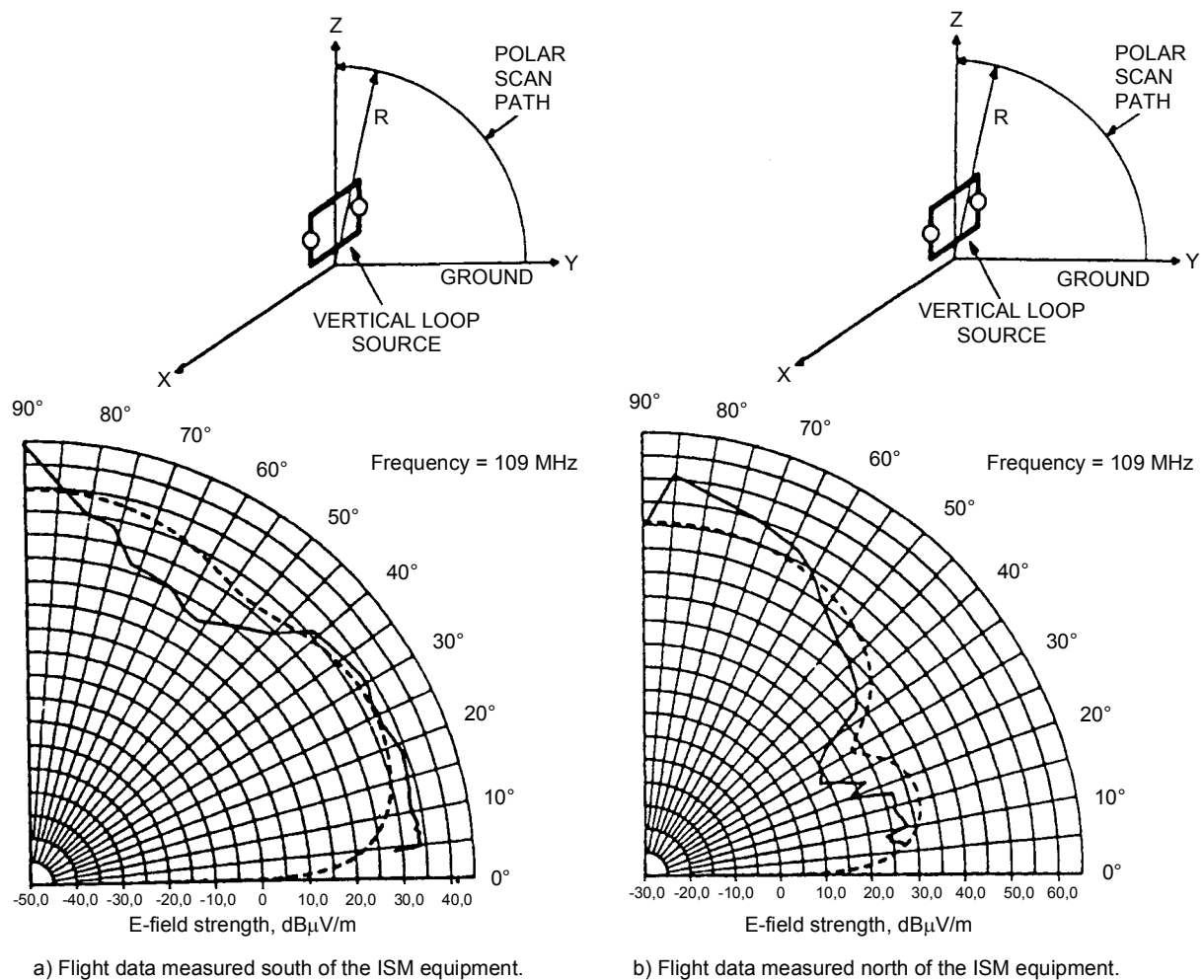


**Figure 4.5-A4 – Vertical radiation patterns of horizontally polarized fields,  
109 MHz, 300 m scan radius (Adapted from [5])**

IEC 841/2000

- Solid curves: Machine D (fundamental RF power 2 kW),  $20^\circ$  azimuth, flight altitude 152 m, RF shields in place, derived from in-flight field strength data in figure A-19 at page 72 in [4].
- a) Dashed curve: Source = small vertical loop, centre height above ground 0,85 m, dipole moment  $I.dA \approx 0,14 \text{ mA} \cdot \text{m}^2$ , radiated power  $\approx 10,4 \mu\text{W}$ .
- b) Dashed curve: Source = small vertical loop, centre height above ground 2 m, dipole moment  $I.dA \approx 0,23 \text{ mA} \cdot \text{m}^2$ , radiated power  $\approx 42,0 \mu\text{W}$ .

#### 4.5.8 References

- [1] ITU-R Recommendation 527-1, *Electrical Characteristics of the Surface of the Earth*, International Consultative Committee on Radio (CCIR), International Telecommunication Union, Geneva, 1982
- [2] ITU-R Report 879-1, *Methods for Estimating Effective Electrical Characteristics of the Surface of the Earth*, International Consultative Committee on Radio (CCIR), International Telecommunication Union, Geneva, 1986
- [3] CISPR 11:1990, *Limits and methods of measurement of electromagnetic disturbance characteristics of industrial, scientific and medical (ISM) radio-frequency equipment*, Second Edition, International Special Committee on Radio Interference (CISPR), International Electrotechnical Commission, Geneva, 1990
- [4] J.D. Nickum and W. Drury, *Measurement of RF Fields Associated With ISM Equipment as it Relates to Aeronautical Services*, Report No. OU/AEC/EER 67-1, Avionics Engineering Center, Department of Electrical and Computer Engineering, Ohio University, Athens, Ohio 45701, USA. Final report to the US Federal Aviation Administration, Systems Engineering Service, Washington, DC 20591, Report No. DOT/FAA/ES-84/2, May 1985. Document disseminated under sponsorship of the US Department of Transportation, publicly available through the National Technical Information Service, Springfield, Virginia 22161, USA
- [5] I.P. Macfarlane, *Harmonic Fields Radiated at Elevated Angles from 27 MHz ISM Apparatus Over Real Ground*, Telstra Research Laboratories Report 8347, Telstra Research Laboratories, 770 Blackburn Road, Clayton, Victoria 3168, Australia, 1995
- [6] G.J. Burke and A.J. Poggio, *Numerical electromagnetics code (NEC) – Method of Moments*, Naval Ocean Systems Center, San Diego, CA 92152, USA, NOSC Technical Document 116, 1981. (Numerical Electromagnetics Code (NEC2) developed at Lawrence Livermore National Laboratory, Livermore, California, File Created 4/11/80, Double Precision 6/4/85).
- [7] A. Sommerfeld, translated by Straus, "Partial Differential Equations in Physics", *Lectures on Theoretical Physics*, Volume VI, Academic Press, New York, 1964, Chapter VI
- [8] W.L. Stutzman and G.A. Thiele, *Antenna Theory and Design*, John Wiley & Sons, New York, 1981, p 123
- [9] **Radio Regulations.** Edition of 1990, International Telecommunication Union (ITU), General Secretariat, Geneva, 1990
- [10] I.P. Macfarlane, *Predictability of Electromagnetic Radiation in the Vertical Plane Over Real Ground at Frequencies Above 30 MHz*, Telstra Research Laboratories Report 8331, Telstra Research Laboratories, 770 Blackburn Road, Clayton, Victoria 3168, Australia, 1995
- [11] I.P. Macfarlane, *Surface Waves and Near Fields Over Ground Planes at Frequencies Above 30 MHz*, Telstra Research Laboratories Report 8329, Telstra Research Laboratories, 770 Blackburn Road, Clayton, Victoria 3168, Australia, 1995
- [12] E.C. Jordan and K.G. Balmain, *Electromagnetic Waves and Radiating Systems*, Prentice-Hall, Inc., Second Edition, 1968, Chapter 16
- [13] US Code of Federal Regulations (CFR), Chapter I – *Federal Communications Commission (FCC), Title 47, Part 18, Industrial, scientific and medical equipment*, US Government Printing Office, issue of October 1992. Measurement techniques to determine compliance are set out in FCC/OST Measurement Procedure MP-5 (1986), *Methods of Measurement of Radio Noise Emissions from Industrial, Scientific and Medical Equipment*, US Department of Commerce, National Technical Information Service, Springfield, VA 22161, February 1986

## 4.6 The predictability of radiation in vertical directions at frequencies up to 30 MHz

### 4.6.1 Scope

This report considers the vertical radiation patterns of the magnetic ( $H$ ) fields and electric ( $E$ ) fields emitted at frequencies up to 30 MHz from electrically small sources located close to the surface of real homogeneous plane ground, for the purpose of studying the predictability of radiation in vertical directions based on measurements of the strength of the  $H$ -field near the ground.

The vertical radiation patterns of the fields have been calculated at a distance of 30 m from various electrically small sources, and then the patterns of the fields at greater distances have been calculated so that the field variations with distance can be quantified. In this way, a general knowledge has been obtained of the shapes of the vertical radiation patterns, showing the magnitudes of the field strengths near ground compared with the magnitudes of the field components at elevated angles, and the ways in which the relative magnitudes can be expected to vary with distance over a plane ground.

The sources considered are electrically small balanced electric and magnetic dipoles excited in the frequency range 100 kHz to 30 MHz. For the purposes of the report, an electrically small source is defined as one whose largest linear dimension is one-tenth or less of the free space wavelength at the frequency of interest.

The report also considers the effects on the vertical radiation patterns of locating the electrically small sources close to real grounds having several different values of electrical conductivity and dielectric constants [1] [2], and includes the special case of a ground that behaves as a perfect conductor.

The possible effects on the vertical radiation patterns produced by walls, buildings, reinforced concrete structures, and the like, in the vicinity of the sources, and the effects on wave propagation near the ground that could be produced by changes with distance of the electrical constants of the ground, caused by intervening roads, watercourses, buried metallic pipes, and so on, are not within the scope of this report. It is important to note, therefore, that the errors in predictability that may be produced by such effects have not been considered.

### 4.6.2 Introduction

CISPR 11 [3] sets limits for the electromagnetic disturbances emitted near the ground from industrial, scientific and medical (ISM) radio-frequency equipment. The limits are intended to provide protection of the reception of radio services. At frequencies below 30 MHz the limits apply to the horizontally oriented components of the  $H$ -fields emitted by the ISM apparatus. For measurements on a test site, the limits apply at a distance of 30 m from the source. When measurements are made *in situ* the distance to the measurement point is defined as 30 m from the exterior wall outside the building in which the ISM equipment is situated; the distance from the source is not defined. Measurements are to be made with a vertically oriented loop, the base of which must be 1 m above the ground.

It is acknowledged in CISPR 11 that many aeronautical communications require the limitation of vertically radiated electromagnetic disturbances, and that work is necessary to determine what provisions may be required to provide protection of such systems.

The aeronautical radio services to be protected may be either horizontally or vertically polarized transmissions. Thus, the field components at elevated angles, emitted from potential interference sources located near the ground, that are of interest in a study of field strength predictability include the vertically and horizontally oriented  $H$ - and  $E$ -field components.

In this report the judgements of predictability of radiation in vertical directions are based on the accuracy with which ground-based measurements of the horizontally oriented *H*-fields emitted from a variety of sources will indicate the maximum strengths of the horizontally or vertically oriented *H*-fields at elevated angles.

As might be expected, at a distance of 30 m from an electrically small source there are significant changes in the field behaviour with changing wavelength as the frequency is varied from 100 kHz to 30 MHz. The report, therefore, concentrates attention at four frequencies, namely 100 kHz, 1 MHz, 10 MHz and 30 MHz. At 100 kHz the distance of 30 m lies well within the electrostatic or inductive near-field region close to the source. At 1 MHz the distance of 30 m is within  $\lambda/10$  of an electrically small source and places the measurement position in what might be called the radiating near-field region. At 10 MHz, a distance of 30 m represents approximately one wavelength from the source, a region where the far-field has become established. At 30 MHz, a distance of 30 m represents approximately three wavelengths from the source and places the measurement position well into the far-field.

In addition to the variations in field behaviour produced by changes from near-field to far-field conditions as the wavelength is varied, in the frequency range 100 kHz to 30 MHz the electrical behaviour of real ground varies. In general, real ground has the characteristics of a lossy conductor at low frequencies and the characteristics of a lossy dielectric at the higher frequencies. Moreover, the values of the electrical constants of real ground can vary widely; they may range typically from a conductivity of  $10^{-4}$  S/m and relative permittivity of 3 to a conductivity of  $10^{-2}$  S/m and relative permittivity of 30 [1] [2]. Even this wide range of values of the ground constants does not encompass all of the values that may be encountered in some localities.

The report shows the limitations of the predictability of radiation in vertical directions. In particular, it identifies the critical importance of a knowledge of the precise measurement distance – the actual distance between the source and the field measuring point near the ground – if it is to be possible to make predictions of the radiated field strengths at elevated angles with a known margin of error.

The report indicates the ranges of magnitude of the significant errors in predictability that can still occur when the precise measurement distance over real ground is 30 m from the sources, and the large errors that can arise from the approximation that the influence of real ground can be determined by assuming it behaves like a perfect conductor. It also shows how magnitudes of the errors in predictability above real ground may be reduced, although they remain significant, by supplementing measurements of horizontally oriented *H*-fields near ground with height scan measurements of vertically oriented *H*-fields at heights up to 6 m, when the measurements are made at a distance of 30 m from the sources.

#### **4.6.3 Method of calculation of the vertical radiation patterns**

The *H*- and *E*-field vertical radiation patterns in this report were calculated using a Method of Moments computer code known as the Numerical Electromagnetics Code (NEC) [4]. A double precision version, NEC2D, with the companion code SOMNEC2D, was used. NEC with SOMNEC allows the Sommerfeld integral evaluation of the field interactions at the air-ground interface [5] to be included in the determination of the *E*-fields above real grounds.

In the version of the NEC codes that were first released for public use, a section of code for calculation of the near *H*-field in the presence of real ground was omitted, which can lead to large errors in the *H*-field calculations [6] [7]. In the version of NEC2D used to calculate the radiation patterns in this report the missing code has been restored, allowing calculation of all the *H*-field components close to the surface of a real ground. The restored section of code calculates the *H*-field components by using a six-point finite-difference approximation of the curl of the *E*-field obtained by the Sommerfeld method.

The spatial sampling interval used in the finite-difference calculation of  $H$ -field in NEC is normally fixed at  $10^{-3} \lambda$ . For the  $H$ -field radiation patterns calculated at the frequencies of 100 kHz and 1 MHz the spatial sampling interval has to be altered to  $10^{-5} \lambda$  and  $10^{-4} \lambda$  respectively in order to obtain accurate calculations of the near  $H$ -fields [7] [8].

Some remaining problems of numerical stability, arising from the finite-difference approximation of the  $H$ -fields from  $E$ -fields which in some cases have components whose curl is mathematically zero but which have become numerically non-zero due to small numerical inaccuracies [9], have required smoothing of some of the calculated  $H$ -field radiation patterns.

#### 4.6.4 The source models

The electrically small sources that form the basis of this report consist of small vertical and horizontal balanced electric dipoles, and vertical and horizontal balanced magnetic dipoles (horizontally and vertically oriented loops respectively), each having a unit dipole moment (i.e. a dipole [current] moment of 1 A·m for the electric dipoles and a dipole moment of 1 A·m<sup>2</sup> for the magnetic dipoles). All were located very close electrically to the air-ground interface (within a small fraction of a wavelength); the height above ground of the base of each dipole was varied between either 7 cm or 15 cm and a maximum of 1 m to determine the sensitivity of the shape of the field-strength patterns to changes in the source height. The patterns considered in this report are those that exhibited the greatest variation in shape with height.

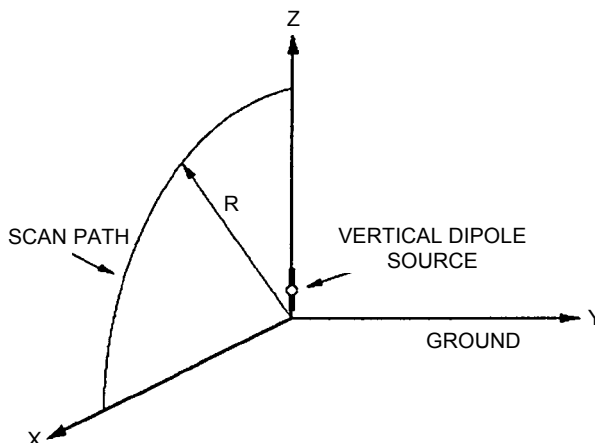
The geometries of the models used for the field-pattern computations are shown in figures 4.6-1 to 4.6-4, including the paths of the radial scans about each source; advantage has been taken of the verified azimuthal symmetry of the fields around the vertical magnetic and vertical electric dipoles to confine attention to the radial scans around those sources in only the Z-X plane.

It will be seen in figures 4.6-3 and 4.6-4 that each loop is driven by two generators. Although the loops used in the models were electrically small it was found that, when driven by one generator only, each displayed sufficient current asymmetry to produce a significant electric dipole contribution to the electromagnetic fields – because of their finite size the small loops did not behave as electrically infinitesimal magnetic dipole sources. Therefore, in the models used here, each loop was driven by two identical aiding generators located as shown, and the electric dipole contribution produced by current asymmetry arising from the use of a single generator was reduced to insignificance. Of course, in the case of the horizontal magnetic dipole (vertical loop), there is always a loop current asymmetry (and a resultant electric dipole moment) caused by proximity to the ground and this effect also occurs in the models used in this report.

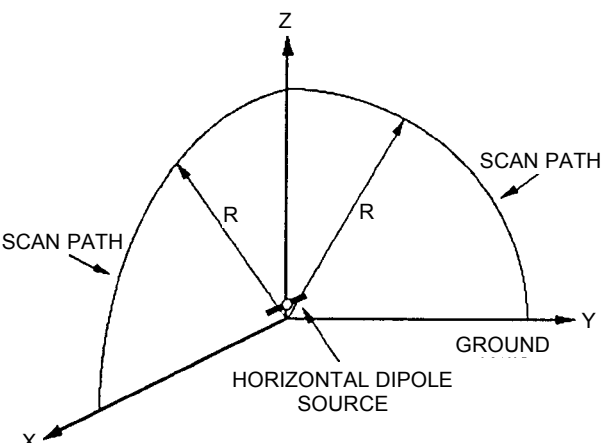
#### 4.6.5 Electrical constants of the ground

Most attention in this report has been devoted to radiation sources located close to a ground having a conductivity,  $\sigma$ , of  $10^{-3}$  S/m and a relative dielectric constant,  $\epsilon_r$  of 15; these electrical constants are in the CCIR category of a medium dry ground [1] [2].

At the upper and lower extremes of the frequency range, 30 MHz and 100 kHz, examples of two other sets of values of ground constants have been used with the small horizontal electric dipole model to illustrate the influence of differing values of the ground constants on the vertical radiation patterns. The electrical constants mentioned in 4.6.2, with the numerical values of  $\sigma = 10^{-2}$  S/m and  $\epsilon_r = 30$  (ITU-R – cultivated land and fresh water marshes) and  $\sigma = 10^{-4}$  S/m and  $\epsilon_r = 3$  (ITU-R – very dry ground and granite mountains in cold regions), were chosen as the examples [1] [2].



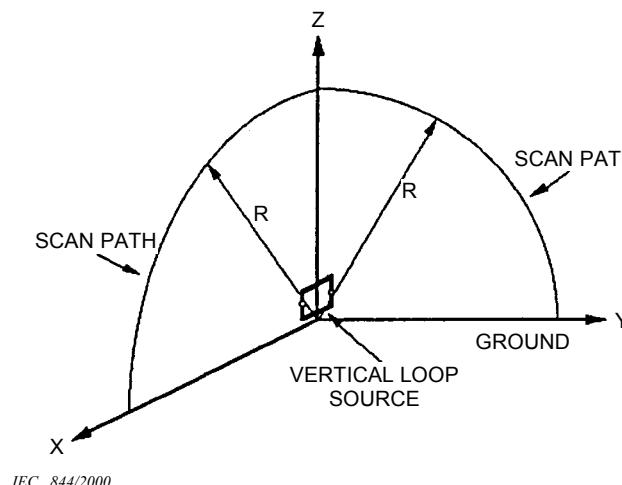
IEC 842/2000



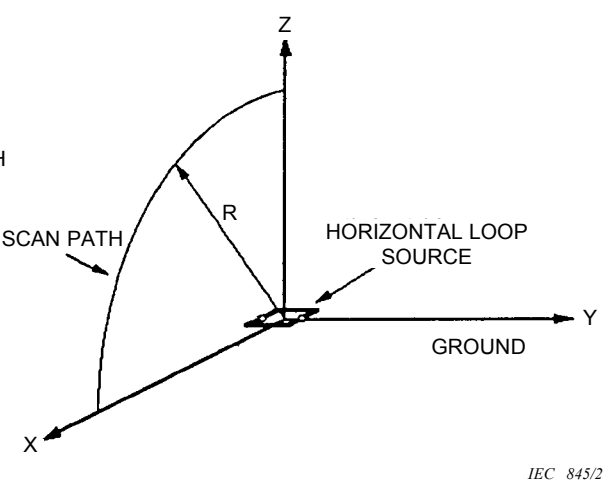
IEC 843/2000

**Figure 4.6-1 – Geometry of the small vertical electric dipole model**

**Figure 4.6-2 – Geometry of the small horizontal electrical dipole model**



IEC 844/2000



IEC 845/2000

**Figure 4.6-3 – Geometry of the small horizontal magnetic dipole model (small vertical loop)**

**Figure 4.6-4 – Geometry of the small vertical magnetic dipole model (small horizontal loop)**

For each type of source, the field patterns above a perfectly conducting ground have also been compared with the patterns generated above real grounds, to identify the errors that can arise from the approximation which is sometimes made that the influence of real ground can be determined by assuming it behaves as a perfect conductor.

In general, it is necessary to recall that specific boundary conditions apply to the fields at the surface of a perfect conductor that do not necessarily apply at the surface of a real ground. In particular, the  $H$ -field component normal to the surface of a perfect conductor must go to zero at the surface, as must the tangential  $E$ -field component at the surface, and it will be recalled that this is why a horizontally polarized surface wave cannot exist at the surface of a perfect conductor. Further, a vertically polarized surface wave travelling on a perfectly conducting ground plane experiences no ohmic loss, it merely attenuates with distance at the free space rate. Those boundary conditions, however, certainly do not apply at the surface of a real ground – thus the boundary conditions identify the most general set of differences between the vertical radiation patterns that will exist close to the surface of a real ground when compared with those calculated close to the surface of a perfectly conducting ground.

#### 4.6.6 Predictability of radiation in vertical directions

##### 4.6.6.1 Tabular summaries of predictability

The vertical radiation patterns on which the judgements of predictability are based are presented in figures 4.6-7 to 4.6-62, polar patterns showing field strength plotted against elevation angle above the ground. To summarize the information presented in those figures, four tables of summary information have been prepared, one for each frequency considered in this report.

**Table 4.6-1 – Predictability of radiation in vertical directions at 100 kHz, using ground-based measurements of horizontally oriented  $H$ -field at distances up to 3 km from the source**

Type of source	Predictability based on measurements near real ground at 30 m distance from the source	Predictability based on <i>in situ</i> measurements near real ground when the measurement distance from the source is not precisely known	Predictability based on vertical radiation patterns calculated at a known distance from the source, assuming the ground behaves as a perfect conductor
Electrically small vertical electric dipole	Excellent (see figures 4.6-7, 4.6-9)	Excellent (see figures 4.6-7, 4.6-8, 4.6-9, 4.6-10)	Excellent (see figure 4.6-7)
Electrically small horizontal electric dipole	Excellent (see figures 4.6-11, 4.6-12, 4.6-13) Notes 1, 2	Very good (see figures 4.6-11, 4.6-13, 4.6-14, 4.6-15)	Poor (see figure 4.6-11) Note 3
Electrically small horizontal magnetic dipole (vertical loop)	Excellent (see figures 4.6-16, 4.6-18) Note 4	Very good (see figures 4.6-16, 4.6-18, 4.6-19, 4.6-20)	Very good (see figures 4.6-16, 4.6-17) Note 5
Electrically small vertical magnetic dipole (horizontal loop)	Poor (see figures 4.6-21, 4.6-25) Note 6	Impossible (see figures 4.6-21, 4.6-23 to 4.6-26) Note 7	Impossible (see figures 4.6-21, 4.6-22) Note 8

NOTE 1 The measurement of horizontally oriented  $H$ -field emitted by the small horizontal electric dipole near the ground can overestimate the maximum vertically oriented  $H$ -field strength emitted at an elevated angle by approximately 1 dB, see figure 4.6-11. Note, however, that the measurement overestimates the strength of the horizontally oriented  $H$ -field emitted in the vertical direction by 5 dB.

NOTE 2 The small influence exerted on the small horizontal electric dipole's vertical radiation patterns at 100 kHz by a wide range of the electrical constants of the ground is shown in figure 4.6-12.

NOTE 3 The horizontal electric dipole's  $H$ -field pattern calculated assuming a perfectly conducting ground shows that such an assumption causes an underestimate of more than 20 dB in the absolute field strength, and falsely indicates that the ground-based measurement underestimates the maximum field strength by 6 dB (refer to Note 1). See figure 4.6-11.

NOTE 4 Measurement of horizontally oriented  $H$ -field emitted by the small horizontal magnetic dipole (vertical loop) near the ground can overestimate the maximum vertically oriented  $H$ -field strength at elevated angles by less than 1 dB, see figure 4.6-16. Note, however, that the measurement overestimates the strength of the horizontally oriented  $H$ -field emitted in the vertical direction by more than 3 dB.

NOTE 5 Vertical patterns of the horizontally oriented  $H$ -fields emitted by the small horizontal magnetic dipole (vertical loop), calculated assuming a perfectly conducting ground, can overestimate absolute values of field strength over real ground by 6 dB, but the shapes of the patterns are a good guide to those over real ground. However, boundary conditions require that the vertically oriented  $H$ -field must go to zero at the surface of the perfectly conducting ground which is not the case at the surface of a real ground. See figures 4.6-16 and 4.6-17.

NOTE 6 Measurement of horizontally oriented  $H$ -field emitted by the small vertical magnetic dipole (horizontal loop) near the ground at a distance of 30 m underestimates the  $H$ -field strengths at elevated angles by more than 16 dB, see figure 4.6-21. However, measurement of the vertically oriented  $H$ -field,  $H_z$ , near the ground improves predictability; it provides an underestimate of the vertically oriented  $H$ -field emitted in the vertical direction by approximately 6 dB, and an underestimate of the maximum horizontally oriented  $H$ -field emitted at elevated angles by about 3 dB.

NOTE 7 The relative magnitudes of the  $H$ -field components near the ground and at elevated angles are strongly dependent on the actual distance from the small horizontal loop. See figures 4.6-21, 4.6-23 and 4.6-24.

NOTE 8 The small horizontal loop's field patterns calculated close to the ground assuming a perfectly conducting ground have no resemblance, in shape and absolute magnitude, to the field patterns calculated close to a real ground. See figures 4.6-21 and 4.6-22.

**Table 4.6-2 – Predictability of radiation in vertical directions at 1 MHz, using ground-based measurements of horizontally oriented  $H$ -field at distances up to 300 m from the source**

Type of source	Predictability based on measurements near real ground at 30 m distance from the source	Predictability based on <i>in situ</i> measurements near real ground when the measurement distance from the source is not precisely known	Predictability based on vertical radiation patterns calculated at a known distance from the source, assuming the ground behaves as a perfect conductor
Electrically small vertical electric dipole	Excellent (see figures 4.6-27, 4.6-28)	Excellent (see figures 4.6-27, 4.6-28, 4.6-29)	Excellent (see figure 4.6-27)
Electrically small horizontal electric dipole	Very good (see figures 4.6-30, 4.6-32) Note 9	Good (see figures 4.6-30, 4.6-31, 4.6-32, 4.6-33)	Poor (see figure 4.6-30) Note 10
Electrically small horizontal magnetic dipole (vertical loop)	Excellent (see figures 4.6-34, 4.6-37) Note 11	Good (see figures 4.6-34, 4.6-36, 4.6-37, 4.6-38)	Fair (see figures 4.6-34, 4.6-35) Note 12
Electrically small vertical magnetic dipole (horizontal loop)	Excellent (see figures 4.6-39, 4.6-42) Note 13	Impossible (see figures 4.6-39, 4.6-41 to 4.6-42) Note 14	Poor (see figures 4.6-40) Note 15

NOTE 9 Measurement of the horizontally oriented  $H$ -field emitted by the horizontal electric dipole near the ground can overestimate the maximum vertically oriented  $H$ -field strength emitted at elevated angles by approximately 3 dB. See figure 4.6-30. Note, however, that the measurement can overestimate the strength of the horizontally oriented  $H$ -field emitted in the vertical direction by more than 9 dB.

NOTE 10 The  $H$ -field patterns calculated at a distance of 30 m from the horizontal electric dipole assuming a perfectly conducting ground show that such an assumption causes an underestimate of 20 dB in the absolute field strength at 1 MHz, and falsely indicates that the ground-based measurement underestimates the maximum field strength emitted in vertical directions by 5 dB. See figure 4.6-30.

NOTE 11 Measurement of the horizontally oriented  $H$ -field emitted by the small vertical loop near the ground can overestimate the maximum field strength emitted at elevated angles by less than 3 dB, see figure 4.6-34.

NOTE 12 The patterns of horizontally oriented  $H$ -field calculated at 30 m from the small vertical loop assuming perfectly conducting ground are very similar to the  $H$ -field patterns over a real ground. See figures 4.6-34 and 4.6-35.

NOTE 13 The measurement of the horizontally oriented  $H$ -field emitted by the small horizontal loop near the ground at 30 m distance can underestimate the maximum vertically oriented  $H$ -field strength emitted in the vertical direction by more than 2 dB, and the maximum horizontally oriented  $H$ -field emitted at elevated angles by less than 1 dB, see figure 4.6-39. A measurement of the vertically oriented  $H$ -field,  $H_z$ , near ground reduces the underestimate of the strength of the vertically oriented  $H$ -field emitted in the vertical direction to about 1 dB, and overestimates the maximum horizontally oriented  $H$ -field strength by more than 1 dB.

NOTE 14 The relative magnitudes of the  $H$ -field components near the ground and at elevated angles are strongly dependent on the actual distance from the horizontal loop source. The horizontally oriented  $H$ -field near the ground is a radially directed component which attenuates more rapidly with increasing distance than does the horizontally oriented  $H$ -field at elevated angles. The vertically oriented  $H$ -field near the ground is a component of the horizontally polarized ground wave launched by the horizontal loop and attenuates very rapidly with increasing distance from the source at 1 MHz. See figures 4.6-39 and 4.6-41.

NOTE 15 At 1 MHz, the vertical radiation pattern of the horizontally oriented  $H$ -field emitted by the small horizontal loop above a perfectly conducting ground has an absolute value more than 15 dB less than the field strength calculated above a real ground. The shape of the vertical pattern of the vertically oriented  $H$ -field calculated close to a perfectly conducting ground bears no resemblance to the vertical pattern calculated close to the real ground. Compare figures 4.6-39 and 4.6-40. In general, the boundary condition which requires the vertically oriented  $H$ -field strength to be zero at the surface of a perfectly conducting ground means that the pattern of vertically oriented  $H$ -field at the real ground, which is non-zero, does not resemble the corresponding pattern at the perfect ground.

**Table 4.6-3 – Predictability of radiation in vertical directions at 10 MHz, using ground-based measurements of horizontally oriented  $H$ -field at distances up to 300 m from the source**

Type of source	Predictability based on measurements near real ground at 30 m distance from the source	Predictability based on <i>in situ</i> measurements near real ground when the measurement distance from the source is not precisely known	Predictability based on vertical radiation patterns calculated at a known distance from the source, assuming the ground behaves as a perfect conductor
Electrically small vertical electric dipole	Excellent (see figures 4.6-43, 4.6-44) Note 16	Excellent (see figures 4.6-43, 4.6-44, 4.6-45) Note 16	Impossible (see figure 4.6-43) Note 17
Electrically small horizontal electric dipole	Poor (see figures 4.6-46, 4.6-47) Note 18	Good (see figures 4.6-46, 4.6-47, 4.6-48) Note 19	Impossible (see figure 4.6-46) Note 20
Electrically small horizontal magnetic dipole (vertical loop)	Very good (see figures 4.6-49, 4.6-50) Note 21	Impossible (see figures 4.6-49, 4.6-50) Note 22	Impossible (see figure 4.6-49) Note 23
Electrically small vertical magnetic dipole (horizontal loop)	Poor (see figures 4.6-51, 4.6-52) Note 24	Impossible (see figures 4.6-51, 4.6-52) Note 25	Fair (see figures 4.6-51) Note 26

NOTE 16 The horizontally oriented  $H$ -field near the ground is a component of the vertically polarized ground wave emitted from the vertical electric dipole. At 10 MHz the vertically polarized wave near the ground attenuates rapidly with increasing distance, such that there is an excess 8 dB ground-wave attenuation in addition to the 20 dB sky-wave attenuation over the distance from 30 m to 300 m. See figure 4.6-43.

NOTE 17 At a distance of 30 m from the vertical electric dipole over a perfectly conducting ground the vertical radiation pattern of the horizontally oriented  $H$ -field is within about 3 dB of the pattern of the  $H$ -field over a real ground. However, the vertically polarized wave near a perfectly conducting ground attenuates with increasing distance at the free space rate and therefore does not attenuate with distance in the way it does over a real ground at 10 MHz (see Note 16). It is thus misleading as a guide to the vertical radiation patterns over real ground at distances much beyond 30 m.

NOTE 18 The measurement of the horizontally oriented  $H$ -field near the real ground at 30 m from the small horizontal electric dipole can underestimate the field strength of the horizontally oriented  $H$ -field emitted in the vertical direction by approximately 8 dB, and the vertically oriented  $H$ -field strength emitted at elevated angles by about 3 dB. Measurements of vertically oriented  $H$ -field near ground cannot improve the predictability in this case. See figure 4.6-46.

NOTE 19 At 10 MHz, the horizontally oriented  $H$ -field components near real ground attenuate more rapidly with increasing distance from the horizontal electric dipole than do the sky-wave components. The excess attenuation is approximately 7 dB over the distance from 30 m to 300 m. See figure 4.6-46.

NOTE 20 The horizontally oriented  $H$ -field near a perfectly conducting ground attenuates by 40 dB as the distance from the small horizontal electric dipole increases from 30 m to 300 m, an excess attenuation of 20 dB more than the sky-wave attenuation over the same distance. Near a real ground the excess attenuation is about 7 dB over the same distance at 10 MHz. The vertical radiation patterns over real and perfectly conducting grounds therefore differ significantly in that range of measuring distances. See figure 4.6-46.

NOTE 21 Measurement of the horizontally oriented  $H$ -field near the real ground at 30 m distance from the small vertical loop can underestimate the horizontally oriented  $H$ -field strength emitted in the vertical direction by less than 3 dB, but it overestimates the strength of the vertically oriented  $H$ -field emitted at elevated angles by approximately 3 dB. See figure 4.6-49.

NOTE 22 The horizontally oriented  $H$ -field components near real ground attenuate much more rapidly with increasing distance from the small vertical loop than do the sky-wave components, at 10 MHz. The excess attenuation is approximately 8 dB over the distance from 30 m to 300 m. See figure 4.6-49.

NOTE 23 At a distance of 30 m from the small vertical loop over a perfectly conducting ground the vertical radiation pattern of the horizontally oriented  $H$ -field is within about 4 dB of the pattern of the  $H$ -field over a real ground. However, the vertically polarized wave near a perfectly conducting ground attenuates with increasing distance at the free space rate, unlike a vertically polarized wave over a real ground which attenuates more rapidly with distance at 10 MHz – see Note 22 and figures 4.6-49 and 4.6-50. Vertical radiation patterns calculated over a perfectly conducting ground can therefore be very misleading as guidance to the patterns to be expected over real ground at distances much beyond 30 m at 10 MHz.

NOTE 24 Measurement of the horizontally oriented  $H$ -field components near the real ground at 30 m distance from the small horizontal loop can underestimate the maximum horizontally and vertically oriented  $H$ -field strengths at elevated angles by more than 6 dB. Note, however, that a measurement of the vertically oriented  $H$ -

field,  $H_z$ , at a height of 6 m underestimates the maximum  $H$ -field, the vertically oriented  $H$ -field, at elevated angles by approximately 5 dB at 10 MHz. See figure 4.6-51.

**NOTE 25** The relative magnitudes of the  $H$ -field components near the ground and at elevated angles are strongly dependent on the actual distance from the horizontal loop source at 10 MHz. The horizontally oriented  $H$ -field near the ground is a radially directed component which attenuates more rapidly with increasing distance than does the horizontally oriented  $H$ -field at elevated angles. The vertically oriented  $H$ -field near the ground is a component of the horizontally polarized ground wave launched by the horizontal loop and attenuates very rapidly with increasing distance from the source. See figure 4.6-51.

**NOTE 26** The shape of the vertical radiation pattern of the horizontally oriented  $H$ -field calculated at a distance of 30 m from the small horizontal loop over perfectly conducting ground is very similar to that calculated over a real ground at 10 MHz. The absolute value of the field strength calculated over perfectly conducting ground is about 5 dB less than the field strength calculated over real ground. Both calculated vertical radiation patterns at 30 m distance indicate that ground-based measurement of horizontally oriented  $H$ -field underestimates the maximum field strength at elevated angles by more than 6 dB. The measurable horizontally oriented  $H$ -field components near the ground in both cases are the remnants of radially directed near-field components, not a part of propagating waves, and they attenuate more rapidly with increasing distance from the source than do the fields at elevated angles. See figure 4.6-51. It must also be recalled that, in general, the boundary condition which requires the vertically oriented  $H$ -field strength to be zero at the surface of a perfectly conducting ground means that at all frequencies up to 30 MHz the patterns of vertically oriented  $H$ -field which are non-zero at the real ground do not resemble the corresponding vertically oriented  $H$ -field patterns which go to zero at the perfectly conducting ground.

**Table 4.6-4 – Predictability of radiation in vertical directions at 30 MHz, using ground-based measurements of horizontally oriented  $H$ -field at distances up to 300 m from the source**

Type of source	Predictability based on measurements near real ground at 30 m distance from the source	Predictability based on <i>in situ</i> measurements near real ground when the measurement distance from the source is not precisely known	Predictability based on vertical radiation patterns calculated at a known distance from the source, assuming the ground behaves as a perfect conductor
Electrically small vertical electric dipole	Very good (see figures 4.6-53, 4.6-54) Note 27	Impossible (see figures 4.6-53, 4.6-54) Note 28	Impossible (see figure 4.6-53) Note 29
Electrically small horizontal electric dipole	Poor (see figures 4.6-55, 4.6-57, 4.6-58) Notes 30, 31	Impossible (see figures 4.6-55, 4.6-56, 4.6-58 Note 32	Impossible (see figures 4.6-55, 4.6-56) Note 33
Electrically small horizontal magnetic dipole (vertical loop)	Good (see figures 4.6-59, 4.6-60) Note 34	Impossible (see figures 4.6-59, 4.6-60) Note 35	Impossible (see figure 4.6-59) Note 36
Electrically small vertical magnetic dipole (horizontal loop)	Poor (see figures 4.6-61, 4.6-62) Note 37	Impossible (see figures 4.6-61, 4.6-62) Note 38	Good (see figure 4.6-61) Note 39

**NOTE 27** The measurement of the horizontally oriented  $H$ -field near the real ground at 30 m distance from the small vertical electric dipole underestimates the maximum field strength at elevated angles by about 3 dB at 30 MHz.

**NOTE 28** The horizontally oriented  $H$ -field near ground is a component of the vertically polarized ground wave emitted from the vertical electric dipole. At 30 MHz the vertically polarized wave attenuates rapidly with increasing distance near ground, such that there is an excess 13 dB attenuation of the ground wave in addition to the 20 dB sky-wave attenuation over the distance from 30 m to 300 m. See figures 4.6-53 and 4.6-54.

**NOTE 29** At a distance of 30 m from the small vertical electric dipole over a perfectly conducting ground, the vertical radiation pattern of the horizontally oriented  $H$ -field is within about 8 dB of the pattern of the  $H$ -field over real ground. However, the very high rate of attenuation with a distance of a vertically polarized ground wave over real ground at 30 MHz is apparent even at the short range of 30 m (see figure 4.6-53). Moreover, at 30 MHz there is an excess 13 dB attenuation of the ground wave in addition to the 20 dB sky-wave attenuation over the distance from 30 m to 300 m. Over a perfectly conducting ground the excess ground-wave attenuation does not occur, so that the vertical radiation patterns over perfectly conducting ground cannot give guidance to the patterns over real ground at the distances from the small vertical electric dipole that are considered in this report.

**NOTE 30** The measurement of horizontally oriented  $H$ -field emitted by the small horizontal electric dipole near the ground can underestimate the maximum horizontally oriented  $H$ -field strength in the vertical direction by more than 16 dB at 30 MHz (see figure 4.6-55). Note, however, that a measurement of the vertically oriented  $H$ -field,  $H_z$ , at a height of 6 m improves predictability and underestimates the magnitude of the horizontally oriented  $H$ -field in the vertical direction by approximately 12 dB. The height scan measurement of  $H_z$  underestimates the magnitude of the vertically oriented  $H$ -field at elevated angles by approximately 7 dB.

**NOTE 31** The small influence exerted by a wide range of the electrical constants of the real ground on the shape and magnitude of the small horizontal electric dipole's vertical radiation pattern at 30 MHz is shown in figure 4.6-57.

NOTE 32 Excess attenuation of the horizontally oriented *H*-field component of the vertically polarized ground wave emitted by the small horizontal electric dipole at the real ground is almost 12 dB more than the sky-wave attenuation over the distance from 30 m to 300 m from the source. If the true measurement distance is not known, the amount of excess attenuation suffered by the ground wave cannot be known when making predictions of the strength of radiation in vertical directions based on measurements at the ground.

NOTE 33 The horizontally oriented *H*-field near a perfectly conducting ground attenuates by 40 dB as the distance from the small horizontal electric dipole increases from 30 m to 300 m, an excess attenuation of 20 dB more than the sky-wave attenuation, as the far-field radiation pattern becomes established over that distance. On the other hand, the excess attenuation of the *H*-field component of the vertically polarized ground wave is about 12 dB near a real ground over the 30 m to 300 m distance. The vertical radiation patterns over real and perfectly conducting grounds therefore differ significantly at 30 MHz in that range of measuring distances. See figures 4.6-55 and 4.6-56.

NOTE 34 Measurement of the horizontally oriented *H*-field near real ground at 30 m distance from the small vertical loop can underestimate the maximum horizontally oriented *H*-field strength emitted in the vertical direction by less than 6 dB. It gives an exact indication of the strength of the vertically oriented *H*-field emitted at elevated angles. See figure 4.6-59.

NOTE 35 The horizontally oriented *H*-field components near real ground attenuate more rapidly with increasing distance from the small vertical loop than do the sky-wave components, at 30 MHz. The excess attenuation is approximately 13 dB over the distance from 30 m to 300 m. See figure 4.6-59.

NOTE 36 At a distance of 30 m from the small vertical loop over a perfectly conducting ground the vertical radiation pattern of the horizontally oriented *H*-field is within about 8 dB of the pattern of the *H*-field over a real ground. However, the vertically polarized wave near a perfectly conducting ground attenuates with distance at the free space rate, unlike the vertically polarized wave over a real ground which attenuates more rapidly with distance at 30 MHz – see figures 4.6-59 and 4.6-60. Vertical radiation patterns calculated over a perfectly conducting ground can therefore be very misleading as guidance to the patterns over real ground at a distance of 30 m and beyond.

NOTE 37 Measurement of the horizontally oriented *H*-field components near the real ground at 30 m distance from the small horizontal loop can underestimate the *H*-field strengths emitted at elevated angles by more than 16 dB. Note, however, that a measurement of the vertically oriented *H*-field, *Hz*, at a height of 6 m underestimates the maximum *H*-field strengths at elevated angles by less than 6 dB. See figure 4.6-61.

NOTE 38 The relative magnitudes of the *H*-field components near the ground and at elevated angles are strongly dependent on the actual distance from the horizontal loop source. The horizontally oriented *H*-field near the ground is a radially directed component which attenuates more rapidly with increasing distance than does the horizontally oriented *H*-field at elevated angles. The vertically oriented *H*-field near the ground is a component of the horizontally polarized ground wave launched by the horizontal loop and at 30 MHz it attenuates very rapidly with increasing distance from the source. See figures 4.6-61 and 4.6-62.

NOTE 39 The shape and magnitude of the vertical radiation pattern of the horizontally oriented *H*-field calculated at a distance of 30 m from the small horizontal loop over perfectly conducting ground at 30 MHz are very similar to the shape and magnitude of the pattern calculated over real ground. Both the calculated patterns indicate that ground-based measurement of horizontally oriented *H*-field will underestimate the maximum field strength at elevated angles by 16 dB or 17 dB. However, the measurable horizontally oriented *H*-field components near the ground in both cases are the remnants of radially directed near-field components, not a part of propagating waves, and they attenuate more rapidly with increasing distance from the small horizontal loop than do the fields at elevated angles. See figure 4.6-61. It must also be recalled that, in general, the boundary condition which requires the vertically oriented *H*-field strength to be zero at the surface of a perfectly conducting ground means that at all frequencies up to 30 MHz the patterns of vertically oriented *H*-field which are non-zero at the real ground do not resemble the corresponding vertically oriented *H*-field patterns which go to zero at the perfectly conducting ground.

#### 4.6.6.2 Error ranges

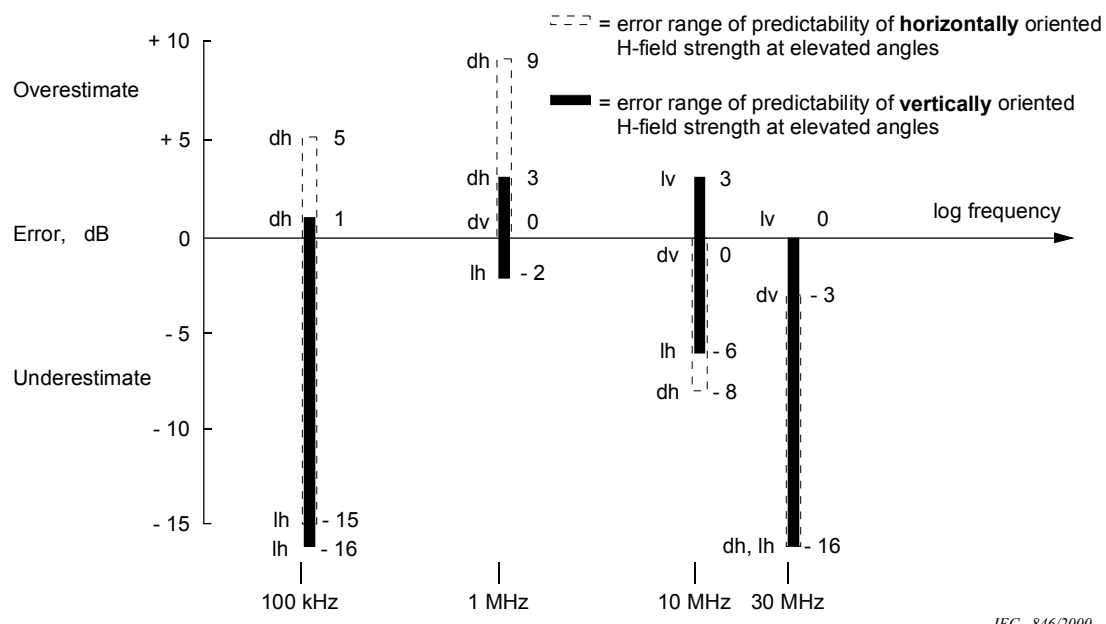
It is possible to present pictorially the ranges of errors of the predictability of radiation in vertical directions at different frequencies, when the precise horizontal measurement distance from the sources is known to be 30 m.

Figure 4.6-5 and 4.6-6 show in bar chart form the error ranges to be expected, in figure 4.6-5 when measurements are made of the horizontally oriented *H*-field near the ground at 30 m distance from the sources, and in figure 4.6-6 when those measurements of horizontally oriented *H*-field are supplemented with measurements of vertically oriented *H*-field in a 6 m height scan near the ground at 30 m distance from the sources.

The error range bar charts summarize the information presented in the various notes to the tables and in the radiation pattern diagrams.

The following examples serve to illustrate the ways in which the error range bar charts can be interpreted.

In figure 4.6-5, which is used when predictability of radiation in vertical directions is to be based only on measurements near ground of the horizontally oriented *H*-field components at 30 m horizontal distance from the sources, the charts show that at 100 kHz the largest overestimation of the strength of radiation in vertical directions occurs in the case of a source behaving as a small horizontal electric dipole, and the error is an overestimate by 5 dB of the maximum strength of the horizontally oriented *H*-field. The largest error in overestimating the maximum vertically oriented *H*-field strength at 100 kHz is an overestimate of only 1 dB, as indicated in the chart by the solid bar, again for the case of a source behaving as a small horizontal electric dipole. At 100 kHz, figure 4.6-5 shows that the largest error in prediction of the strength of radiation in vertical directions occurs in the case of a source behaving as a small vertical magnetic dipole (horizontal loop) and the error is an underestimate by 16 dB of the maximum vertically oriented *H*-field. The largest error at 100 kHz in predicting the maximum horizontally oriented *H*-field strength emitted in vertical directions is an underestimate by 15 dB, again in the case of a source behaving as a small vertical magnetic dipole (horizontal loop).



**Figure 4.6-5 – Ranges of errors in the predictability of radiation in vertical directions from electrically small sources located close to the ground, based on measurements of the horizontally oriented *H*-field near ground at a distance of 30 m from the sources.**

Electrical constants of the ground:  $\sigma = 1 \text{ mS/m}$ ,  $\epsilon_r = 15$ .

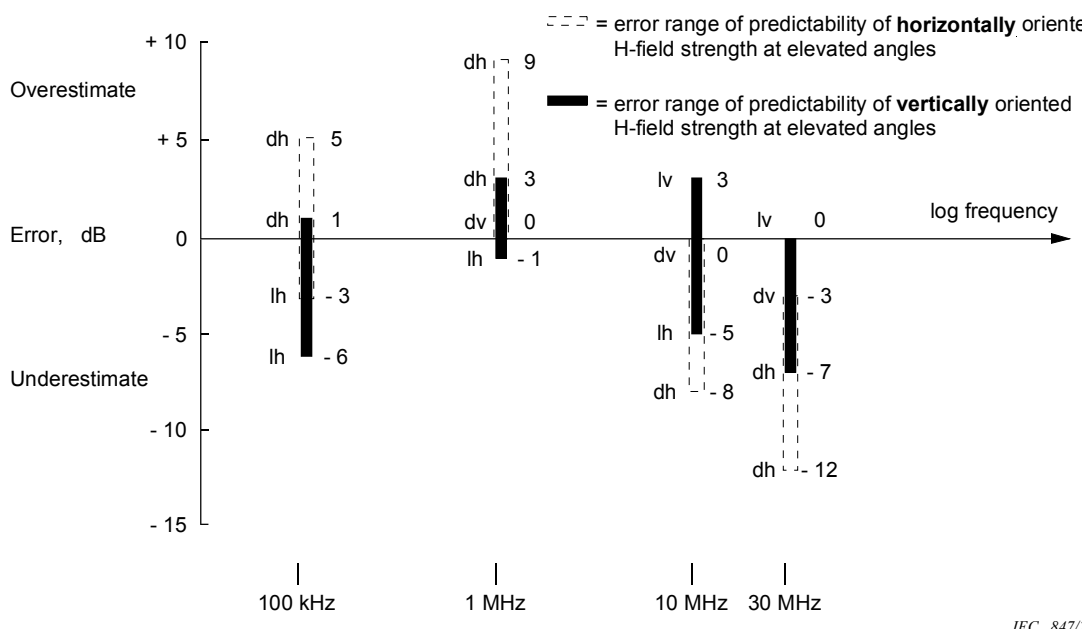
Source identification:

dh = horizontal electric dipole

dv = vertical electric dipole

lv = horizontal magnetic dipole (vertical loop)

lh = vertical magnetic dipole (horizontal loop)



IEC 847/2000

**Figure 4.6-6 – Ranges of errors in the predictability of radiation in vertical directions from electrically small sources located close to the ground, based on measurements of the horizontally oriented H-field at the ground supplemented with measurements of the vertically oriented H-field in a height scan up to 6 m at a distance of 30 m from the sources**

Electrical constants of the ground:  $\sigma = 1 \text{ mS/m}$ ,  $\epsilon_r = 15$ .

Source identification:

dh = horizontal electric dipole

dv = vertical electric dipole

lv = horizontal magnetic dipole (vertical loop)

lh = vertical magnetic dipole (horizontal loop)

In figure 4.6-6, which is used when predictability of radiation in vertical directions is to be based on measurements near ground of the horizontally oriented H-field components supplemented with 6 m height-scan measurements of the vertically oriented H-field components at 30 m distance, the charts show that at 100 kHz the worst error in the prediction of the strength of radiation in vertical directions still occurs for the vertically oriented H-field components emitted from a source behaving as a small vertical magnetic dipole (horizontal loop), but that the magnitude of the error has been reduced to an underestimate by 6 dB (solid bar). The magnitude of the largest underestimate at 100 kHz of the maximum strength of the horizontally oriented H-fields emitted in vertical directions has been reduced to 3 dB, and this also occurs for the case of a source behaving as a small vertical magnetic dipole (horizontal loop).

#### 4.6.7 Conclusions

Vertical radiation patterns have been calculated for electrically small sources located close to real homogeneous plane ground, ignoring the possible contributions to pattern distortion that might arise from the presence of nearby buildings or other field disturbing objects, or from discontinuities in the electrical constants of the ground. Nevertheless, even with such a simplification, the studies still show that in the case of solitary electrically small sources located close to a plane homogeneous ground the predictability of radiation in vertical directions can be subject to large errors, when the predictions are to be based on measurements of the strength of the horizontally oriented H-field at the ground in the manner presently described in CISPR 11.

In particular, the report has identified many examples of the impossibility of making predictions of field strength at elevated angles with a known margin of error, using ground-based measurements, when the measuring distances from the sources are not precisely known. The limits and methods of measurement of radiation *in situ* for which the precise measurement distance from the ISM equipment is not defined in CISPR 11 cannot provide a known level of protection of aeronautical communication services. For example, this

limitation applies over the entire frequency range from 100 kHz to 30 MHz if the radiation source behaves like an electrically small vertical magnetic dipole (horizontal loop).

The large errors in calculation of the vertical radiation patterns that can arise from the approximation, which is sometimes made, that the influence of real ground can be determined by assuming it behaves like a perfect conductor have also been indicated. Apart from the more complex interaction between the source and its image in a real ground, two more obvious reasons for the errors are that the boundary condition which requires the vertically oriented *H*-field strength and the horizontally oriented *E*-field strength to be zero at the surface of a perfectly conducting ground does not apply at the surface of a real ground, and the vertically polarized ground wave attenuation with distance over real ground is greater than the attenuation with distance over a perfectly conducting ground, especially at the higher frequencies.

The report has also shown that, even when the measurement distance over real ground is precisely known, predictability of the strength of radiation in vertical directions based on measurements near the ground at a distance of 30 m remains subject to significant errors.

Figure 4.6-5 depicts the error ranges that can apply when predictability is based solely on measurement of the horizontally oriented *H*-field near ground at 30 m distance. It can be seen that over the frequency range from 100 kHz to 30 MHz the margin for error can be as much as +9 dB (overestimate) at 1 MHz, or as much as -16 dB (underestimate) at the extremes of the frequency range, 100 kHz and 30 MHz.

Figure 4.6-6 illustrates the reduced error ranges obtained for predictability of radiation in vertical directions when measurements of horizontally oriented *H*-field near the ground are supplemented with measurements of vertically oriented *H*-field at heights up to 6 m above the ground. It can be seen that the potential overestimate of 9 dB at 1 MHz remains a possibility, but the potential underestimate of 16 dB at 100 kHz and 30 MHz has become a possible underestimate of 6 dB at 100 kHz and of 12 dB at 30 MHz.

The studies in this report have identified some of the factors that must be taken into account when determining limits and methods of measurement of radiated electromagnetic disturbances from ISM apparatus to ensure the protection of aeronautical communication services operating below 30 MHz.

In addition, the comparisons of the vertical radiation patterns over real ground with those over perfectly conducting ground have also shown the large differences that can occur in the assessments of the potential for interference made by measurements on a test site having a conducting metal ground plane compared with assessments using measurements made on a test site having a real ground reference plane.

#### 4.6.8 References

- [1] ITU-R Recommendation 527-1, *Electrical Characteristics of the Surface of the Earth*, International Telecommunication Union, Geneva, 1982
- [2] ITU-R Report 879-1, *Methods of Estimating Effective Electrical Characteristics of the Surface of the Earth*, International Telecommunication Union, Geneva, 1986
- [3] CISPR 11, *Limits and methods of measurement of electromagnetic disturbance characteristics of industrial, scientific and medical (ISM) radio-frequency equipment*, Second edition, International Electrotechnical Commission, Geneva, 1990
- [4] Burke, G.J. and Poggio, A.J., *Numerical electromagnetics code (NEC) – Method of Moments*, Naval Ocean System Center, San Diego, CA, NOSC Tech. Document 116, 1981. (Numerical Electromagnetics Code (NEC2) developed at Lawrence Livermore National Laboratory, Livermore, California, File Created 4/11/80, Double precision 6/4/85).

- [5] Sommerfeld A, translated by Straus, "Partial Differential Equations in Physics, *Lectures on Theoretical Physics*", Volume VI, Academic Press, New York, 1964, Chapter VI
- [6] Macfarlane, I.P., Error in the Numerical Electromagnetic Code (NEC2) Calculation of Magnetic Field Strength Near Ground, Australian telecommunication Research (ATR), Vol. 24, No.1, 1990
- [7] Macfarlane, I.P., Fleming, A.H.J., Iskra, S. and Haack, G. Pilgrims' Progress – Learning to Use the Numerical Electromagnetics Code (NEC) to Calculate Magnetic Field Strength Close to a Sommerfeld Ground, *Applied Computational Electromagnetics Society (ACES) Journal*, Vol. 5, No. 2, Winter 1990
- [8] Macfarlane, I.P., Addendum to: Error in the Numerical Electromagnetics Code (NEC2). Calculation of Magnetic Field Strength Near Ground, Australian Telecommunication Research (ATR), Vol. 24, No. 2, 1990
- [9] Haack, G.R. and Fleming, A.H.J., Using the Numerical Electromagnetics Code (NEC) to Calculate Magnetic Field Strength Close to a Sommerfeld Ground, Proceedings of the Seventh Annual Review of Progress in *Applied Computational Electromagnetics*, Monterey, California, March 18-22, 1991, pp 493-506, Managing Editor: Richard W. Adler, U.S. Naval Postgraduate School, Code EC/AB, Monterey, CA 93943, USA

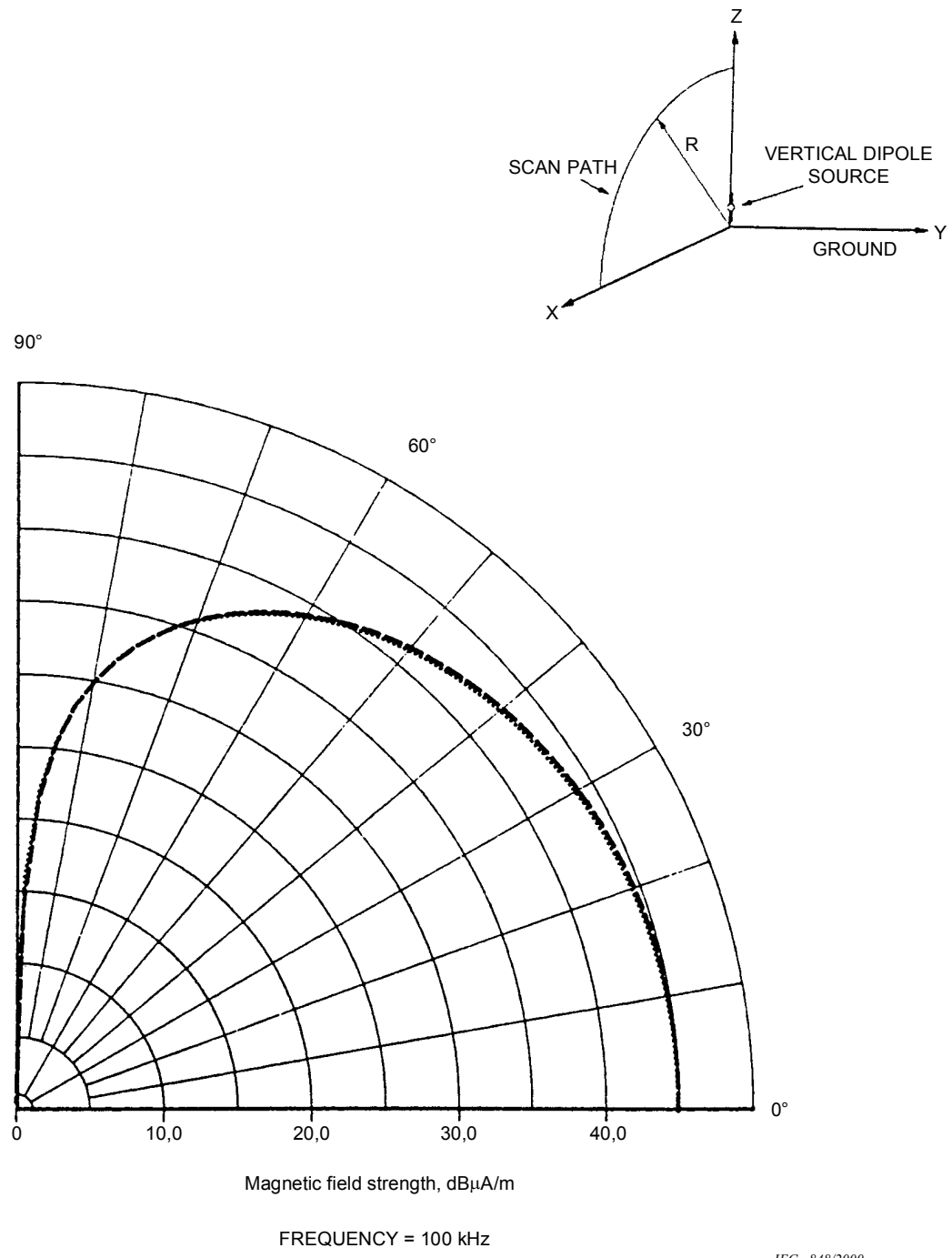
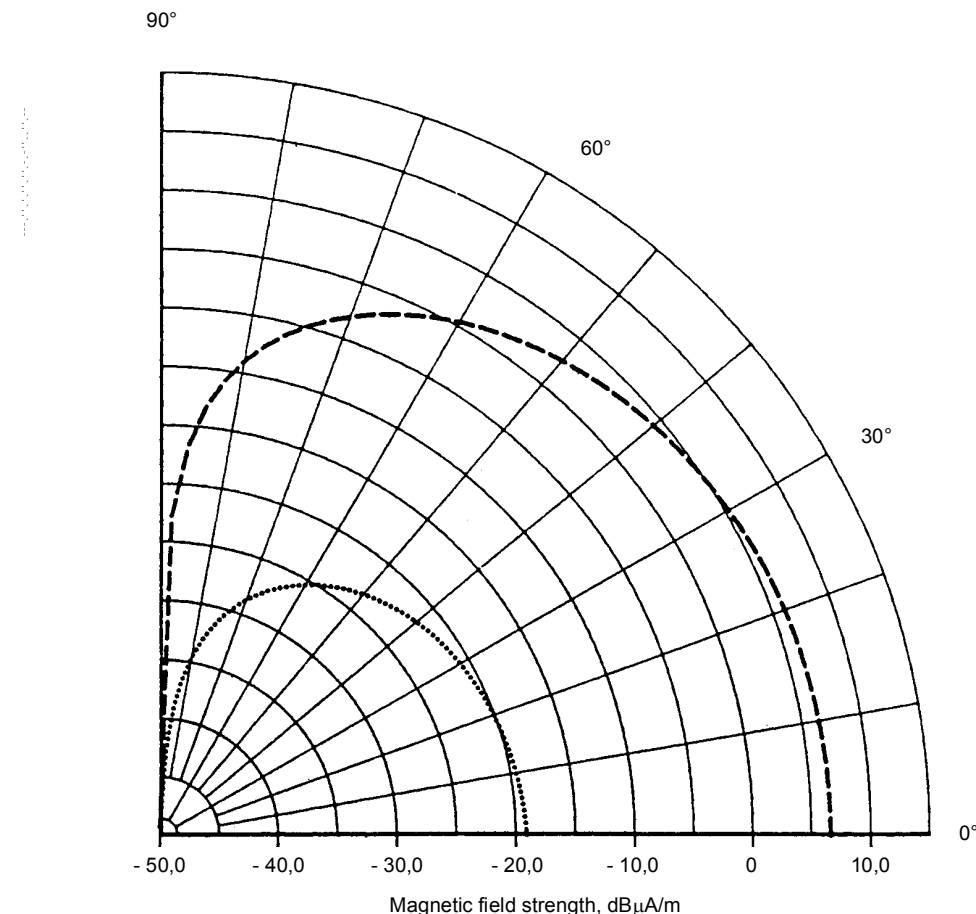
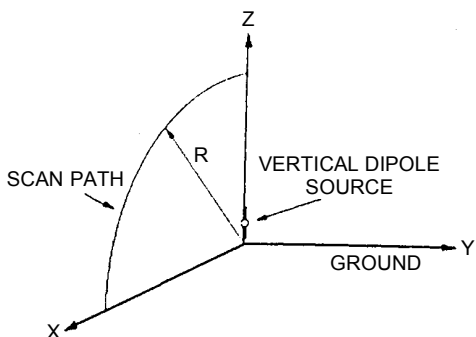


**Figure 4.6-7 – Vertical radiation patterns of the horizontally oriented  $H$ -fields emitted by a small vertical electric dipole located close to the ground**

Dipole length 3 m. Dipole base at a height above ground of 0,15 m. Dipole moment 1 A·m.

Dashed line curve –  $Hy$  at a scan distance of 30 m  
 Electrical constants of the ground:  $\sigma = 1 \text{ mS/m}$ ,  $\epsilon_r = 15$

Dotted line curve –  $Hy$  at a scan distance of 30 m  
 Perfectly conducting ground



FREQUENCY = 100 kHz

IEC 849/2000

**Figure 4.6-8 – Vertical radiation patterns of the horizontally oriented  $H$ -fields emitted by a small vertical electric dipole located close to the ground**

Dipole length 3 m. Dipole base at a height above ground of 0,15 m. Dipole moment 1 A·m.

Dashed line curve –  $Hy$  at a scan distance of 300 m

Dotted line curve –  $Hy$  at a scan distance of 3 000 m

Electrical constants of the ground:  $\sigma = 1 \text{ mS/m}$ ,  $\epsilon_r = 15$

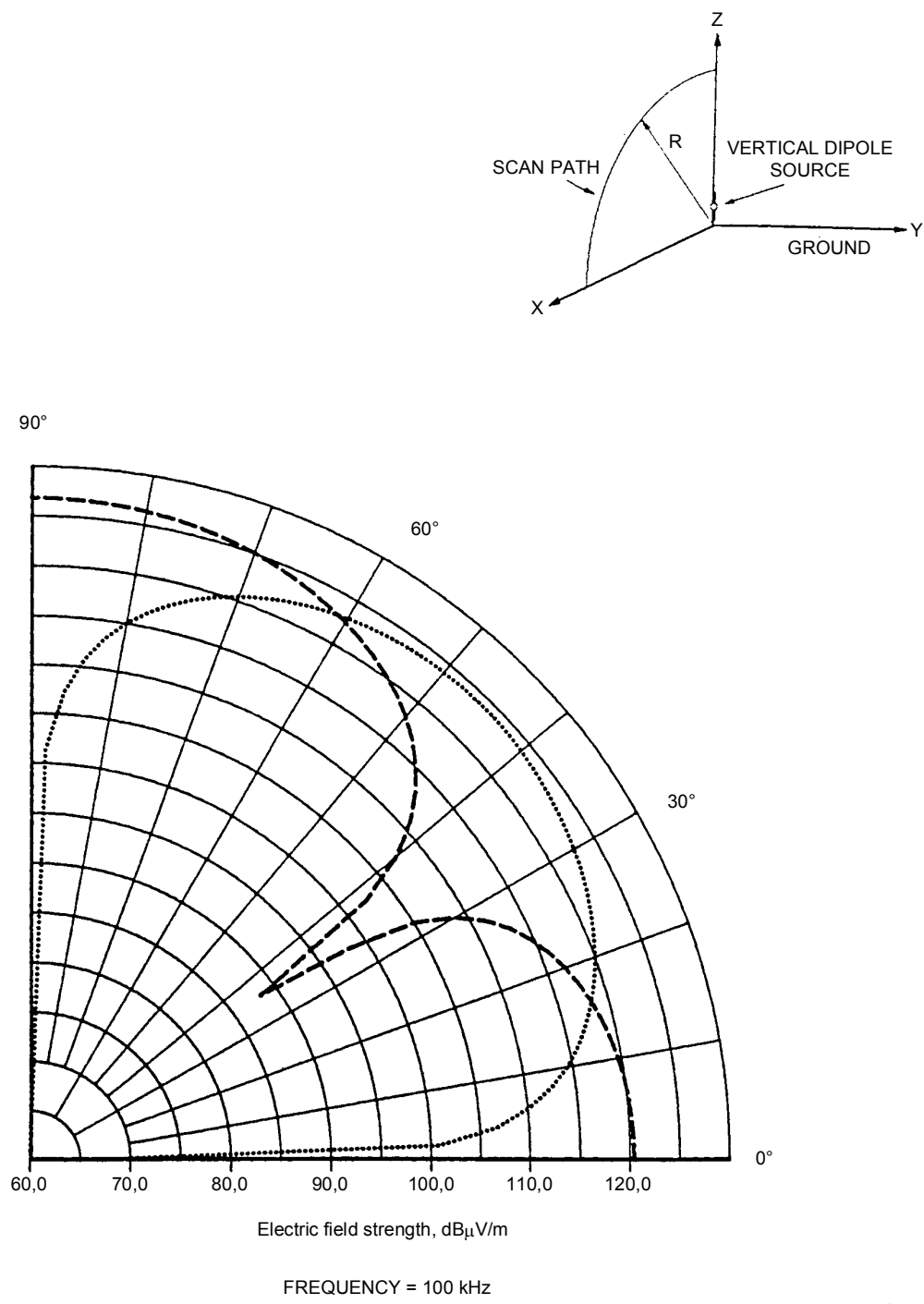


**Figure 4.6-9 – Vertical radiation patterns of  $E$ -fields emitted by a small vertical electric dipole located close to the ground**

Dipole length 3 m. Dipole base height above ground 0,15 m. Dipole moment 1 A·m.

Dashed line curve – vertically oriented  $E_z$  at a scan distance of 30 m  
 Dotted line curve – horizontally oriented  $E_x$  at a scan distance of 30 m  
 Electrical constants of the ground:  $\sigma = 1 \text{ mS/m}$ ,  $\epsilon_r = 15$

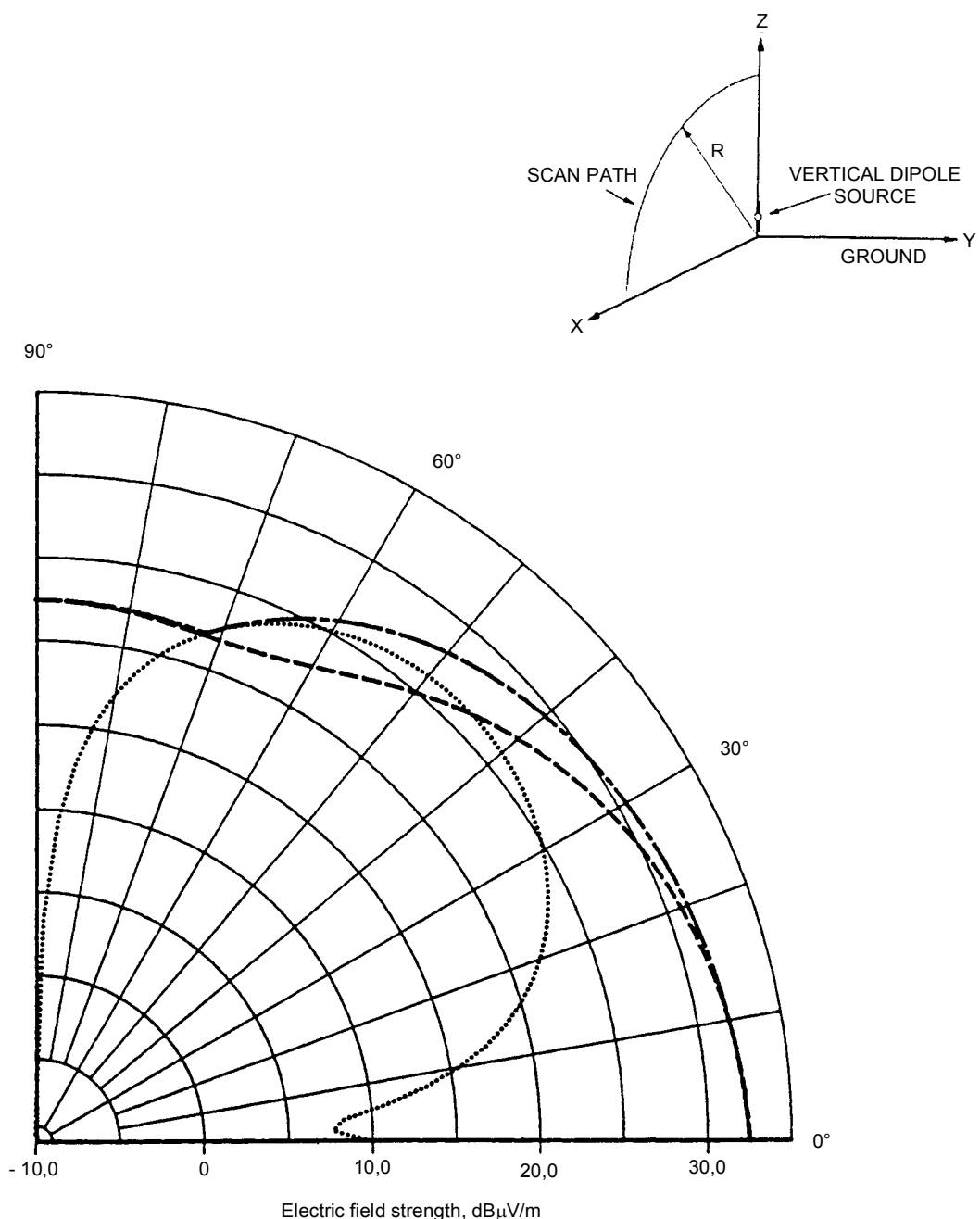


**Figure 4.6-10 – Vertical radiation patterns of the  $E$ -fields emitted by a small vertical electric dipole located close to the ground**

Dipole length 3 m. Dipole base height above ground 0,15 m. Dipole moment 1 A·m.

- Dashed line curve – vertically oriented  $E_z$  at a scan distance of 3 000 m
  - Dotted line curve – horizontally oriented  $E_x$  at a scan distance of 3 000 m
  - dash-dot line curve – total vector/phasor sum of  $E_z$  and  $E_x$  at a scan distance of 3 000 m, the vertically polarized  $E$ -field
- Electrical constants of the ground:  $\sigma = 1 \text{ mS/m}$ ,  $\epsilon_r = 15$

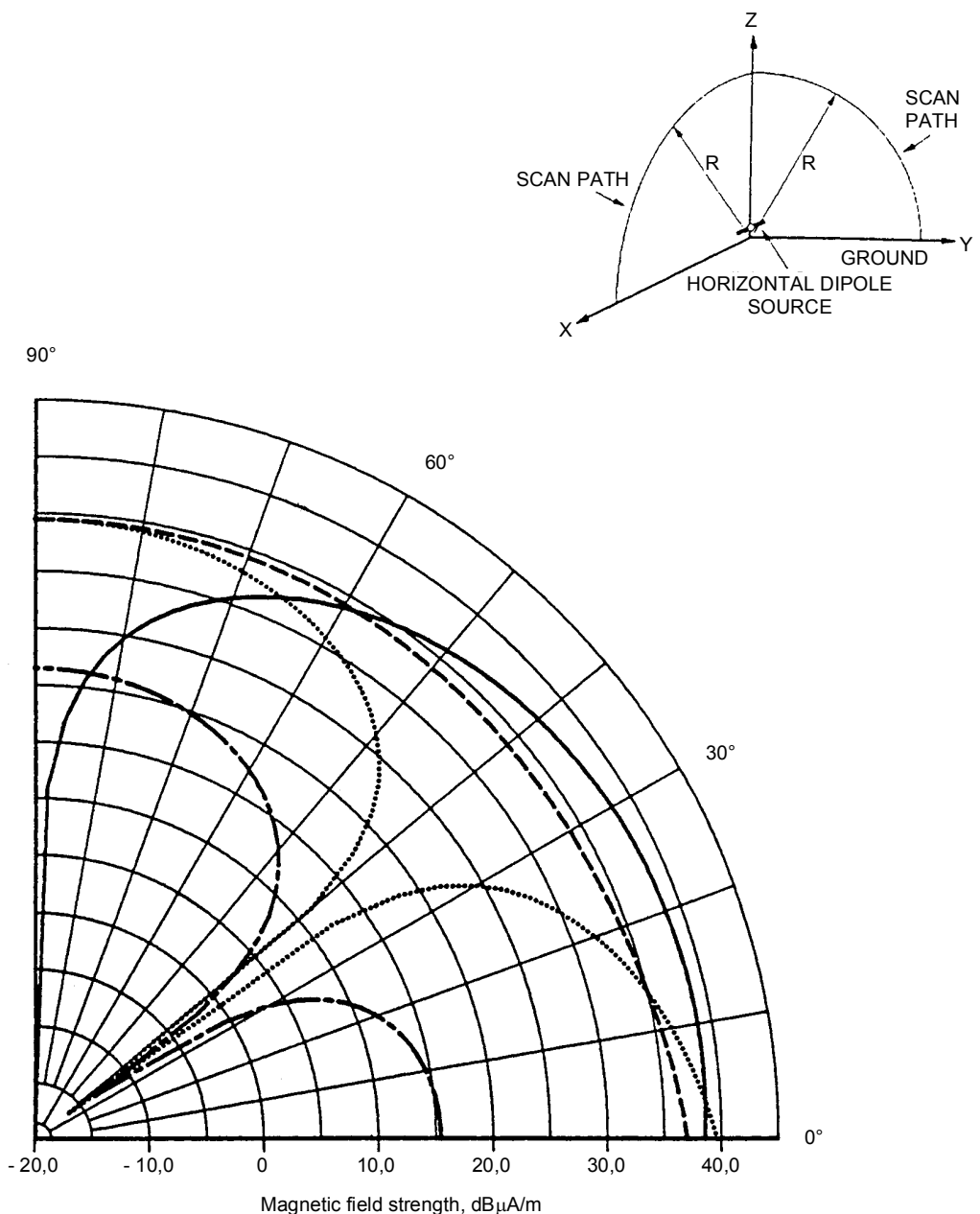


**Figure 4.6-11 – Vertical radiation patterns of the *H*-fields emitted by a small horizontal electric dipole located close to the ground**

Dipole length 3 m. Dipole height above ground 1 m. Dipole moment 1 A·m.

- Dashed line curve – horizontally oriented *Hy* at a scan distance of 30 m in the Z-X plane
- Dotted line curve – horizontally oriented *Hy* at a scan distance of 30 m in the Y-Z plane
- Solid line curve – vertically oriented *Hz* at a scan distance of 30 m in the Y-Z plane
- Electrical constants of the ground:  $\sigma = 1 \text{ mS/m}$ ,  $\epsilon_r = 15$
- Dash-dot line curve – horizontally oriented *Hy* at a scan distance of 30 m in the Z-X plane
- Perfectly conducting ground

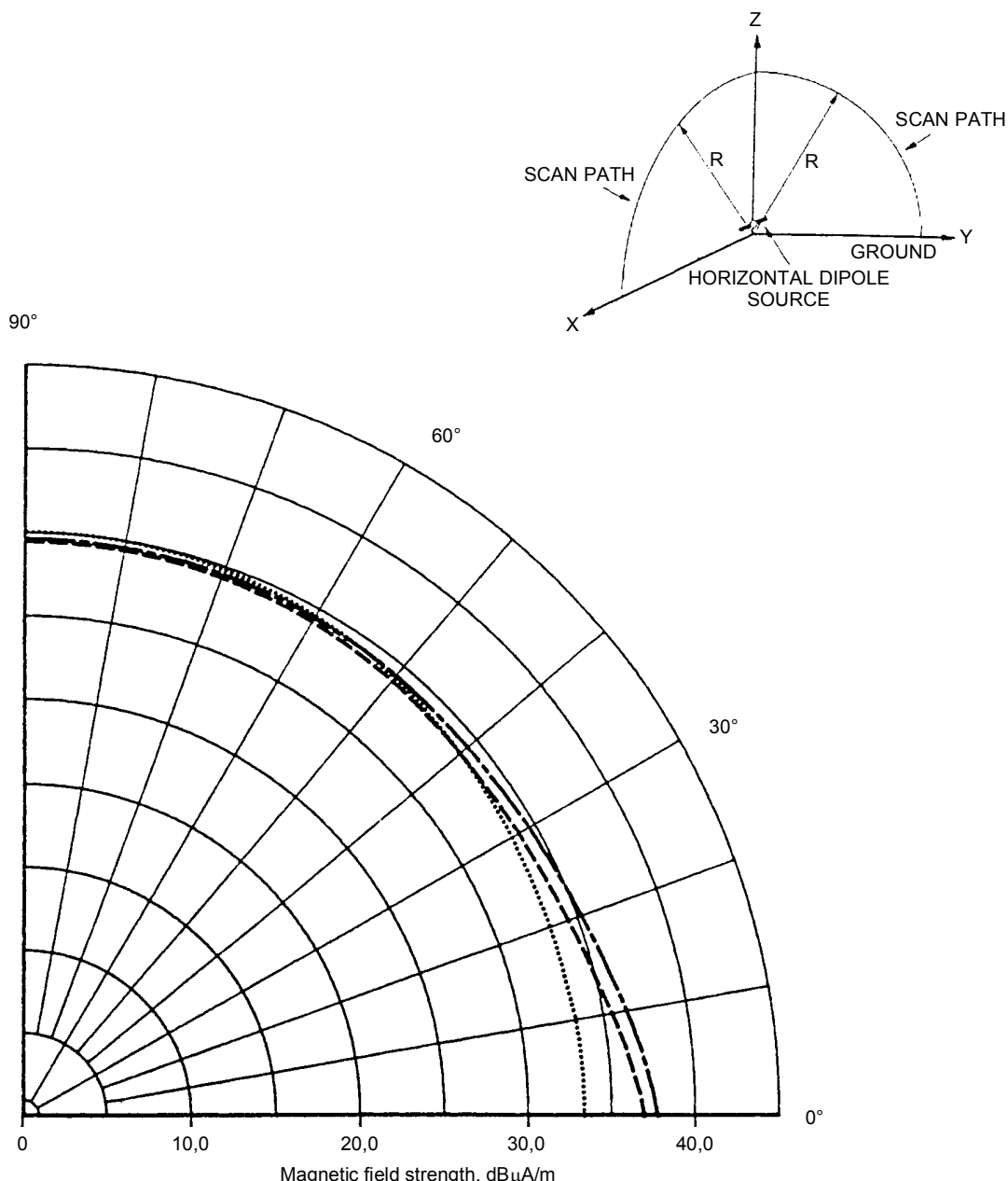


**Figure 4.6-12 – Influence of a wide range of values of the electrical constants of the ground on the vertical radiation patterns of the horizontally oriented  $H$ -fields emitted by a small horizontal electric dipole located close to the ground**

Dipole length 3 m. Dipole height above ground 1 m. Dipole moment 1 A·m.

$H_y$  at a scan distance of 30 m in the Z-X plane

Dash-dot line curve – ground constants are  $\sigma = 0,1 \text{ mS/m}$ ,  $\epsilon_r = 3$

Dashed line curve – ground constants are  $\sigma = 1 \text{ mS/m}$ ,  $\epsilon_r = 15$

Dotted line curve – ground constants are  $\sigma = 10 \text{ mS/m}$ ,  $\epsilon_r = 30$

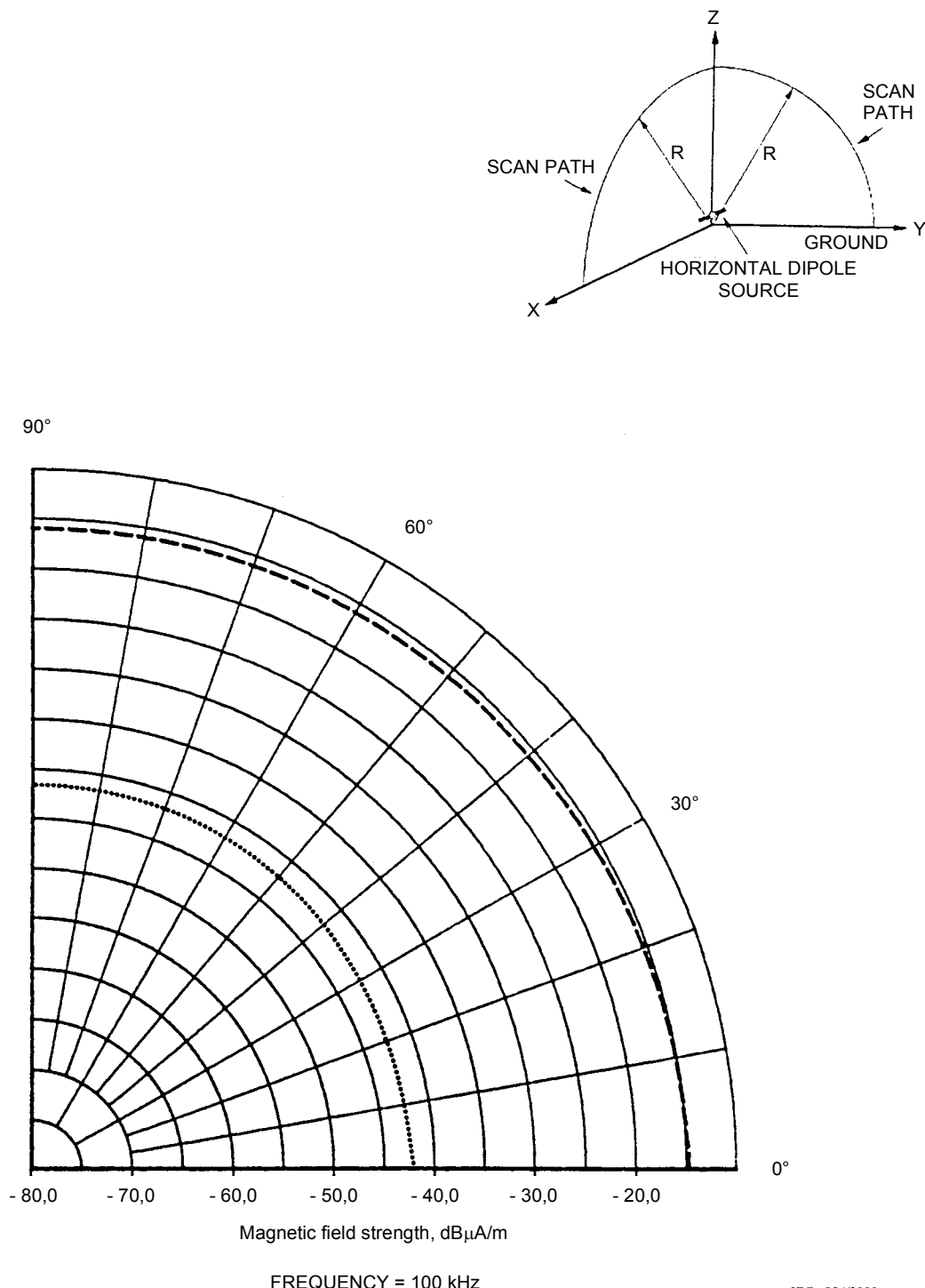


**Figure 4.6-13 – Vertical radiation patterns of the horizontally oriented *H*-fields emitted by a small horizontal electric dipole located close to the ground**

Dipole length 3 m. Dipole height above ground 1 m. Dipole moment 1 A·m.

Dashed line curve –  $Hy$  at a scan distance of 300 m in the Z-X plane  
 Dotted line curve –  $Hy$  at a scan distance of 3 000 m in the Z-X plane  
 Electrical constants of the ground  $\sigma = 1 \text{ mS/m}$ ,  $\epsilon_r = 15$

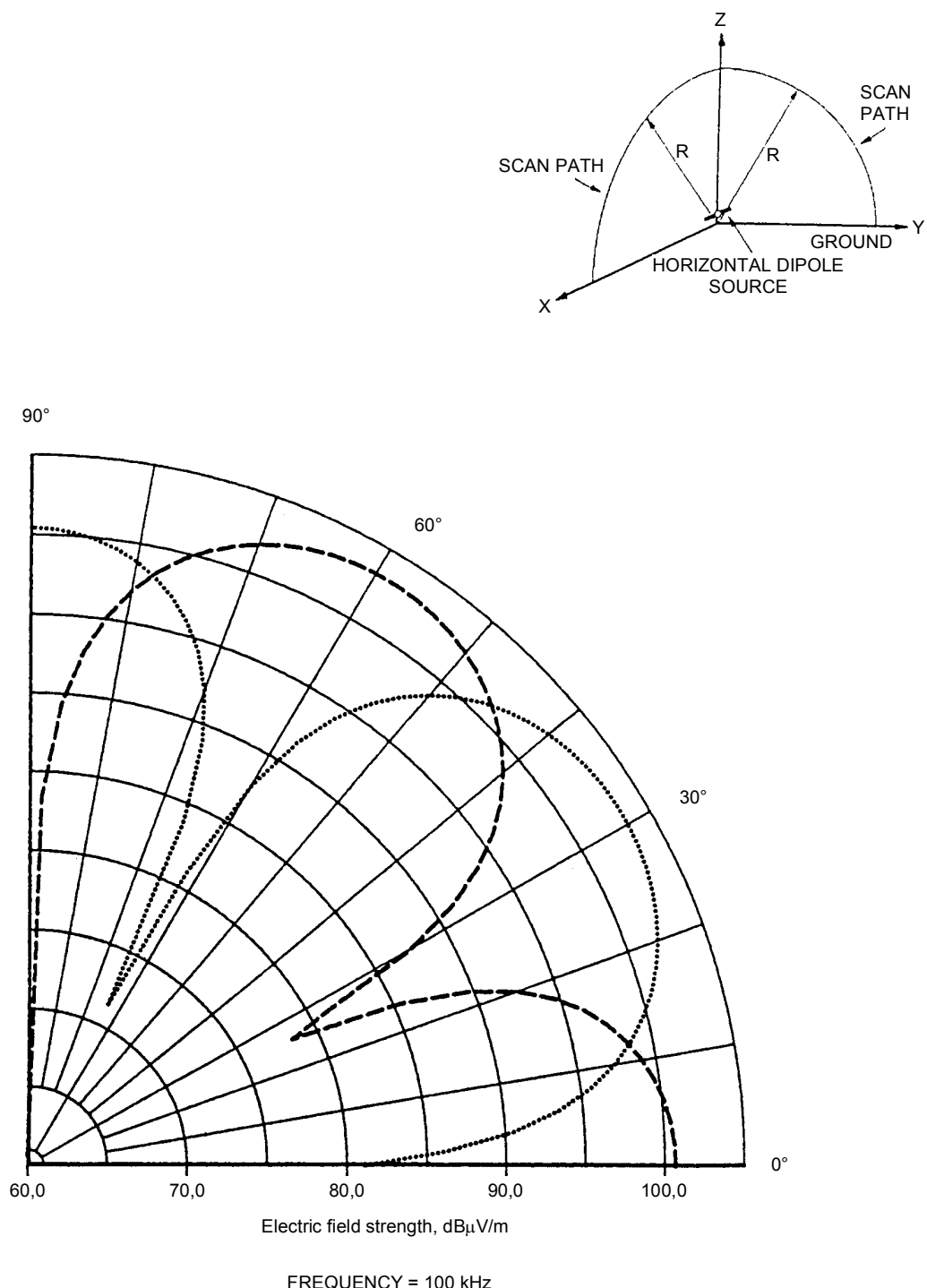


**Figure 4.6-14 – Vertical radiation patterns of the  $E$ -fields emitted by a small horizontal electric dipole located close to the ground**

Dipole length 3 m. Dipole height above ground 1 m. Dipole moment 1 A·m.

Dashed line curve – vertically oriented  $E_z$  at a scan distance of 30 m in the Z-X plane  
 Dotted line curve – horizontally oriented  $E_x$  at a scan distance of 30 m in the Z-X plane  
 Electrical constants of the ground  $\sigma = 1 \text{ mS/m}$ ,  $\epsilon_r = 15$

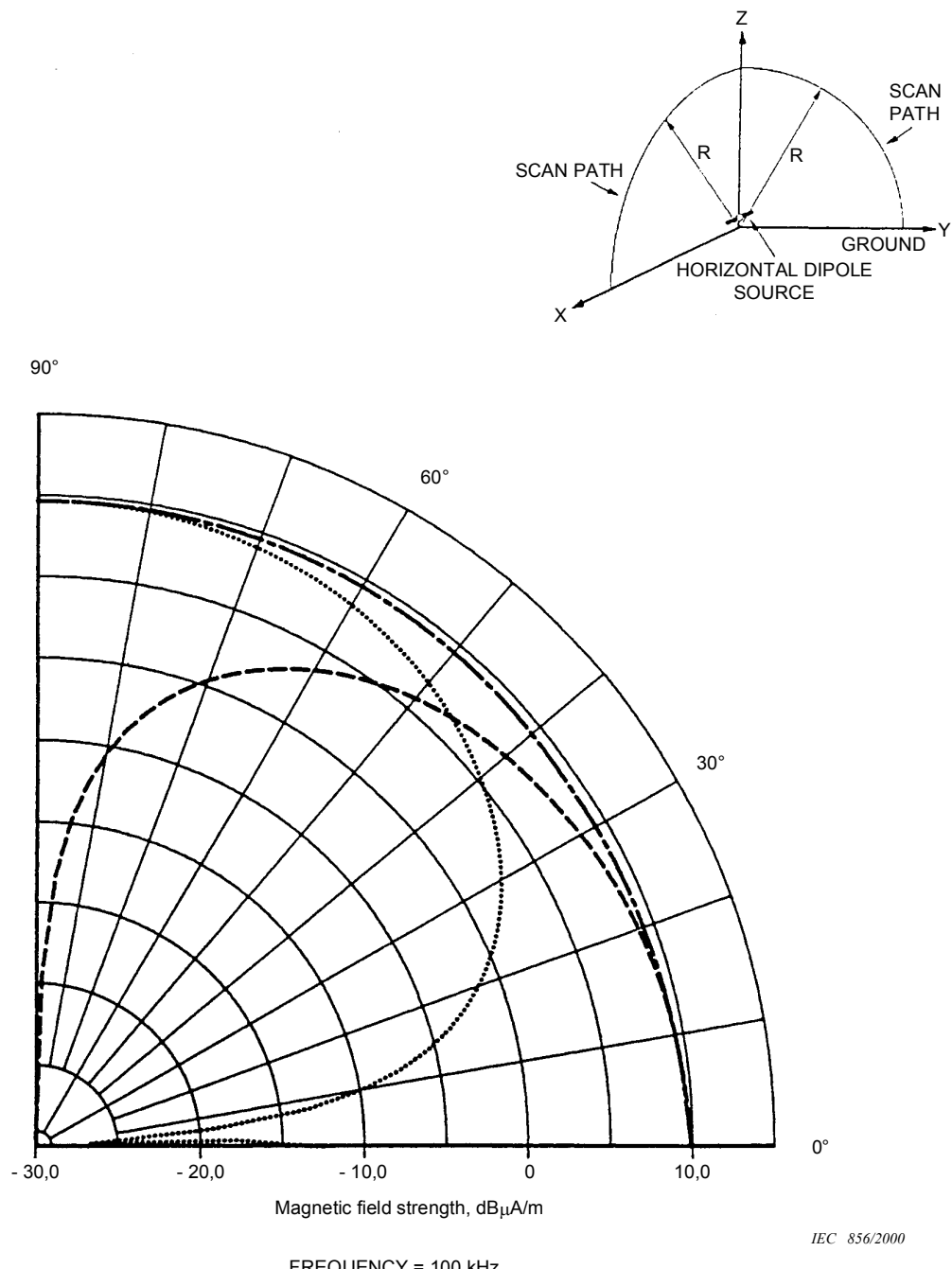


**Figure 4.6-15 – Vertical radiation patterns of the  $E$ -fields emitted by a small horizontal electric dipole located close to the ground**

Dipole length 3 m. Dipole height above ground 1 m. Dipole moment 1 A·m.

- Dashed line curve – vertically oriented  $E_z$  at a scan distance of 3 000 m in the Z-X plane
  - Dotted line curve – horizontally oriented  $E_x$  at a scan distance of 3 000 m in the Z-X plane
  - Dash-dot line curve – total vector/phasor sum of  $E_z$  and  $E_x$  at a scan distance of 3 000 m in the Z-X plane, the vertically polarized  $E$ -field
- Electrical constants of the ground  $\sigma = 1 \text{ mS/m}$ ,  $\epsilon_r = 15$

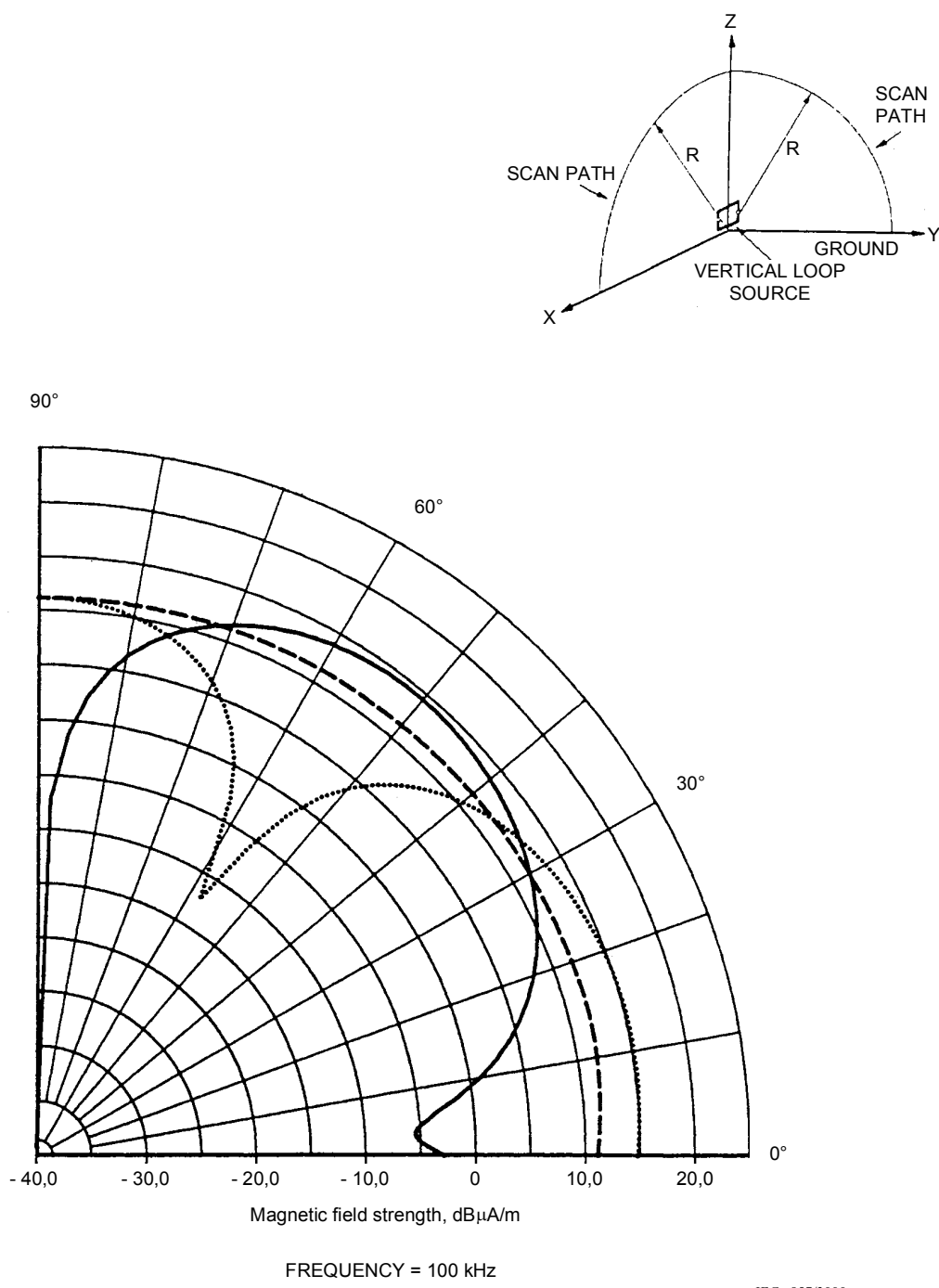


**Figure 4.6-16 – Vertical radiation patterns of the  $H$ -fields emitted by a small horizontal magnetic dipole (vertical loop) located close to the ground**

Square loop  $3\text{ m} \times 3\text{ m}$ . Loop base height above the ground  $1\text{ m}$ . Dipole moment  $1\text{ A}\cdot\text{m}^2$ .

Dashed line curve – horizontally oriented  $H_y$  at a scan distance of  $30\text{ m}$  in the Z-X plane  
 Dotted line curve – horizontally oriented  $H_y$  at a scan distance of  $30\text{ m}$  in the Y-Z plane  
 Solid line curve – vertically oriented  $H_z$  at a scan distance of  $30\text{ m}$  in the Y-Z plane  
 Electrical constants of the ground:  $\sigma = 1\text{ mS/m}$ ,  $\epsilon_r = 15$

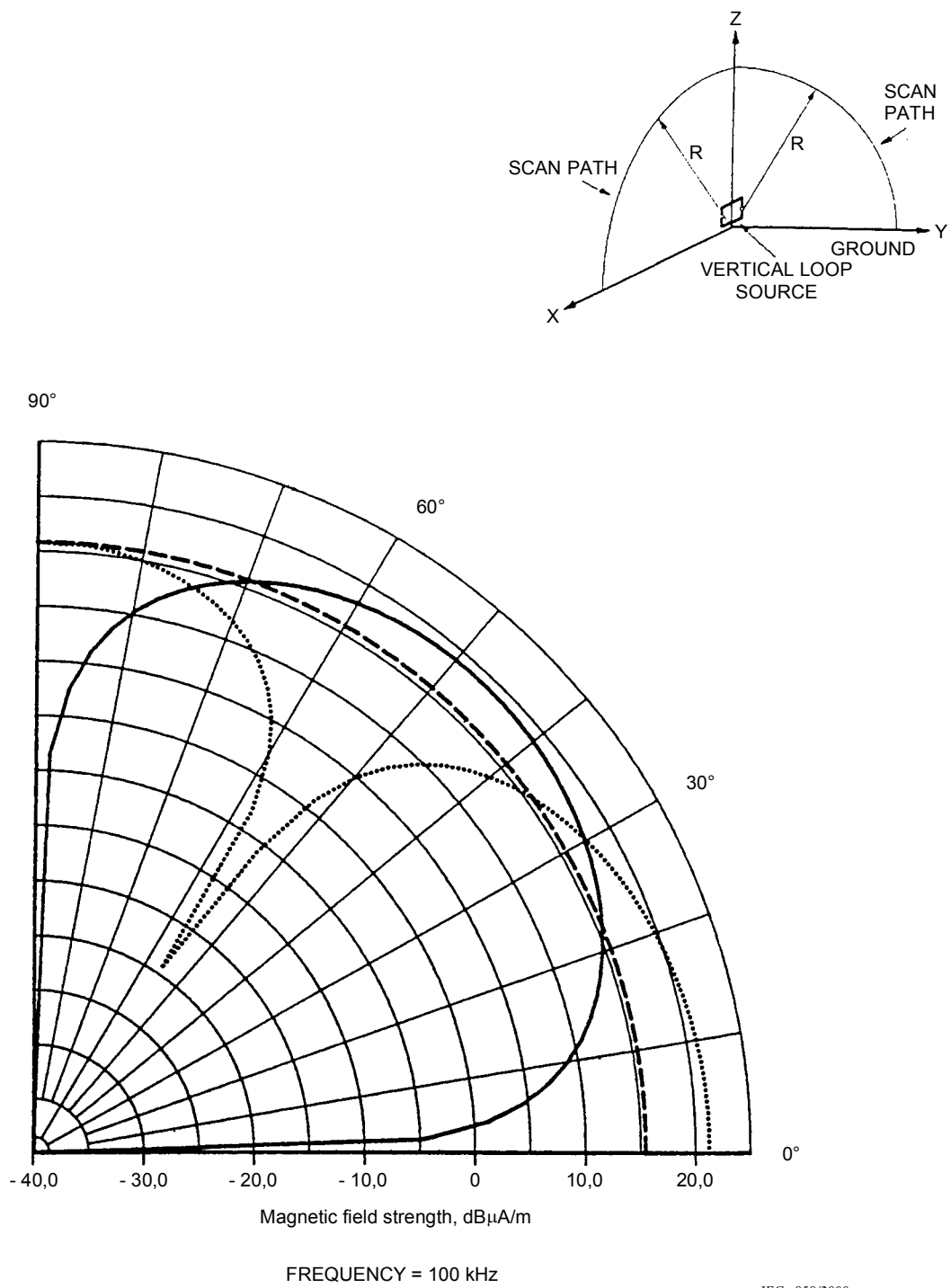


**Figure 4.6-17 – Vertical radiation patterns of the horizontally oriented  $H$ -fields emitted by a small horizontal magnetic dipole (vertical loop) located close to the ground**

Square loop  $3 \text{ m} \times 3 \text{ m}$ . Loop base height above ground 1 m. Dipole moment  $1 \text{ A}\cdot\text{m}^2$ .

- Dashed line curve – horizontally oriented  $H_y$  at a scan distance of 30 m in the Z-X plane
- Dotted line curve – horizontally oriented  $H_y$  at a scan distance of 30 m in the Y-Z plane
- Solid line curve – vertically oriented  $H_z$  at a scan distance of 30 m in the Y-Z plane
- Perfectly conducting ground

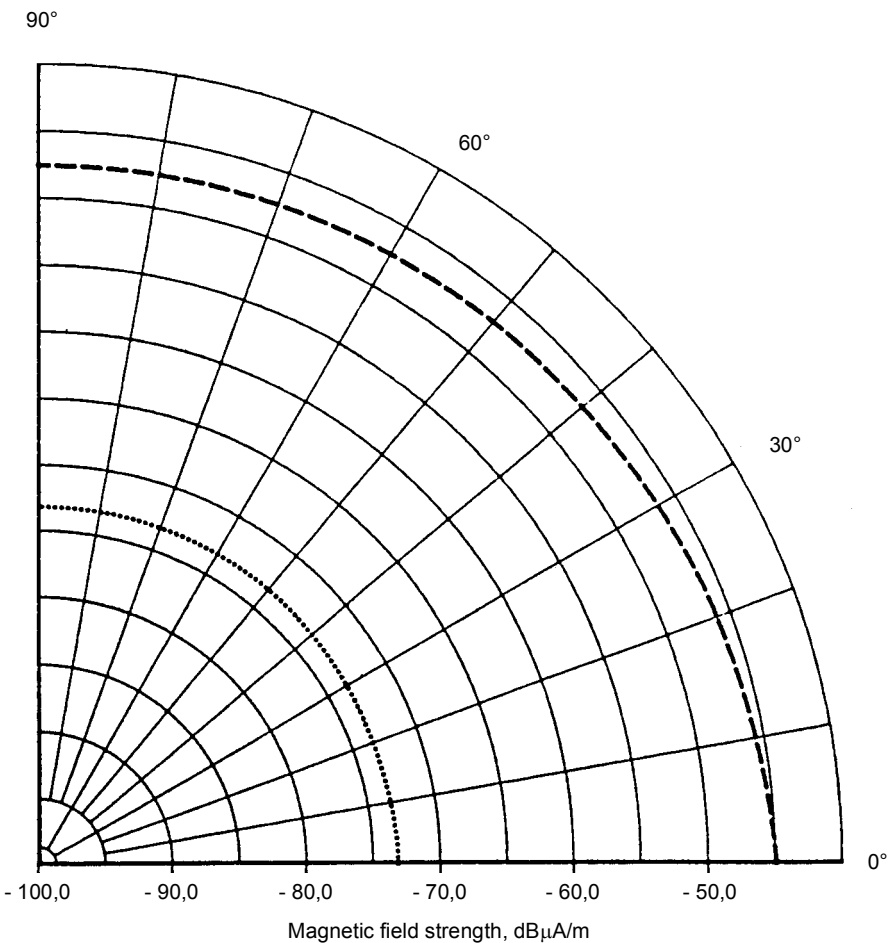
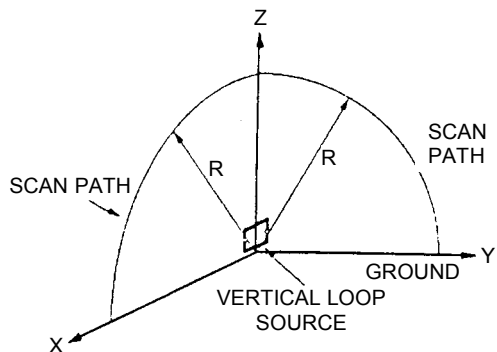


**Figure 4.6-18 – Vertical radiation patterns of the horizontally oriented  $H$ -fields emitted by a small horizontal magnetic dipole (vertical loop) located close to the ground**

Square loop  $3 \text{ m} \times 3 \text{ m}$ . Loop base height above ground  $1 \text{ m}$ . Dipole moment  $1 \text{ A}\cdot\text{m}^2$ .

Dashed line curve –  $Hy$  at a scan distance of  $300 \text{ m}$  in the  $Z$ - $X$  plane  
 Dotted line curve –  $Hy$  at a scan distance of  $3000 \text{ m}$  in the  $Z$ - $X$  plane  
 Electrical constants of the ground  $\sigma = 1 \text{ mS/m}$ ,  $\epsilon_r = 15$

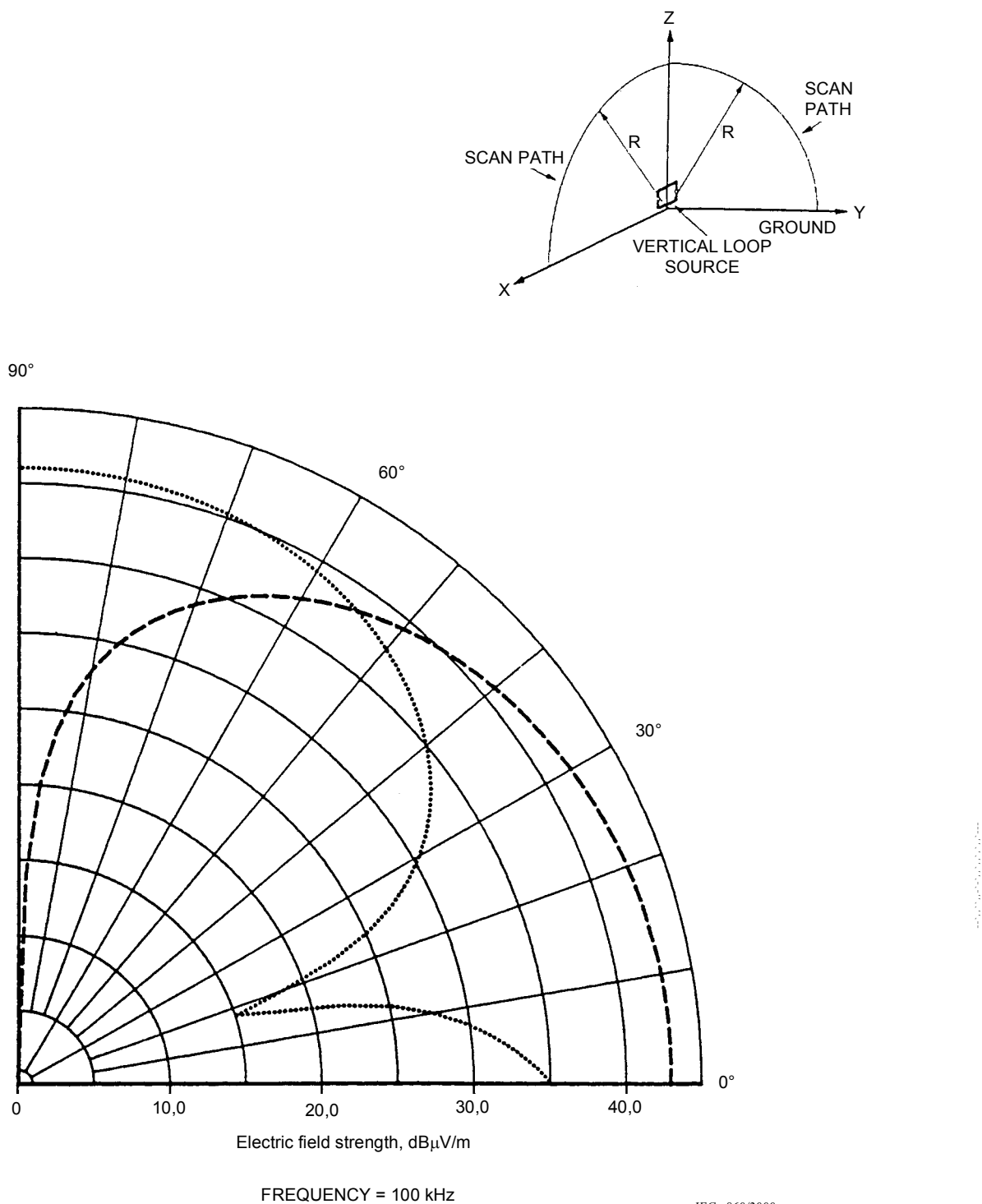


**Figure 4.6-19 – Vertical radiation patterns of the *E*-fields emitted by a small horizontal magnetic dipole (vertical loop) located close to the ground**

Square loop  $3\text{ m} \times 3\text{ m}$ . Loop base height above ground 1 m. Dipole moment  $1\text{ A}\cdot\text{m}^2$ .

Dashed line curve – vertically oriented *Ez* at a scan distance of 30 m in the Z-X plane  
 Dotted line curve – horizontally oriented *Ex* at a scan distance of 30 m in the Z-X plane  
 Electrical constants of the ground  $\sigma = 1\text{ mS/m}$ ,  $\epsilon_r = 15$

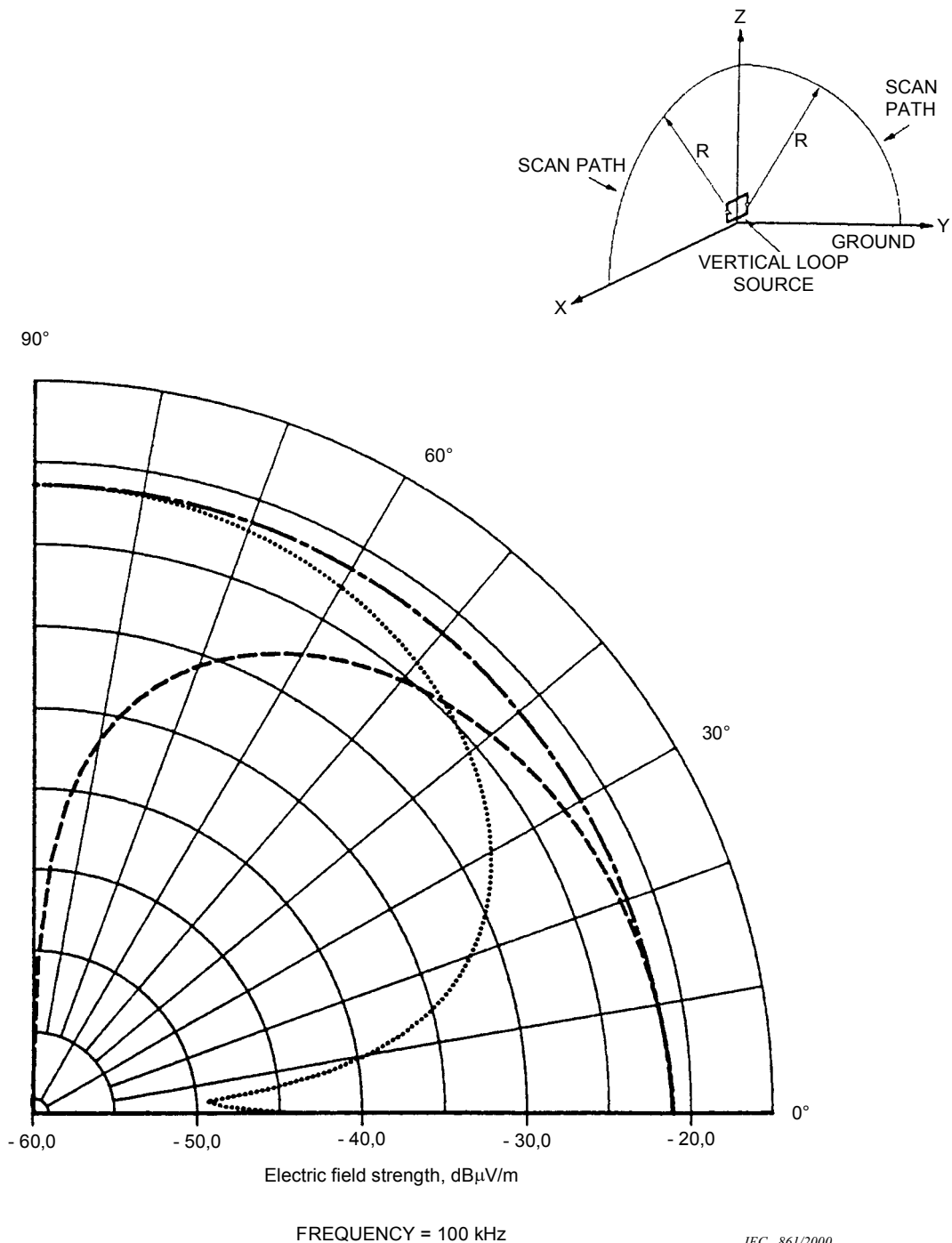


**Figure 4.6-20 – Vertical radiation patterns of the  $E$ -fields emitted by a small horizontal magnetic dipole (vertical loop) located close to the ground**

Square loop  $3\text{ m} \times 3\text{ m}$ . Loop base height above ground 1 m. Dipole moment  $1\text{ A}\cdot\text{m}^2$ .

- Dashed line curve – vertically oriented  $E_z$  at a scan distance of 3 000 m in the Z-X plane
  - Dotted line curve – horizontally oriented  $E_x$  at a scan distance of 3 000 m in the Z-X plane
  - Dash-dot line curve – total vector/phasor sum of  $E_z$  and  $E_x$  at a scan distance of 3 000 m in the Z-X plane, the vertically polarized  $E$ -field
- Electrical constants of the ground  $\sigma = 1\text{ mS/m}$ ,  $\epsilon_r = 15$

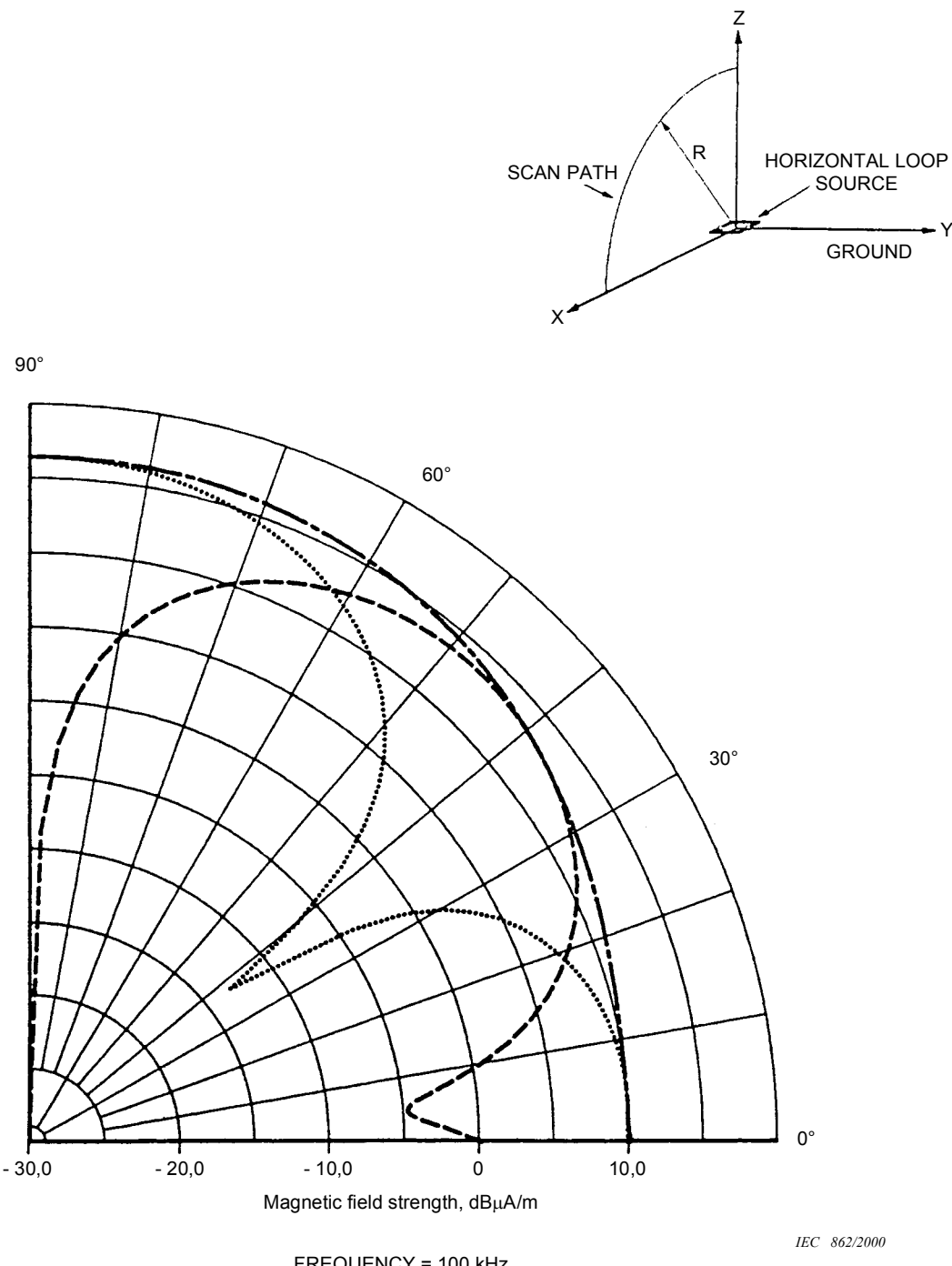
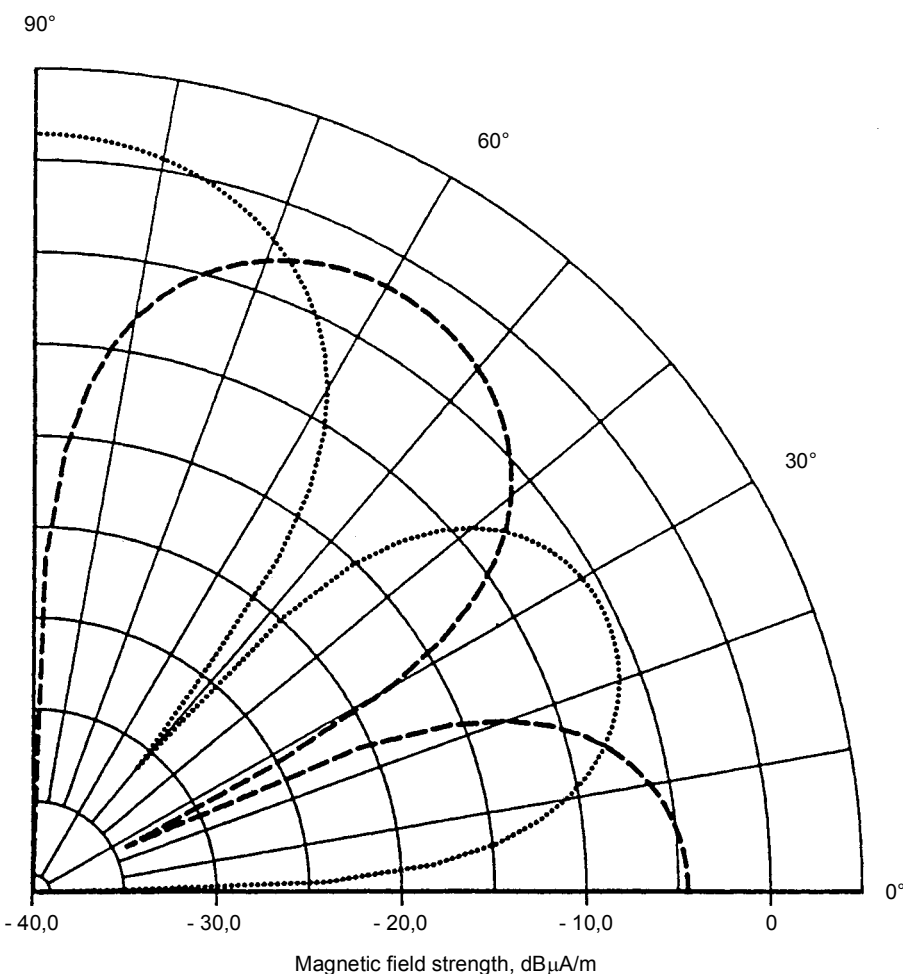
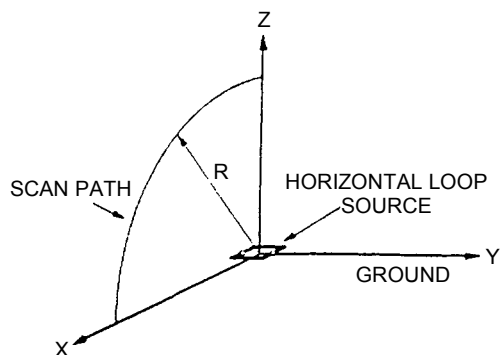


**Figure 4.6-21 – Vertical radiation patterns of the  $H$ -fields emitted by a small vertical magnetic dipole (horizontal loop) located close to the ground**

Square loop  $3\text{ m} \times 3\text{ m}$ . Loop height above ground  $1\text{ m}$ . Dipole moment  $1\text{ A}\cdot\text{m}^2$ .

- Dashed line curve – horizontally oriented  $H_x$  at a scan distance of  $30\text{ m}$
  - Dotted line curve – horizontally oriented  $H_z$  at a scan distance of  $30\text{ m}$
  - dash-dot line curve – total vector/phasor sum of  $H_x$  and  $H_z$  at a scan distance of  $30\text{ m}$ , the total  $H$ -field component of the horizontally polarized radiation
- Electrical constants of the ground  $\sigma = 1\text{ mS/m}$ ,  $\epsilon_r = 15$



FREQUENCY = 100 kHz

IEC 863/2000

**Figure 4.6-22 – Vertical radiation patterns of the  $H$ -fields emitted by a small vertical magnetic dipole (horizontal loop) located close to the ground**

Square loop 3 m × 3 m. Loop height above ground 1 m. Dipole moment 1 A·m<sup>2</sup>.

Dashed line curve – horizontally oriented  $H_x$  at a scan distance of 30 m  
 Dotted line curve – vertically oriented  $H_z$  at a scan distance of 30 m  
 Perfectly conducting ground

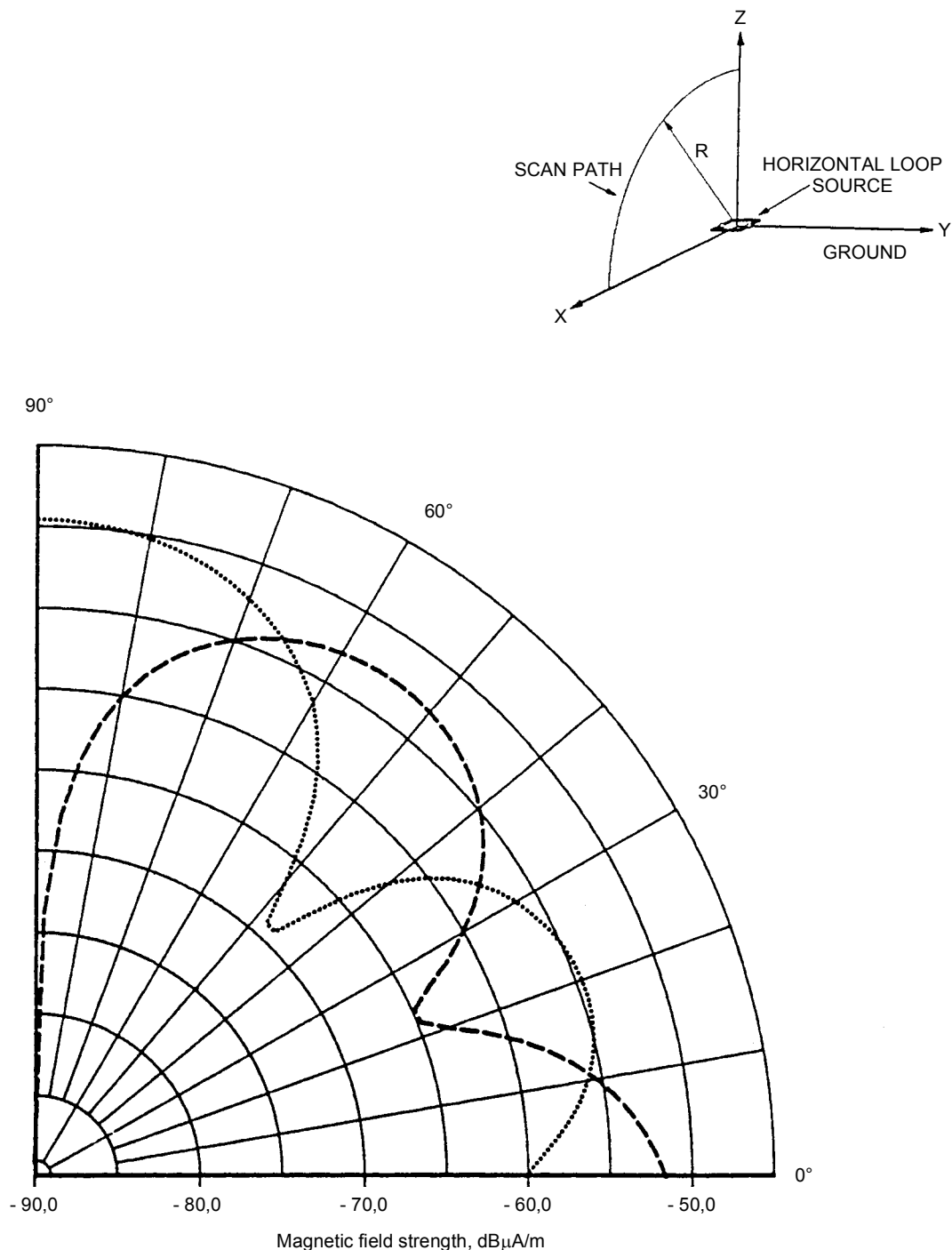


**Figure 4.6-23 – Vertical radiation patterns of the  $H$ -fields emitted by a small vertical magnetic dipole (horizontal loop) located close to the ground**

Square loop  $3\text{ m} \times 3\text{ m}$ . Loop height above ground 1 m. Dipole moment  $1\text{ A}\cdot\text{m}^2$ .

Dashed line curve – horizontally oriented  $H_x$  at a scan distance of 300 m  
 Dotted line curve – vertically oriented  $H_z$  at a scan distance of 300 m  
 Electrical constants of the ground  $\sigma = 1\text{ mS/m}$ ,  $\epsilon_r = 15$

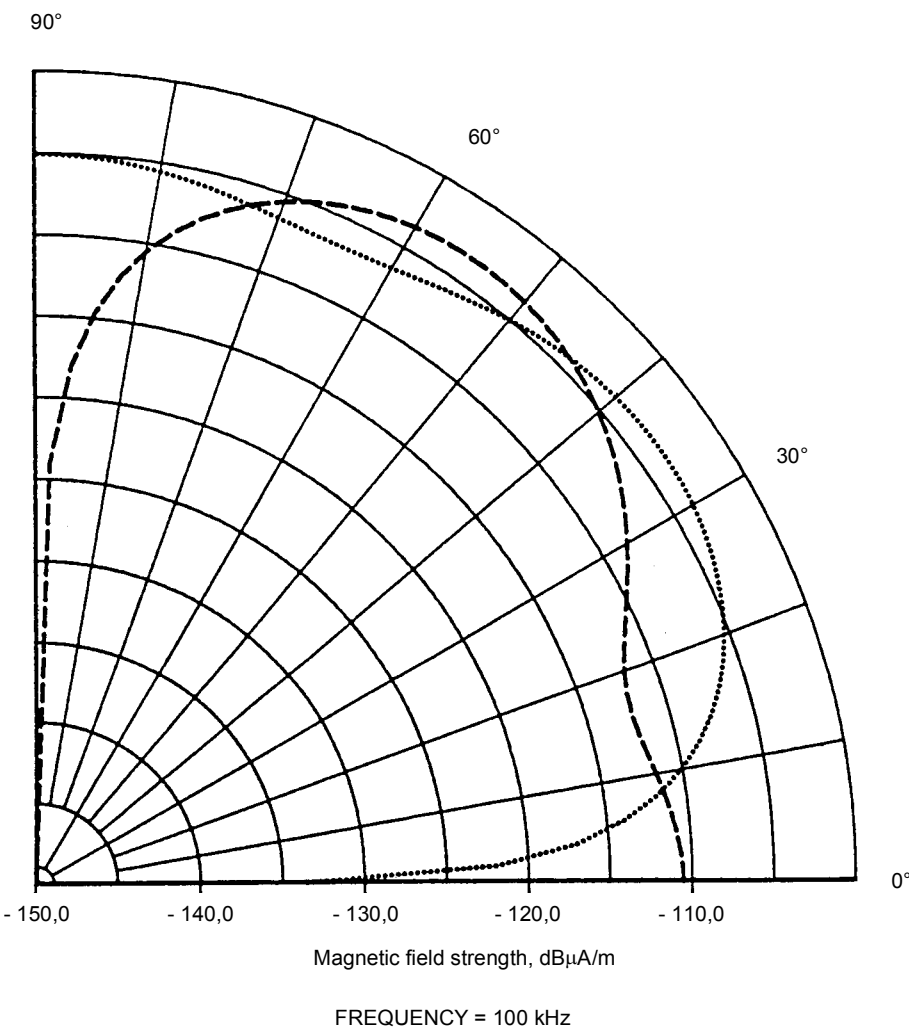
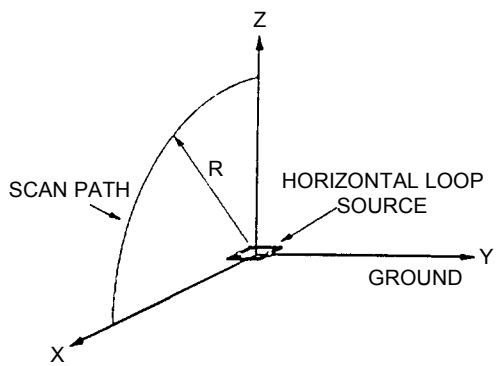


**Figure 4.6-24 – Vertical radiation patterns of the *H*-fields emitted by a small vertical magnetic dipole (horizontal loop) located close to the ground**

Square loop 3 m × 3 m. Loop height above ground 1 m. Dipole moment 1 A·m<sup>2</sup>.

Dashed line curve – horizontally oriented *Hx* at a scan distance of 3 000 m  
 Dotted line curve – vertically oriented *Hz* at a scan distance of 3 000 m  
 Electrical constants of the ground  $\sigma = 1 \text{ mS/m}$ ,  $\epsilon_r = 15$

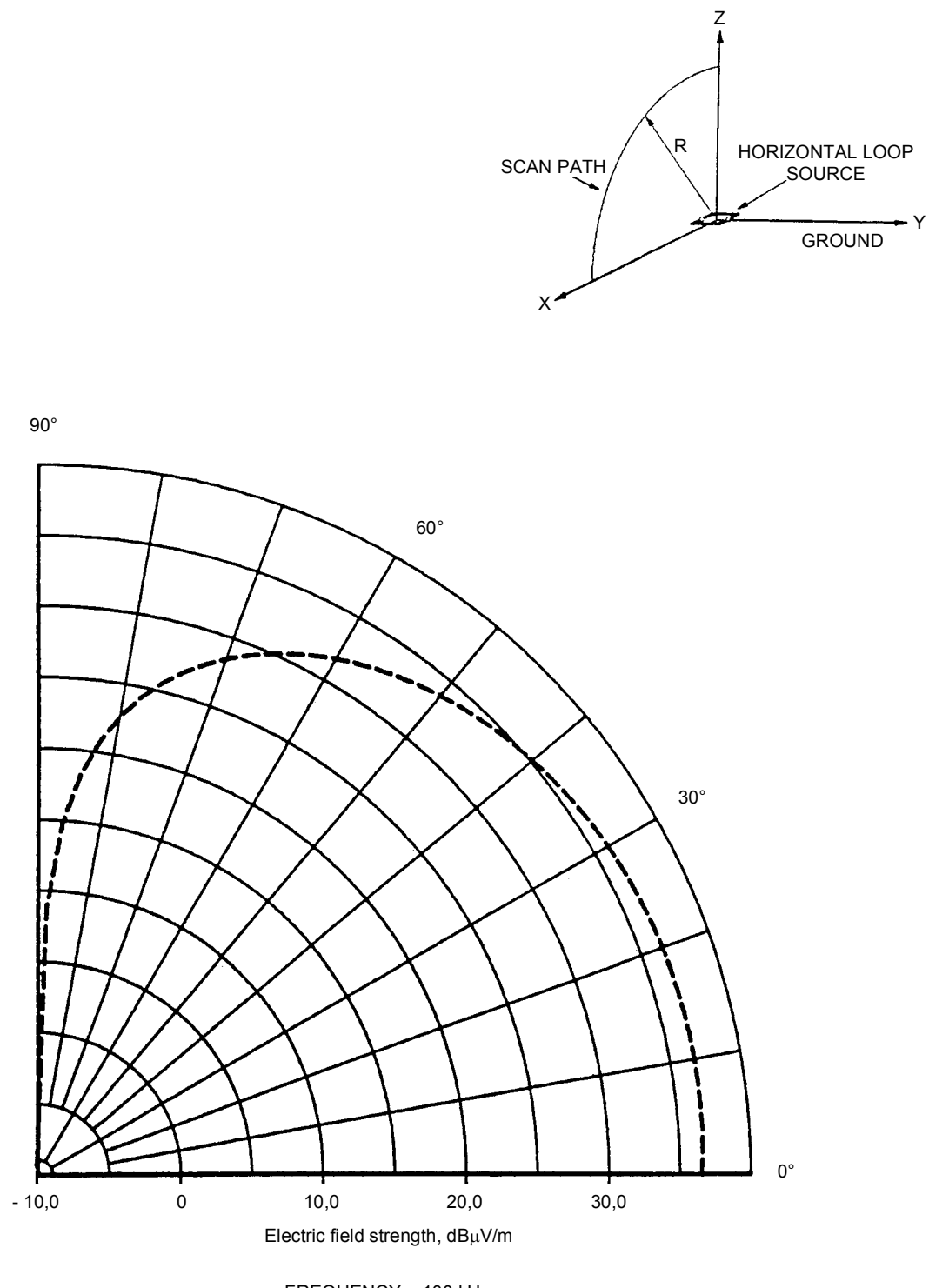


**Figure 4.6-25 – Vertical radiation pattern of the  $E$ -field emitted by a small vertical magnetic dipole (horizontal loop) located close to the ground**

Square loop  $3 \text{ m} \times 3 \text{ m}$ . Loop height above ground  $1 \text{ m}$ . Dipole moment  $1 \text{ A}\cdot\text{m}^2$ .

Dashed line curve – horizontally oriented  $E_y$  at a scan distance of  $30 \text{ m}$   
 Electrical constants of the ground  $\sigma = 1 \text{ mS/m}$ ,  $\epsilon_r = 15$

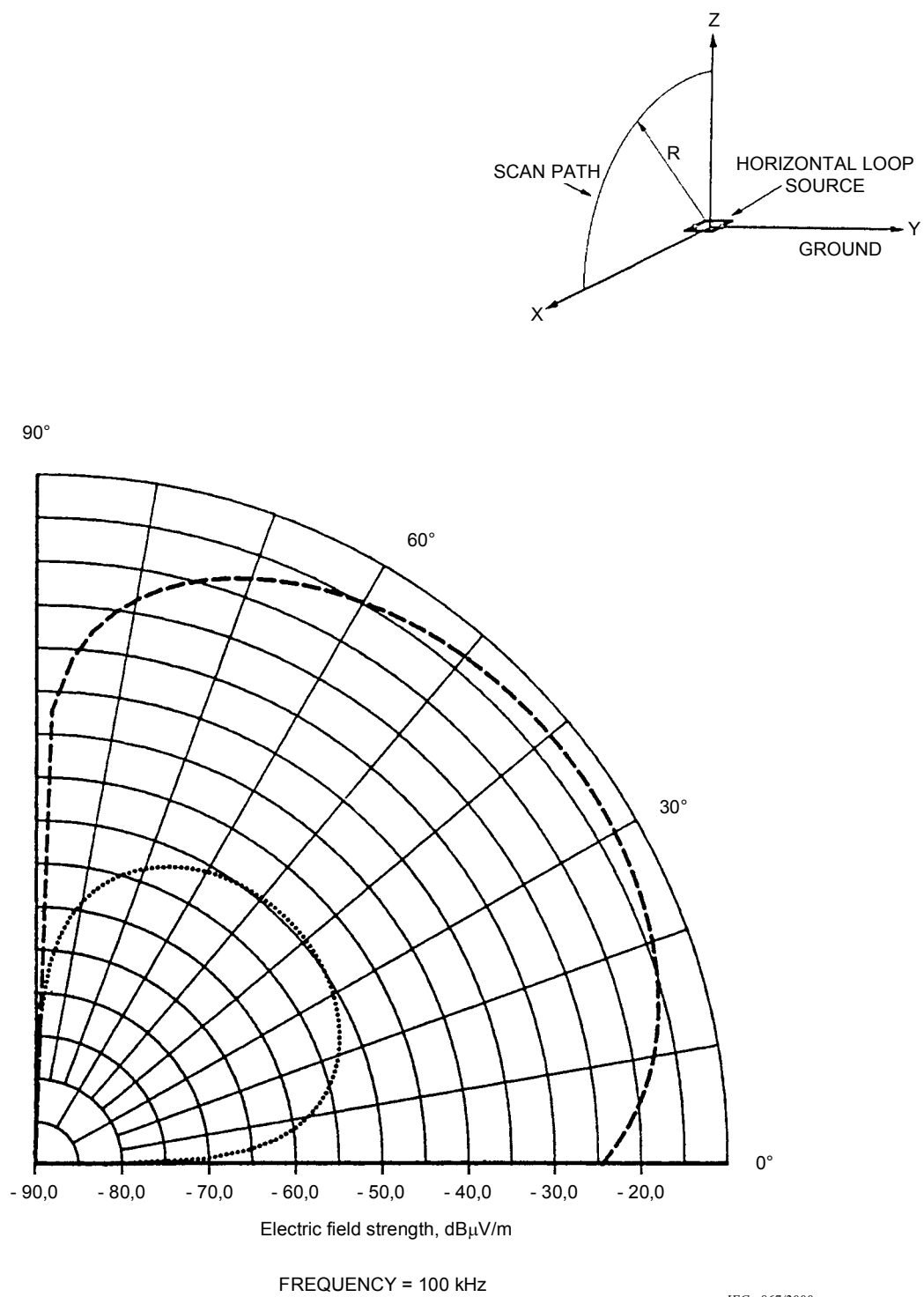


**Figure 4.6-26 – Vertical radiation patterns of the  $E$ -fields emitted by a small vertical magnetic dipole (horizontal loop) located close to the ground**

Square loop  $3 \text{ m} \times 3 \text{ m}$ . Loop height above ground 1 m. Dipole moment  $1 \text{ A}\cdot\text{m}^2$ .

Dashed line curve – horizontally oriented  $E_y$  at a scan distance of 300 m  
 Dotted line curve – horizontally oriented  $E_y$  at a scan distance of 3 000 m  
 Electrical constants of the ground  $\sigma = 1 \text{ mS/m}$ ,  $\epsilon_r = 15$

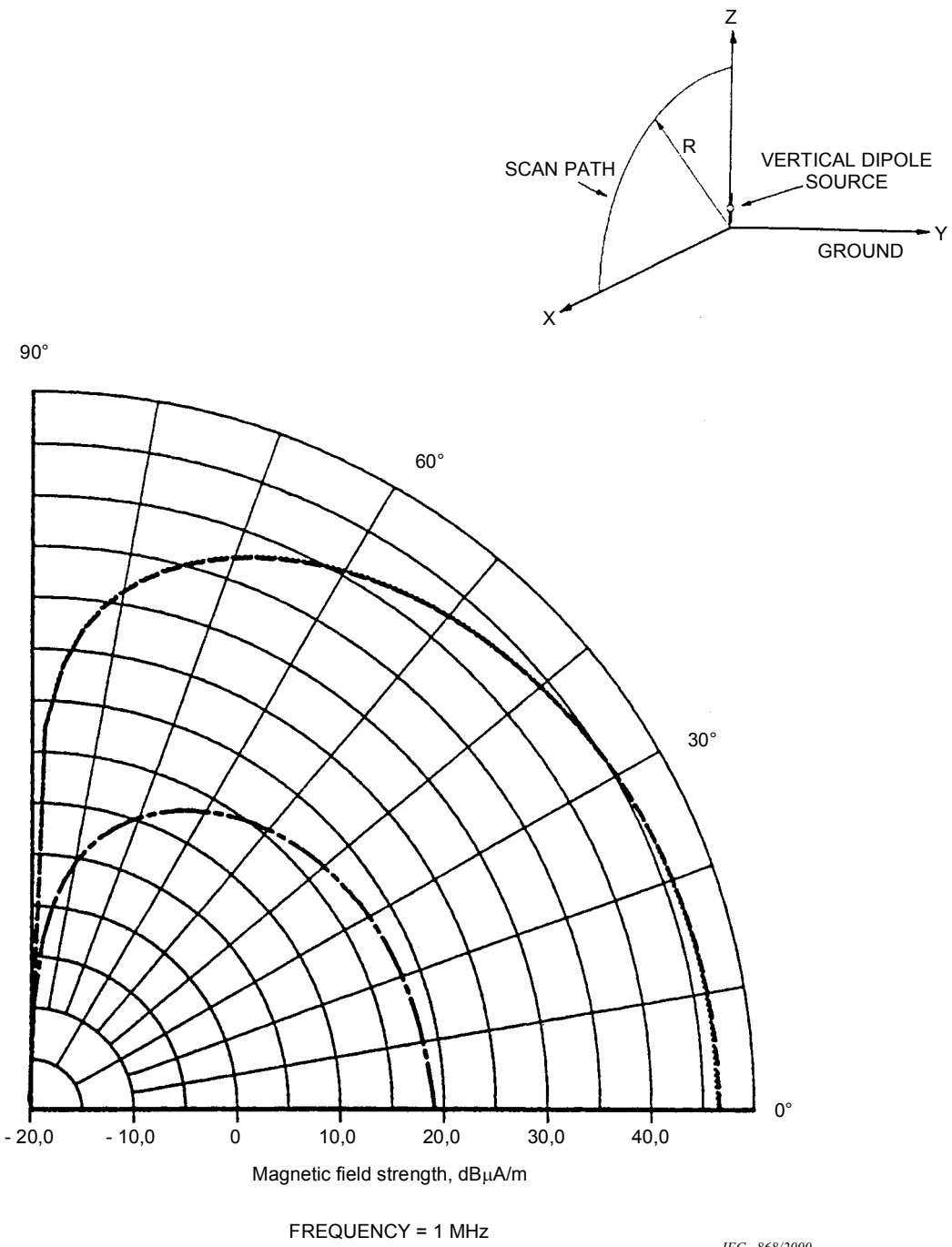


**Figure 4.6-27 – Vertical radiation patterns of the horizontally oriented  $H$ -fields emitted by a small vertical electric dipole located close to the ground**

Dipole length 3 m. Dipole base at a height above ground of 0,15 m. Dipole moment 1 A·m.

- Dashed line curve –  $H_y$  at a scan distance of 30 m
- Dash-dot line curve –  $H_y$  at a scan distance of 300 m
- Electrical constants of the ground  $\sigma = 1 \text{ mS/m}$ ,  $\epsilon_r = 15$
- Dotted line curve –  $H_y$  at a scan distance of 30 m
- Perfectly conducting ground

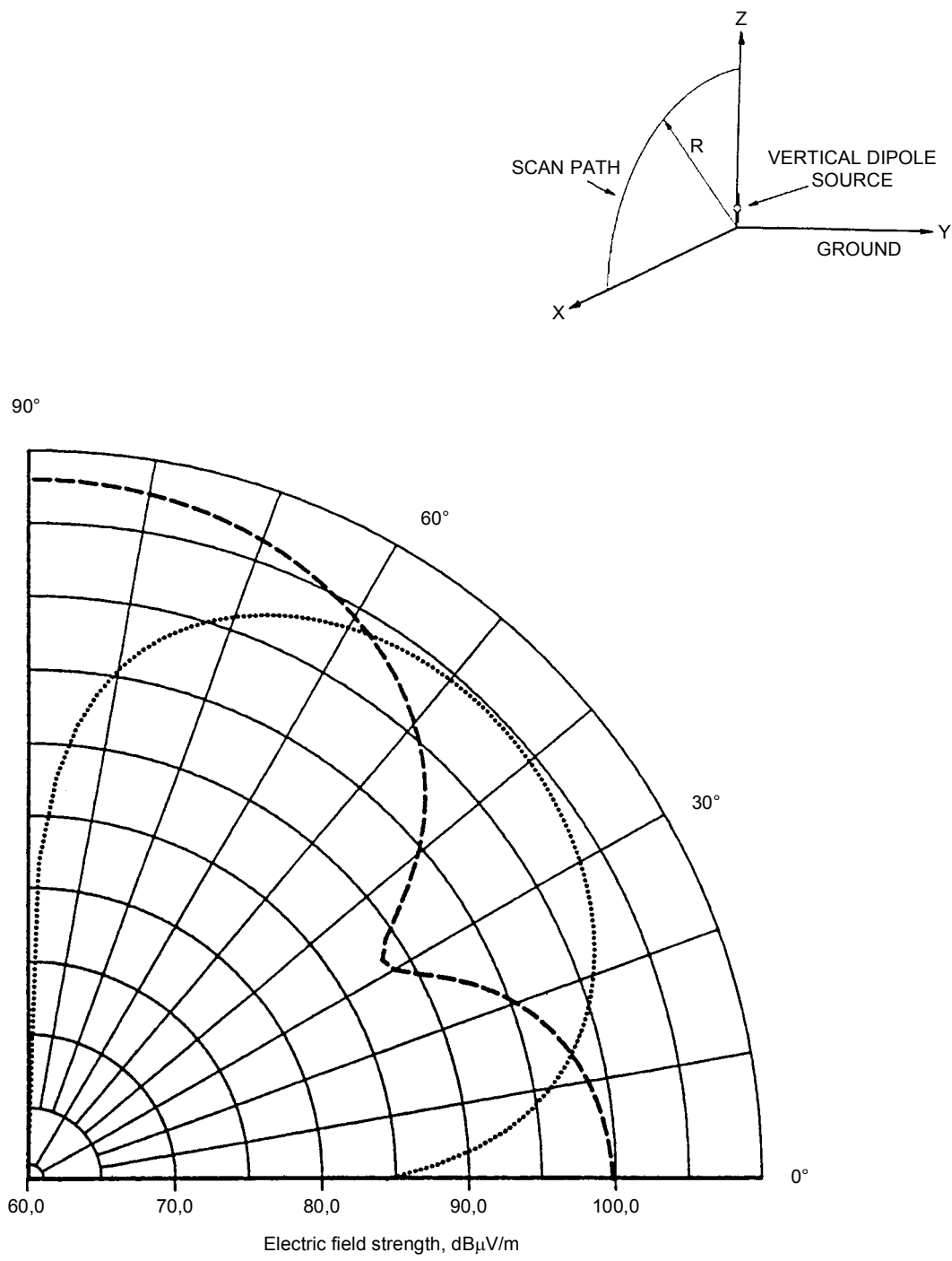


**Figure 4.6-28 – Vertical radiation patterns of the  $E$ -fields emitted by a small vertical electric dipole located close to the ground**

Dipole length 3 m. Dipole base at a height above ground of 0,15 m. Dipole moment 1 A·m.

Dashed line curve – vertically oriented  $E_z$  at a scan distance of 30 m

Dotted line curve – horizontally oriented  $E_x$  at a scan distance of 30 m

Electrical constants of the ground  $\sigma = 1 \text{ mS/m}$ ,  $\epsilon_r = 15$

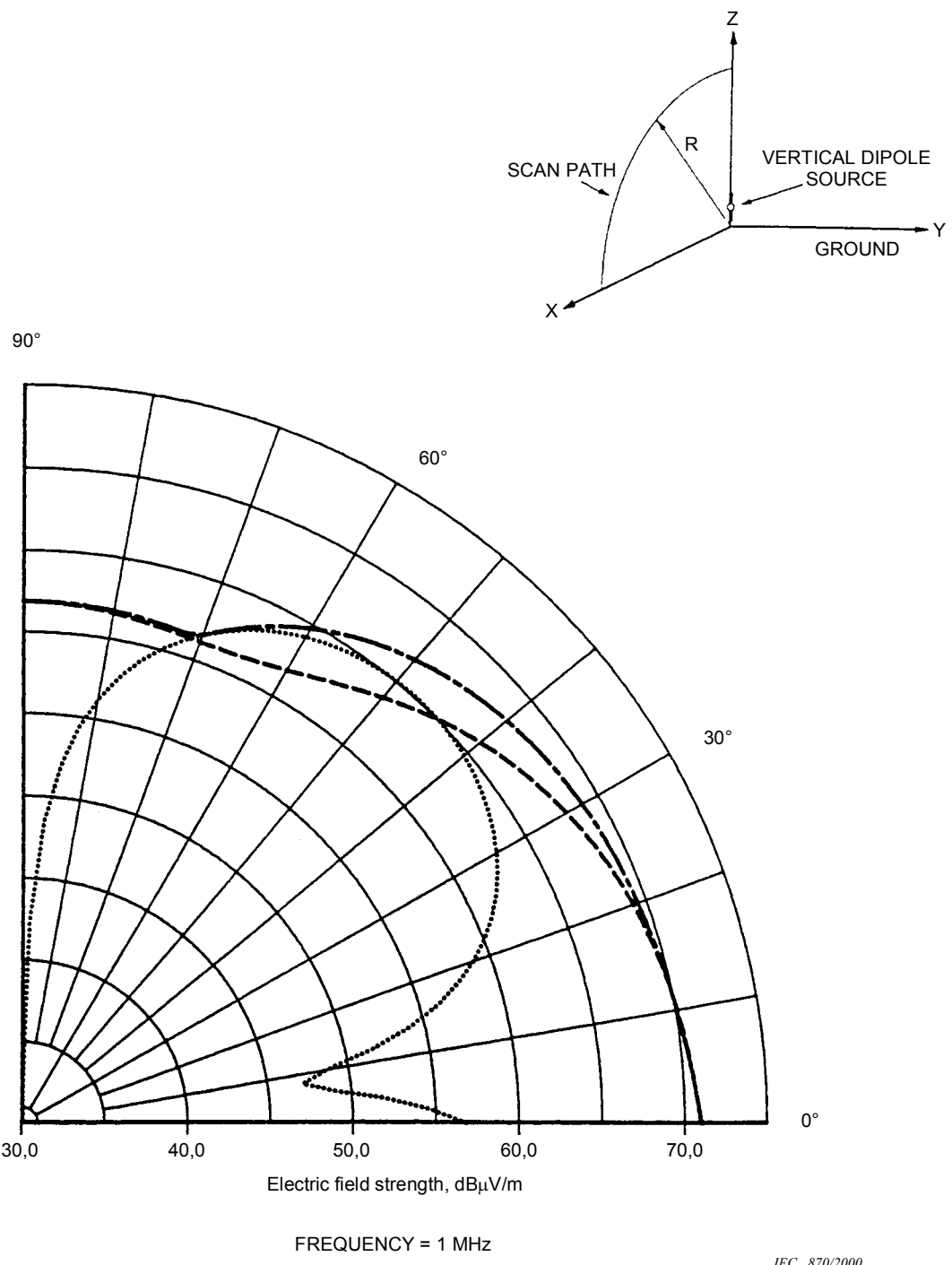


**Figure 4.6-29 – Vertical radiation patterns of the  $E$ -fields emitted by a small vertical electric dipole located close to the ground**

Dipole length 3 m. Dipole base height above ground 0,15 m. Dipole moment 1 A·m.

- Dashed line curve – vertically oriented  $E_z$  at a scan distance of 300 m
  - Dotted line curve – horizontally oriented  $E_x$  at a scan distance of 300 m
  - dash-dot line curve – total vector/phasor sum of  $E_z$  and  $E_x$  at a scan distance of 300 m, the vertically polarized  $E$ -field
- Electrical constants of the ground  $\sigma = 1 \text{ mS/m}$ ,  $\epsilon_r = 15$

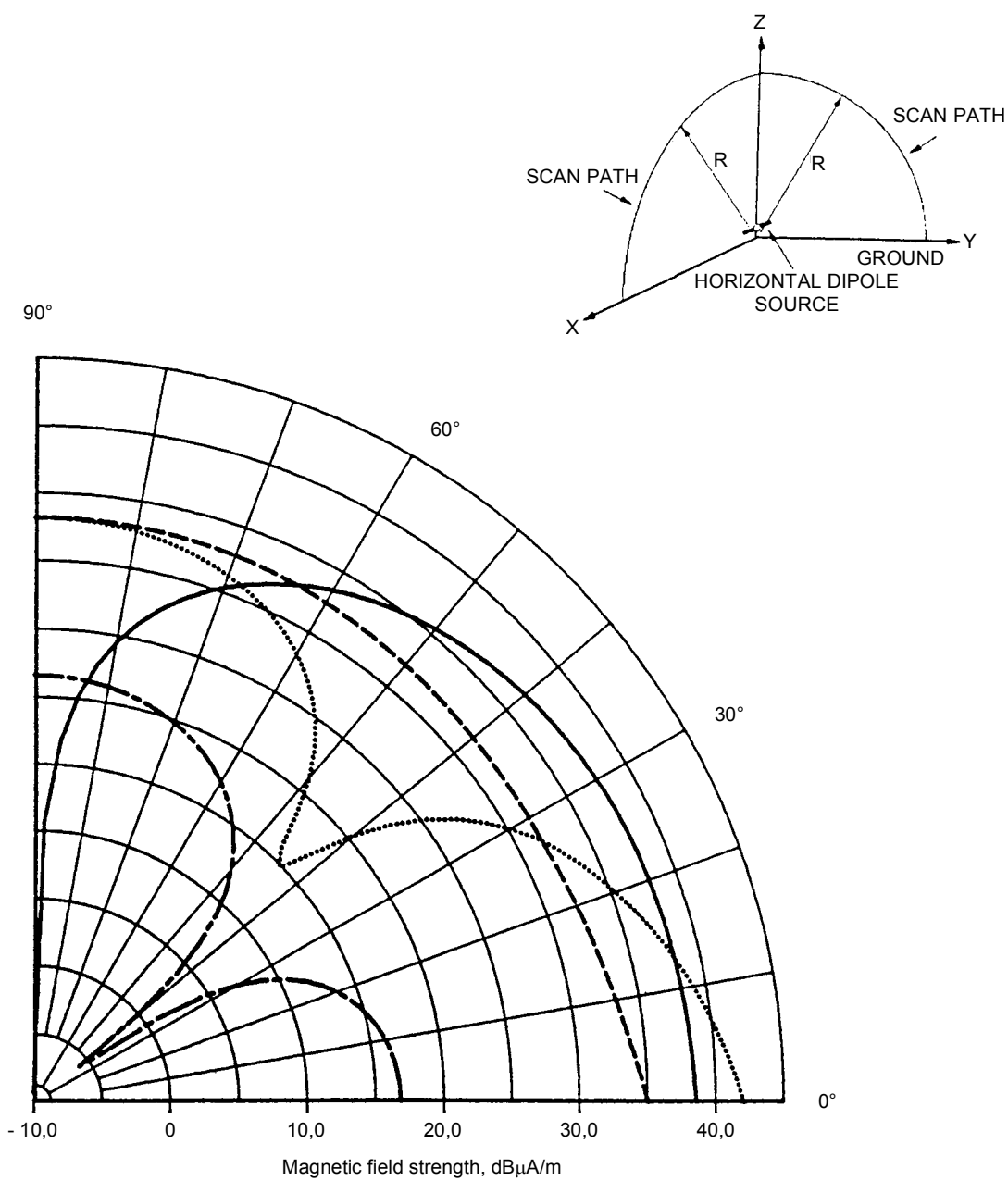


**Figure 4.6-30 – Vertical radiation patterns of the  $H$ -fields emitted by a small horizontal electric dipole located close to the ground**

Dipole length 3 m. Dipole height above ground 1 m. Dipole moment 1 A·m.

- Dashed line curve – horizontally oriented  $Hy$  at a scan distance of 30 m in the Z-X plane
- Dotted line curve – horizontally oriented  $Hy$  at a scan distance of 30 m in the Y-Z plane
- Solid line curve – vertically oriented  $Hz$  at a scan distance of 30 m in the Y-Z plane
- Electrical constants of the ground  $\sigma = 1 \text{ mS/m}$ ,  $\epsilon_r = 15$
- Dash-dot line curve – horizontally oriented  $Hy$  at a scan distance of 30 m in the Z-X plane
- Perfectly conducting ground

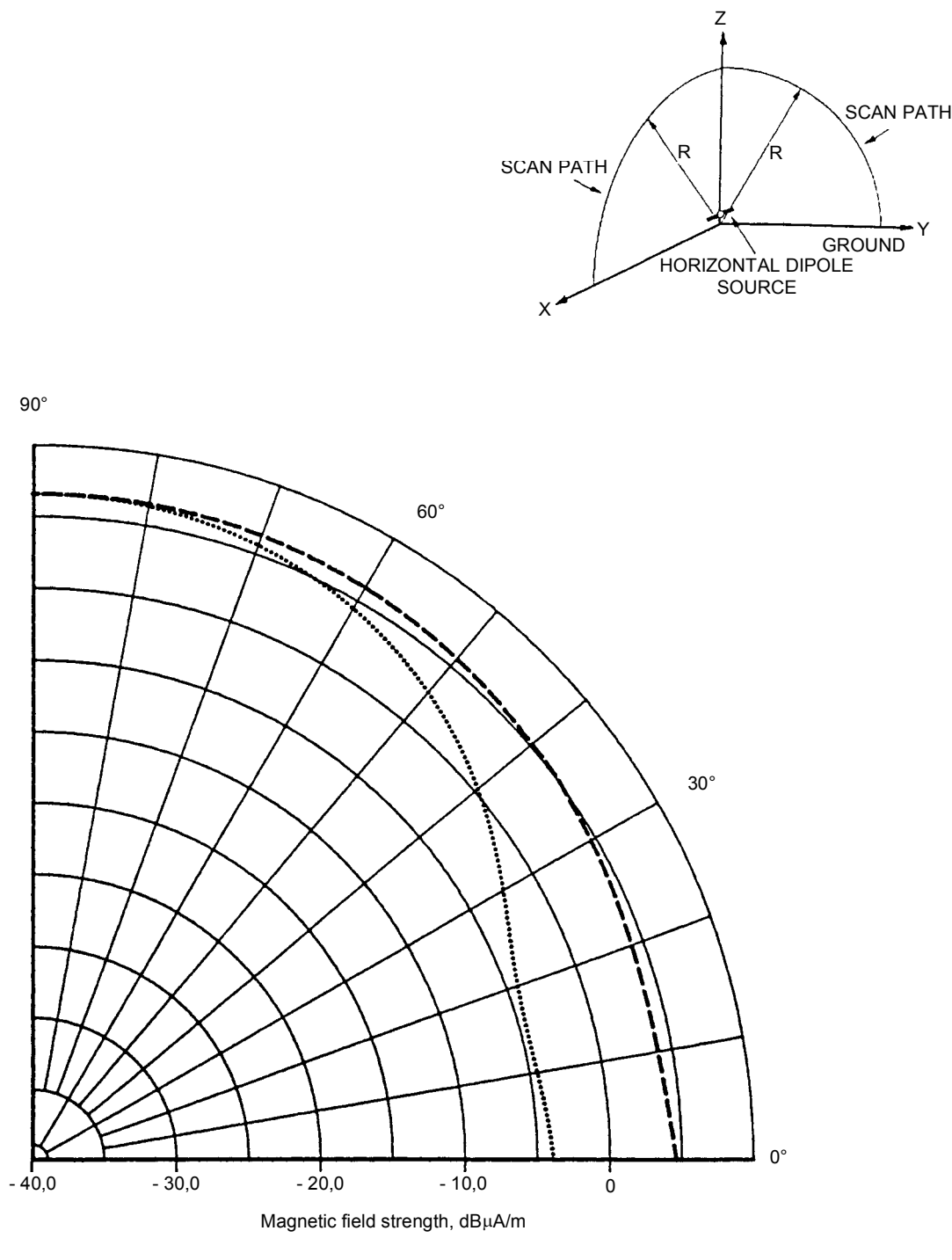


**Figure 4.6-31 – Vertical radiation patterns of the horizontally oriented *H*-fields emitted by a small horizontal electric dipole located close to the ground**

Dipole length 3 m. Dipole height above ground 1 m. Dipole moment 1 A·m.

Dashed line curve –  $Hy$  at a scan distance of 300 m in the Z-X plane  
 Dotted line curve –  $Hy$  at a scan distance of 300 m in the Y-Z plane  
 Electrical constants of the ground  $\sigma = 1 \text{ mS/m}$ ,  $\epsilon_r = 15$

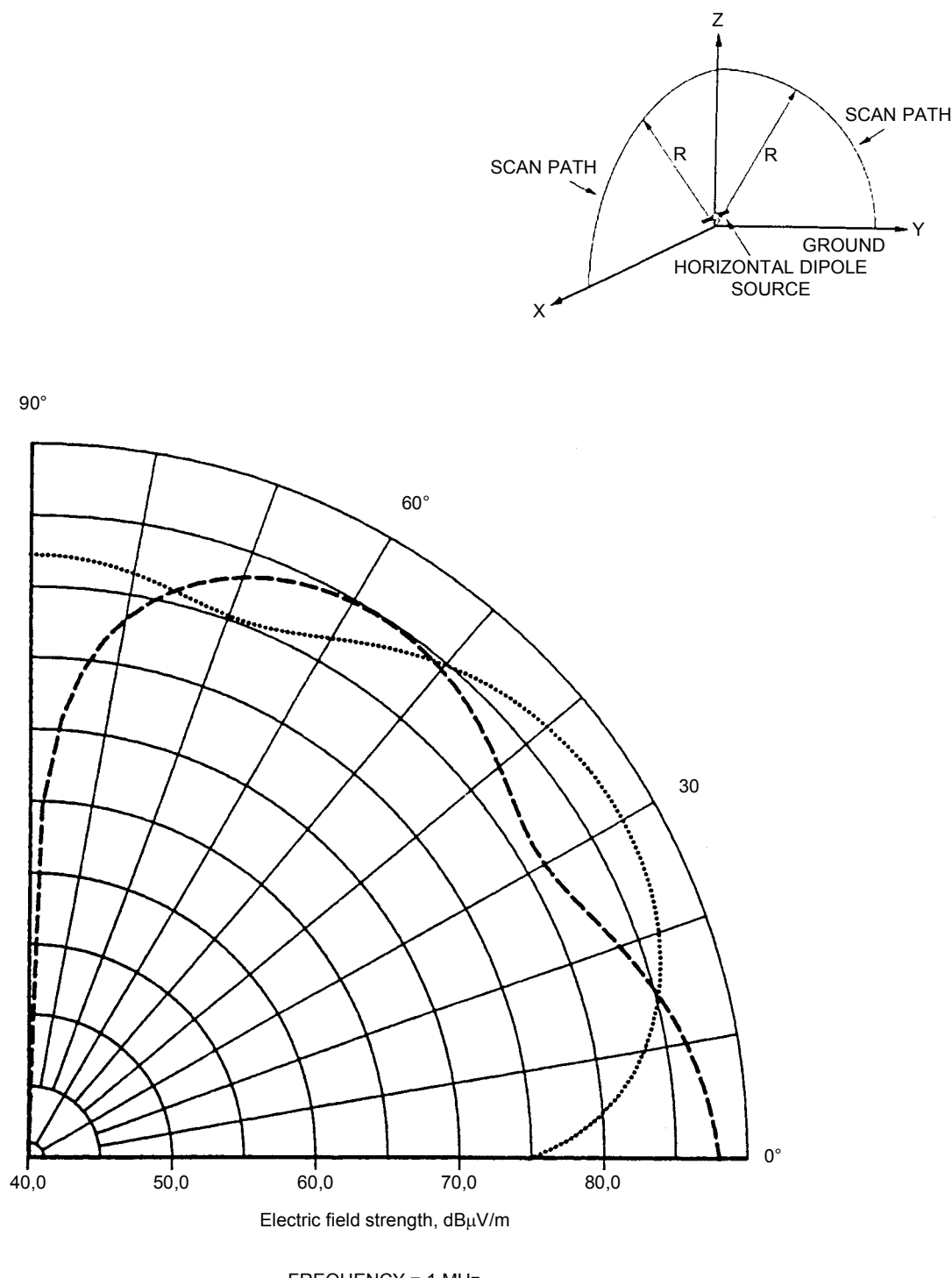


**Figure 4.6-32 – Vertical radiation patterns of the  $E$ -fields emitted by a small horizontal electric dipole located close to the ground**

Dipole length 3 m. Dipole height above ground 1 m. Dipole moment 1 A·m.

Dashed line curve – vertically oriented  $E_z$  at a scan distance of 30 m in the Z-X plane  
 Dotted line curve – horizontally oriented  $E_x$  at a scan distance of 30 m in the Z-X plane  
 Electrical constants of the ground  $\sigma = 1 \text{ mS/m}$ ,  $\epsilon_r = 15$

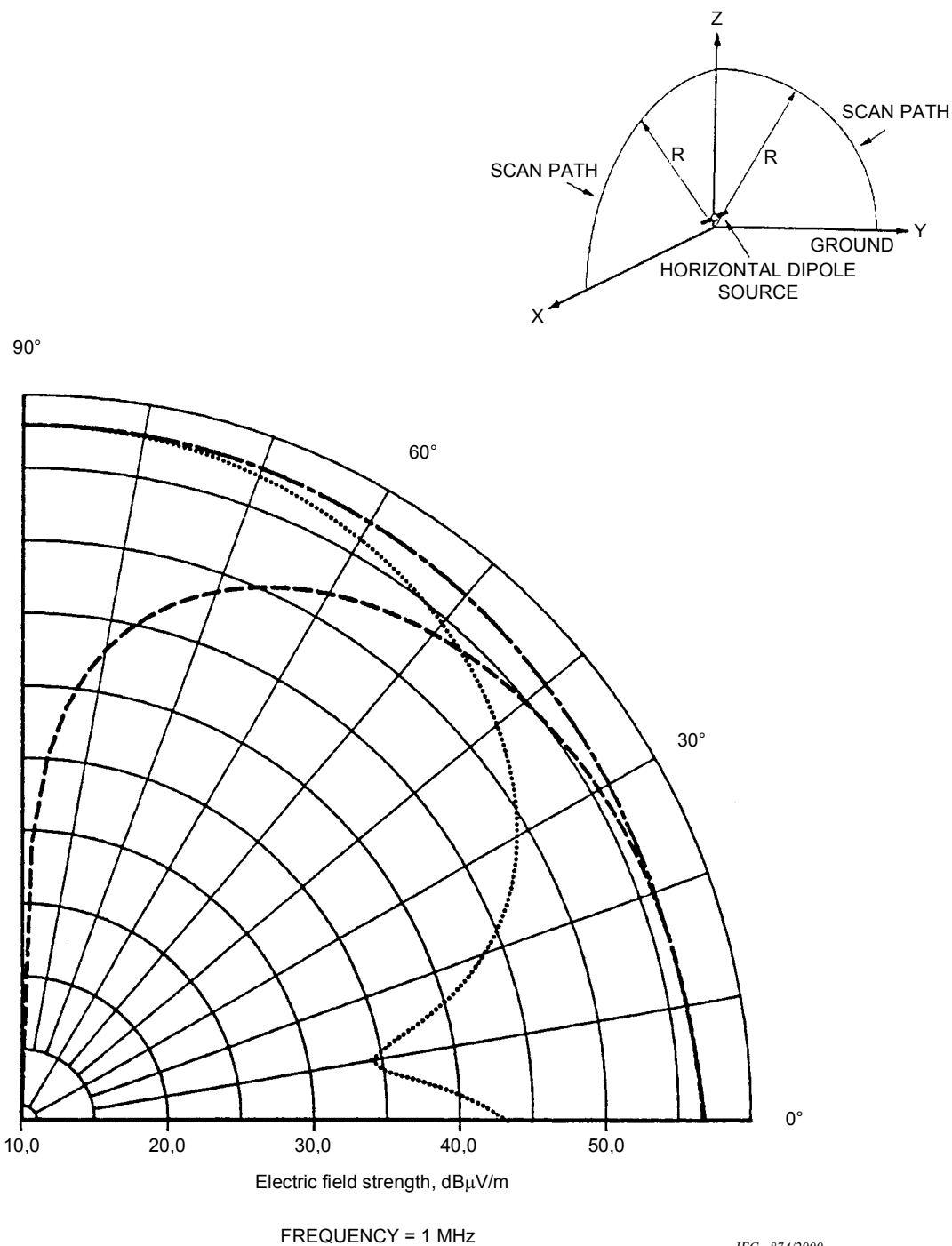


**Figure 4.6-33 – Vertical radiation patterns of the  $E$ -fields emitted by a small horizontal electric dipole located close to the ground**

Dipole length 3 m. Dipole height above ground 1 m. Dipole moment 1 A·m.

- Dashed line curve – vertically oriented  $E_z$  at a scan distance of 300 m in the Z-X plane
  - Dotted line curve – horizontally oriented  $E_x$  at a scan distance of 300 m in the Z-X plane
  - dash-dot line curve – total vector/phasor sum of  $E_z$  and  $E_x$  at a scan distance of 300 m in the Z-X plane, the vertically polarized  $E$ -field
- Electrical constants of the ground  $\sigma = 1 \text{ mS/m}$ ,  $\epsilon_r = 15$

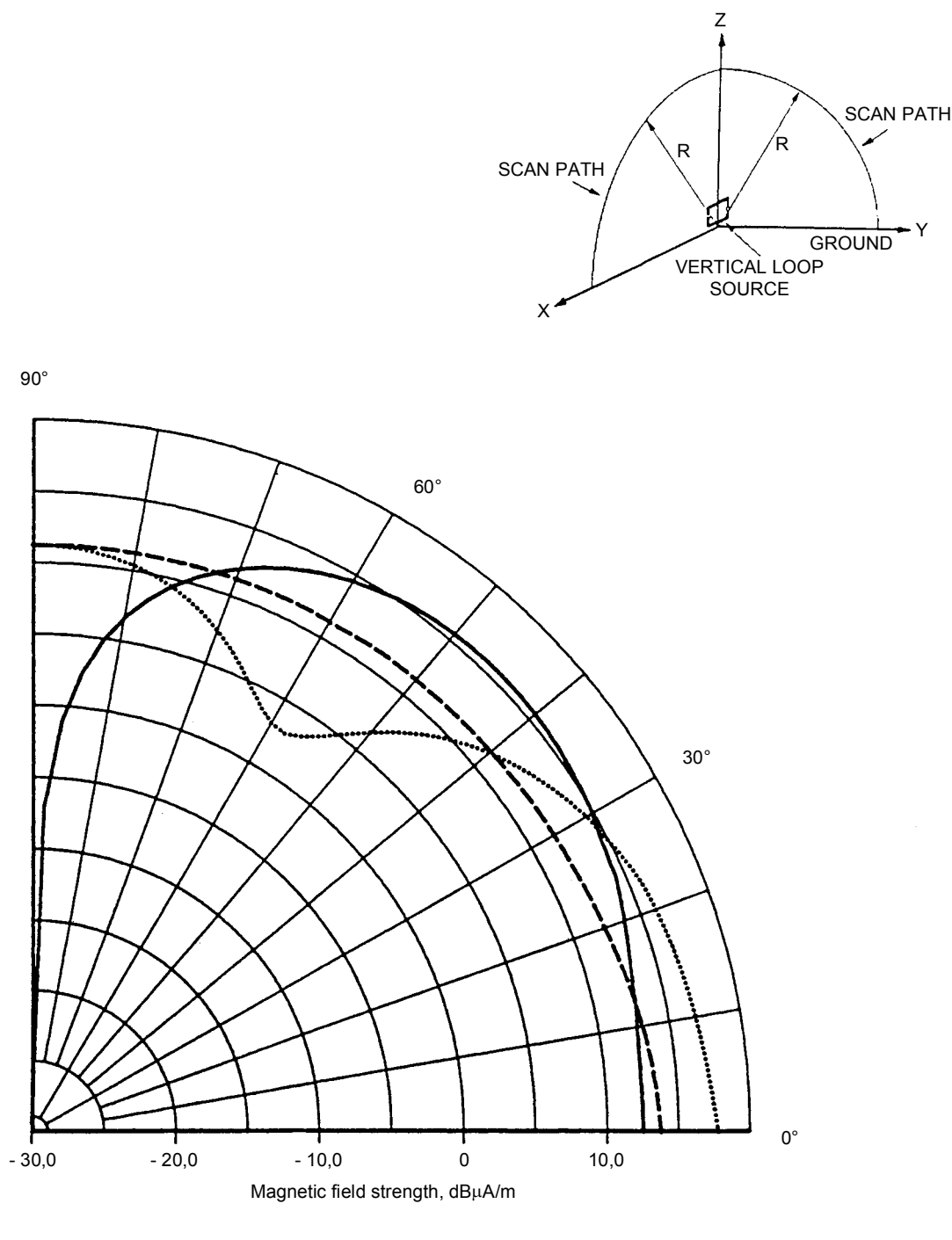


**Figure 4.6-34 – Vertical radiation patterns of the  $H$ -fields emitted by a small horizontal magnetic dipole (vertical loop) located close to the ground**

Square loop 3 m × 3 m. Loop base height above ground 0,15 m. Dipole moment 1 A·m<sup>2</sup>.

Dashed line curve – horizontally oriented  $Hy$  at a scan distance of 30 m in the Z-X plane  
 Dotted line curve – horizontally oriented  $Hy$  at a scan distance of 30 m in the Y-Z plane  
 Solid line curve – vertically oriented  $Hz$  at a scan distance of 30 m in the Y-Z plane  
 Electrical constants of the ground  $\sigma = 1 \text{ mS/m}$ ,  $\epsilon_r = 15$

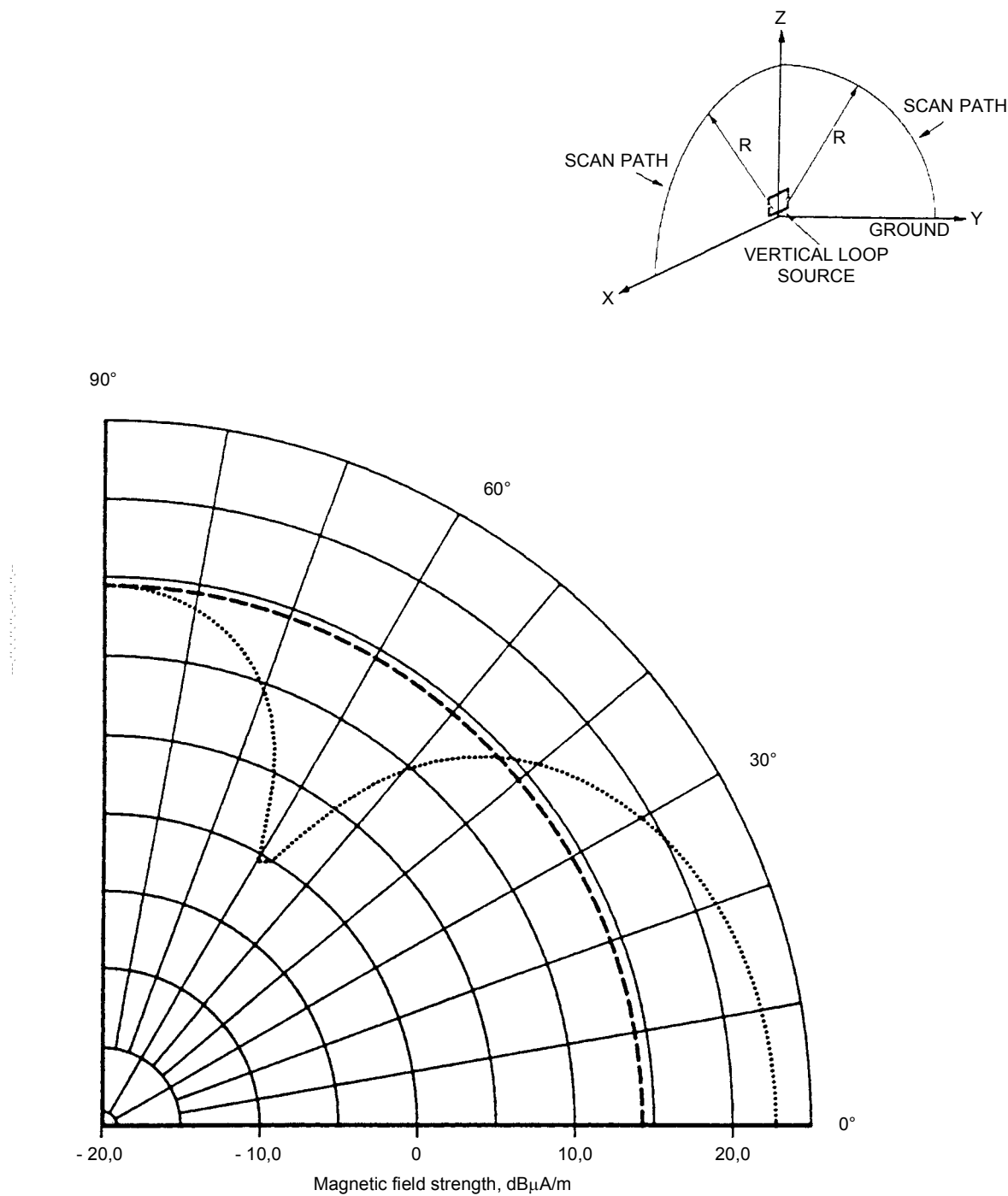


**Figure 4.6-35 – Vertical radiation patterns of the horizontally oriented  $H$ -fields emitted by a small horizontal magnetic dipole (vertical loop) located close to the ground**

Square loop  $3\text{ m} \times 3\text{ m}$ . Loop base height above ground  $0,15\text{ m}$ . Dipole moment  $1\text{ A}\cdot\text{m}^2$ .

Dashed line curve –  $H_y$  at a scan distance of  $30\text{ m}$  in the Z-X plane  
 Dotted line curve –  $H_y$  at a scan distance of  $30\text{ m}$  in the Y-Z plane  
 Perfectly conducting ground

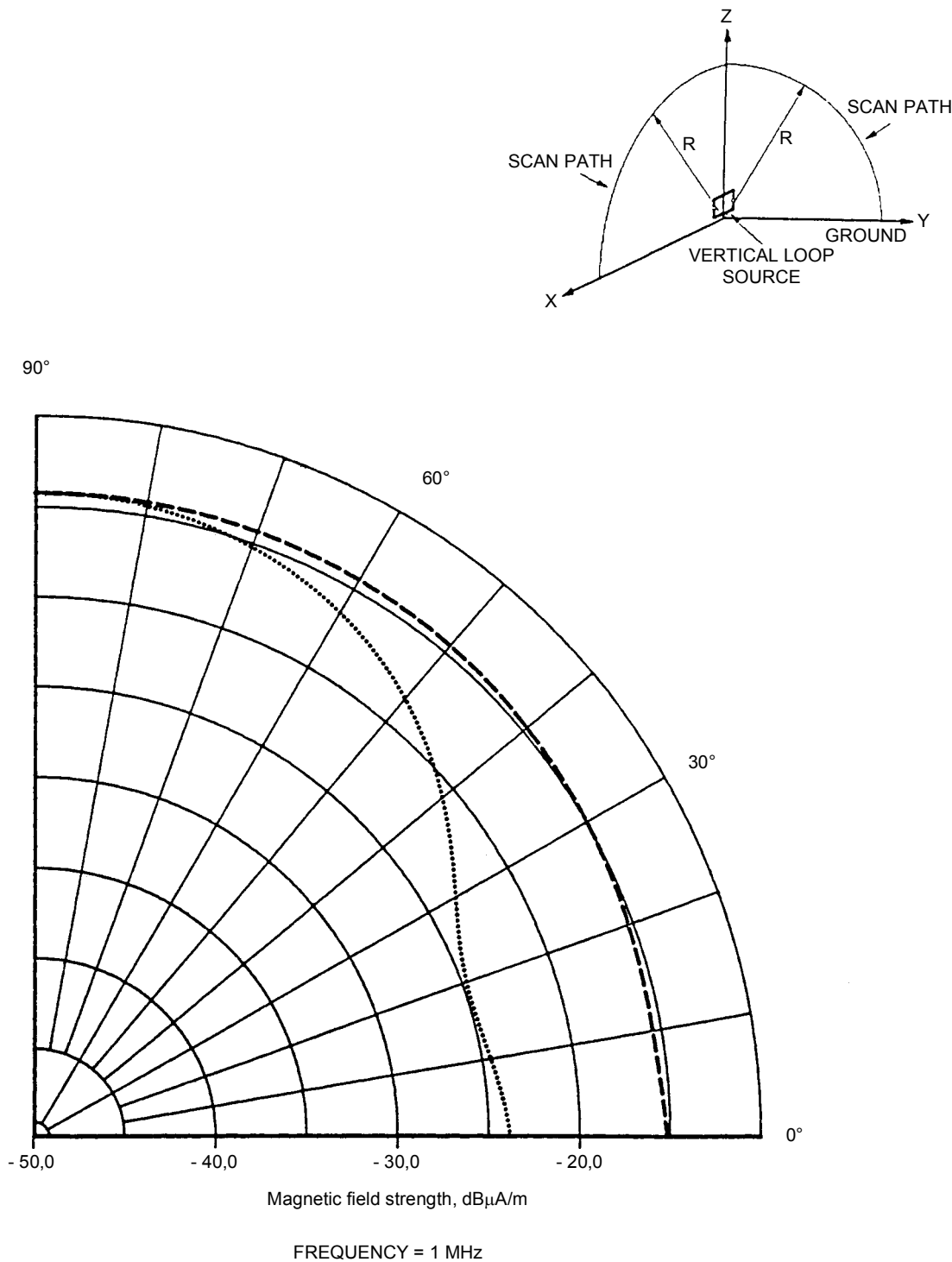


**Figure 4.6-36 – Vertical radiation patterns of the horizontally oriented  $H$ -fields emitted by a small horizontal magnetic dipole (vertical loop) located close to the ground**

Square loop  $3\text{ m} \times 3\text{ m}$ . Loop base height above ground  $0,15\text{ m}$ . Dipole moment  $1\text{ A}\cdot\text{m}^2$ .

Dashed line curve –  $Hy$  at a scan distance of  $300\text{ m}$  in the  $Z\text{-}X$  plane  
 Dotted line curve –  $Hy$  at a scan distance of  $300\text{ m}$  in the  $Y\text{-}Z$  plane  
 Electrical constants of the ground  $\sigma = 1\text{ mS/m}$ ,  $\epsilon_r = 15$

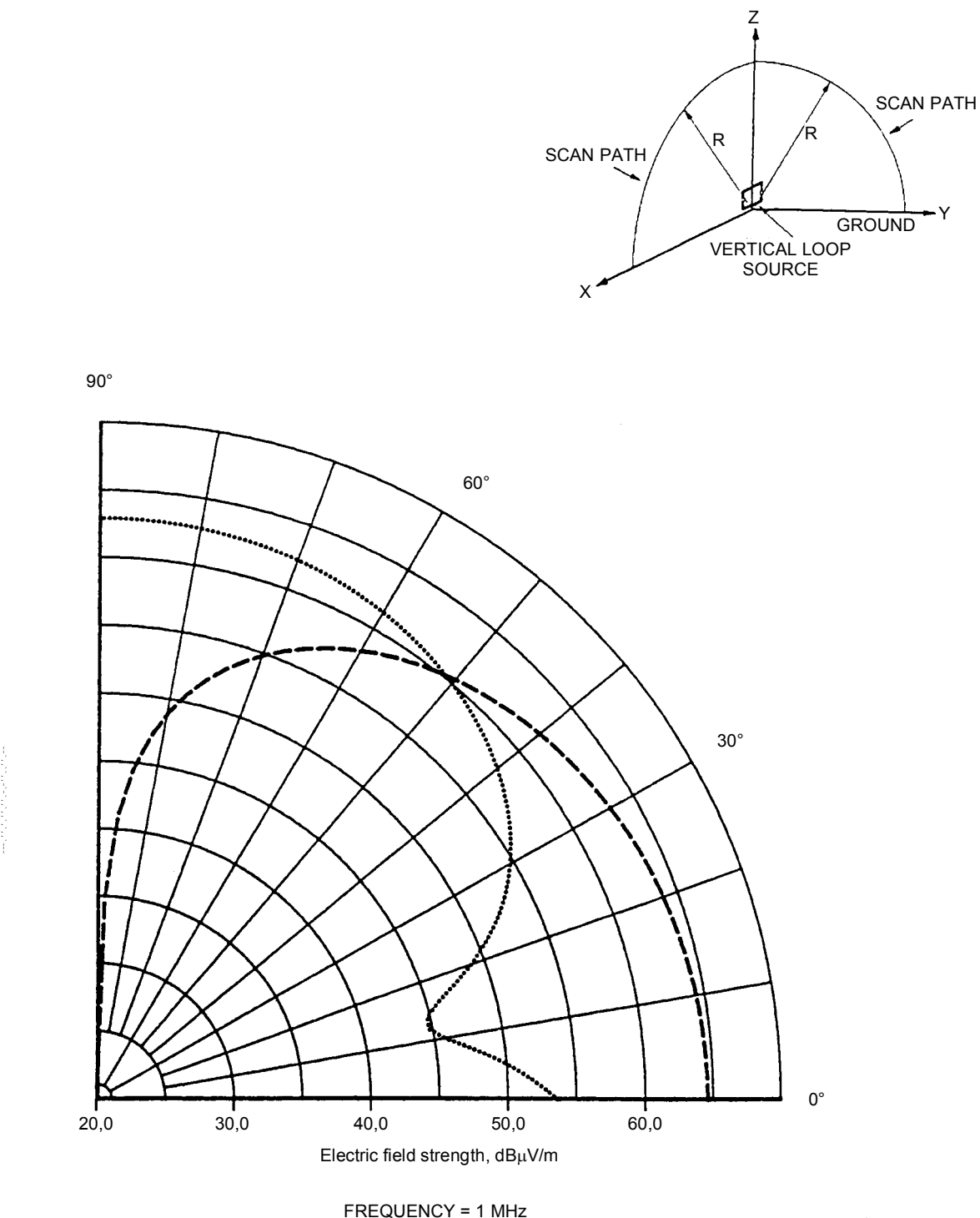


**Figure 4.6-37 – Vertical radiation patterns of the  $E$ -fields emitted by a small horizontal magnetic dipole (vertical loop) located close to the ground**

Square loop  $3\text{ m} \times 3\text{ m}$ . Loop base height above ground  $0,15\text{ m}$ . Dipole moment  $1\text{ A}\cdot\text{m}^2$ .

Dashed line curve – vertically oriented  $E_z$  at a scan distance of  $30\text{ m}$  in the Z-X plane  
 Dotted line curve – horizontally oriented  $E_x$  at a scan distance of  $30\text{ m}$  in the Z-X plane  
 Electrical constants of the ground  $\sigma = 1\text{ mS/m}$ ,  $\epsilon_r = 15$

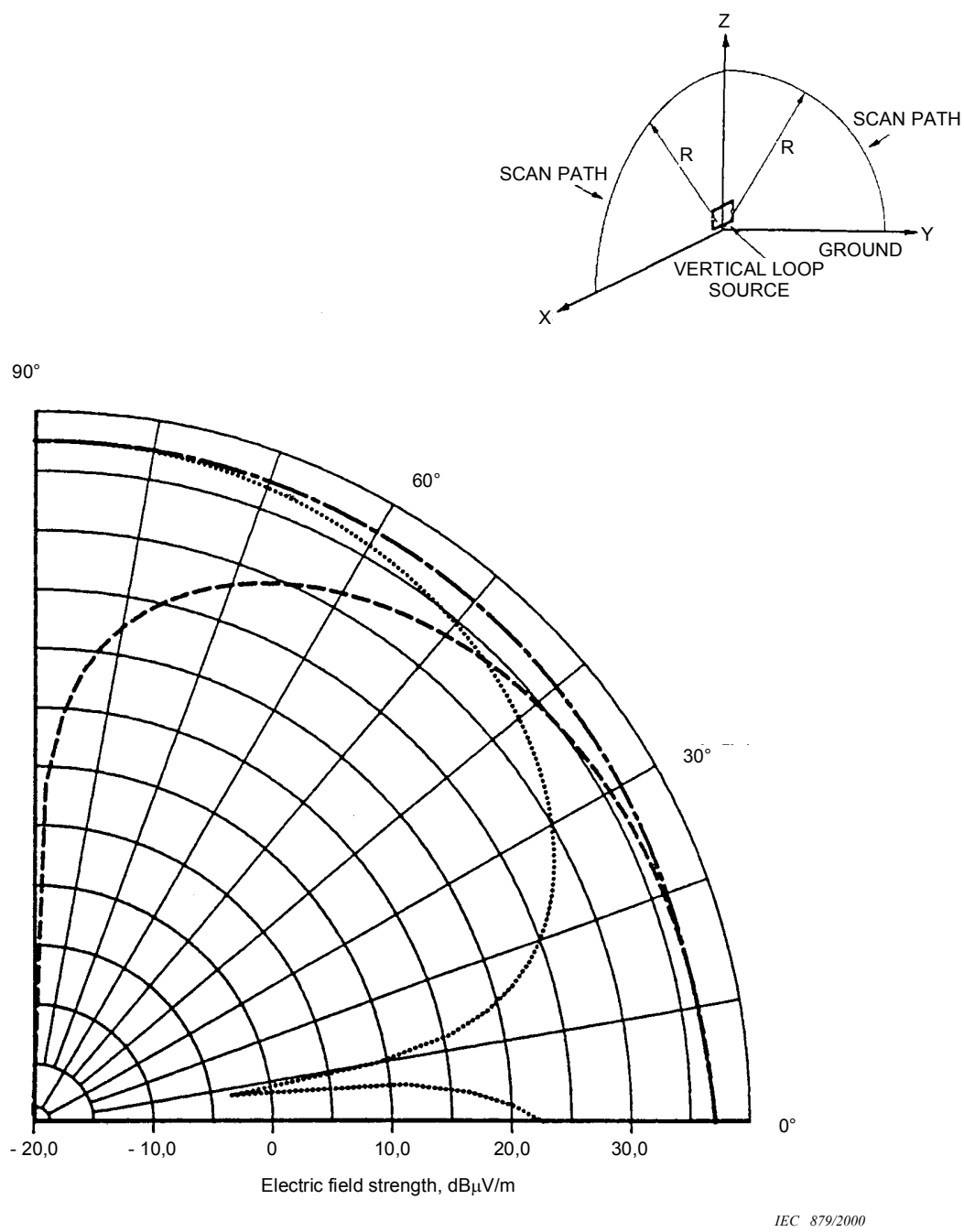


**Figure 4.6-38 – Vertical radiation patterns of the  $E$ -fields emitted by a small horizontal magnetic dipole (vertical loop) located close to the ground**

Square loop  $3\text{ m} \times 3\text{ m}$ . Loop base height above ground  $0,15\text{ m}$ . Dipole moment  $1\text{ A}\cdot\text{m}^2$ .

- Dashed line curve – vertically oriented  $E_z$  at a scan distance of  $300\text{ m}$  in the Z-X plane
  - Dotted line curve – horizontally oriented  $E_x$  at a scan distance of  $300\text{ m}$  in the Z-X plane
  - dash-dot line curve – total vector/phasor sum of  $E_z$  and  $E_x$  at a scan distance of  $300\text{ m}$  in the Z-X plane, the vertically polarized  $E$ -field
- Electrical constants of the ground  $\sigma = 1\text{ mS/m}$ ,  $\epsilon_r = 15$

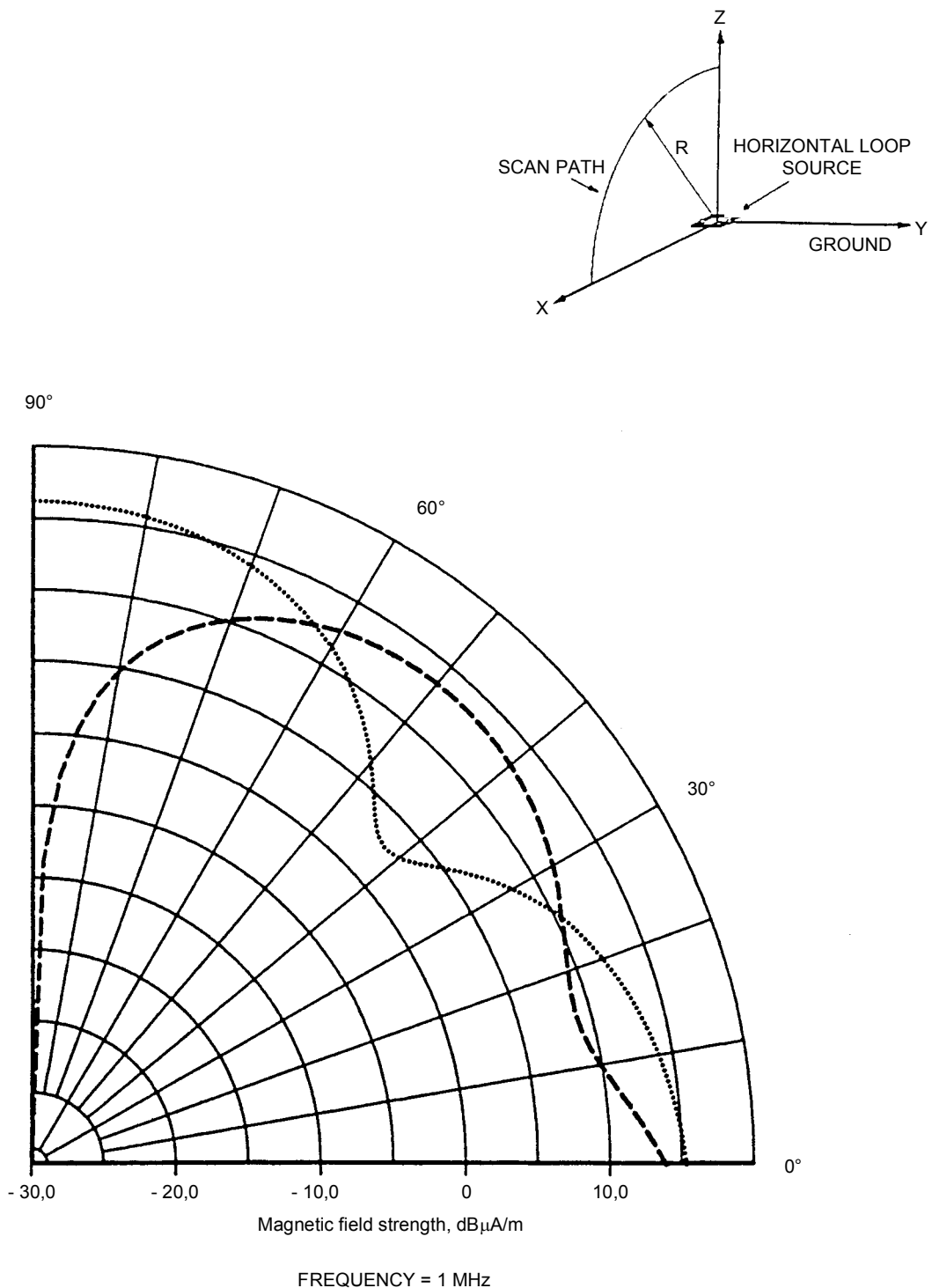


**Figure 4.6-39 – Vertical radiation patterns of the  $H$ -fields emitted by a small vertical magnetic dipole (horizontal loop) located close to the ground**

Square loop 3 m × 3 m. Loop height above ground 1 m. Dipole moment 1 A·m<sup>2</sup>.

Dashed line curve – horizontally oriented  $H_x$  at a scan distance of 30 m  
 Dotted line curve – vertically oriented  $H_z$  at a scan distance of 30 m  
 Electrical constants of the ground  $\sigma = 1 \text{ mS/m}$ ,  $\epsilon_r = 15$

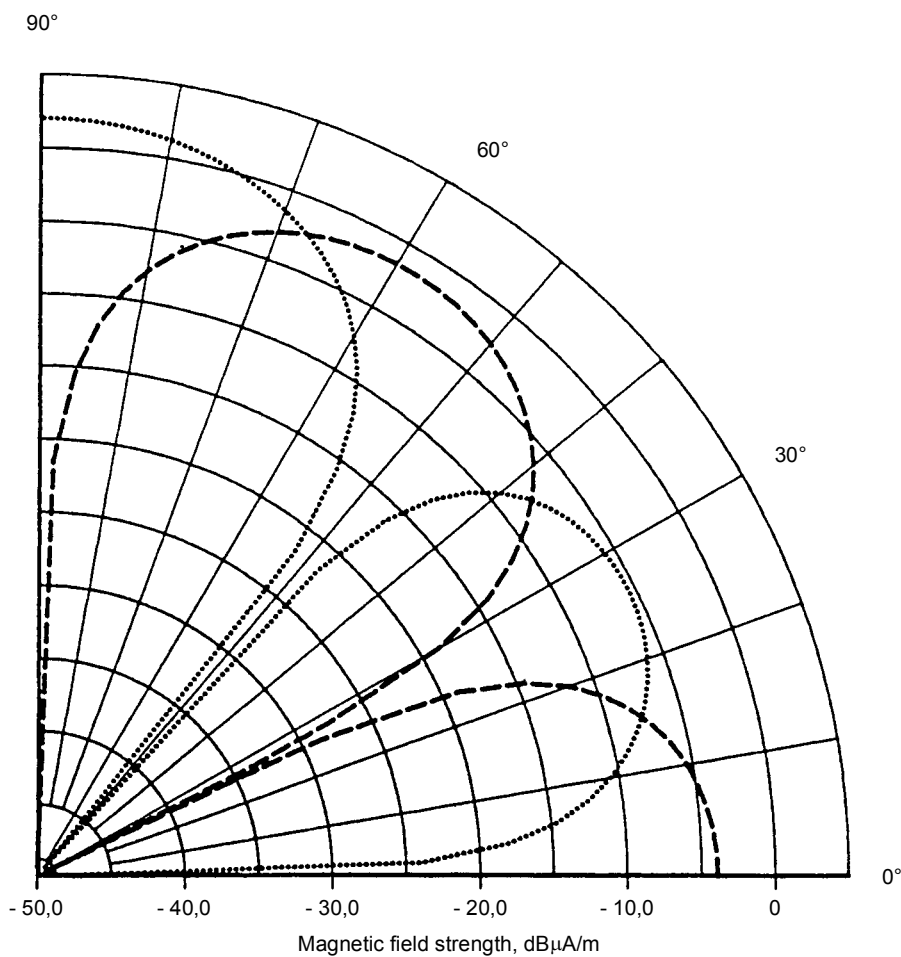
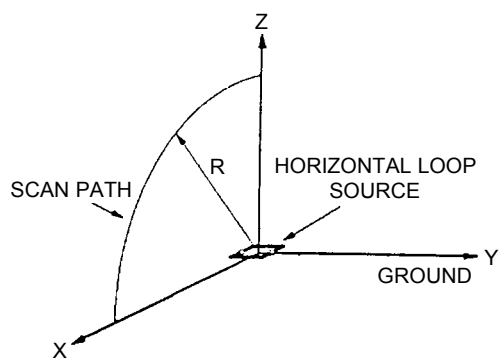


**Figure 4.6-40 – Vertical radiation patterns of the *H*-fields emitted by a small vertical magnetic dipole (horizontal loop) located close to the ground**

Square loop 3 m × 3 m. Loop height above ground 1 m. Dipole moment 1 A·m<sup>2</sup>.

Dashed line curve – horizontally oriented *Hx* at a scan distance of 30 m  
 Dotted line curve – vertically oriented *Hz* at a scan distance of 30 m  
 Perfectly conducting ground

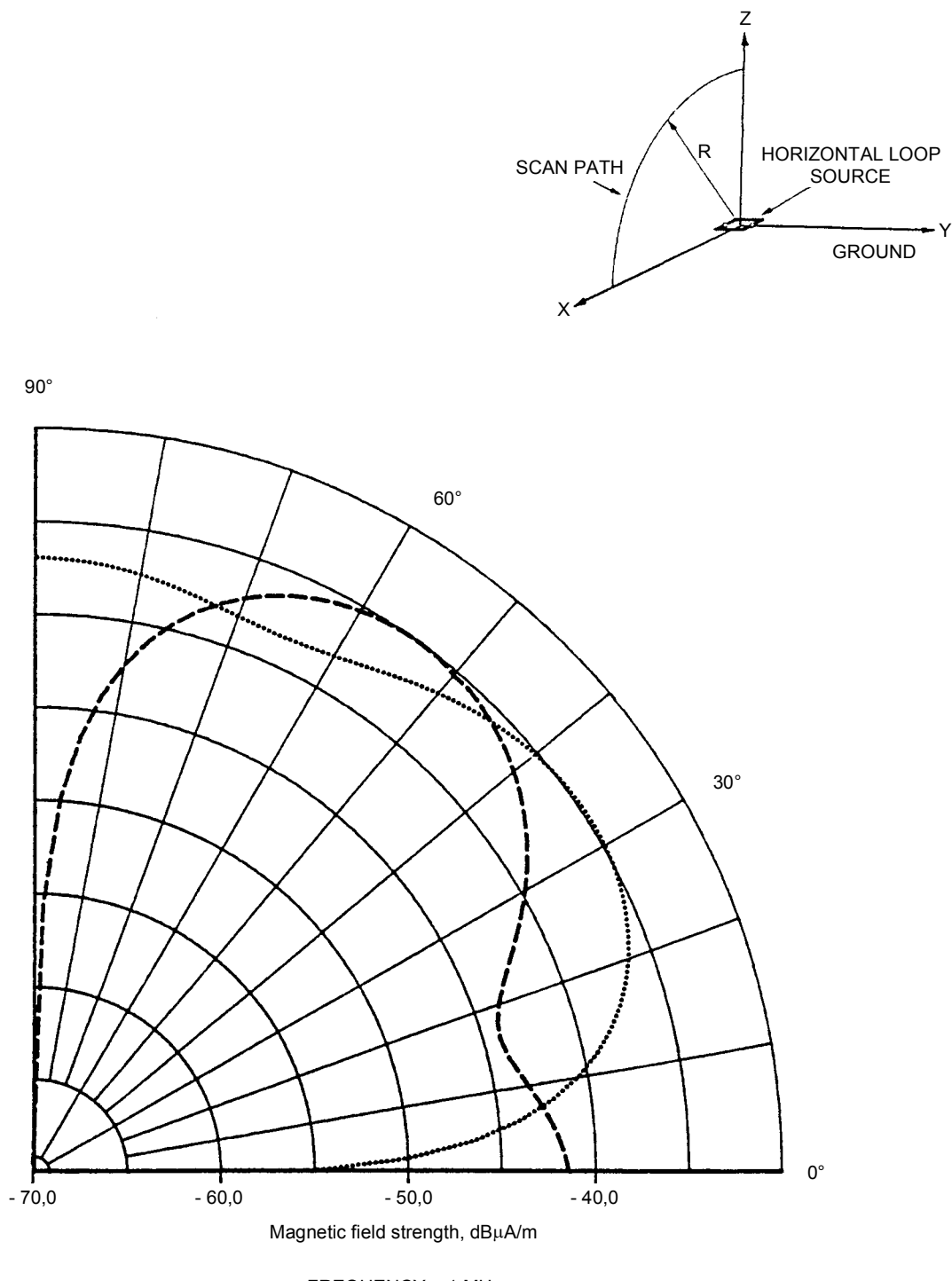
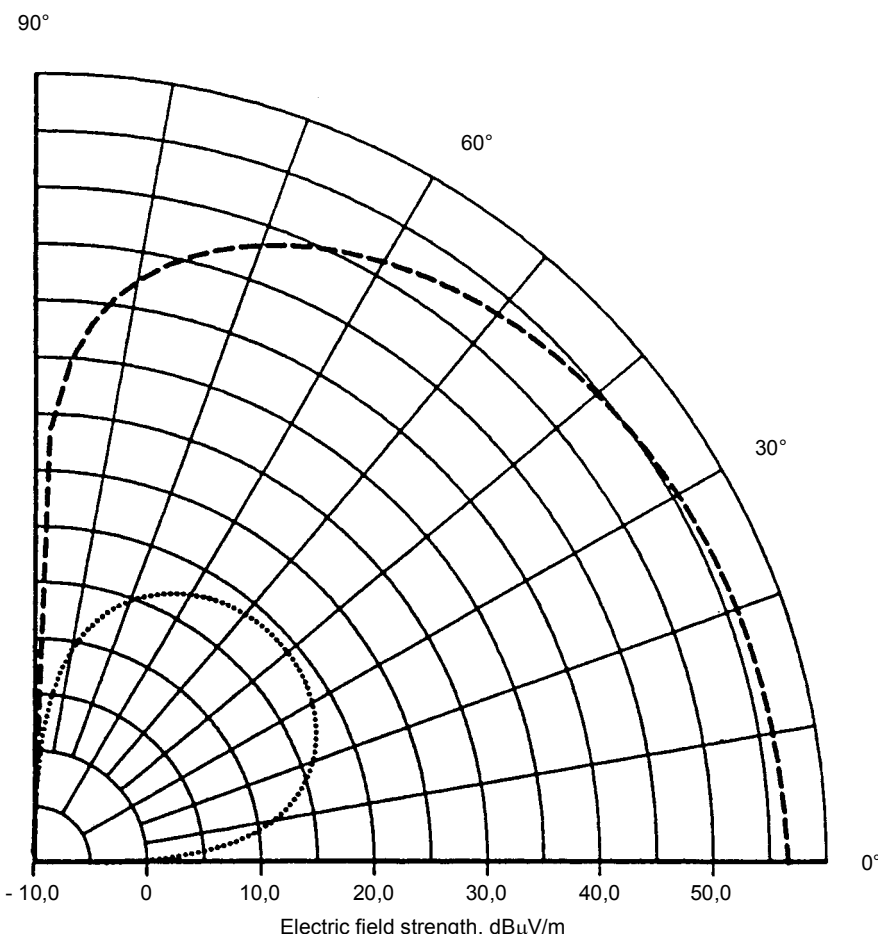
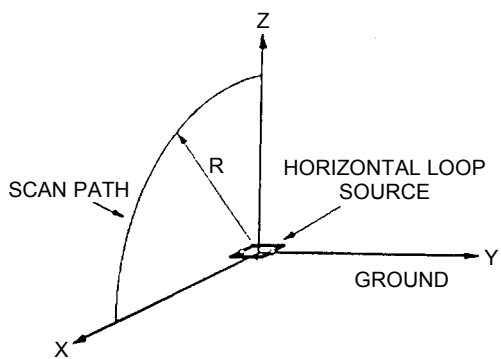


**Figure 4.6-41 – Vertical radiation patterns of the *H*-fields emitted by a small vertical magnetic dipole (horizontal loop) located close to the ground**

Square loop  $3\text{ m} \times 3\text{ m}$ . Loop height above ground 1 m. Dipole moment  $1\text{ A}\cdot\text{m}^2$ .

Dashed line curve – horizontally oriented *Hx* at a scan distance of 300 m  
 Dotted line curve – vertically oriented *Hz* at a scan distance of 300 m  
 Electrical constants of the ground  $\sigma = 1\text{ mS/m}$ ,  $\epsilon_r = 15$



FREQUENCY = 1 MHz

IEC 883/2000

**Figure 4.6-42 – Vertical radiation patterns of the *E*-fields emitted by a small vertical magnetic dipole (horizontal loop) located close to the ground**

Square loop 3 m × 3 m. Loop height above ground 1 m. Dipole moment 1 A·m<sup>2</sup>.

Dashed line curve – horizontally oriented *Ey* at a scan distance of 30 m

Dotted line curve – horizontally oriented *Ey* at a scan distance of 300 m

Electrical constants of the ground  $\sigma = 1$  mS/m,  $\epsilon_r = 15$

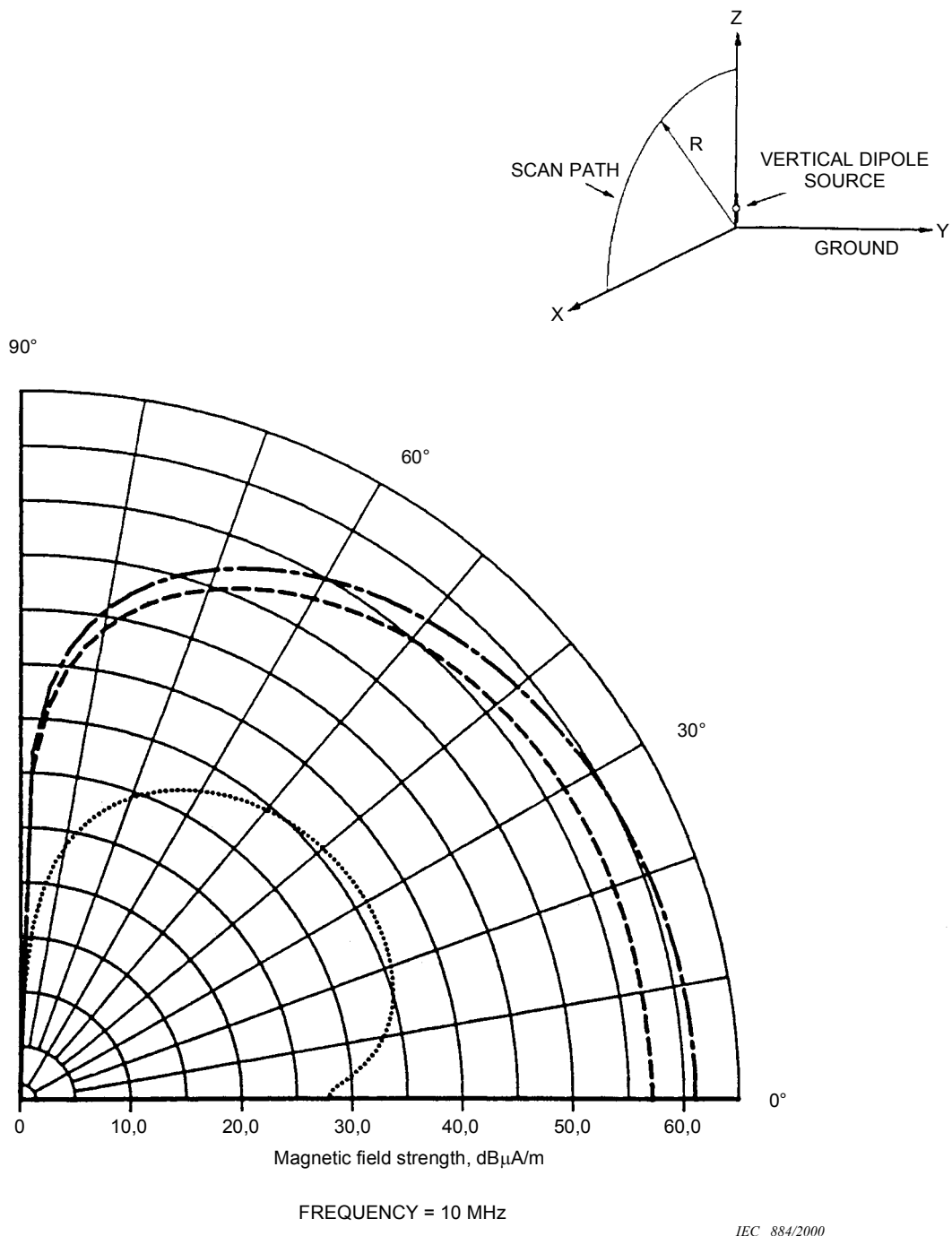


**Figure 4.6-43 – Vertical radiation patterns of the horizontally oriented  $H$ -fields emitted by a small vertical electric dipole located close to the ground**

Dipole length 1 m. Dipole base at a height above ground of 0,15 m. Dipole moment 1 A·m.

- Dashed line curve –  $Hy$  at a scan distance of 30 m
- Dotted line curve –  $Hy$  at a scan distance of 300 m
- Electrical constants of the ground  $\sigma = 1 \text{ mS/m}$ ,  $\epsilon_r = 15$
- Dash-dot line curve –  $Hy$  at a scan distance of 30 m  
Perfectly conducting ground

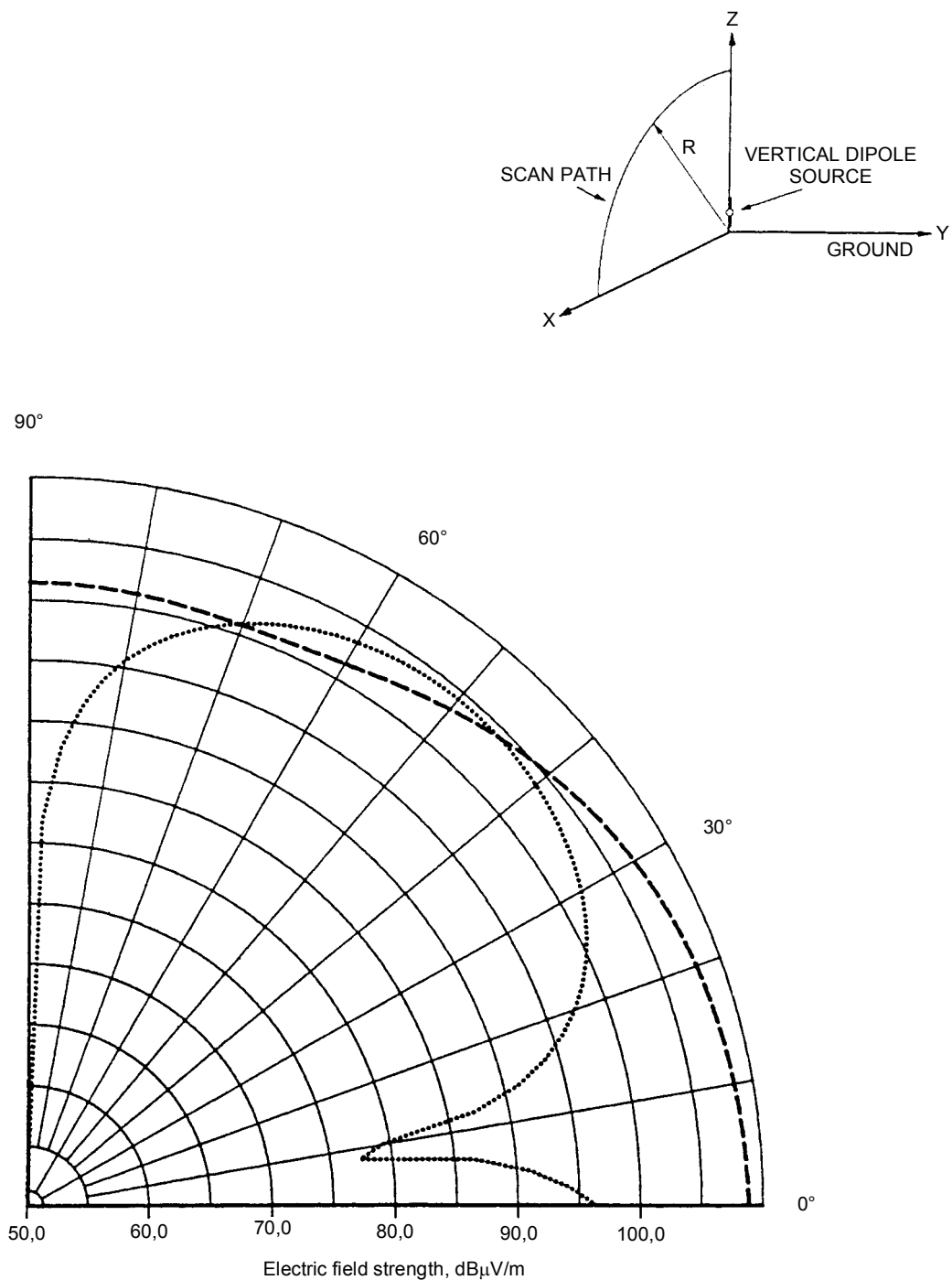


**Figure 4.6-44 – Vertical radiation patterns of the  $E$ -fields emitted by a small vertical electric dipole located close to the ground**

Dipole length 1 m. Dipole base at a height above ground of 0,15 m. Dipole moment 1 A·m.

Dashed line curve – vertically oriented  $E_z$  at a scan distance of 30 m  
 Dotted line curve – horizontally oriented  $E_x$  at a scan distance of 30 m  
 Electrical constants of the ground  $\sigma = 1 \text{ mS/m}$ ,  $\epsilon_r = 15$

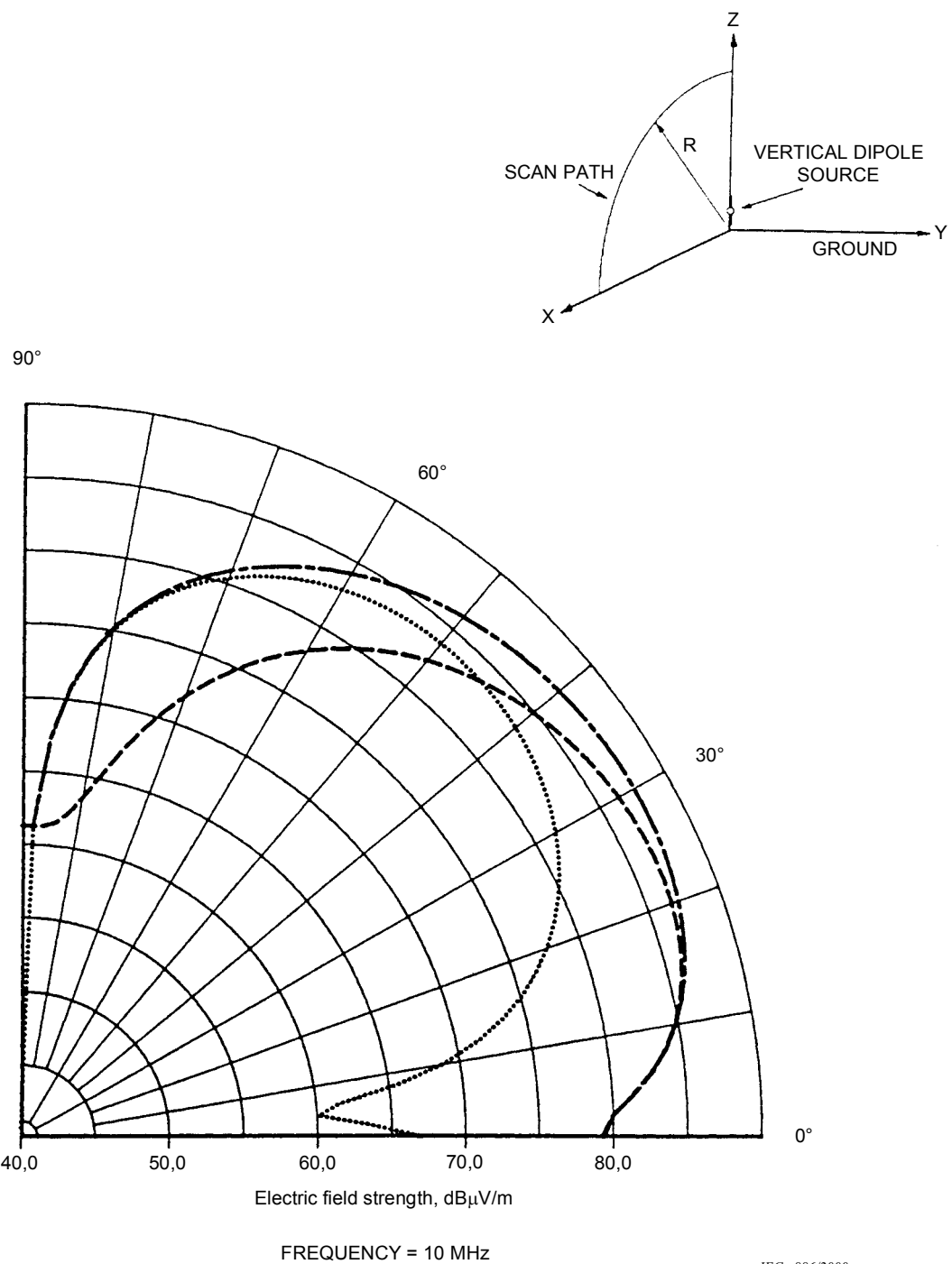


**Figure 4.6-45 – Vertical radiation patterns of the  $E$ -fields emitted by a small vertical electric dipole located close to the ground**

Dipole length 1 m. Dipole base height above ground 0,15 m. Dipole moment 1 A·m.

- Dashed line curve – vertically oriented  $E_z$  at a scan distance of 300 m
  - Dotted line curve – horizontally oriented  $E_x$  at a scan distance of 300 m
  - dash-dot line curve – total vector/phasor sum of  $E_z$  and  $E_x$  at a scan distance of 300 m, the vertically polarized  $E$ -field
- Electrical constants of the ground  $\sigma = 1 \text{ mS/m}$ ,  $\epsilon_r = 15$

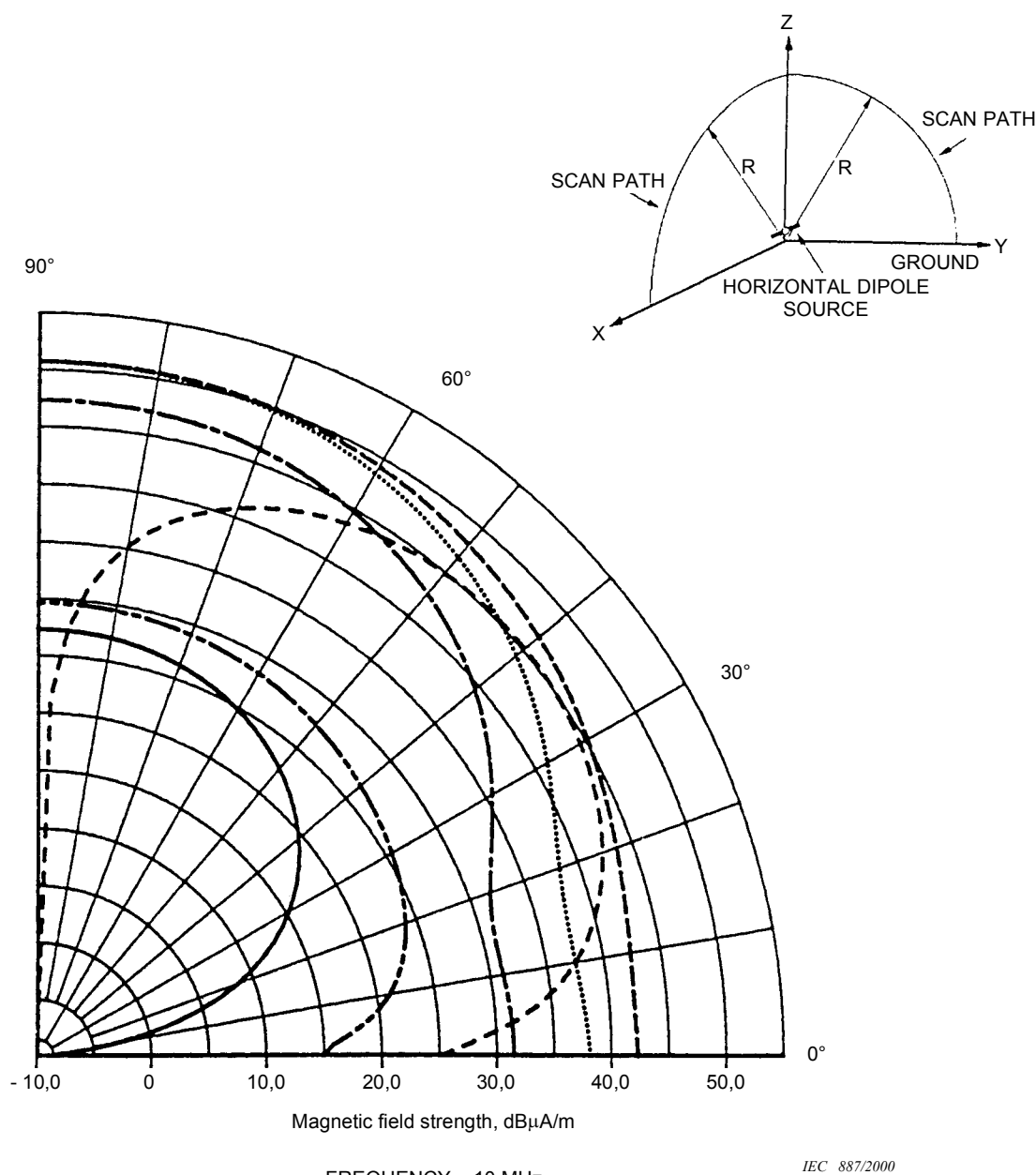


**Figure 4.6-46 – Vertical radiation patterns of the *H*-fields emitted by a small horizontal electric dipole located close to the ground**

Dipole length 1 m. Dipole height above ground 1 m. Dipole moment 1 A·m.

- Long-dash line curve – horizontally oriented  $Hy$  at a scan distance of 30 m in the Z-X plane
- Short-dash line curve – vertically oriented  $Hz$  at a scan distance of 30 m in the Y-Z plane
- Dotted line curve – horizontally oriented  $Hy$  at a scan distance of 30 m in the Y-Z plane
- Dash-double-dot curve – horizontally oriented  $Hy$  at a scan distance of 300 m in the Z-X plane
- Electrical constants of the ground  $\sigma = 1 \text{ mS/m}$ ,  $\epsilon_r = 15$
- Dash-dot line curve – horizontally oriented  $Hy$  at a scan distance of 30 m in the Z-X plane
- Solid line curve – horizontally oriented  $Hy$  at a scan distance of 300 m in the Z-X plane
- Perfectly conducting ground

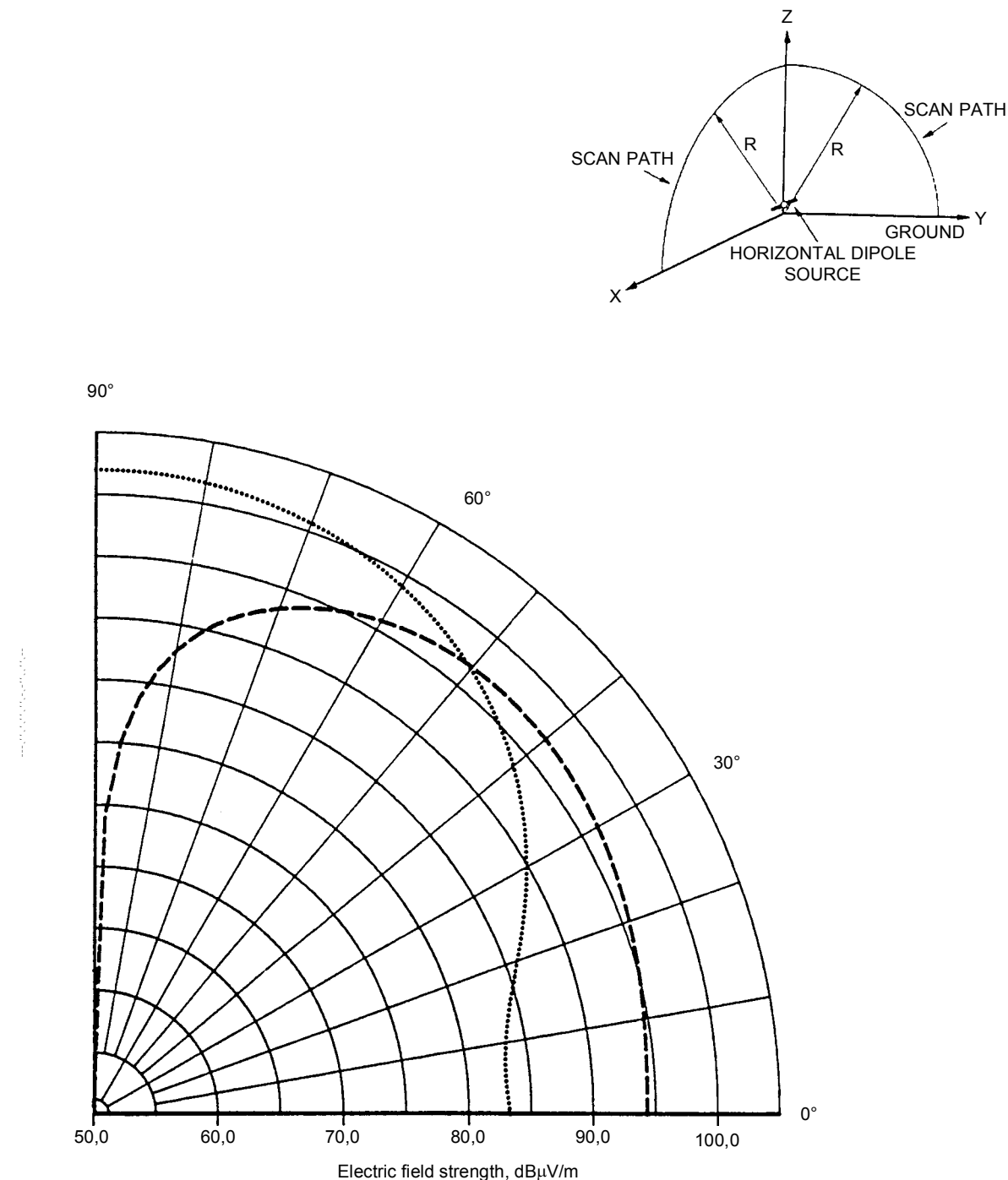


**Figure 4.6-47 – Vertical radiation patterns of the  $E$ -fields emitted by a small horizontal electric dipole located close to the ground**

Dipole length 1 m. Dipole height above ground 1 m. Dipole moment 1 A·m.

Dashed line curve – vertically oriented  $E_z$  at a scan distance of 30 m in the Z-X plane  
 Dotted line curve – horizontally oriented  $E_x$  at a scan distance of 30 m in the Z-X plane  
 Electrical constants of the ground  $\sigma = 1 \text{ mS/m}$ ,  $\epsilon_r = 15$

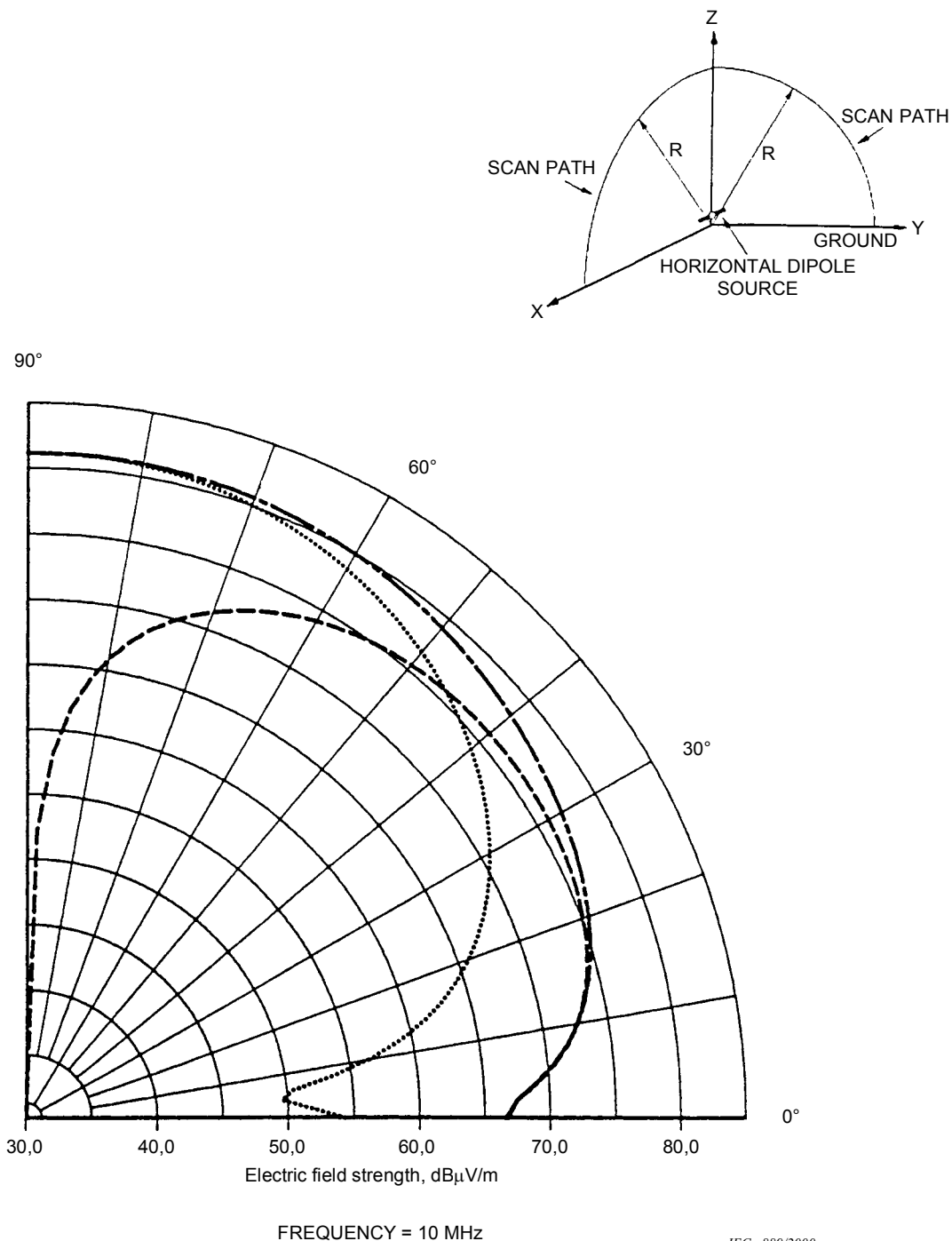


**Figure 4.6-48 – Vertical radiation patterns of the  $E$ -fields emitted by a small horizontal electric dipole located close to the ground**

Dipole length 1 m. Dipole height above ground 1 m. Dipole moment 1 A·m.

- Dashed line curve – vertically oriented  $E_z$  at a scan distance of 300 m in the Z-X plane
  - Dotted line curve – horizontally oriented  $E_x$  at a scan distance of 300 m in the Z-X plane
  - Dash-dot line curve – total vector/phasor sum of  $E_z$  and  $E_x$  at a scan distance of 300 m in the Z-X plane, the vertically polarized  $E$ -field
- Electrical constants of the ground  $\sigma = 1 \text{ mS/m}$ ,  $\epsilon_r = 15$

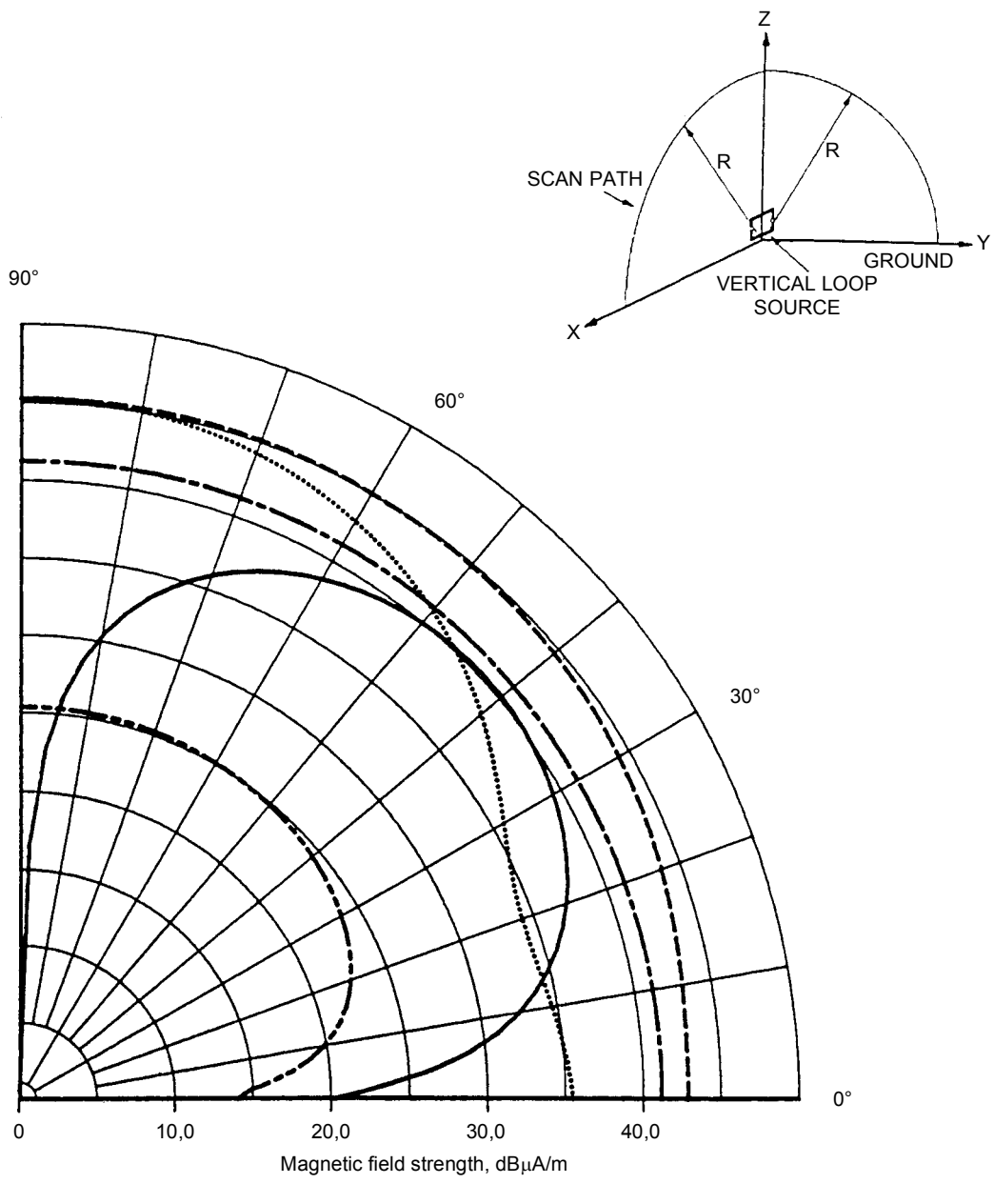


**Figure 4.6-49 – Vertical radiation patterns of the *H*-field emitted by a small horizontal magnetic dipole (vertical loop) located close to the ground**

Square loop  $0,6 \text{ m} \times 0,6 \text{ m}$ . Loop base height above ground  $0,07 \text{ m}$ . Dipole moment  $1 \text{ A}\cdot\text{m}^2$ .

- Dashed line curve – horizontally oriented *Hy* at a scan distance of 30 m in the *Z*-*X* plane
- Dotted line curve – horizontally oriented *Hy* at a scan distance of 30 m in the *Y*-*Z* plane
- Solid line curve – vertically oriented *Hz* at a scan distance of 30 m in the *Y*-*Z* plane
- Dash-double-dot curve – horizontally oriented *Hy* at a scan distance of 300 m in the *Z*-*X* plane
- Electrical constants of the ground  $\sigma = 1 \text{ mS/m}$ ,  $\varepsilon_r = 15$
- Dash-dot line curve – horizontally oriented *Hy* at a scan distance of 30 m in the *Z*-*X* plane
- Perfectly conducting ground

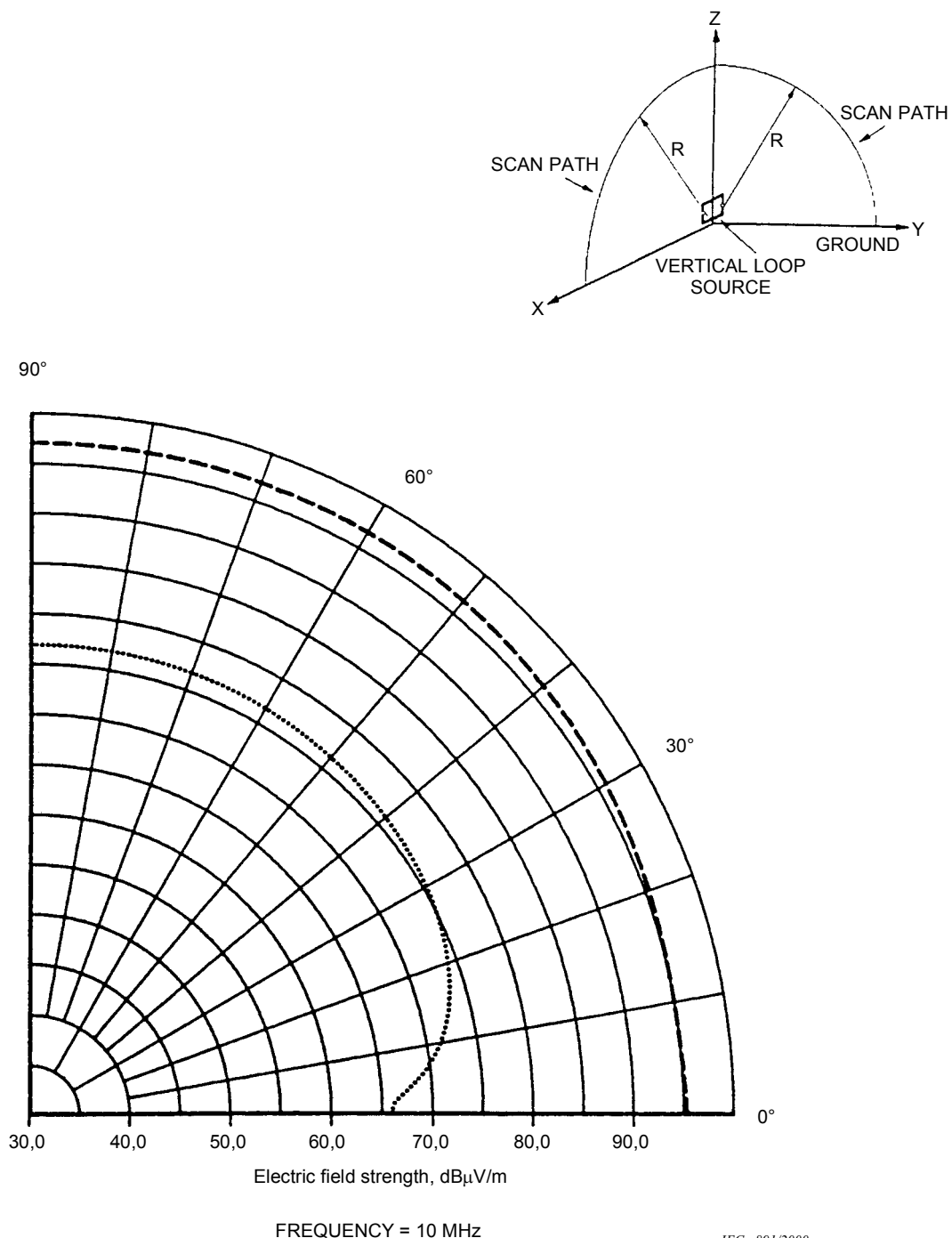


**Figure 4.6-50 – Vertical radiation patterns of the vertically polarized  $E$ -fields emitted by a small horizontal magnetic dipole (vertical loop) located close to the ground**

Square loop  $0,6 \text{ m} \times 0,6 \text{ m}$ . Loop base height above ground  $0,07 \text{ m}$ . Dipole moment  $1 \text{ A}\cdot\text{m}^2$ .

- Dashed line curve – total vector/phasor sum of  $E_z$  and  $E_x$  at a scan distance of  $30 \text{ m}$  in the Z-X plane, the vertically polarized  $E$ -field
  - Dotted line curve – total vector/phasor sum of  $E_z$  and  $E_x$  at a scan distance of  $300 \text{ m}$  in the Z-X plane, the vertically polarized  $E$ -field
- Electrical constants of the ground  $\sigma = 1 \text{ mS/m}$ ,  $\epsilon_r = 15$

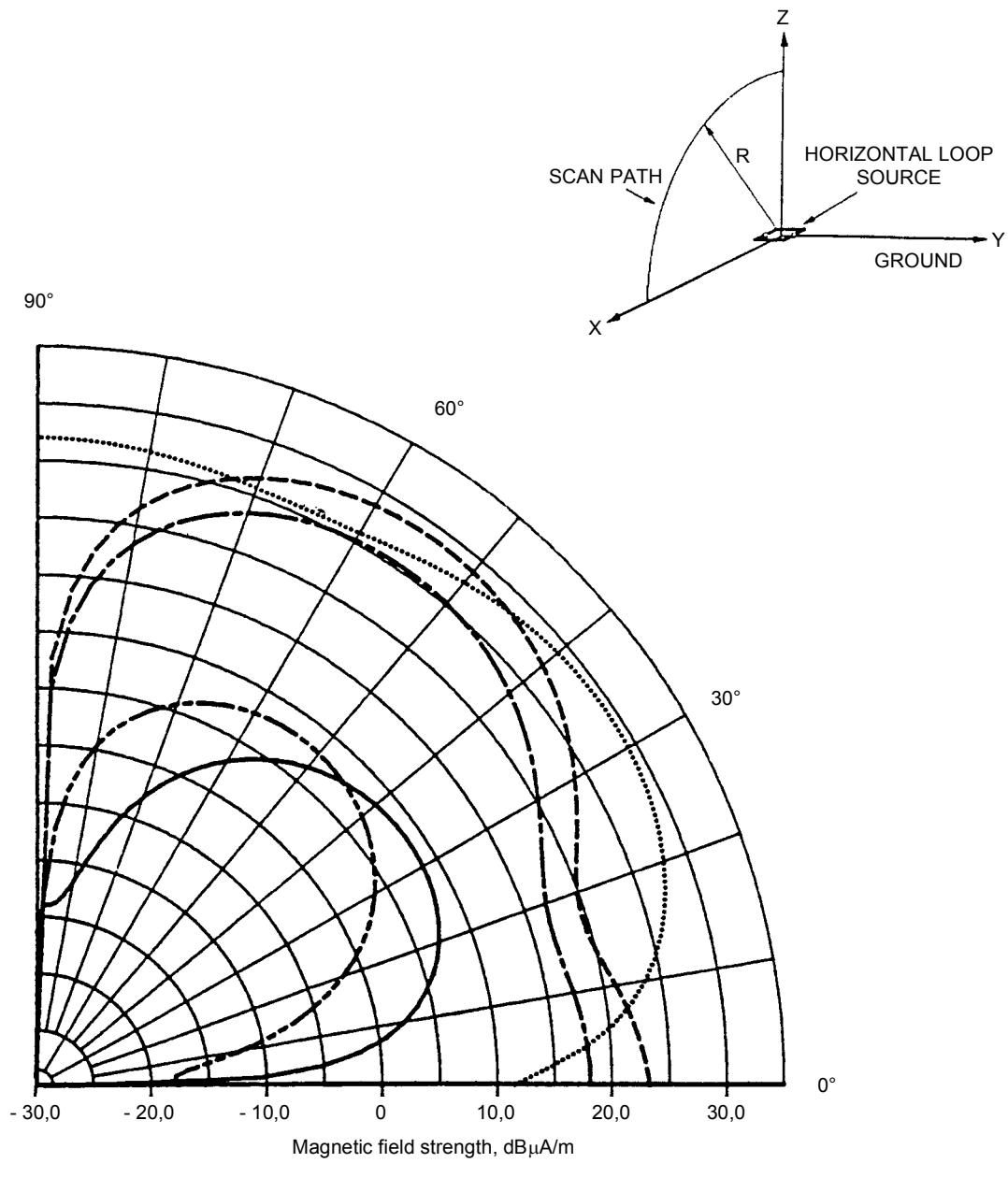
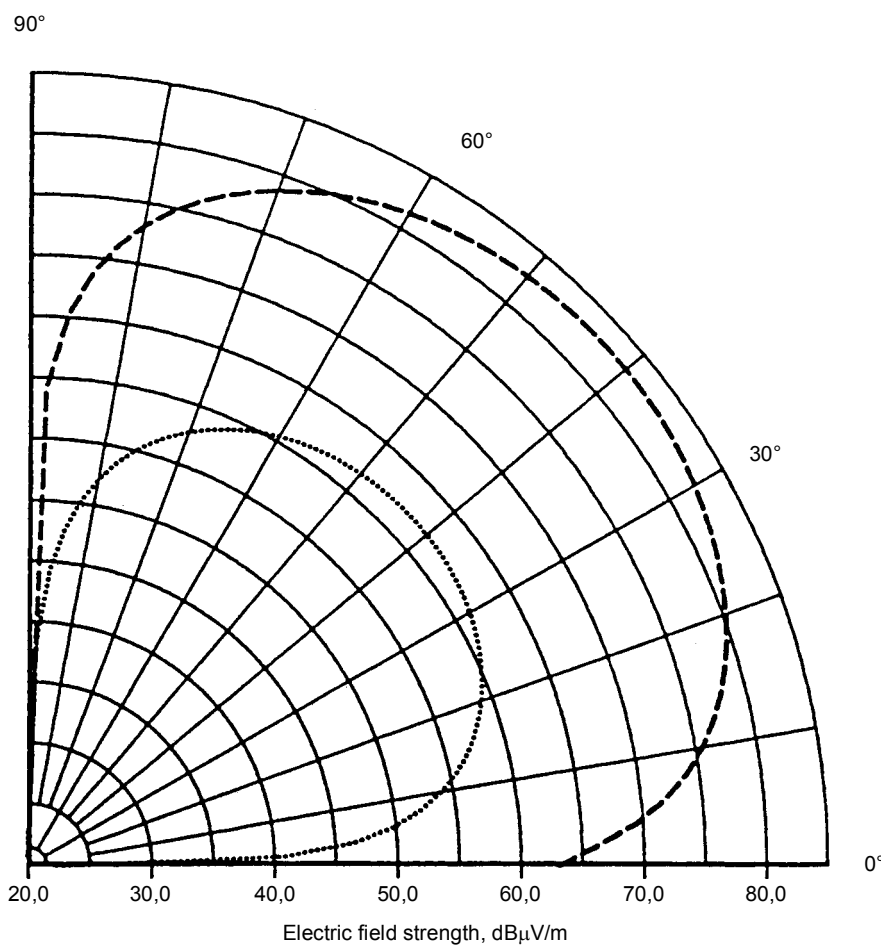
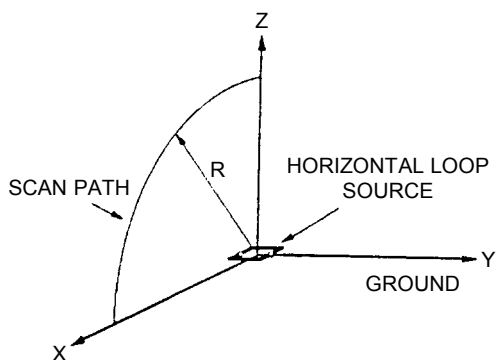


**Figure 4.6-51 – Vertical radiation patterns of the  $H$ -field emitted by a small vertical magnetic dipole (horizontal loop) located close to the ground**

Square loop  $0,2\text{ m} \times 0,2\text{ m}$ . Loop height above ground 1 m. Dipole moment  $1\text{ A}\cdot\text{m}^2$ .

- Dashed line curve – horizontally oriented  $H_x$  at a scan distance of 30 m
- Dotted line curve – vertically oriented  $H_z$  at a scan distance of 30 m
- Dash-double-dot curve – horizontally oriented  $H_x$  at a scan distance of 300 m
- Solid line curve – vertically oriented  $H_z$  at a scan distance of 300 m
- Electrical constants of the ground  $\sigma = 1\text{ mS/m}$ ,  $\epsilon_r = 15$
- Dash-dot line curve – horizontally oriented  $H_x$  at a scan distance of 30 m
- Perfectly conducting ground



FREQUENCY = 10 MHz

IEC 893/2000

**Figure 4.6-52 – Vertical radiation patterns of the  $E$ -fields emitted by a small vertical magnetic dipole (horizontal loop) located close to the ground**

Square loop  $0,2 \text{ m} \times 0,2 \text{ m}$ . Loop height above ground  $1 \text{ m}$ . Dipole moment  $1 \text{ A}\cdot\text{m}^2$ .

Dashed line curve – horizontally oriented  $E_y$  at a scan distance of  $30 \text{ m}$   
 Dotted line curve – horizontally oriented  $E_y$  at a scan distance of  $300 \text{ m}$   
 Electrical constants of the ground  $\sigma = 1 \text{ mS/m}$ ,  $\epsilon_r = 15$

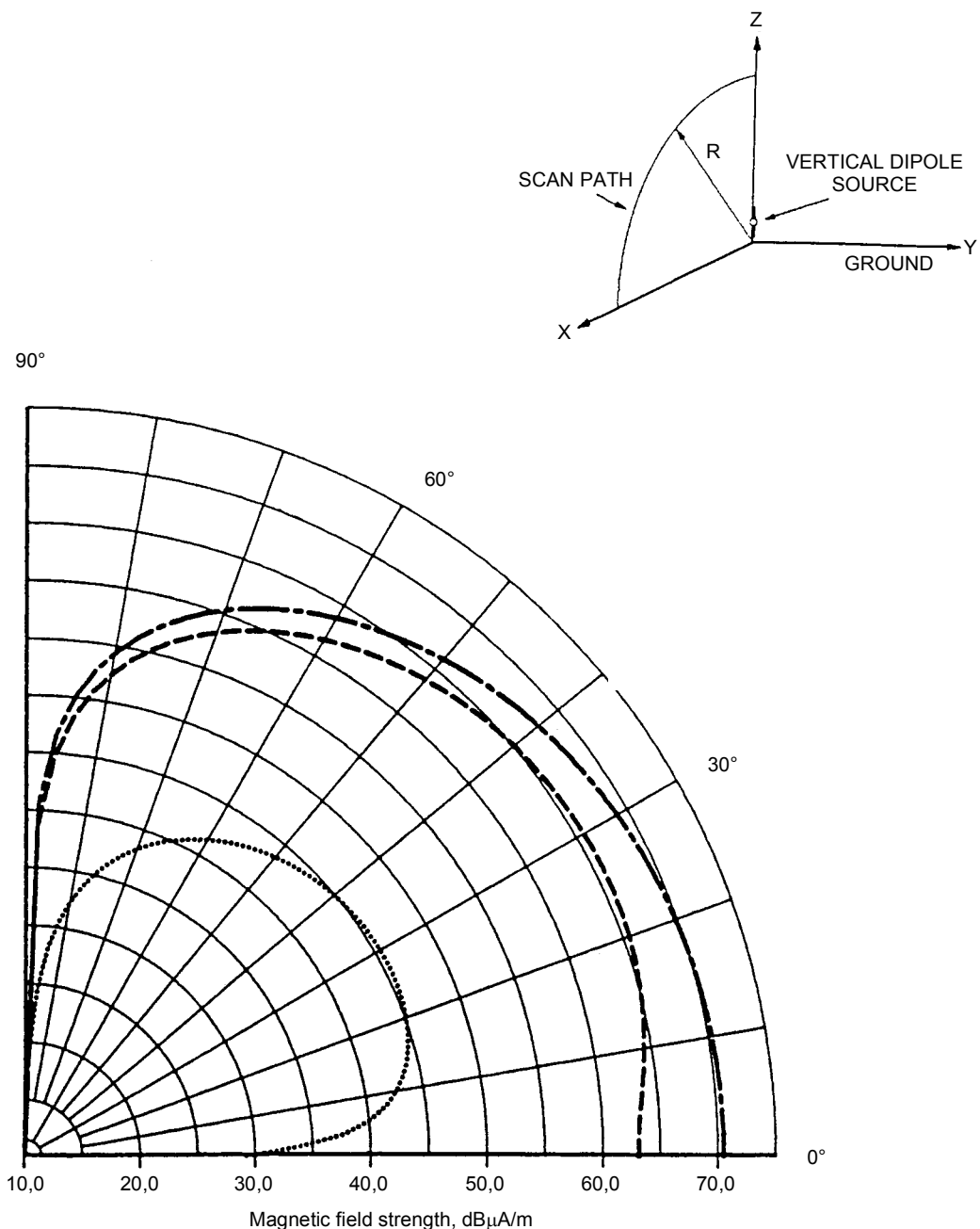


**Figure 4.6-53 – Vertical radiation patterns of the horizontally oriented  $H$ -fields emitted by a small vertical electric dipole located close to the ground**

Dipole length 1 m. Dipole base at a height above ground of 0,15 m. Dipole moment 1 A·m.

Dashed line curve –  $H_y$  at a scan distance of 30 m  
 Dotted line curve –  $H_y$  at a scan distance of 300 m  
 Electrical constants of the ground  $\sigma = 1 \text{ mS/m}$ ,  $\epsilon_r = 15$   
 Dash-dot line curve –  $H_y$  at a scan distance of 30 m  
 Perfectly conducting ground

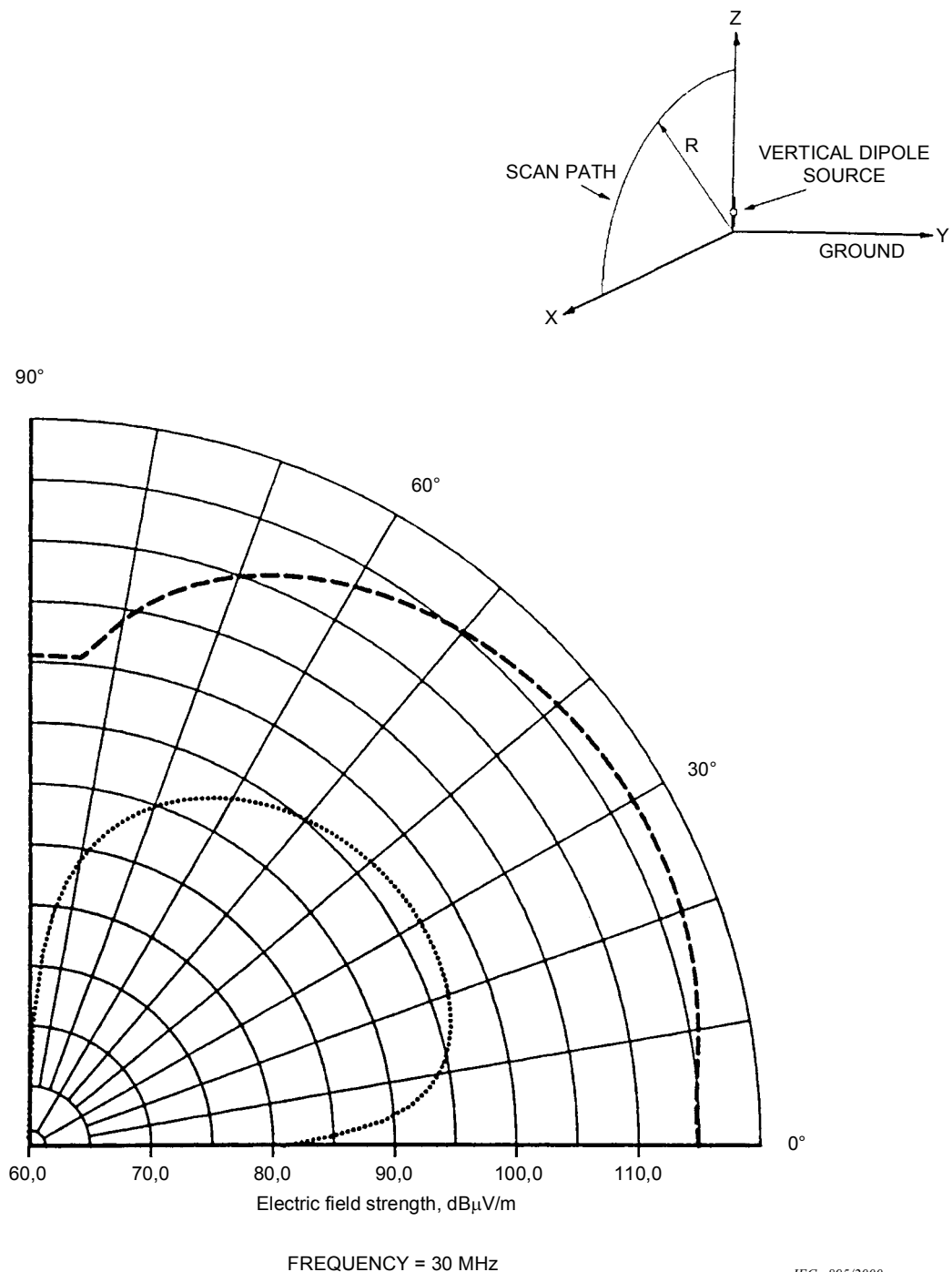


**Figure 4.6-54 – Vertical radiation patterns of the vertically polarized  $E$ -fields emitted by a small vertical electric dipole located close to the ground**

Dipole length 1 m. Dipole base at a height above ground of 0,15 m. Dipole moment 1 A·m.

- Dashed line curve – total vector/phasor sum of  $E_z$  and  $E_x$  at a scan distance of 30 m in the Z-X plane, the vertically polarized  $E$ -field
  - Dotted line curve – total vector/phasor sum of  $E_z$  and  $E_x$  at a scan distance of 300 m in the Z-X plane, the vertically polarized  $E$ -field
- Electrical constants of the ground  $\sigma = 1 \text{ mS/m}$ ,  $\epsilon_r = 15$

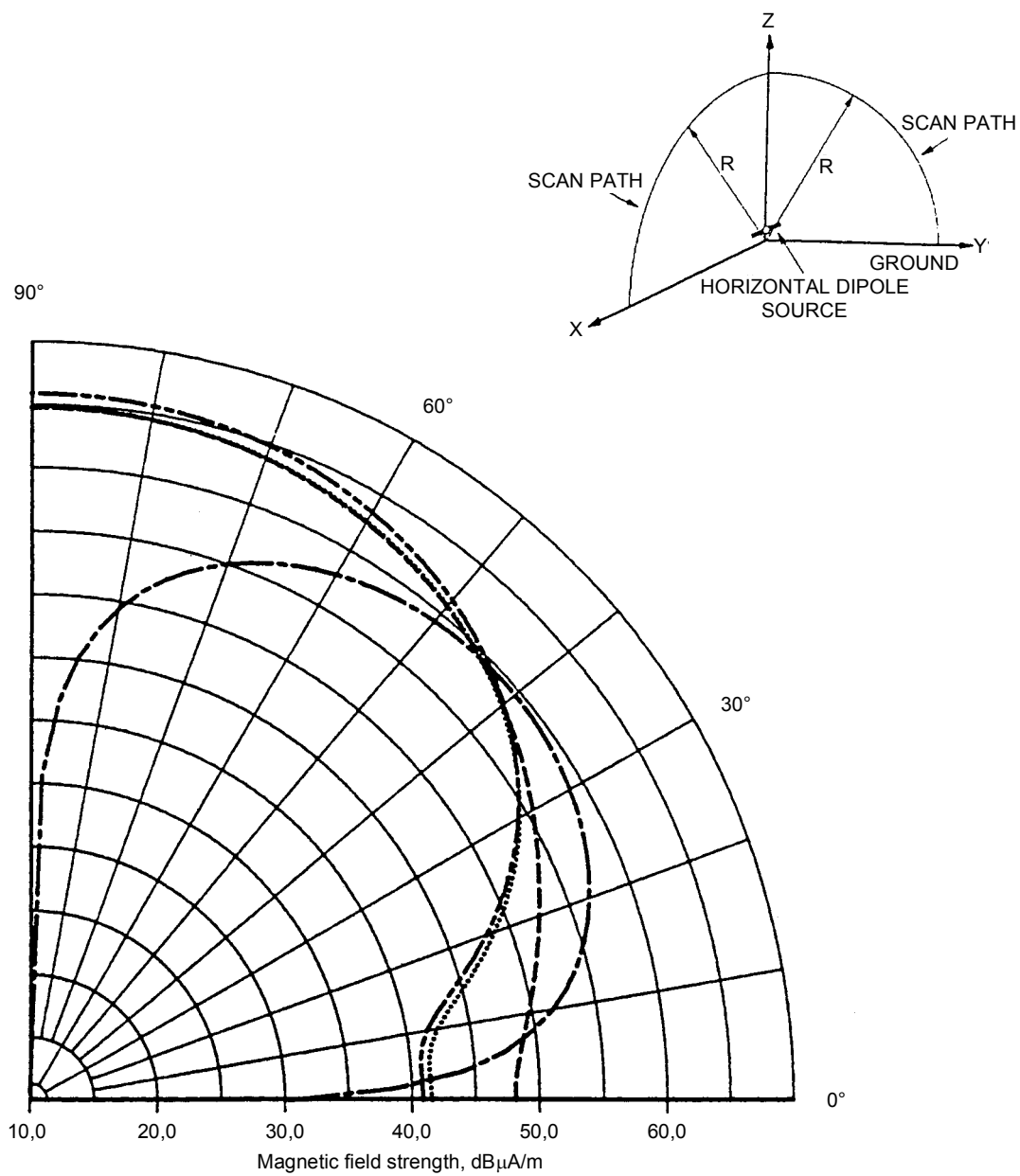


**Figure 4.6-55 – Vertical radiation patterns of the *H*-fields emitted by a small horizontal electric dipole located close to the ground**

Dipole length 1 m. Dipole height above ground 1 m. Dipole moment 1 A·m.

- Dashed line curve – horizontally oriented  $Hy$  at a scan distance of 30 m in the Z-X plane
- Dotted line curve – horizontally oriented  $Hy$  at a scan distance of 30 m in the Y-Z plane
- dash-dot line curve – vertically oriented  $Hz$  at a scan distance of 30 m in the Y-Z plane
- Electrical constants of the ground  $\sigma = 1 \text{ mS/m}$ ,  $\epsilon_r = 15$
- Dash-double-dot curve – horizontally oriented  $Hy$  at a scan distance of 30 m in the Z-X plane
- Perfectly conducting ground

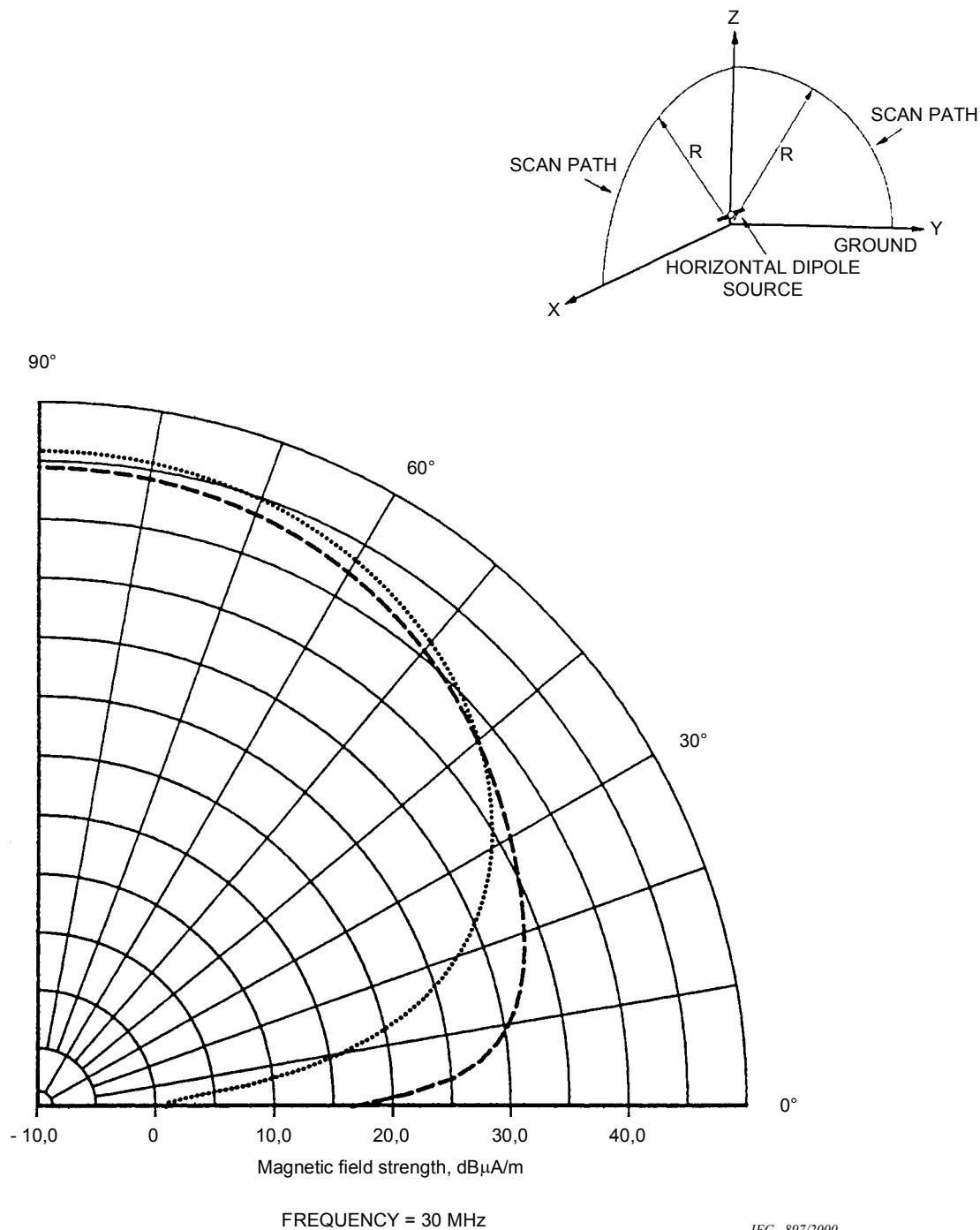


**Figure 4.6-56 – Vertical radiation patterns of the horizontally oriented  $H$ -fields emitted by a small horizontal electric dipole located close to the ground**

Dipole length 1 m. Dipole height above ground 1 m. Dipole moment 1 A·m.

Dashed line curve –  $H_y$  at a scan distance of 300 m in the Z-X plane  
Electrical constants of the ground  $\sigma = 1 \text{ mS/m}$ ,  $\epsilon_r = 15$

Dotted line curve –  $H_y$  at a scan distance of 300 m in the Z-X plane  
Perfectly conducting ground

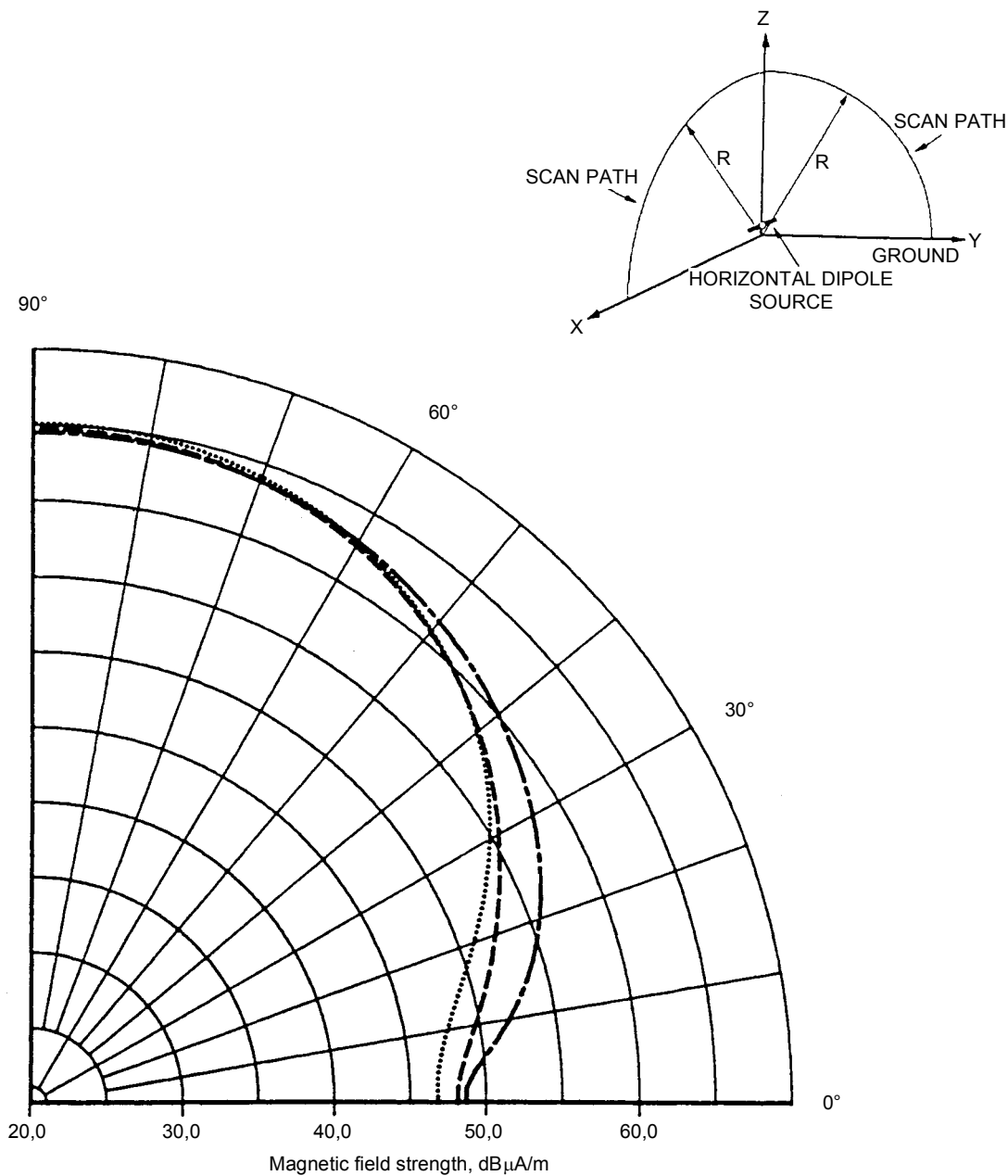


**Figure 4.6-57 – Influence of a wide range of values of the electrical constants of the ground on the vertical radiation patterns of the horizontally oriented H-fields emitted by a small horizontal electric dipole located close to the ground**

Dipole length 1 m. Dipole height above ground 1 m. Dipole moment 1 A·m.

$H_y$  at a scan distance of 30 m in the Z-X plane

Dash-dot line curve – ground constants are  $\sigma = 0,1 \text{ mS/m}$ ,  $\epsilon_r = 3$

Dashed line curve – ground constants are  $\sigma = 1 \text{ mS/m}$ ,  $\epsilon_r = 15$

Dotted line curve – ground constants are  $\sigma = 10 \text{ mS/m}$ ,  $\epsilon_r = 30$

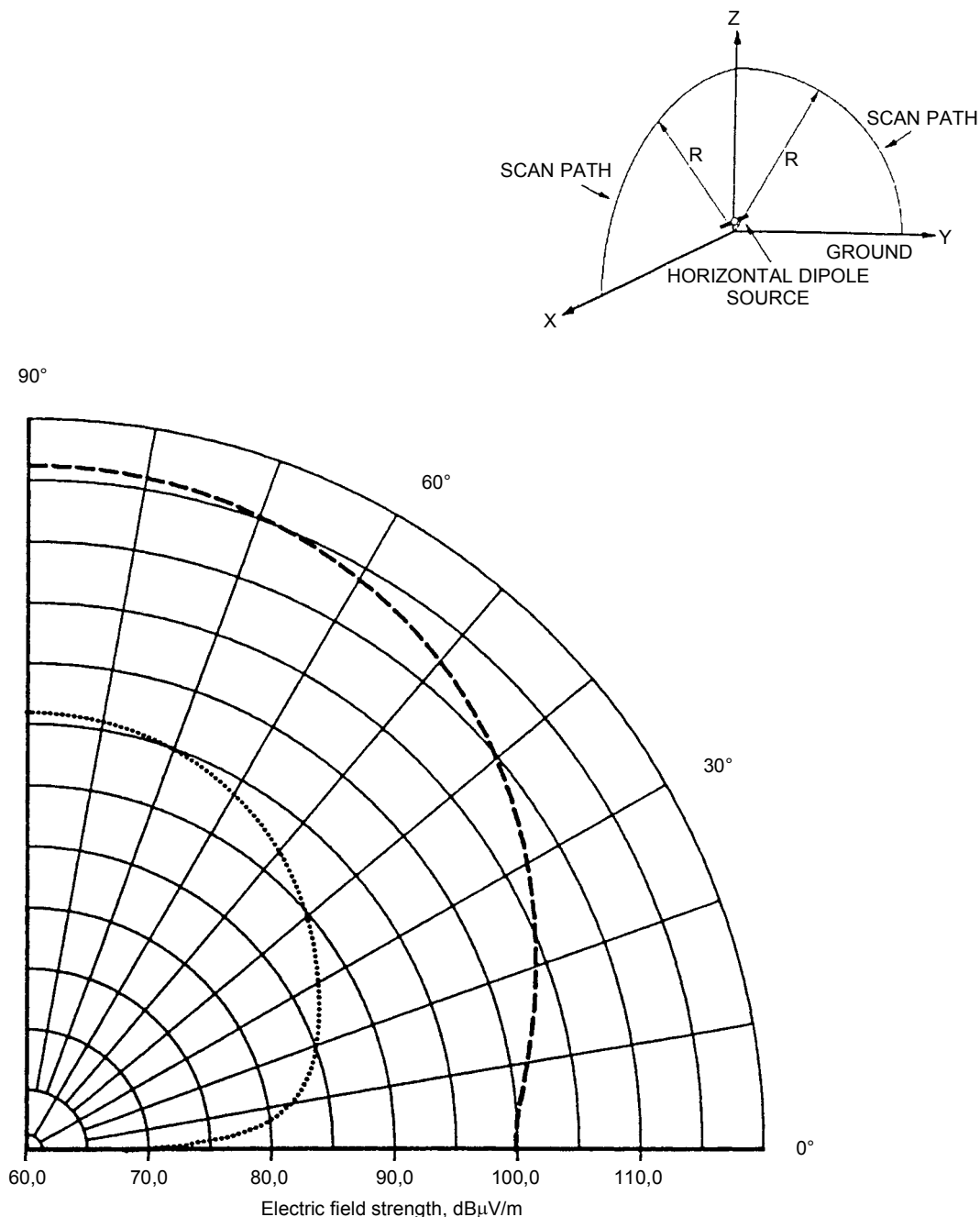


**Figure 4.6-58 – Vertical radiation patterns of the vertically polarized  $E$ -fields emitted by a small horizontal electric dipole located close to the ground**

Dipole length 1 m. Dipole height above ground 1 m. Dipole moment 1 A·m.

- Dashed line curve – total vector/phasor sum of  $E_z$  and  $E_x$  at a scan distance of 30 m in the Z-X plane, the vertically polarized  $E$ -field
- Dotted line curve – total vector/phasor sum of  $E_z$  and  $E_x$  at a scan distance of 300 m in the Z-X plane, the vertically polarized  $E$ -field
- Electrical constants of the ground  $\sigma = 1 \text{ mS/m}$ ,  $\epsilon_r = 15$

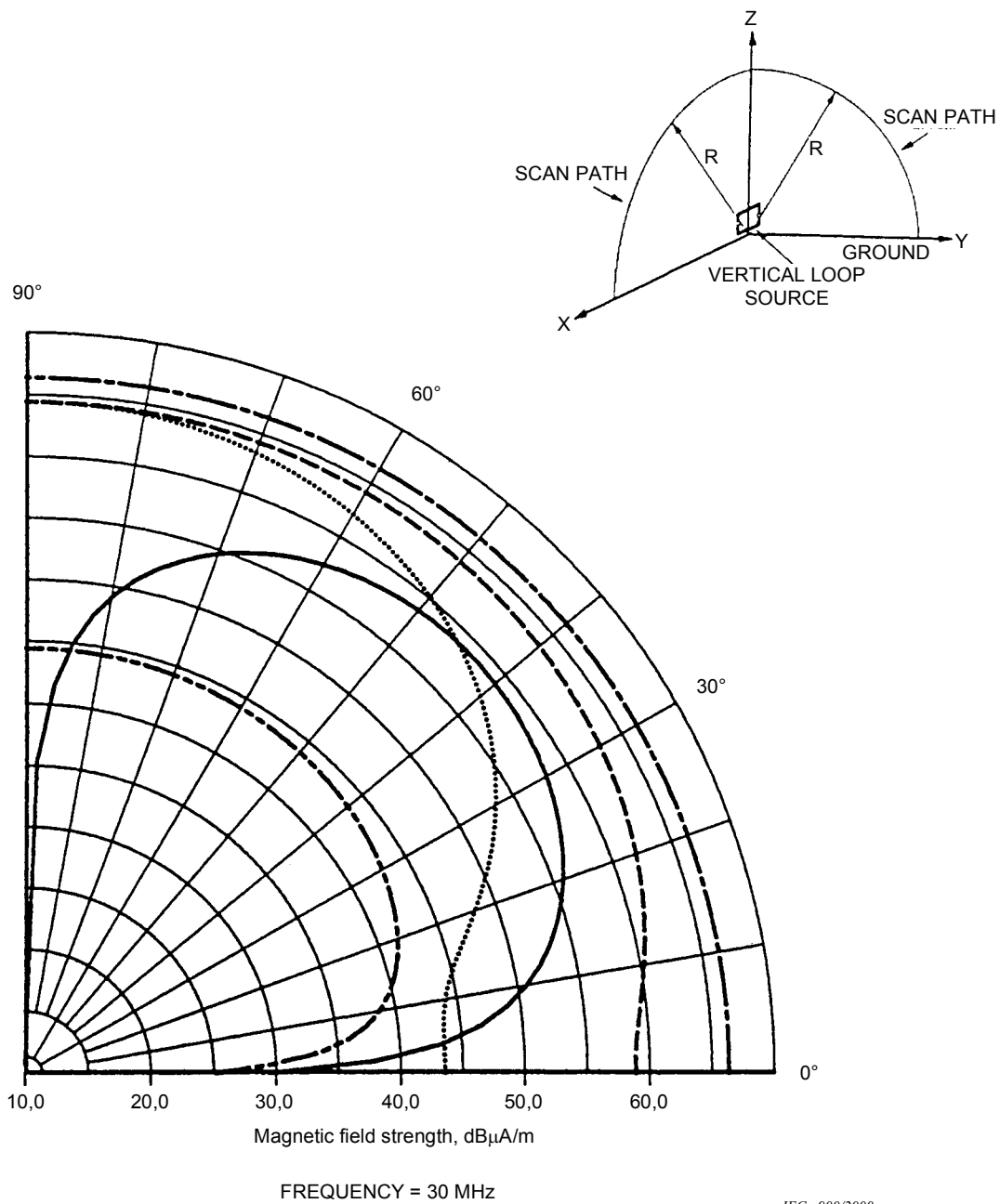


**Figure 4.6-59 – Vertical radiation patterns of the *H*-fields emitted by a small horizontal magnetic dipole (vertical loop) located close to the ground**

Square loop  $0,1 \text{ m} \times 0,1 \text{ m}$ . Loop base height above ground  $0,07 \text{ m}$ . Dipole moment  $1 \text{ A}\cdot\text{m}^2$ .

- Dashed line curve – horizontally oriented *Hy* at a scan distance of 30 m in the *Z*-*X* plane
- Dotted line curve – horizontally oriented *Hy* at a scan distance of 30 m in the *Y*-*Z* plane
- Solid line curve – vertically oriented *Hz* at a scan distance of 30 m in the *Y*-*Z* plane
- Dash-double-dot curve – horizontally oriented *Hy* at a scan distance of 300 m in the *Z*-*X* plane
- Electrical constants of the ground  $\sigma = 1 \text{ mS/m}$ ,  $\epsilon_r = 15$
- Dash-dot line curve – horizontally oriented *Hy* at a scan distance of 30 m in the *Z*-*X* plane
- Perfectly conducting ground

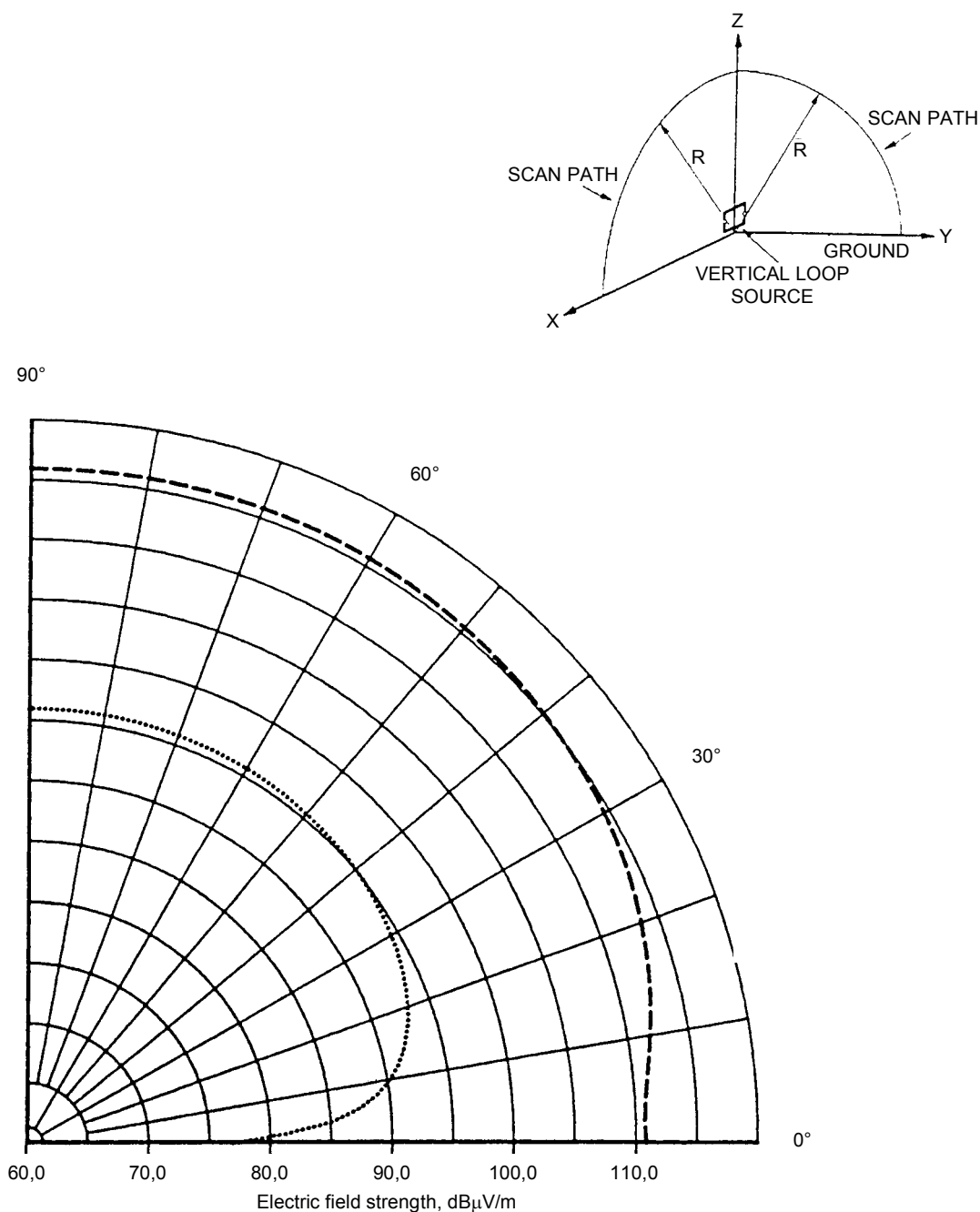
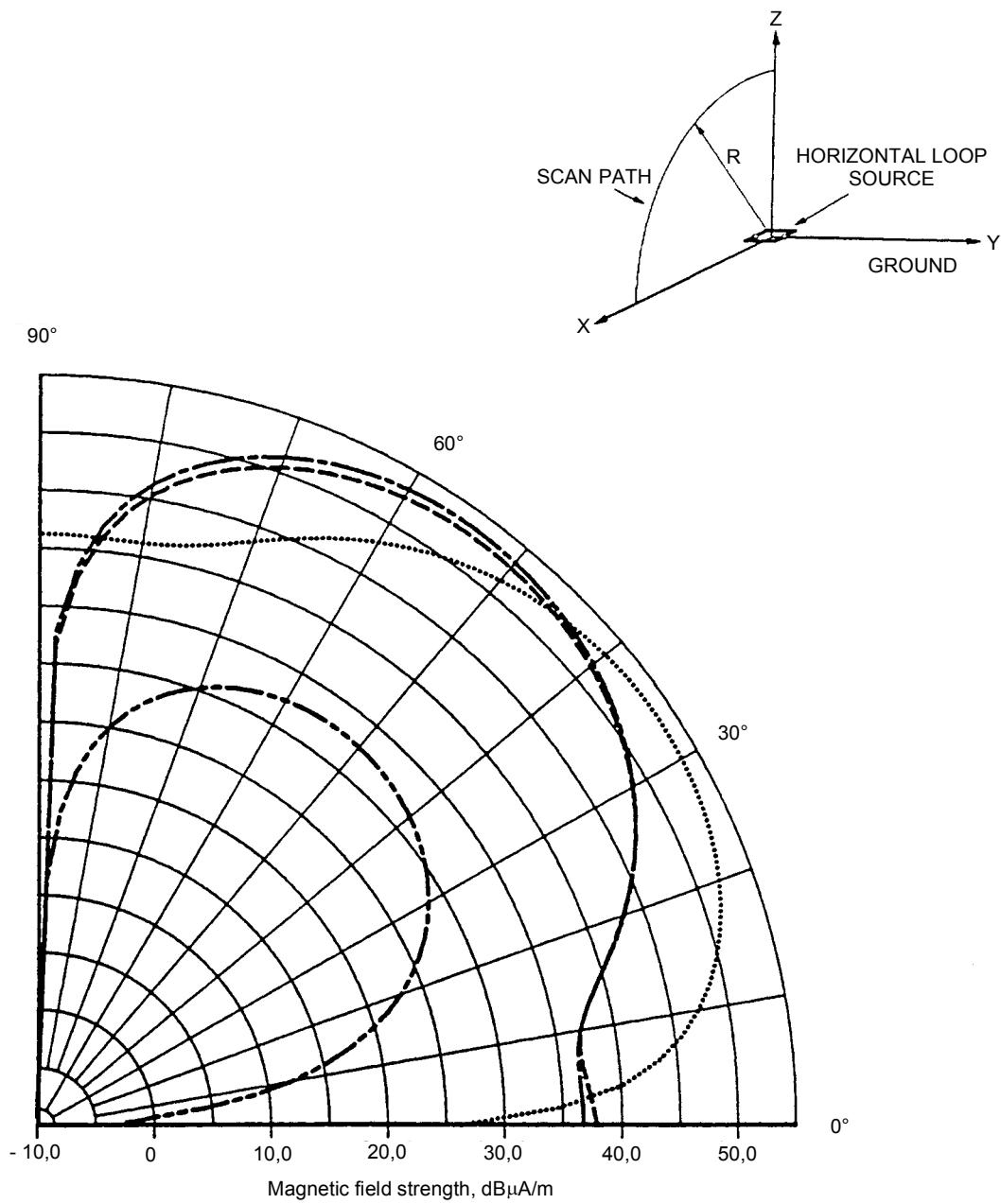


**Figure 4.6-60 – Vertical radiation patterns of the vertically polarized  $E$ -fields emitted by a small horizontal magnetic dipole (vertical loop) located close to the ground**

Square loop  $0,1 \text{ m} \times 0,1 \text{ m}$ . Loop base height above ground  $0,07 \text{ m}$ . Dipole moment  $1 \text{ A}\cdot\text{m}^2$ .

- Dashed line curve – total vector/phasor sum of  $E_z$  and  $E_x$  at a scan distance of  $30 \text{ m}$  in the Z-X plane, the vertically polarized  $E$ -field
  - Dotted line curve – total vector/phasor sum of  $E_z$  and  $E_x$  at a scan distance of  $300 \text{ m}$  in the Z-X plane, the vertically polarized  $E$ -field
- Electrical constants of the ground  $\sigma = 1 \text{ mS/m}$ ,  $\epsilon_r = 15$



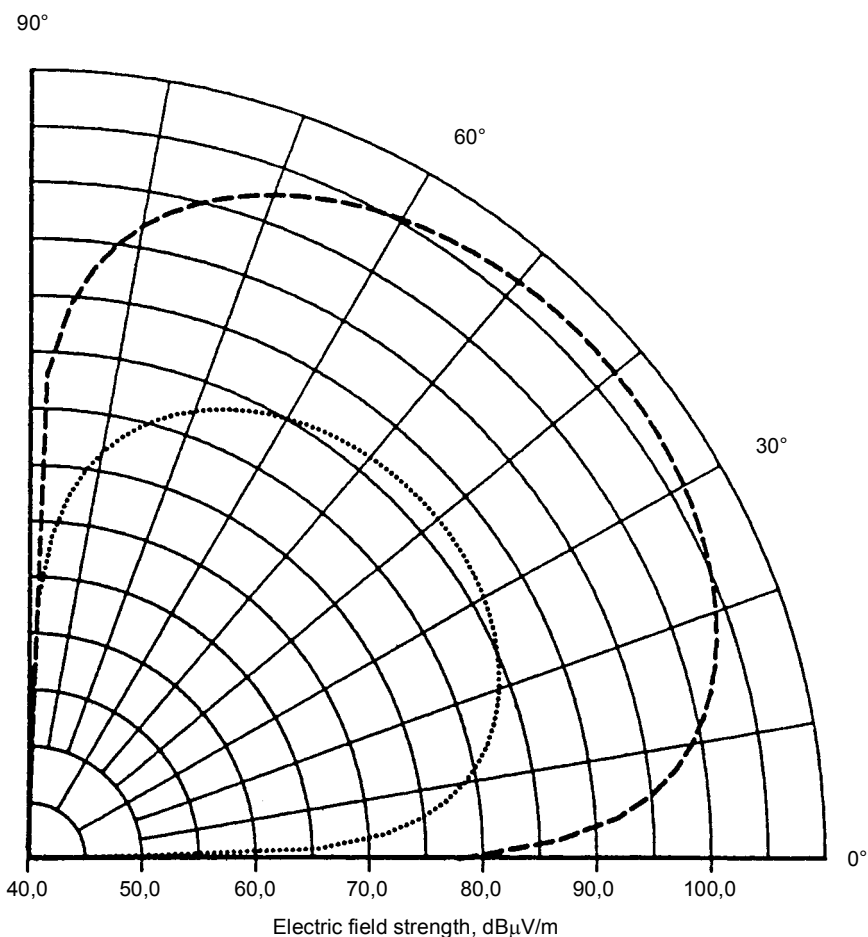
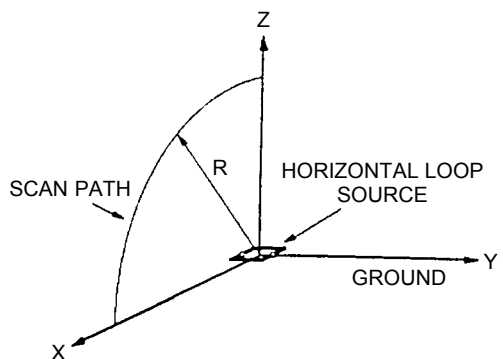
FREQUENCY = 30 MHz

IEC 902/2000

**Figure 4.6-61 – Vertical radiation patterns of the  $H$ -fields emitted by a small vertical magnetic dipole (horizontal loop) located close to the ground**

Square loop  $0,1 \text{ m} \times 0,1 \text{ m}$ . Loop height above ground 1 m. Dipole moment  $1 \text{ A}\cdot\text{m}^2$ .

- Dashed line curve – horizontally oriented  $H_x$  at a scan distance of 30 m
- Dotted line curve – vertically oriented  $H_z$  at a scan distance of 30 m
- dash-double-dot curve – horizontally oriented  $H_x$  at a scan distance of 300 m
- Electrical constants of the ground  $\sigma = 1 \text{ mS/m}$ ,  $\epsilon_r = 15$
- Dash-dot line curve – horizontally oriented  $H_x$  at a scan distance of 30 m
- Perfectly conducting ground



FREQUENCY = 30 MHz

IEC 903/2000

**Figure 4.6-62 – Vertical radiation patterns of the  $E$ -fields emitted by a small vertical magnetic dipole (horizontal loop) located close to the ground**

Square loop  $0,1 \text{ m} \times 0,1 \text{ m}$ . Loop height above ground 1 m. Dipole moment  $1 \text{ A}\cdot\text{m}^2$ .

Dashed line curve – horizontally oriented  $E_y$  at a scan distance of 30 m

Dotted line curve – horizontally oriented  $E_y$  at a scan distance of 300 m

Electrical constants of the ground  $\sigma = 1 \text{ mS/m}$ ,  $\epsilon_r = 15$

## 5 Background and history

### 5.1 The history of the CISPR

#### 5.1.1 The early years: 1934-1984

An *ad hoc* conference of interested international organizations was held in 1933 in Paris to decide how the subject of radio interference should be dealt with internationally. There was general agreement that the most urgent international problem was to secure some uniformity in the method of measurement and stipulation of limits to avoid difficulties in the exchange of goods and services.

The result of this meeting was to form the Comité International Spécial des Perturbations Radioélectriques (CISPR) or in English, International Special Committee on Radio Interference. The first meeting was held in 1934. The first Chairman was Sir Clifford Patterson and members were appointed by their national committees. In 1935, the specification for the measuring set including the Mains Network (LISN in the US) was drafted. After this specification was finalized, it was found that the measuring sets produced by different countries, produced different data. Consequently, the Belgian Electrotechnical Committee took on the task to construct the standard CISPR measuring set. In 1939, 12 copies of this set were delivered to different countries.

The work with interference limits progressed slowly. At the first CISPR meeting the lowest protected field strength was set at 1 mV/m (60 dB $\mu$ V/m) with a modulation index of 80 %. The lowest protection ratio was to be 100 (40 dB). Various limits were proposed but none even came close to (the then required) 20 dB $\mu$ V/m. There was no agreement on limits before WW II. Agreement was reached on the antenna height to be used for measurement and for the model for coupling from the mains to the antenna. This proved valuable for future work. The requirements for the electrical parameters of interference-suppression capacitors were also established.

During WW II no meetings were held. The work started again in 1946 under the then CISPR Chairman: Dr. S. Whitehead. During WW II many individual countries had set up services for the suppression of interference to aid the war effort. A significant unifying effort was based on the 12 measuring sets delivered to different national committees by the Belgian Electrotechnical Committee at the brink of WW II. On the basis of this set, the frequency range was extended to 30 MHz to give coverage from 150 kHz to 30 MHz with the quasi-peak detector that was also in the Belgian set. This measuring set specification was approved in The Hague in 1958. The specification was considerably improved over the 1935 version and the building of a simple prototype was no longer necessary. Further work led to the approval of the ISM specification in 1965 and the artificial hand specification in 1968. These specifications were merged into one specification in 1972 with an amendment issued in 1975.

The CISPR measuring set specifications were extended from 30 MHz to 300 MHz in 1958 with an amendment for ISM in 1965. The same year, the measuring set specifications was extended from 300 MHz to 1 000 MHz. Mr. Meyer de Stadelhofen's absorbing clamp appeared in 1966 and was added to the specification in 1970.

New editions of the measuring set specifications appeared as follows:

CISPR 1 (1972), 0,15 MHz to 30 MHz

CISPR 2 (1985), 30 MHz to 300 MHz

CISPR 4 (1967), 300 MHz to 1 000 MHz

In addition several supplements were released until 1993 when CISPR 16-1 merged all specifications into one document.

Limits were first proposed in 1950 for the 150 kHz to 285 kHz and the 150 kHz to 1 605 kHz frequency ranges for domestic, industrial and commercial appliances up to 1 kW and for connection to the low-voltage power network. The adopted limits were reduced or increased at every CISPR meeting. The frequency range was extended to 25 MHz and abolished again at the whim of the delegates. For some years, a voltage range was given as the limit since agreement could not be reached for a specific value. Until 1964, when higher limits were specified for motor-operated appliances for domestic and similar use and for portable tools. The permissible voltages were measured with the  $150 \Omega$  V-network between each line and ground. The limits were amended again in 1973. The working conditions of the appliances were specified in 1961 and amended in 1967, 1970 and 1973. The limits of interference power radiated from the power cord from 30 MHz to 300 MHz and as measured with the MDS absorbing clamp were agreed upon in 1970 and amended in 1973.

Interference from low repetition transient events was first controlled in 1961 and limits for regulating controls incorporating semiconductors and for thermostatically controlled appliances were specified in 1970. Limits for program-controlled appliances were set in 1967. In 1973, the limits for the transient events were combined into one document: Rules for the Evaluation of Radio Noise Produced by Switching Operations in Appliances for Household and similar purposes in the 0,15 MHz to 300 MHz Frequency Range.

Limits for radiation from sound and TV broadcast receivers were specified in 1961 with amendments issued in 1964, 1967 and 1970. Limits for the mains interference immunity factor for long- and medium-wave receivers were given in 1961 with amendments in 1964 and 1967.

Limits for ISM-frequencies were requested by the ITU WARC in 1959. CISPR published limits for out-of-band frequencies in 1961 with amendments in 1964, 1967 and 1973.

Limits for ignition systems in the automotive field were given in 1961 with amendments given in 1964, 1970 and 1973.

The limits for fluorescent lighting fixtures for the long and medium waves were specified in 1964 with amendments in 1967, 1970 and 1973.

The characteristics of spectrum analyzers required for interference measurements from 0,3 GHz to 18 GHz of microwave equipments for heating and medical purposes were released in 1973.

Methods for estimation of compliance with limits for appliances in large-scale production were agreed upon in 1961 and 1964. The "Significance of a CISPR Limit" rule was established in 1970.

The safety aspects of filters and capacitors used for suppression on the power mains was discussed since before WW II. The initial discussions were extensive throughout the 1950s, but then subsided since the CISPR interests concentrated on suppression of higher frequencies which required smaller values of capacitance.

The first standard on industrial, scientific and medical (ISM) equipment was published in 1973. Five further publications were released in 1975 on the general topic of "Limits and Methods of Measurement" for:

- 1) ISM equipment excluding surgical diathermy apparatus.
- 2) Vehicles, motor boats and devices which utilized ignition systems.
- 3) Sound and television receivers.
- 4) Household electrical appliances, portable tools and similar devices.
- 5) Fluorescent lamps and luminaries.

Subsequent work continuously updated these documents.

### 5.1.2 The division of work

In 1973 it became apparent that the work of the CISPR needed to be subdivided and organized along major product families. The following subcommittees were established:

- CISPR/A defines the instrumentation and the measurement methods;
- CISPR/B is concerned with the interference from industrial, scientific and medical equipment (ISM);
- CISPR/C is concerned with the interference from overhead power lines, high-voltage equipment and traction systems;
- CISPR/D is concerned with the interference from motor vehicles and internal combustion engines;
- CISPR/E is concerned with the interference from and to TV and broadcast receivers;
- CISPR/F is concerned with the interference from and to household appliances, motor-operated equipment, lighting apparatus and similar equipment;
- CISPR/G is concerned with the interference from and to computers and information technology equipment (ITE).

### 5.1.3 The computer years: 1984 to 1998

Since 1984, much attention has been concerned with refining the measurements methods and the limits for information technology equipment. In principle, this is any equipment that uses a microprocessor and switching frequencies or clocks above 9 kHz. The CISPR work was and is primarily concerned with refining the Open-Area Test Site (OATS) requirements, as well as replacing the OATS with anechoic room, TEM and GTEM test sites. In addition, much effort has been expended on CISPR Publication 16, "The CISPR Handbook", which contains all instrument specifications and measurement methods.

The CISPR work since 1984 is best described by the number of documents that were produced. The titles are reduced to the keywords and the number and year identifying each publication:

- 10 (1990) Rules and Procedures of CISPR
- 11 (1990) Limits and Measurement Methods, ISM
- 12 (1990) Automobiles and Ignition Systems
- 13 (1996) Sound and TV Receivers
- 14 (1993) Household Appliances and Electric Tools
- 15 (1993) Fluorescent and RF Lighting Fixtures
- 16-1 (1993) Specification for EMC Measurement Equipment
- 16-2 (1996) Methods of EMC Measurements
- 17 (1981) Specification for Filters
- 18-1 (1982) Overhead Power Line, Phenomena
- 18-2 (1986) Overhead Power Line, Limits and Methods
- 18-3 (1986) Overhead Power Line, Suppression
- 19 (1983) Microwave Oven Substitution Measurements
- 20 (1996) Immunity of Sound and RV Receivers
- 21 (1985) Reception of Radio in the Presence of Noise
- 22 (1993), (1997) Information Technology Equipment
- 23 (1987) Determination of ISM Limits
- 24 (1997) Immunity of ITE
- 25 (1995) Emission Limits to Protect Radios in Cars

The future is unknown. However, the work of the CISPR will go on to address any problem that may occur because of the new technologies proposed.

### 5.1.4 The people in CISPR

As in any organization it takes dedication and perseverance in the task at hand. Some of the key people in CISPR were and are as follows:

#### Chairmen of CISPR

Sir C.C. Patterson (UK)	Paris 1934
Prof. A.F. Enström (SE)	Berlin 1935
Mr. R. Braillard (BE)	1934-1939
Dr. S. Whitehead (UK)	1946-1953
Mr. O.W. Humphreys (BG)	1953-1961
Prof. L. Morren (BE)	1961-1967
Prof. F.L. Stumpers (NL)	1967-1973
Mr. J. Meyer de Stadelhofen (CH)	1973-1977
Mr. P. Akerlind (SE)	1977-1979
Prof. R.M. Showers (USA)	1979-1985
Mr. G.A. Jackson (UK)	1985-1991
Prof. A. Warner (DE)	1991-1994
Mr. P. Kerry (UK)	1995-present

## 5.2 Historical background to the method of measurement of the interference power produced by electrical household and similar appliances in the VHF range

### 5.2.1 Historical detail

Measurement of field strength is, in theory, most suitable for determining the interference capability of all types of appliances at frequencies higher than 30 MHz. However, the methods involved together with the precautions to be taken prove troublesome in application. Consequently, engineers have for a long time used the terminal voltage method, while waiting for something more satisfactory. Several methods have been explained to replace those involving electro-magnetic field measurements on an OATS by radiation measurements in the laboratory. Among the most interesting are the stop filter method and the earth current method. These are substitution methods, in which a slotted coaxial filter with negligible losses is used to adjust the radiating length of the supply lead of the source of interference to obtain maximum radiation. In these methods, the interference capability of an appliance is defined as the power which a standard generator must inject into a simple antenna of known characteristics in order to obtain the same effect on an antenna connected to the measuring receivers as that produced by the source of interference. Several more convenient methods have been developed from those just mentioned.

The measurement of terminal voltages has been considerably improved by replacing the artificial mains V-network by a Y-network so as to obtain the true asymmetric voltage produced by the source of interference. A similar method using a reactive slotted coaxial filter was developed. A method for measuring the power which the source of interference may inject into the supply lead has also been proposed. This method is based on the measurement of the current at the input of an absorbent coaxial device.

The advantage of the latter over the terminal voltage method is that it is not necessary to disconnect the supply lead. It indicates values of the interference power corresponding closely with those obtained by the methods in which the radiation of the supply lead is measured in the resonant condition.

Although, through their ease of operation, the terminal voltage and the absorbing coaxial device methods were preferable to the stop filter and the earth current methods, it remained to be shown that the results which they gave conformed with those obtained in practice.

Statistical measurements on the interference sources have shown that the interference measured by the stop filter method agrees, more closely than that measured by the terminal voltage method, with the effect of the same sources measured at the input of receivers located in the same building. Measurements made by the absorbent device method gave results intermediate between the two previous ones. Other methods have been compared.

### 5.2.2 Development of the method

In the stop filter method, a value directly related to the current at the centre of a resonant half-way dipole antenna is measured. The most important factor is not the radiating system itself but the power that the source of interference is capable of coupling into the radiating system. The same principle applies to the earth current method. If it were possible to measure this power without measuring the field-strength, all the disadvantages arising from the influence of surrounding objects on the propagation between the radiating element and the receiving aerial would be removed. The attempt to replace the coaxial stop filter by a ferrite tube showed that a large part of the energy produced by the source of interference was dissipated in this tube. It was then thought that the measurements of the current at the input of the ferrite tube might replace, at least in part, the measurement of the field by the stop filter method. This gave rise to the device described in 4.1.3 of CISPR 2.

The following question was then studied: how do the different methods of measurement compare in the particular case of a shielded source of interference of given available power, with a purely resistive internal impedance and transmitting all its interference energy to the supply lead in the asymmetrical mode when the size of this source is varied? Experimental investigations showed the remarkable fact that the new device gave results which were practically independent of the dimensions of those obtained by the other methods.

In fact, one can reduce the absorbing device measuring system to the following circuit: a source of interference of internal impedance  $Z_s$  supplying a load  $Z_c$  through a low-loss line of characteristic impedance  $Z_L$ . If the length of the line is varied from zero, the power absorbed by the load  $Z_c$  passes (when  $Z_c$  is different from  $Z_L$ ) through maxima and minima corresponding to resonance and anti-resonance of the system.

Neglecting the radiation and other losses of the line and discussing the case in which the load is located at a distance corresponding to the first maximum, we consider the point in the line at which the source and the load appear as pure resistances  $R_s$  and  $R_c$ . It can thus be shown that if  $P_d$  is the available power of the source,  $P_c$  the power absorbed by the load and

$$m = \frac{R_s}{R_c}$$

then:

$$\frac{P_c}{P_d} = \frac{4m}{(m+1)^2}$$

This gives for:

$m =$	0,1	0,2	0,5	1	2	5	10	20	30
$M = 10 \log \frac{P_c}{P_d} =$	4,8	2,5	0,5	0	0,5	2,5	4,8	7,4	9 dB

It will be seen that the matching of the source of the lead is not very critical and that if an absorbent clamp is used to constitute a load, for example of the order of  $200 \Omega$ , the results obtained will not be very different from those obtained if a load is applied to the output of the source of interference in the form of a line brought to resonance by means of a coaxial stop filter.

It can therefore be concluded that this device, developed primarily in order to avoid the disadvantage of the test site for measuring the radiation, and the necessity to interrupt or disconnect the lead supplying the source of interference, has technical qualities which justify its adoption for the measurement of the interference produced by domestic and similar electrical appliances.

---



## Standards Survey



The IEC would like to offer you the best quality standards possible. To make sure that we continue to meet your needs, your feedback is essential. Would you please take a minute to answer the questions overleaf and fax them to us at +41 22 919 03 00 or mail them to the address below. Thank you!

Customer Service Centre (CSC)

**International Electrotechnical Commission**

3, rue de Varembé  
1211 Genève 20  
Switzerland

or

Fax to: **IEC/CSC** at +41 22 919 03 00

Thank you for your contribution to the standards-making process.

**A Prioritaire**

Nicht frankieren  
Ne pas affranchir



Non affrancare  
No stamp required

**RÉPONSE PAYÉE**

**SUISSE**

Customer Service Centre (CSC)  
**International Electrotechnical Commission**  
3, rue de Varembé  
1211 GENEVA 20  
Switzerland



<p><b>Q1</b> Please report on <b>ONE STANDARD</b> and <b>ONE STANDARD ONLY</b>. Enter the exact number of the standard: (e.g. 60601-1-1)</p> <p>.....</p>	<p><b>Q6</b> If you ticked NOT AT ALL in Question 5 the reason is: (<i>tick all that apply</i>)</p> <p>standard is out of date <input type="checkbox"/>      standard is incomplete <input type="checkbox"/>      standard is too academic <input type="checkbox"/>      standard is too superficial <input type="checkbox"/>      title is misleading <input type="checkbox"/>      I made the wrong choice <input type="checkbox"/>      other .....</p>
<p><b>Q2</b> Please tell us in what capacity(ies) you bought the standard (<i>tick all that apply</i>). I am the/a:</p> <p>purchasing agent <input type="checkbox"/>      librarian <input type="checkbox"/>      researcher <input type="checkbox"/>      design engineer <input type="checkbox"/>      safety engineer <input type="checkbox"/>      testing engineer <input type="checkbox"/>      marketing specialist <input type="checkbox"/>      other .....</p>	<p><b>Q7</b> Please assess the standard in the following categories, using the numbers:      (1) unacceptable,      (2) below average,      (3) average,      (4) above average,      (5) exceptional,      (6) not applicable</p> <p>timeliness .....</p> <p>quality of writing .....</p> <p>technical contents .....</p> <p>logic of arrangement of contents .....</p> <p>tables, charts, graphs, figures .....</p> <p>other .....</p>
<p><b>Q3</b> I work for/in/as a: (<i>tick all that apply</i>)</p> <p>manufacturing <input type="checkbox"/>      consultant <input type="checkbox"/>      government <input type="checkbox"/>      test/certification facility <input type="checkbox"/>      public utility <input type="checkbox"/>      education <input type="checkbox"/>      military <input type="checkbox"/>      other .....</p>	<p><b>Q8</b> I read/use the: (<i>tick one</i>)</p> <p>French text only <input type="checkbox"/>      English text only <input type="checkbox"/>      both English and French texts <input type="checkbox"/></p>
<p><b>Q4</b> This standard will be used for: (<i>tick all that apply</i>)</p> <p>general reference <input type="checkbox"/>      product research <input type="checkbox"/>      product design/development <input type="checkbox"/>      specifications <input type="checkbox"/>      tenders <input type="checkbox"/>      quality assessment <input type="checkbox"/>      certification <input type="checkbox"/>      technical documentation <input type="checkbox"/>      thesis <input type="checkbox"/>      manufacturing <input type="checkbox"/>      other .....</p>	<p><b>Q9</b> Please share any comment on any aspect of the IEC that you would like us to know:</p> <p>.....</p> <p>.....</p> <p>.....</p> <p>.....</p> <p>.....</p>
<p><b>Q5</b> This standard meets my needs: (<i>tick one</i>)</p> <p>not at all <input type="checkbox"/>      nearly <input type="checkbox"/>      fairly well <input type="checkbox"/>      exactly <input type="checkbox"/></p>	<p>.....</p> <p>.....</p> <p>.....</p> <p>.....</p>



++\*/\*\*/\*/\*=/\*/\*/\*/\*/\*++

ISBN 2-8318-7314-2

A standard linear barcode representing the ISBN number 2-8318-7314-2.

9 782831 873145

---

**ICS 33.100.10; 33.100.20**

---

Typeset and printed by the IEC Central Office  
GENEVA, SWITZERLAND